Improving Seismic Collapse Risk Assessments of Steel Moment Frame Buildings

Thesis by
John Kenneth (Kenny) Buyco

In Partial Fulfillment of the Requirements for the
Degree of
Doctor of Philosophy

CALIFORNIA INSTITUTE OF TECHNOLOGY
Pasadena, California

2018
Defended May 23, 2018

John Kenneth (Kenny) Buyco
ORCID: 0000-0002-8182-7119

ACKNOWLEDGEMENTS

I would like to start by thanking my advisor, Dr. Thomas Heaton, for giving me guidance when needed and also allowing me the freedom to the pursue research ideas that were interesting to me. In my career, I hope to emulate his persistence in pursuit of the truth, even when it is inconvenient. Thanks to the other members of my PhD Committee, Dr. John Hall, Dr. Domniki Asimaki, and Dr. Monica Kohler, for taking the time to read through and provide feedback on this dissertation.

Thanks to Dr. Anthony Massari for being an irreplaceable office-mate for two years. His willingness to share insights from his industry experience made this dissertation possible, as I came to Caltech with virtually no knowledge of seismic design. Thanks to Becky Roh for providing the processed ground motions that are used in Chapter 4 of this dissertation and for answering my many questions about engineering seismology. Thanks to Dr. Abel Dizon for providing the designs for a 55-story building that is modeled in Chapter 4 of this dissertation. Thanks to Dr. Chris Janover for getting me started with Frame-2d and for being patient with me through my countless questions about finite element modeling and seismic design when I was starting my research at Caltech. Thanks to the Drinkward family for generously providing funding for my research activities during the latter stages of my graduate studies. I was fortunate enough to meet some members of the Drinkward family and the connections run deep, from the Pacific Northwest, to Harvey Mudd, to Caltech. And thanks to the MCE department at large for giving me a family at work. I feel very fortunate to have been around you all for the last five years.

I would also like to thank my family and friends outside of work. To my parents, who remain my biggest role models to this day and who have been unconditionally supportive throughout my education. I am more thankful each day that you are my parents. To my brothers, who have been my longest-standing friends, I am proud of the men you have become, and I thank you for reminding me what life is all about, especially when my mind gets caught up with work. And lastly, to my many friends from Lakeside to Harvey Mudd to Caltech, who have stuck with me through the ups and downs, thank you for always being supportive and for listening to me go on long diatribes about earthquakes over the last five years.

This material is based upon work supported by the National Science Foundation Graduate Research Fellowship Program under Grant No. DGE-1144469. Any

opinions, findings, and conclusions or recommendations expressed in this material are those of the authors and do not necessarily reflect the views of the National Science Foundation.

ABSTRACT

It is important to be able to accurately assess seismic risk so that vulnerabilities can be prioritized for retrofit, emergency response procedures can be properly informed, and insurance rates can be sustainably priced to manage risk. To assess the risk of a building (or class of buildings) collapsing in a seismic event, procedures exist for creating one or more mathematical models of the structure of interest and performing nonlinear time history analysis with a large suite of input ground motions to calculate the building's seismic fragility and collapse risk. In this dissertation, three aspects of these procedures for assessing seismic collapse risk are investigated for the purpose of improving their accuracy.

It is common to use spectral acceleration with a damping ratio of 5%, $Sa^{5\%}(T)$, as a ground motion intensity measure (IM) for assessing collapse fragility. In this dissertation, the use of spectral acceleration with a damping ratio of 70%, $Sa^{70\%}(T)$, as an IM is investigated, with a focus on evaluating its sufficiency and efficiency. Incremental dynamic analysis (IDA) is performed for 22 steel moment frame (SMF) models with 50 biaxial ground motion records to formally evaluate the performance of $Sa^{70\%}(T)$ as an IM for highly nonlinear response and collapse. It is found that $Sa^{70\%}(T)$ is much more efficient than $Sa^{5\%}(T)$ and much more sufficient with respect to $\varepsilon(T)$ for all considered levels of highly nonlinear response. Its efficiency and sufficiency compares also compares well with more advanced IMs such as average spectral acceleration, Sa_{avg}.

When selecting input ground motions for nonlinear time history analysis, most engineers select ground motion records from the NGA-West2 database, which are processed with high-pass filters to remove long-period noise. In this dissertation, the extent to which these filters remove actual ground motion that is relevant to nonlinear time history analysis is evaluated. 52 near-source ground motion records from large-magnitude events are considered. Some records are processed by applying high-pass filters and others are processed by record-specific tilt corrections. Raw and NGA-West2 records are also considered. IDA is performed for 9-, 20-, and 55-story steel moment frame models with these processed records to assess the effects of ground motion processing on the calculated collapse capacity. It is found that if the cutoff period (T_c) is at least 40 seconds, then applying a high-pass filter does not have more than a negligible effect on collapse capacity for any of the considered records or building models. For smaller T_c (e.g. 10 or 15 seconds), it is found that the filters

sometimes have a large effect on calculated collapse capacity, in some cases by over 50%, even if T_c is much larger than T_1. Of the considered ground motions, simply using the raw, uncorrected records usually yields more accurate results than using ground motions that have been processed with $T_c \leq 20$ seconds.

For an existing building with unknown design plans, one might perform a collapse risk assessment using an archetype model for which the specific member sizes are assumed based on the relevant design code and building site. In this dissertation, the sensitivity of seismic collapse risk estimates to design criteria and procedures are evaluated for six 9-story and four 20-story post-Northridge SMFs. These SMFs are designed for downtown Los Angeles using different design procedures according to ASCE 7-05 and ASCE 7-10. Seismic risk analysis is performed using the results of IDA with 44 ground motion records and the results are compared to those of pre-Northridge models. It is found that the collapse risk of 9-story SMFs designed according to performance-based design vary by 3x, owing to differences in GMPEs used to generate site-specific response spectra. There is generally less variation in the collapse risk estimates of 20-story post-Northridge SMFs when compared to 9-story post-Northridge SMFs because wind drift limits control the design of many members of the 20-story SMFs. Differences in collapse risk between pre- and post-Northridge SMFs are found to be at least 4x and 8x for the 9- and 20-story models, respectively. Furthermore, in response to four strong ground motion records from large-magnitude events, some of the 9-story and all of the 20-story pre-Northridge SMFs experience collapse and most of the post-Northridge SMFs experience significant damage (MIDR > 0.03).

TABLE OF CONTENTS

LIST OF ILLUSTRATIONS

LIST OF TABLES

Chapter 1

INTRODUCTION

1.1 Seismic Risk

The fundamental goal of many aspects of earthquake engineering and engineering seismology is to reduce and/or accurately evaluate seismic risk. When seismic risk analysis is performed probabilistically, the results provide a frequency (or probability) of exceedance (e.g. once per 500 years) for some measure of damage or loss (e.g. structural collapse). Seismic risk is often calculated with respect to a specific structure. When defined in this manner, assessing collapse risk can be done for the purpose of evaluating if the design of a new building meets the current design code's performance objectives, determining if an existing building needs to be retrofitted, or calculating what the earthquake insurance premiums should be for a structure in order to cover expected losses. Seismic risk can also be defined to encompass a class of structures (e.g. steel moment frames) or infrastructure (e.g. water pipelines). When defined to incorporate a larger scale of assets, the results of seismic risk analysis can inform policymakers and prepare emergency responders.

The common probabilistic framework for calculating seismic risk that is used in this study follows the following steps:

1. Evaluate seismic hazard via probabilistic seismic hazard analysis (PHSA) at the site (or sites) of interest.
2. Calculate the fragility of the structure (or structures or assets) to damage (or loss) from ground motion.
3. Combine the fragility of the structure (or structures or assets) with the seismic hazard at the site (or sites) of interest to compute the seismic risk of damage (or loss).

For a specific structure and site, the above framework is relatively straightforward. Step 1 requires the combination of one or more rupture forecast models and ground motion prediction equations (GMPEs) to evaluate the frequency (or probability) of exceedance of a ground motion intensity measure (IM) at the site(s) of interest.

The user has the freedom to choose any IM so long as a GMPE exists so that the hazard can be calculated. Though simplified procedures exist, Step 2 usually entails performing a number of nonlinear time history analyses with a finite element model of the structure. The damage (or loss) variable must be defined. Often, an engineering demand parameter (EDP) such as maximum interstory drift ratio (MIDR) or peak floor acceleration (PFA) is chosen. The procedure for calculating fragility for a structure using incremental dynamic analysis (IDA) is explained in Section 2.3. In Step 3, the site's seismic hazard is combined with the structure's seismic fragility at each IM level and integrated to calculate the overall risk. The equation governing this calculation can be found in Equation 3.1 in Section 3.1.

Even though collapse risk analysis procedures have been well established, there is still room for improvement, particularly as computational power increases and allows for more computationally intensive techniques. Properly selecting an IM for nonlinear time history analysis is still an active area of research, and engineering practice often lags behind what is considered state of the art in academia. Procedures for selecting and/or modifying ground motion records for nonlinear time history analysis (NLTHA) are being added to design codes at a rapid pace as performing NLTHA with a large suite of ground motions becomes computationally more practical, so it is crucial to ensure that these input ground motions represent actual shaking that may be experienced by structures. Lastly, as performing NLTHA becomes computationally faster, there will be a greater desire to perform seismic risk analysis on a large number of structures, perhaps spanning an urban scale, but it will be difficult to create accurate models of so many structures without access to their design plans. And although the most up-to-date design codes generally reflect criteria and procedures that are deemed to be satisfactory by the current engineering community, it is important to understand how existing structures with designs based on previous generations of design codes compare to newer structures in terms of seismic safety.

1.2 Steel Moment Frames

This dissertation investigates some of the topics discussed in Section 1.1 with specific application to steel moment frame (SMF) buildings. Mid- and high-rise SMF buildings are common in areas of high seismic risk and if detailed properly are expected to perform well during earthquake shaking because of the high ductility of steel. However, after the 1994 Northridge earthquake, unexpected damage occurred in many welded beam-to-column moment connections. A number of these connections experienced brittle failure due to weld fracture, compromising

the expected ductility of the SMF system. Following the Northridge earthquake, many researchers investigated the ramifications of the observed brittle failures of welded moment connections (e.g. [1–5]). As a result of these observations and subsequent studies, SMF buildings designed and constructed after the Northridge earthquake (post-Northridge SMFs) are expected to have much more reliable moment connections and thus perform better during earthquake shaking than those designed and constructed before the Northridge earthquake (pre-Northridge SMFs).

In this dissertation, finite element models of SMFs are generated for analysis. Some of these models assume perfect moment connections while others incorporate possible brittle failure of moment connections in pre-Northridge SMFs. This is done to compare the observations made in this dissertation between SMFs with and without reliable, ductile connections. That said, the analysis methods for the studies presented in this dissertation are not unique to SMFs. Similar studies could be done with other types of lateral force-resisting systems (e.g. reinforced concrete moment frames, steel braced frames, reinforced concrete shear walls, etc.). SMFs are the focus of this study because of their ubiquity in existing mid- and high-rise buildings, the general interest in quantifying the performance of pre-Northridge SMFs, and the wealth of research that has previously been conducted into modeling the inelastic behavior of SMFs.

1.3 Description of Chapters

Chapter 2 describes the steel moment frame models used in this dissertation. It also explains how incremental dynamic analysis (IDA) is performed with a suite of ground motions to generate fragility curves for a given structure and EDP.

The next three chapters consist of three relatively distinct studies that investigate different topics related to seismic collapse risk analysis. These chapters stand alone in that the results of one chapter do not depend on the results of another. However, some references are made between chapters so that basic information is not repeated and also to reinforce common themes.

Chapter 3 investigates the use of spectral acceleration with a damping ratio of 70%, $Sa^{70\%}(T)$, as an IM for highly nonlinear response and collapse. IDA is performed for twenty-two SMF models with 50 biaxial ground motion records to formally evaluate the performance of $Sa^{70\%}(T)$ as an IM. It is compared with other advanced IMs, with particular attention paid to average spectral acceleration, Sa_{avg}.

Chapter 4 looks into the effects of long-period processing of ground motion records

on nonlinear time history analysis. Some records are processed by applying high-pass filters and others by record-specific tilt corrections. Raw and NGA-West2 records are also considered. IDA is performed for 9-, 20-, and 55-story SMFs with these processed versions of 52 near-source ground motion records.

Chapter 5 evaluates the sensitivity of seismic collapse risk estimates to SMF design criteria and procedures. Archetype 9- and 20-story post-Northridge SMFs are designed for downtown Los Angeles using ELF, RSA, and PBD procedures according to ASCE 7-05 and ASCE 7-10. Seismic risk analysis is performed using the results of IDA with 44 ground motion records. The results are compared to those of pre-Northridge models.

Chapter 2

MODELING CONSIDERATIONS

In each of the studies described in subsequent chapters, incremental dynamic analysis (IDA) is performed on steel moment frame building models using Frame-2d, a computer program that is specifically designed to calculate the seismic response of steel moment frame and braced frame buildings. This chapter describes Frame-2d, the suite of building models used in these studies, and how IDA is used to estimate fragility functions for different engineering demand parameters (EDPs).

2.1 Frame-2d

For structural analysis, finite element models of every building model are developed in Frame-2d, which uses fiber elements to model the behavior of beams and columns. The cross-section of each element is divided into fibers, as shown in Figure 2.1. Each steel fiber (numbered 1-8) has a hysteretic axial stress-strain relationship, equipped with a yield plateau and strain-hardening/softening region (Figure 2.2). Fibers 9 and 10 represent the steel deck and concrete slab, respectively, to model composite action of the beam. Fiber 9 is given the same stress-strain behavior as the beam fibers. The stress-strain behavior of Fiber 10 is elastic-perfectly plastic in compression and linear to cracking in tension. Each element is divided lengthwise into eight segments, with shorter segments near the ends to accurately model plastic hinges (Figure 2.3). Geometric nonlinearities (e.g. P-Δ) are accounted for by updating the nodal positions at each time step. Hall [2], Challa [6], Challa and Hall [7], and Hall [8] validated the special features of Frame-2d, such as panel zone modeling, nodal updating, and weld fracture, by extensive numerical testing and comparison with experimental data. Wall and foundation elements are available in Frame-2d but are not implemented here. Frame-2d is not modified for use in this dissertation except that the capability to add doubler plates of arbitrary thickness to panel zones is added. Previous versions of Frame-2d automatically added doubler plates to panel zones such that the requirements of the 1994 UBC are satisfied.

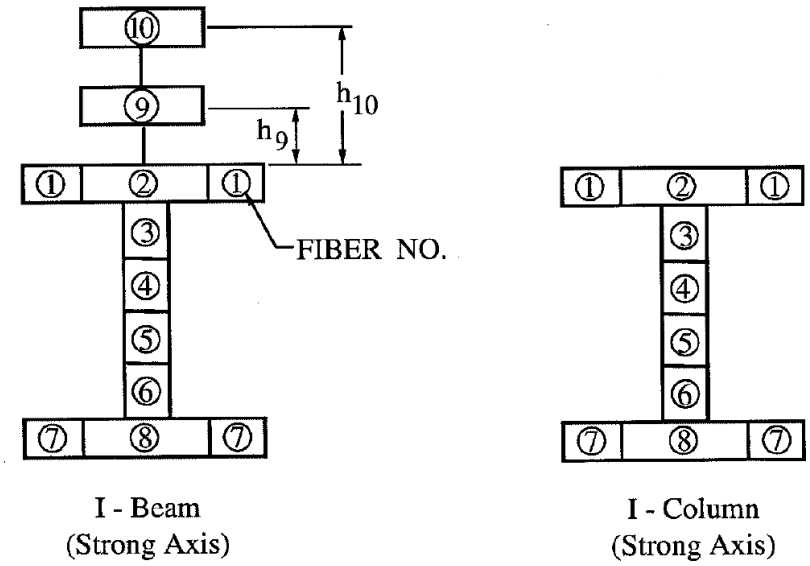

Figure 2.1: Cross section of fiber layout and labels for I-beams and I-columns in Frame-2d [9].

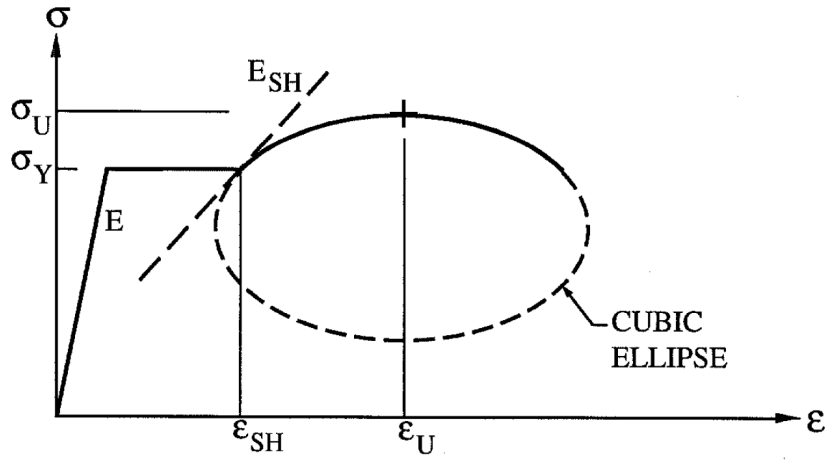

Figure 2.2: Backbone curve of stress vs. strain for beam or column fiber [9].

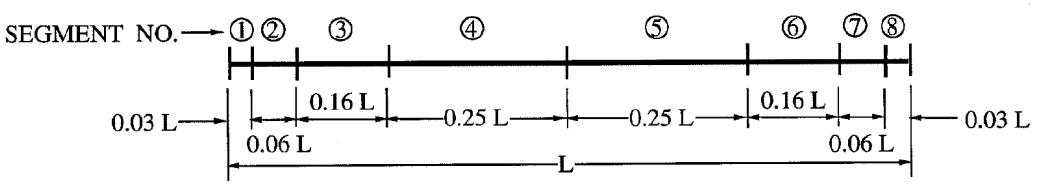

Figure 2.3: Segmentation layout and labels for beams and columns in Frame-2d [9].

To model moment connections and simple connections, Frame-2d allows the user to modify the area of individual fibers. For connection modeling, the short fibers in Segments 1 and 8 (Figure 2.3) at the ends of beams are modified. To model bolted shear tab connections, the area of the web fibers (i.e. Fibers 3-6 in Figure 2.1) are reduced to 0.3 times their original area. This is done for both moment connections and simple connections. For simple connections, the areas of the flange fibers (i.e. Fibers 1,2, 7 and 8) are reduced to zero, but for moment connections, the areas of the flange fibers are left unaltered. These fiber area modifiers are the same as those employed in Frame-2d by Bjornsson [10]. There are many different types of modern moment connections (e.g. reduced beam sections) that are prequalified for use in special and intermediate steel moment frames [11]. For simplicity, post-Northridge models are assigned the same fiber area modifiers at the connections as the pre-Northridge models, which are meant to model welded beam flanges and shear tabs bolted to the beam webs. The effects of how different types of post-Northridge connections may influence structural response is not considered in this dissertation.

The ability of Frame-2d to model weld fracture is important for modeling the behavior of pre-Northridge steel moment frames. In this dissertation, two models are developed for each pre-Northridge design: one with "perfect" moment connections ("P model") and one with pre-Northridge "brittle" moment connections ("B model"). The brittle connections model the failures of welded moment connections observed after the 1994 Northridge earthquake, in which the welds fractured at strains much smaller than expected. In B models, the short fibers at the ends of beam elements that are connected to columns via welded moment connections represent weld fibers and are assigned a random fracture strain according to a user-defined probability distribution. When a fiber fractures, it can no longer resist tension, but is allowed to resist compression if the fracture gap closes. For a beam's bottom flange, the following distribution is used, where ε_y is the fiber's yield strain: $\varepsilon_f = 0.9\varepsilon_y$, $2\varepsilon_y$, $5\varepsilon_y$, $15\varepsilon_y$, and $40\varepsilon_y$ each have a 20% probability of assignment. For a beam's top flange and web, the following distribution is used: $\varepsilon_f = 10\varepsilon_y$ and $20\varepsilon_y$ each have a 30% probability of assignment, and $\varepsilon_f = 40\varepsilon_y$ and $80\varepsilon_y$ each have a 30% probability of assignment. These fracture distributions are the same as those used by Krishnan and Muto [12] and similar to those used by Hall [8], which were calibrated to weld fracture observations in the Northridge earthquake. Note that the bottom flange weld is more susceptible to fracture than the rest of the cross-section, consistent with observations in Northridge. Frame-2d models of post-Northridge designs in this dissertation are assumed to have perfect moment connections and thus would all be

classified as P models.

In the models considered in this dissertation, Rayleigh damping is employed by specifying a damping ratio of 2% at $0.2T_1$ and T_1 for each model. It should be noted that implementing Rayleigh damping can lead to unrealistically large damping forces [13] and Frame-2d provides the capability to introduce shear dampers at each story with a capped damping force. These advanced damping features are not implemented in the models in this disseration because the results of the studies presented in this dissertation were not found to be highly sensitive to the damping implementation. Most of the results are the statistics of IDA performed with many different ground motions, and sensitivity analyses performed by the author on the statistics of some of these results with Rayleigh damping vs. "capped damping" found that the differences were small and did not change the conclusions. As such, in lieu of justifying a choice of particular capped damping forces, Rayleigh damping is implemented here for simplicity.

In addition to the relatively simple damping implementation, the models used in this study contain a number of other simplifying assumptions. For example, cyclic degradation and local flange buckling can be important for accurately simulating collapse (e.g. [14]), but neither effect is captured in Frame-2d. Soil-structure interaction can be modeled in Frame-2d with nonlinear foundation springs, but this feature is not considered in this dissertation. Soil-structure interaction can be important to incorporate for accurate results in nonlinear time history analysis, though for the above-ground responses of relatively flexible SMFs analyzed in this dissertation, the effects of not including soil-structure interaciton are probably modest [15]. To in part account for these simplifying modeling assumptions, a range of EDPs other than collapse that represent nonlinear response are considered in this dissertation, as discussed in Section 2.3.

2.2 Steel Moment Frame Models

In the building models analyzed in this dissertation, three different grades of structural steel are modeled: A36, A572, and A992. The expected properties of these three grades are used in analysis. For all three grades E = 200 GPa (29,000 ksi), E_{SH} = 4.0 GPa (580 ksi), σ_{RES} = 41 MPa (6.0 ksi), and G = 80 GPa (11,600 ksi). Other relevant properties for modeling in Frame-2d are given in Table 2.1. Values of σ_Y, σ_U, and τ_Y for A36 and A572 are taken from a study by the Steel Shape Producers Council [16]. Values of ε_{SH} and ε_U for A36 are taken from Hall [9] and values for

A572 are assumed to be identical to those of A36. Properties of A992 are taken from the flange properties reported by Arasaratnam et al. [17]. Values of E_{SH} and σ_{RES} are not reported by Arasaratnam et al. [17], so values used by Hall [9] for A36 are also used for A992. For the slab concrete, as in Hall [9], E_C = 20.7 GPa (3,000 ksi), σ_{CY} = 27.6 MPa (4 ksi), and $\sigma_{CF} = 0.1\sigma_{CY}$.

Table 2.1: Expected steel properties for different steel grades used in Frame-2d.

Steel Grade	σ_Y (MPa)	σ_U (MPa)	ε_{SH}	ε_U	τ_Y (MPa)
A36	339	472	0.012	0.16	165
A572	397	521	0.012	0.16	230
A992	444	577	0.0042	0.138	256

Models for Chapter 3

In Chapter 3, the considered building models were developed for the SAC Joint Venture by Gupta and Krawinkler [18] and Lee and Foutch [19], who designed 3-, 9-, and 20-story steel moment frame buildings based on the 1973, 1985, and 1994 UBC for a site in downtown Los Angeles. It should be noted that the 1994 UBC designs are considered "pre-Northridge" by the aforementioned citations. That is, seismic design requirements for steel moment frames that were added after observations from the 1994 Northridge earthquake were not included in the designs that were developed according to the 1994 UBC. To more easily meet strong-column/weak-beam requirements, the moment frames were designed with A36 steel for the girders and A572 steel for the columns. The 1973 UBC does not include seismic drift provisions, but according to Lee and Foutch [19], in practice, wind drift limits were sometimes used as seismic drift limits to seismic design loads for steel moment frames. Thus, Lee and Foutch [19] developed two designs with and without seismic drift limits according to the 1973 UBC for the 3- and 9-story configurations. There is only one 1973 UBC 20-story design because the wind drift limit to wind design loads controlled its member properties. In total, four 3-story, four 9-story, and three 20-story building designs are analyzed in Chapter 3. Member sizes of these models are available in the aforementioned citations.

All the designs of a given height have the same geometry. Elevation views of the 3-story, 9-story, and 20-story designs are shown in Figure 2.4. The above-ground height of the 3-story models is 11.9 meters (39 feet), of the 9-story models is 37.2 meters (122 feet), and of the 20-story models is 80.8 meters (265 feet). The boundary conditions are also shown in Figure 2.4. The base of every 3-story model is assumed to be fixed. Each of the 9-story models has a one-story basement with pinned

boundary conditions. Each of the 20-story models has a two-story basement with pinned boundary conditions. Plan views of the designs are shown in Figure 2.5, which also shows the dimensions of the different designs and the locations of the perimeter moment frames. On each side in the N-S direction, the 3-story models have 6 moment connections per story, the 9-story models have 9 moment connections per story, and the 20-story models have 10 moment connections per story.

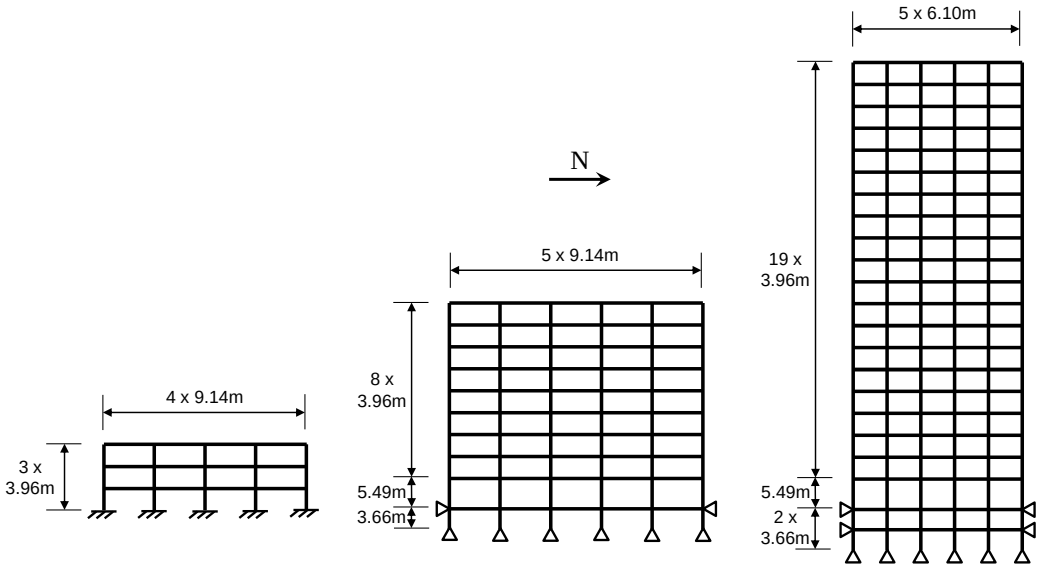

Figure 2.4: Elevation view of N-S direction of 3-, 9-, and 20-story designs.

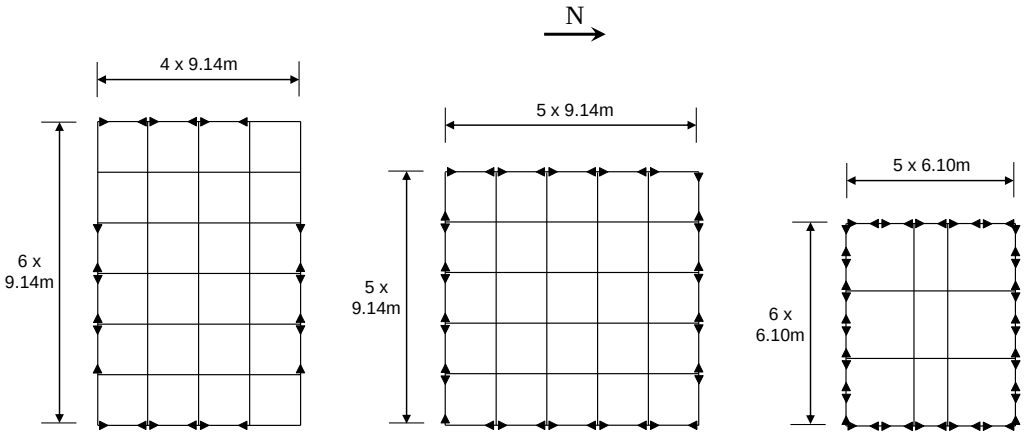

Figure 2.5: Plan view of 3-, 9-, and 20-story designs. Moment connections are indicated by triangles.

Frame-2d models are two-dimensional, so models of these designs are created only in the N-S direction and ground motions are applied in this direction. To take advantage of the symmetry of the designs, half-models are created in Frame-2d that consist of only one perimeter moment frame and one interior gravity frame, which are linked together at each floor by a connecting element. A connecting element between two frames for a single floor constrains the average horizontal displacements of the joints of each of the two frames to be the same. As seen in Figure 2.5, there are two gravity frames in the N-S direction in the 20-story models, but there are four in the 9-story models and five in the 3-story models. As such, to create a half-model in Frame-2d of the 20-story designs, members sizes of the gravity frames are not modified. However, for the 3- and 9-story models, member sizes of the gravity frames must be scaled to represent all the gravity frames. This is further complicated by the penthouse on the roof, which, as described by Gupta and Krawinkler [18], results in slightly larger column sizes in gravity frames beneath the penthouse compared to those in gravity frames not beneath the penthouse. It was determined from sensitivity analysis in Frame-2d by the author that the gravity frames not beneath the penthouse are approximately 95% as stiff as those that are beneath the penthouse. As such, in the Frame-2d models of the 3-story designs, the gravity frame consists of member sizes from beneath the penthouse scaled by 2.45 and in the Frame-2d models of the 9-story designs, the gravity frame consists of member sizes from beneath the penthouse scaled by 1.95.

Boundary conditions, gravity loads, and seismic masses are applied in accordance with the modeling conducted by Gupta and Krawinkler [18]. Gravity loads and seismic masses are calculated from floor and roof dead loads of 4.60 kPa (96 psf) and 3.97 kPa (83 psf), a roof penthouse dead load of 5.55 kPa (116 psf), a cladding load of 1.20 kPa (25 psf), and reduced floor and roof live loads of 0.96 kPa (20 psf). These loads include member weight. For mass calculations, the floor dead load is 4.12 kPa (86 psf). Gravity loads are applied directly to the columns and the seismic mass of each story is assigned directly to the nodes of that story. The floor-by-floor seismic masses are provided by Gupta and Krawinkler [18]. The seismic weight, W, of Frame-2d 3-, 9-, and 20-story half-models are 14,460 kN (3,250 kips), 44,170 kN (9,930 kips), and 54,270 kN (12,200 kips), respectively. The expected material properties (Table 2.1) of A36 and A572 steel are assigned to the beams and columns, respectively.

Recall that Frame-2d models can incorporate weld fracture. As such, from these 11 designs, 22 models are generated - one P model and one B model for each design. Pushover analysis is performed for all 22 building models, calculated according to the procedure described by Hall [9]. The building models used in pushover analysis are modified so the masses assigned to the horizontal degrees of freedom are proportioned in accordance with equivalent first-mode seismic design loads according to ASCE 7-10 [20]. To model a quasi-static lateral load, a horizontal ground acceleration is applied to this modified building model at a linearly increasing, slow rate of 0.3 g per minute and the response is evaluated dynamically. This method introduces some dynamic vibrations in the building model, particularly after abrupt rupture of welds in the models with brittle connections, but also models strength loss without issues related to non-uniqueness. Damping is removed so as not to introduce large damping forces near the end of the strength-degrading part of the curve.

Figure 2.6 shows the pushover curve (base shear vs. roof drift) for each of the 22 models. Each design is denoted first by the number of stories (3, 9, or 20) and then by the design year (94, 85, or 73). 1973 UBC designs that did and did not incorporate seismic drift limits are denoted “wD” and “noD,” respectively. The solid lines represent the P models and the dashed lines represent the B models. The B models are generated probabilistically, so the shown pushover curves for the B models represent only one realization for each design. The global behavior of the B models do not usually vary dramatically from realization to realization.

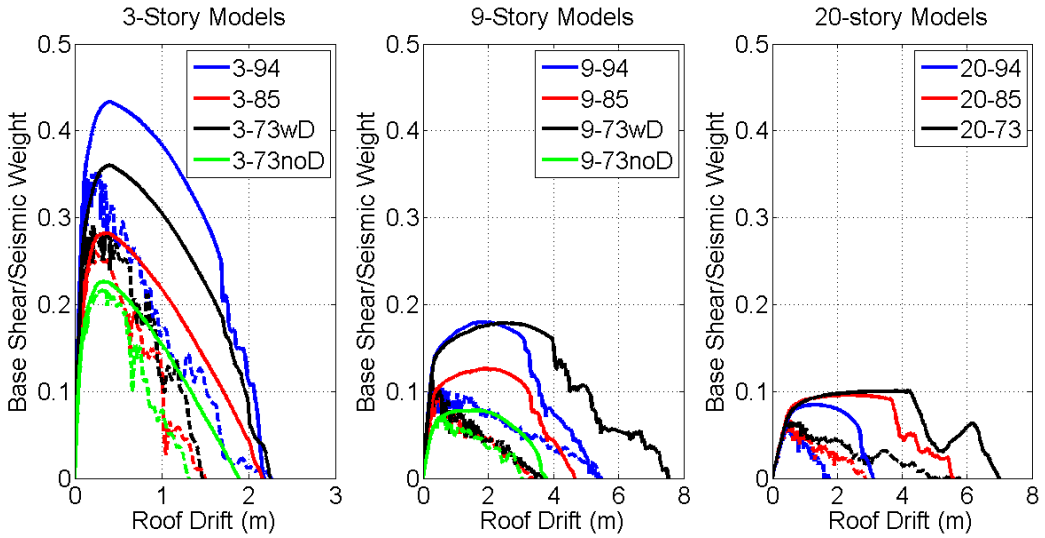

Figure 2.6: Pushover curves of models analyzed in Chapter 3. Solid lines represent P models and dashed lines represent B models.

There are a few interesting observations to be made from the pushover curves. As expected, the P models are all stronger and more ductile than the corresponding B models. There is also significant variation in the shape of the pushover curves based on the design. The models based on the 3-73noD and 9-73noD designs have the least strength relative to other designs with the same height. This makes sense, as they were designed with no seismic drift requirements.

For the 3- and 9- story models, the models designed according to the 1994 UBC tend to be the among the strongest and most ductile, but the opposite is true among the 20-story models. In particular, the ductility (which can be qualitatively measured by the maximum roof drift in the pushover curve) of the models based on the 20-94 design are much less than those of the 20-73 and 20-85 designs. This is because the 20-73 design was completely controlled by wind loads while the 20-85 design was only partially controlled by wind loads and the 20-94 design was completely controlled by seismic loads. The vertical distribution of wind and seismic loads are different, which resulted in the 20-73 design having extremely large sections near the base when compared to 20-85 design and especially when compared to 20-94 design. Conversely, the 20-73 and 20-85 designs have relatively smaller sections near the roof when compared to the 20-94 design. The observation that P-Δ effects initiate collapse during pushover analysis at a smaller roof drift in the 20-94 design than in the 20-85 or 20-73 design is also seen in the pushover analysis performed by Lee and Foutch [19].

In pushover analysis, these differences manifest themselves in the collapse mechanisms, shown in Figure 2.7. Figure 2.7(a) shows the drifts of each story of the 3-story models during pushover analysis when the roof drift reaches 1.5 meters. Figures 2.7(b) and Figure 2.7(c) show the same plots for the 9- and 20-story models when the roof drift reaches 2 meters. Like in Figure 2.6, the P models are indicated by solid lines and the B models are indicated by dashed lines. For both the P and B models, the 20-73 design experiences most of its deformation in the upper stories, most of the deformation of the 20-85 P and B models occurs at the mid-height, while deformation of the 20-94 P and B models is concentrated near the base. Since P-Δ effects eventually cause collapse of the 20-story models in pushover analysis, the onset of global collapse occurs more quickly if the collapse mechanism is in the lower stories because there is more mass above these stories with which to produce the overturning moment. This explains why the 20-94 models collapse at a much lower roof drift than the other models. Note that the collapse mechanisms of the 3- and 9-story models during pushover analysis are relatively similar regardless of the design.

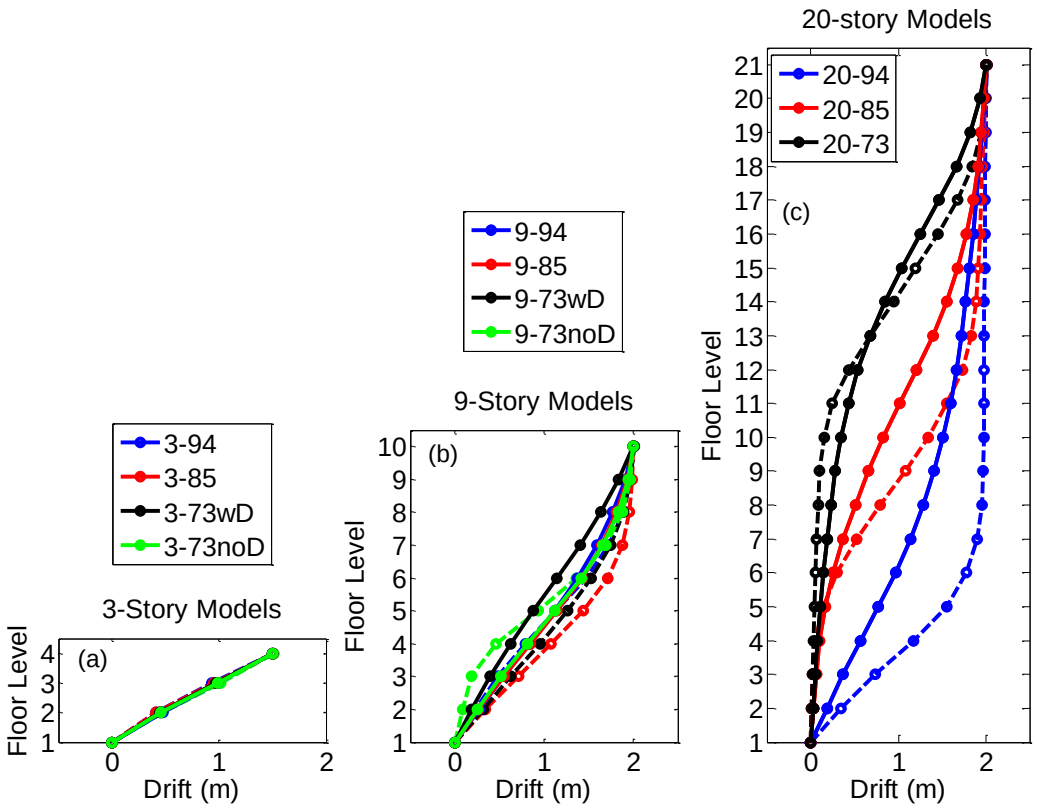

Figure 2.7: Drifts of each story during pushover analysis when the roof drift is 1.5 meters for the 3-story models and 2 meters for the 9- and 20-story models analyzed in Chapter 3. Solid lines represent P models and dashed lines represent B models.

To summarize the models, Table 2.2 shows the maximum base shear ($V_{\max}$), defined as the maximum of the pushover curve, normalized by W for each building model along with T_1. The reported $V_{\max}/W$ values for the B models are the mean of three pushover analyses with different fracture strain assignments, which were generated independently. Among the P models of different designs, the $V_{\max}/W$ values are generally similar to those found via pushover analysis by Lee and Foutch [19]. The only notable difference is that the values of $V_{\max}/W$ for the 20P-85 and 20P-73 models reported here are about 10-15% larger than those found by Lee and Foutch [19]. Lee and Foutch do not provide information about the collapse mechanisms of these pushover analyses, so such a comparison cannot be made to explain the discrepancies. Different plastic hinge modeling techniques (e.g. bilinear rotational springs vs. fiber elements) may partially explain the discrepancies, but more work would need to be done to fully characterize these effects.

Table 2.2: Building model characteristics of models analyzed in Chapter 3.

		V_{max}/W	
Design	T_1 (s)	P model	B model
3-94	0.78	0.433	0.340
3-85	0.94	0.282	0.242
3-73wD	0.84	0.360	0.298
3-73noD	1.01	0.226	0.211
9-94	1.88	0.180	0.115
9-85	2.16	0.126	0.089
9-73wD	1.83	0.179	0.117
9-73noD	2.72	0.078	0.065
20-94	3.50	0.085	0.062
20-85	3.21	0.096	0.064
20-73	3.10	0.101	0.066

Models for Chapter 4

In Chapter 4, six steel moment frame models are used in analysis, denoted 9P, 9B, 20P, 20B, 55P, and 55B. The 9P, 9B, 20P, and 20B models are the same as the previously-described P and B models based on the 9-94 and 20-94 designs. The 55P and 55B models are P and B models, respectively, of a 55-story steel moment frame building designed according to the 1994 UBC with a procedure and floor plan similar to that presented in Chapter 8 of Dizon [21]. This building was designed by the author of Dizon [21] and was generously provided to the author of this dissertation for analysis. The section properties and design information are provided in Appendix A. The above-ground height of the 55-story design is 220.0 meters (722 feet).

For computational efficiency, the gravity frames on the interior of the 55-story design are not included. This assumption may be non-conservative. The gravity loads that would be assigned to these frames are assigned to special columns in Frame-2d with no lateral stiffness so that the P-Δ effects accurately incorporate these gravity loads. Material properties for A572 steel are assigned to the beams and columns as this grade of steel is assumed in design. A fixed base is the assumed boundary condition with no basement stories modeled. T_1 for the 55P and 55B models is 6.12 seconds. Pushover curves comparing all six steel moment frame models used in Chapter 4 can be found in Figure 4.5(a).

Models for Chapter 5

In Chapter 5, designs are made of 9- and 20-story steel moment frames with the same geometry as the 9- and 20-story steel moment designs used in Chapter 3. The

modeling of SMFs in Chapter 5 is done identically to those in Chapter 3 except A992 steel is used in the design of the beams and columns because the designs are made in accordance with more recent building codes. As such, the expected properties for A992 steel (Table 2.1) are used in modeling. The design of these buildings and a discussion of their relative structural properties are an important result of Chapter 5, so that information is omitted here and instead can be found in Sections 5.4, 5.5, and 5.6.

2.3 Incremental Dynamic Analysis and Fragility Functions

In every chapter in this dissertation, IDA is performed with a suite of ground motions and a set of building models. In most applications, the purpose of IDA is to generate a fragility function (or curve) for each building model for a given EDP. For a single ground motion and building model, IDA is performed by multiplying the ground motion by incrementally larger scale factors and performing nonlinear time history analysis with these scaled ground motions on the building model. In this manner the capacity of the building model to the ground motion for a specific EDP can be evaluated. For example, the "collapse capacity" of the 3P-85 model (P model of the 3-85 design) to the 1995 Kobe NIS 000 ground motion record can be calculated using IDA as shown in Figure 2.8. In this case, the input ground motion is scaled with increments of 0.05 and the collapse capacity is found to be a scale factor of 6.25. The y-axis can be expressed as some ground motion intensity measure (IM) other than the scale factor (e.g. peak ground acceleration), in which case the collapse capacity is expressed as the IM value. Note that the capacity of the model to EDPs other than collapse (e.g. a maximum interstory drift ratio of 0.1) could be computed in the same manner. In this disseration, the capacity of a model to an EDP for a given ground motion is defined to correspond to the smallest scale factor for the ground motion that induces the EDP.

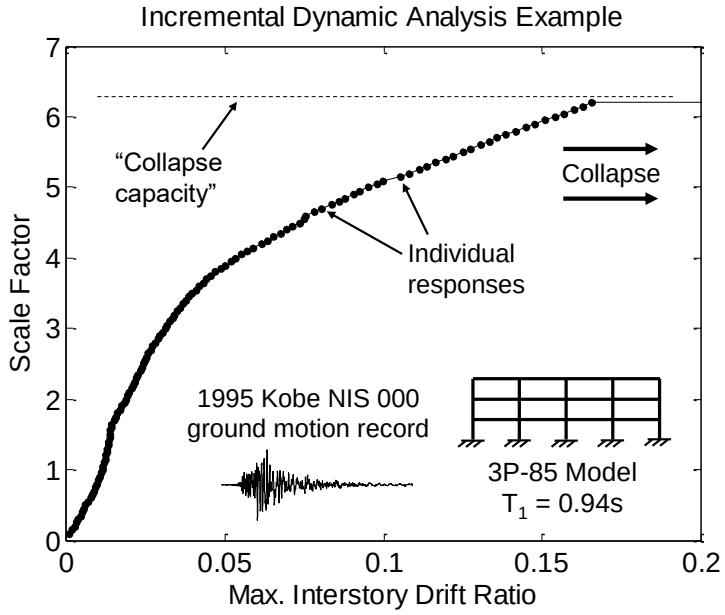

Figure 2.8: Example of incremental dynamic analysis with the 3P-85 model and the 1995 Kobe NIS 000 ground motion record.

In Chapters 3-5, particular attention is paid to a set of four EDPs representing highly nonlinear response. Three of these EDPs are maximum interstory drift ratio (MIDR) values: 0.03, 0.06, and 0.1. MIDR = 0.03 is chosen because it is the collapse prevention limit for many performance-based applications (e.g. [22, 23]). MIDR = 0.06 is approximately the ultimate limit of modern ductile moment connections [11], at which point failure due to local flange buckling may occur. This effect is not captured by Frame-2d. MIDR = 0.1 corresponds to a severely damaged building and is considered by some to be the default global collapse limit [19]. The fourth considered EDP is "collapse," defined in this dissertation to be the point at which the building model succumbs to P-Δ collapse in simulation, where the interstory drifts of the model increase with bounds, eventually leading to numerical instability. It should be noted that all three considered MIDR values (0.03, 0.06, and 0.1) are "collapse limits" in some sense. The particular choice depends on the application, but all are investigated for completeness.

When IDA is performed for a building model with a suite of ground motions, fragility curves can be developed for a given EDP. To represent record-to-record variability, a lognormal distribution of IMs for a given EDP is assumed in this dissertation. The assumption of a lognormal distribution is standard practice and previous researchers

(e.g. [14, 24]) have found that lognormal distributions pass goodness-of-fit tests when the EDP is highly nonlinear response or collapse. Eads [24] also explored Weibull and Gamma distributions and found that the lognormal distribution fit best.

An example of a fragility curve is shown in Figure 2.9 for a suite of 50 ground motions, the 3P-85 model, and MIDR = 0.1. Here, the 5%-damped spectral acceleration evaluated at T_1, $Sa^{5\%}(T_1)$, is used as the ground motion IM. First, IDA is performed for each ground motion record and the $Sa^{5\%}(T_1)$ value at which MIDR > 0.1 is first exceeded is recorded. From this data, a lognormal cumulative distribution function can be fit to the data using the geometric mean, $\mu_{\ln}$, and lognormal standard deviation, $\sigma_{\ln}$. This cumulative distribution is also called a "fragility function" or "fragility curve." It represents the probability of exceeding some EDP given some ground motion intensity. The corresponding probability density function, $G[EDP|IM]$, is used in conjunction with seismic hazard analysis to perform seismic risk assessments. Issues concerning the calculation and application of $G[EDP|IM]$ are explored in the subsequent chapters.

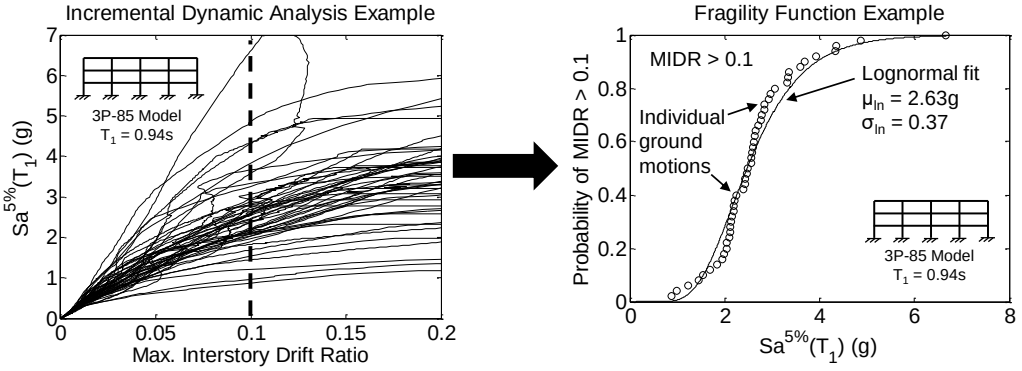

Figure 2.9: Example of generating a fragility function from incremental dynamic analysis. Here, the fragility function for MIDR = 0.1 is developed for the 3P-85 based on incremental dynamic analysis with a suite of 50 ground motion records.

Chapter 3

70%-DAMPED SPECTRAL ACCELERATION AS A GROUND MOTION INTENSITY MEASURE

In this chapter, a study is presented that investigates the use of 70%-damped spectral acceleration as a ground motion intensity measure for predicting highly nonlinear response and collapse of steel moment frames. Section 3.1 provides background information about evaluating intensity measures and summarizes past work on the development of advanced intensity measures that improve upon the more common 5%-damped spectral acceleration. Section 3.2 describes the procedure used in this study in which incremental dynamic analysis is performed with 50 ground motions and 22 building models. Sections 3.3 and 3.4 evaluate the efficiency and sufficiency, respectively, of 70%-damped spectral acceleration as a ground motion intensity measure and show that is more effective than 5%-damped spectral acceleration when the structure experiences highly nonlinear response. Section 3.5 provides a physical interpretation for 70%-damped spectral acceleration by comparing it to the base shear experienced by a building model during shaking. Section 3.6 shows how amplitude-scaling a suite of ground motions to a target value of 70%-damped spectral acceleration compares to other ground motion modification methods, such as spectrum-matching, with regards to reducing the variation in structural responses. Section 3.7 compares 70%-damped spectral acceleration to average spectral acceleration, an advanced intensity measure with similar characteristics. Lastly, Section 3.8 summarizes the conclusions of this study and suggests some avenues of future work.

3.1 Ground Motion Intensity Measures

A ground motion intensity measure (IM) quantifies the intensity of shaking of a ground motion and can have a multitude of applications in earthquake engineering. One application is the performance assessment of buildings to seismic hazards, such as in FEMA P-58 [25]. The underlying methodology for seismic performance assessment in FEMA P-58 can be expressed, with some simplifications, as the integral in Equation 3.1 [26, 27]:

$$\lambda[EDP] = \int_{IM} G[EDP|IM]\lambda[IM]dIM, \tag{3.1}$$

where EDP is an engineering demand parameter (e.g. maximum interstory drift ratio), IM is a ground motion intensity measure value (e.g. peak ground acceleration), $G[x|y]$ is a probability density function denoting the probability that x will be exceeded given y, and $\lambda[x]$ is a function representing the mean frequency of exceeding x over some time interval (e.g. 50 years). Thus for a structure at a given site, Equation 3.1 relates the seismic hazard (defined by some user-selected IM) at that site to the mean frequency of some given EDP being exceeded for that structure.

In this formulation, calculation of $\lambda[IM]$ requires seismic hazard analysis at the site of interest. This is commonly done using probabilistic seismic hazard analysis (PSHA), which requires the development of ground motion prediction equations (GMPEs) for the chosen IM. $G[EDP|IM]$ is normally estimated by performing time history analysis with a mathematical model of the specific structure when subjected to a suite of ground motions.

In selecting an appropriate IM, it is important to evaluate its *efficiency* and *sufficiency* with regards to $G[EDP|IM]$ [27]. An IM is efficient if the variability (e.g. lognormal standard deviation) associated with the cumulative distribution function $G[EDP|IM]$ is low. For example, if peak ground acceleration (PGA) is the IM and structural collapse is the EDP, then the efficiency of PGA as an IM could be measured by the lognormal standard deviation of the PGA values from a set of ground motions that are scaled to just barely induce collapse in the given structure. A more efficient IM reduces the number of ground motion time history analyses necessary to estimate $G[EDP|IM]$ to a given level of confidence, reducing the computation time necessary for performance evaluation.

An IM is sufficient if $G[EDP|IM]$ is not dependent on ground motion characteristics other than the IM, such as earthquake magnitude. A more sufficient IM broadens the set of ground motions that can be used in analyses, as other factors do not need to be considered when estimating $G[EDP|IM]$. Note that the evaluation of efficiency and sufficiency for a given IM will depend on the EDP or EDPs of interest.

In addition to efficiency and sufficiency, there are other characteristics that can make some IMs more preferable than others. For practicality, some researchers restrict choices of IMs to those for which $\lambda[IM]$ can be readily calculated using existing GMPEs and PSHA. This restriction is not considered in this study, but is important for application. Though not of statistical importance for implementation into Equation 3.1, it can also be preferable for an IM to have a physical interpretation. If an IM represents a physical quantity, the intensity of a ground motion can be more easily

communicated to a variety of stakeholders (e.g. engineers, owners, tenants, etc.).

If one was to naïvely select an IM, the first choices would probably include PGA, peak ground velocity (PGV), and peak ground displacement (PGD) because they are easy to calculate from a ground motion record. Furthermore, they have physical meanings with regards to what they are measuring about a ground motion. However, there some drawbacks to using these simple IMs. The most significant drawback is probably that these IMs are not structure-specific, so their performance as judged by efficiency and sufficiency is highly dependent on the structure of interest. For example, the PGA of a ground motion is usually an indicator of the intensity of short-period, or equivalently, high-frequency, shaking. As such, PGA often works well as an IM for predicting the response of short and stiff structures, but not as well for taller and more flexible structures. Despite the lack of structure-specificity, PGA and PGV are still somewhat common IMs. PGA is sometimes the default IM if no information is known about the structure. PGV is commonly used in Japan (e.g. [28]) as the IM for generating input ground motions for the design of tall buildings.

Spectral Acceleration

In general, the most common IM used in design and performance assessment is 5%-damped spectral acceleration, calculated at the fundamental period (T_1) of the building of interest. Calculating spectral acceleration using T_1 makes it a structure-specific IM, unlike PGA, PGV, and PGD. Spectral acceleration with damping ratio ζ and period T will be denoted here as $Sa^{\zeta}(T)$. Note that in most applications, the damping ratio ζ is dropped from the notation of spectral acceleration because the value of 5% is so prevalent, so 5%-damped spectral acceleration is often denoted $Sa(T)$, with $\zeta = 5\%$ implicitly assumed.

In general, $Sa^{\zeta}(T)$ is calculated for a ground acceleration $\ddot{u}_g(t)$ according to Equation 3.2:

$$Sa^{\zeta}(T) = \omega^2 \max_t |u(t)|, \tag{3.2}$$

where $u(t)$ is the solution to Equation 3.3:

$$\ddot{u}(t) + 2\zeta\omega\dot{u}(t) + \omega^2 u(t) = -\ddot{u}_g(t) \tag{3.3}$$

and $\omega = 2\pi/T$. Note that Equations 3.2 and 3.3 technically define the "pseudo-spectral acceleration" (PSA). In practice, the above definition is the most common for calculating the spectral acceleration of a ground motion, but some analysts may distinguish between the pseudo-spectral acceleration and the true spectral

acceleration, which is simply the maximum amplitude of $\ddot{u}(t)$ during shaking from Equation 3.3. However, for the remainder of this dissertation, the spectral acceleration of a ground motion will be equivalent to the pseudo-spectral acceleration and defined according to Equations 3.2 and 3.3.

Often the "response spectrum" of a ground motion will be generated, which is simply a plot of $Sa^{\zeta}(T)$ vs. T. Shown in Figure 3.1 are the response spectra of the ground motion recorded in the EW direction at station TCU102 in the 1999 M7.6 Chi-Chi earthquake calculated with $\zeta = 2\%$, $\zeta = 5\%$, $\zeta = 20\%$, $\zeta = 70\%$, and $\zeta = 200\%$. As ζ increases, two main changes occur in the shape of the response spectrum. First, the response spectra for small ζ have more "spikes" with lots of fluctuations as a function of T. That is, the calculation of $Sa^{\zeta}(T)$ for small ζ is very sensitive even to small variations in T. Second, the response spectra for small ζ generally have larger values for a given T.

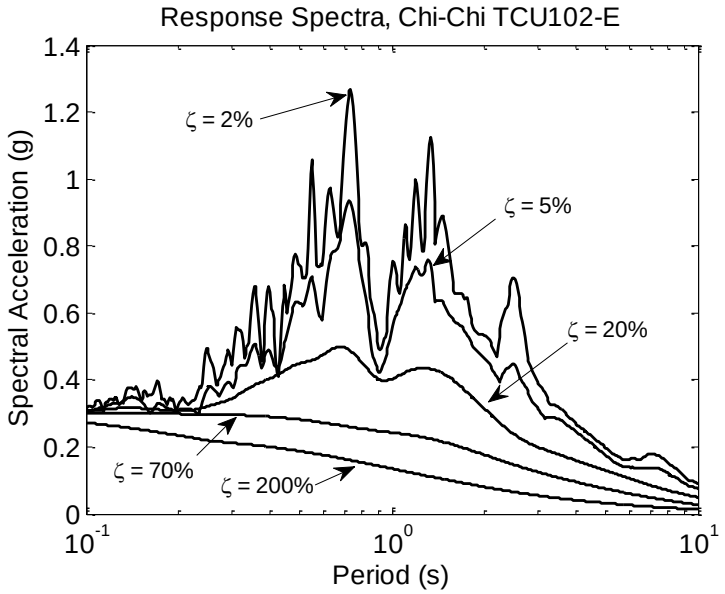

Figure 3.1: Response spectra of the Chi-Chi TCU102-E ground motion record calculated with different damping ratios.

The differences in the response spectra of a given ground motion for different values of ζ can be explained by Figure 3.2. Here, it is assumed that the ground acceleration in Equation 3.3 is a simple harmonic with angular frequency ω_g and unit amplitude. That is, $\ddot{u}_g(t) = \cos(\omega_g t)$. In this case, the steady-state solution for $u(t)$ from Equation 3.3 is $u_{ss}(t) = U_{ss}\cos(\omega_g t + \delta)$, where δ is the phase difference between $u_{ss}(t)$ and

$\ddot{u}_g(t)$ and U_{ss} is given by

$$U_{ss} = [(\omega^2 - \omega_g^2)^2 + (2\zeta\omega\omega_g)^2]^{-1/2}. \tag{3.4}$$

Shown in Figure 3.2 are plots of $\omega^2 U_{ss}$ vs. T_g/T for $\zeta = 2\%$, $\zeta = 5\%$, $\zeta = 20\%$, $\zeta = 70\%$, and $\zeta = 200\%$. This demonstrates the extent to which different periods in a ground motion $\ddot{u}_g(t)$ influence the calculation of $Sa^{\zeta}(T)$. For small values of ζ, there is a narrow "resonance peak," with a maximum value at T_g^*, where

$$\frac{T_g^*}{T} = (1 - 2\zeta^2)^{-1/2}. \tag{3.5}$$

For small values of ζ with these narrow resonance peaks, the corresponding response spectra for a ground motion will tend to have lots of spikes, as observed in Figure 3.1. Figure 3.2 also explains why the response spectra for small ζ generally have larger values for a given T: for every excitation period T_g, $\omega^2 U_{ss}$ is larger for smaller values of ζ.

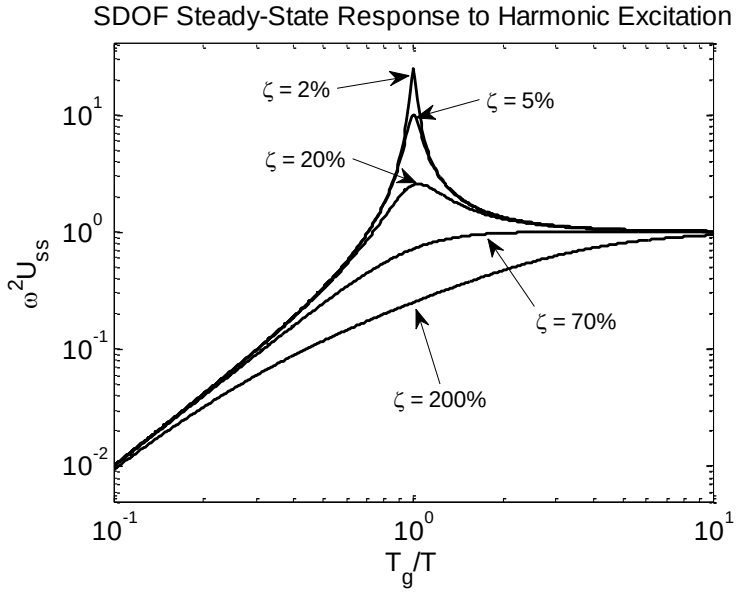

Figure 3.2: Steady-state response U_{ss} of SDOFs with period $T = 2\pi/\omega$ and different damping ratios to harmonic acceleration excitation with period T_g and unit amplitude.

An interesting feature of Equation 3.5 is that $T_g^*/T \to \infty$ as $\zeta \to 1/\sqrt{2} \approx 70\%$. This means for $\zeta > 70\%$, there is no resonance peak. Instead, $\omega^2 U_{ss}$ is always increasing as a function of T_g and asymptotically approaching a value of one. As ζ gets larger beyond 70%, the asymptotic approach to one becomes more gradual. It should be

noted that if $\zeta = 1/\sqrt{2}$, the response function shown in Figure 3.2 is equivalent to that of a low-pass 2nd-order Butterworth filter. This will be discussed further in Section 3.5.

Physically, $Sa^{\zeta}(T)$ approximately represents the maximum acceleration experienced by a ζ-damped single-degree-of-freedom (SDOF) system with period T when it is subjected to the given ground acceleration $\ddot{u}_g(t)$. When used in building codes (e.g. ASCE 7-10 [20]), $Sa^{5\%}(T_1)$ of a given ground motion multiplied by the building's mass is supposed to approximate the maximum base shear experienced by the building during excitation from the ground motion.

The use of $Sa^{\zeta}(T_1)$ as an IM dates back early in the history of earthquake engineering with the original development of the response spectrum (e.g. [29]). After researchers (e.g. [30]) recorded the approximate damping ratios of real buildings in strong ground motions, $\zeta = 5\%$ became standard for generating design spectra and calculating response spectra from recorded ground motions [31]. At this time, the goal of $Sa^{5\%}(T_1)$ was to be a physical representation of the expected response to the ground motion from a building with period T_1. That is, $Sa^{5\%}(T_1)$ and the corresponding spectral displacement $Sd^{5\%}(T_1) = (1/\omega_1^2)Sa^{5\%}(T_1)$ were defined to approximately equal the maximum base shear (normalized by building weight) and modal displacement, respectively, experienced by the building during shaking.

Advanced Intensity Measures

Within the modern framework for developing and evaluating IMs, $Sa^{5\%}(T_1)$ has been shown to generally be an effective IM [32], but there is still significant room for improvement, particularly with regards to its efficiency and sufficiency when the EDP of interest represents highly nonlinear response. Modern improvements to $Sa^{5\%}(T_1)$ have tried to account for the "spectral shape" of a ground motion's 5%-damped response spectrum in some manner. Spectral shape describes $Sa^{5\%}(T)$ of a ground motion over some range of T, often at periods longer than T_1 and sometimes at the natural periods of vibration of higher modes (i.e. T_2, T_3, etc.). Periods longer than T_1 are especially important when considering nonlinear structural response because a building will experience "period-lengthening" as it accumulates damage.

The importance of spectral shape can be seen in Figure 3.3. As a demonstration, 100 ground motion records (described in Section 3.2) are scaled to have the same value of $Sa^{5\%}(T_1)$, where $T_1 = 1.88$ seconds for the 9P-94 model. $Sa^{5\%}(T_1) = 0.53$ g is chosen as the target value so that highly nonlinear response is induced in the model.

The 100 ground motions are input into the given building model and the median maximum interstory drift ratio (MIDR) in response to the 100 ground motions is 0.031. The spectra of the 50 ground motions that induce interstory drift ratios greater than 0.031 are colored blue (above-median EDP) in Figure 3.3 while the other 50 are colored red (below-median EDP). The geometric mean of each set of 50 spectra is shown in bold color. At every period other than T_1, where the geometric mean spectra are equal, the blue geometric mean spectrum is greater than the red geometric mean spectrum. At periods sufficiently far from T_1, the blue geometric mean spectrum is about 1.5 times greater than the red geometric mean spectrum. The purpose of Figure 3.3 is to show that the response of a structure to a ground motion requires information about the response spectrum at more periods than just T_1.

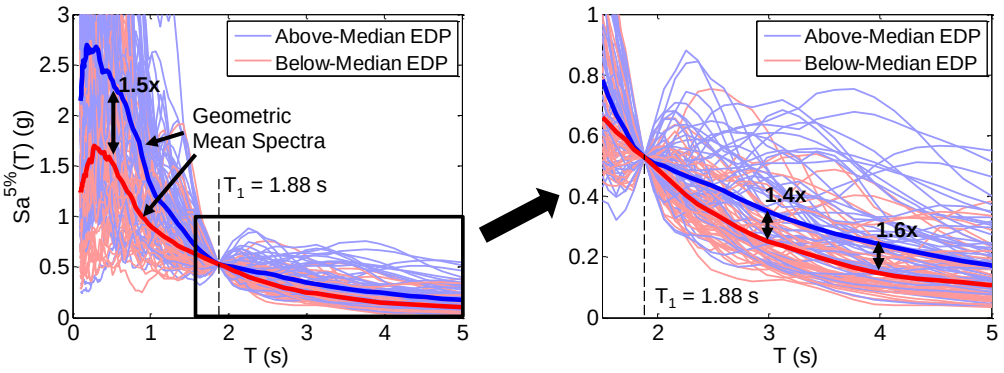

Figure 3.3: 5%-damped response spectra of 100 ground motions scaled to have $Sa^{5\%}(1.88s) = 0.53$ g. These ground motions are input into the 9P-94 model ($T_1 = 1.88s$) and the median MIDR in response is 0.031. The 50 ground motions that induce MIDR > 0.031 are colored blue and the 50 ground motions that induce MIDR < 0.0307 are colored red.

The period-lengthening phenomenon is well-studied, and the inelastic displacement spectrum $Sd_i^{5\%}(T)$, which calculates $Sd^{5\%}(T)$ for elasto-plastic SDOFs, is a direct approach that has been in use for some time [33]. However, the ubiquity of $Sa^{5\%}$ in GMPEs and subsequent seismic hazard assessments has directed most modern IMs that account for spectral shape to be some combination of $Sa^{5\%}(T)$ values at different periods or other quantities that can be extracted from current GMPEs. Haselton and Baker [34] found that, for most typical structures, $Sa^{5\%}(2T_1)$ is a more efficient IM than $Sa^{5\%}(T_1)$ when the EDP is collapse. They noted that, generally, $Sa^{5\%}(T)$ calculated with T in the range of $1.5T_1$ to $2.5T_1$ is an efficient IM for predicting collapse. Eads et al. [35] found that average spectral acceleration, Sa_{avg}, defined

as $Sa^{5\%}(T)$ averaged over a range of T from $0.2T_1$ to $3T_1$, was a more efficient and sufficient IM than $Sa^{5\%}(T_1)$ for collapse prediction. It should be noted that others (e.g. [36, 37]) have provided different definitions of average spectral acceleration (i.e. different ranges of spectral periods), but only the definition for Sa_{avg} used by Eads et al. [35] is considered in this study. Cordova et al. [38] developed the intensity measure $S^* = Sa^{5\%}(T_1) \cdot (R_{Sa})^{0.5}$, where $R_{Sa} = Sa^{5\%}(2T_1)/Sa^{5\%}(T_1)$, and found it to be more efficient than $Sa^{5\%}(T_1)$ for a wide range of MIDRs beyond the linear range. Note that the values of Sa_{avg} and S^* do not represent any physical quantities about the structural response or the ground motion despite being effecient IMs.

To date, the most common measure of spectral shape in practice is $\varepsilon(T_1)$, which combines with $Sa^{5\%}(T_1)$ to form a vector-valued intensity measure. $\varepsilon(T_1)$ of a ground motion record is the number of standard deviations by which the recorded $Sa^{5\%}(T_1)$ is greater than what a user-selected GMPE would predict as the median expected $Sa^{5\%}(T_1)$ given the source and site characteristics for the record. For every period, a GMPE will produce a median $Sa^{5\%}(T)$ and an associated standard deviation, so $\varepsilon(T)$ can be easily included in seismic risk analysis. Though $\varepsilon(T_1)$ is not a direct measure of spectral shape, if a GMPE under-predicts $Sa^{5\%}(T_1)$ (i.e. $\varepsilon(T_1) > 0$) for a ground motion record, then $\varepsilon(T)$ at surrounding periods are likely to be less than $\varepsilon(T_1)$ [39]. As such, if a set of ground motions have identical $Sa^{5\%}(T_1)$, the ground motions in that set with less positive $\varepsilon(T_1)$ are likely to cause more damage than those with more positive $\varepsilon(T_1)$. As an example, for the ground motions shown in Figure 3.3, the mean $\varepsilon(T_1)$ for the blue ground motions (above-median demand) is 0.05 while the mean $\varepsilon(T_1)$ for the red ground motions (below-median demand) is 0.74, as calculated using the "BA08" GMPEs developed by Boore and Atkinson [40]. Furthermore, $Sa^{5\%}(T_1)$ is extremely insufficient with respect to $\varepsilon(T_1)$ for collapse prediction when compared to other IMs such as Sa_{avg} [35], which means $\varepsilon(T_1)$ is important to account for if $Sa^{5\%}(T_1)$ is the IM.

Highly Damped Spectral Acceleration

It may be surprising that spectral acceleration calculated with ζ as high as 70% could be an effective IM considering researchers have found the effective damping of actual structures in earthquakes to be around 5% [30], with some finding the effective damping of severely damaged structures to be in the range of 10%-20% [41, 42], and others setting a theoretical upper bound of 40% [43]. To briefly justify the use of high damping, consider Equation 3.3. If $\zeta \to \infty$, then Equation 3.3 simplifies to

$$u(t) \approx -(1/2\zeta\omega)\dot{u}_g(t). \tag{3.6}$$

Inserting into Equation 3.2 yields

$$\lim_{\zeta \to \infty} Sa^{\zeta}(T) = \omega/(2\zeta) \max_{t} |\ddot{u}_g(t)| \propto PGV. \tag{3.7}$$

Constant scaling does not change the effectiveness of an IM, so $\lim_{\zeta \to \infty} Sa^{\zeta}(T)$ is equivalent to PGV as an IM, regardless of T. PGV has been shown to be an effective IM for predicting nonlinear response [44] and is used in Japan as the IM when scaling ground motions to a specified hazard in performance-based seismic design of high-rise buildings [28]. This leads to the somewhat surprising conclusion that $\lim_{\zeta \to \infty} Sa^{\zeta}(T)$ must also be an effective IM for predicting nonlinear response, despite the fact that $\zeta \to \infty$ is clearly not a physically realistic measure of the effective damping of any structure. As such, the fact that previous research has indicated that $\zeta = 70\%$ is not physically representative of the effective damping of structures does not preclude the possibility that $Sa^{70\%}(T)$ is an effective IM.

The benefit of highly damped spectral acceleration as an IM for predicting nonlinear response is that its calculation incorporates spectral content from many periods in the ground motion. This is clear from Figure 3.2, which shows that as ζ increases, the resonance peak becomes less and less pronounced, eventually disappearing completely. Since the goal of many advanced intensity measures is to account for a wide range of periods in a ground motion, it follows that highly damped spectral acceleration would be a logical choice as an IM.

In this study, highly damped spectral acceleration is evaluated as an IM for predicting highly nonlinear response based on its efficiency and sufficiency. 22 steel moment-resisting frame building models are considered and incremental dynamic analysis (IDA) is performed on each model with a set of 50 recorded ground motions. Based on the results, $\zeta = 70\%$ is chosen because it compares well to other values of damping and because it is approximately equal to $1/\sqrt{2}$, which is the lowest damping value for which there is no resonance peak. The performance of $Sa^{70\%}(T)$ is compared to other IMs with regards to efficiency and sufficiency, with an emphasis on $Sa^{5\%}(T_1)$ and Sa_{avg}. A physical interpretation of $Sa^{70\%}(T)$ as an estimate of the base shear experienced by a building during shaking is analyzed as well as the utility of amplitude-scaling to $Sa^{70\%}(T)$ as a method of ground motion modification.

3.2 Incremental Dynamic Analysis

The building designs considered in this study were developed for the SAC Joint Venture by Gupta and Krawinkler [18] and Lee and Foutch [19], who designed three-,

nine-, and twenty-story steel moment frame buildings based on the 1973, 1985, and 1994 UBCs. These models are described in Chapter 2, with T_1 and $V_{\max}$ for each model given in Table 2.2. Corresponding pushover curves are shown in Figure 2.6. All eleven designs are considered, each with a corresponding P and B model, so a total of 22 Frame-2d models are analyzed in this study.

The set of 50 biaxial ground motion records used in this study are from the ground motion record sets generated as part of the ATC-63 project for collapse assessment of building structures [45]. These processed recorded ground motion records are available in the PEER NGA-West2 database [46]. The records span a magnitude range of $6.50 \leq M \leq 7.90$ and a source-to-site Joyner-Boore distance (km) range of $0.0 \leq R_{JB} \leq 26.0$. Response spectra of both horizontal components of these ground motion records are shown in Figure 3.4.

Incremental dynamic analysis (IDA) [47] is performed on all 22 building models with all 50 biaxial ground motions. Frame-2d performs two-dimensional analysis, so each ground motion provides two analyses per building model. Vertical ground motion is not considered. IDA is performed for each building model and ground motion for both horizontal components by multiplying the ground motion by a scale factor and performing the dynamic analysis. The scale factor on the input ground motion starts at 0.05 and increments by 0.05 for each successive analysis. The MIDR for each dynamic analysis is recorded. For a given biaxial ground motion, scale factor, and building model, the corresponding MIDR is taken to be the maximum of the two MIDRs computed for the two horizontal components. When calculating an IM for a ground motion, the horizontal component for which the MIDR of interest is first achieved is used. Consideration in this study of only the direction for which the maximum response is recorded is similar to the procedure by Haselton and Deierlein [48] for evaluating collapse risk. As described in Section 2.3, the four EDPs that are the focus of this study are MIDR = 0.03, MIDR = 0.06, MIDR = 0.1, and collapse, each of which represents highly nonlinear response and could be considered to be a "collapse limit" depending on the application.

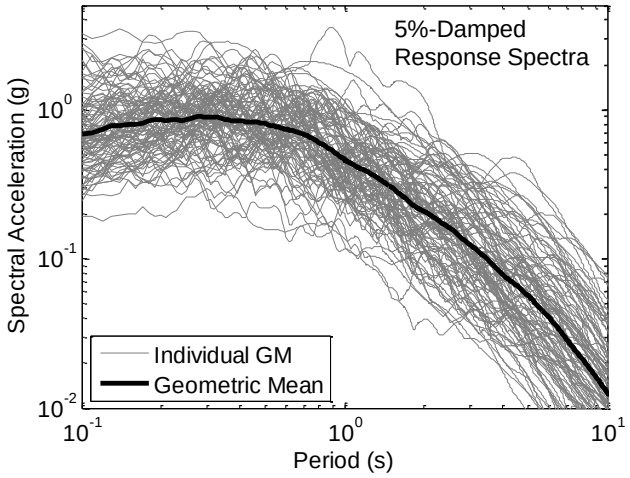

Figure 3.4: 5%-damped response spectra of both horizontal components from 50 ground motion records selected for the ATC-63 project [45] that are used in this study as input ground motions for IDA.

3.3 Efficiency of $Sa^{70\%}(T)$

In this section, the efficiency of $Sa^{70\%}(T)$ is evaluated and compared to other IMs. To calculate the efficiency for a given EDP, IM, and building model, $\sigma_{\ln}$ (the lognormal standard deviation) of the IM values of the 50 scaled ground motions that elicit the EDP in the building model is calculated. $\sigma_{\ln}$ measures the variability of the IM values that produce the same response, so a more efficient IM will have a low $\sigma_{\ln}$. For a given EDP, IM, and set of building models (e.g. the four 3P models), $\sigma_{\ln}$ is evaluated by first normalizing the IM value of each scaled ground motion by the geometric mean of the IM values for the specific model. This process is shown in Figure 3.5 for the 3P models.

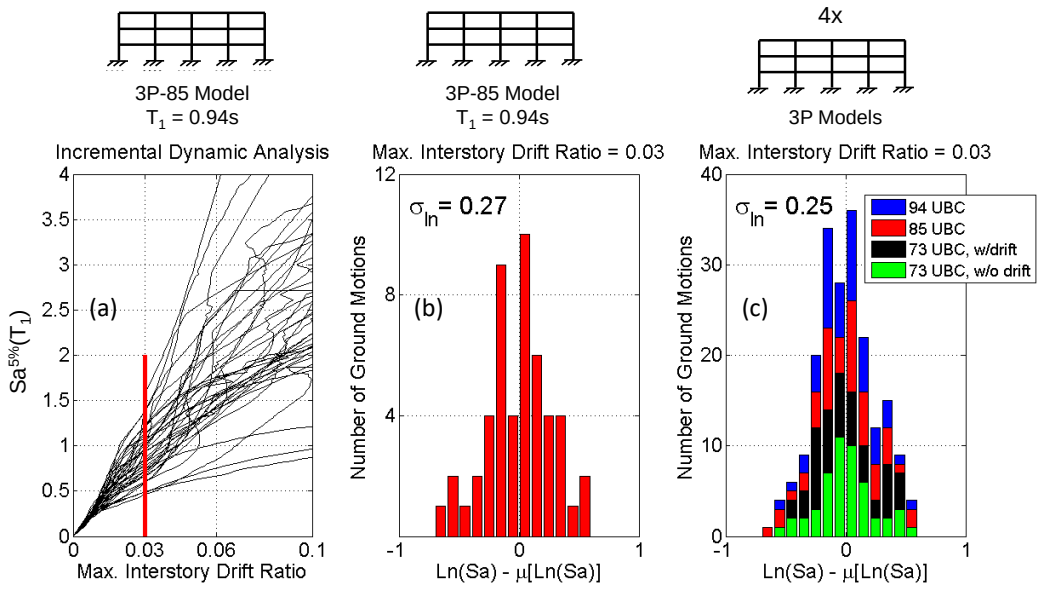

Figure 3.5: Example of the steps to calculate $\sigma_{\ln}$ for an EDP (e.g. MIDR = 0.03), IM (e.g. $Sa^{5\%}(T_1)$), and set of building models (e.g. 3P). (a) Incremental dynamic analysis is performed on the 3P-85 model for the set of 50 ground motions. (b) The values of $Sa^{5\%}(T_1)$ that induce MIDR = 0.03 in the 3P-85 model are collected and normalized by $\mu[\ln(Sa^{5\%}(T_1))]$. (c) These normalized values of $Sa^{5\%}(T_1)$ for the 3P-85 model are combined with those from the other 3P models and $\sigma_{\ln}$ is calculated.

Evaluating Efficiency of $Sa^{\zeta}(T)$ for all T and ζ

To demonstrate how the most efficient choices of T and ζ for $Sa^{\zeta}(T)$ change as MIDR increases, the 3P models are considered, whose responses are first-mode dominated. For MIDRs of 0.005, 0.03, and 0.1, contour plots of $\sigma_{\ln} = \sigma_{\ln}(T, \zeta)$ of $Sa^{\zeta}(T)$ with ζ ranging from 1% to 1,000% and T ranging from $0.1T_1$ to $3T_1$ are shown for the 3P models in Figure 3.6. For MIDR = 0.005, which is within the structure's linear range, $Sa^{\zeta}(T)$ calculated with ζ in the range of 1%-10% and $T = T_1$ yields the lowest $\sigma_{\ln}$. This makes sense, as the linear response of a 3-story building is generally dominated by its first mode. For MIDR = 0.03, the lowest $\sigma_{\ln}$ is achieved with ζ in the larger range of 10%-100% with periods from $0.8T_1$ to $1.5T_1$. For MIDR = 0.1, the lowest $\sigma_{\ln}$ occurs when $Sa^{\zeta}(T)$ is calculated with T and ζ from $1.5T_1$ to $2.5T_1$ and 50% to 200%, respectively.

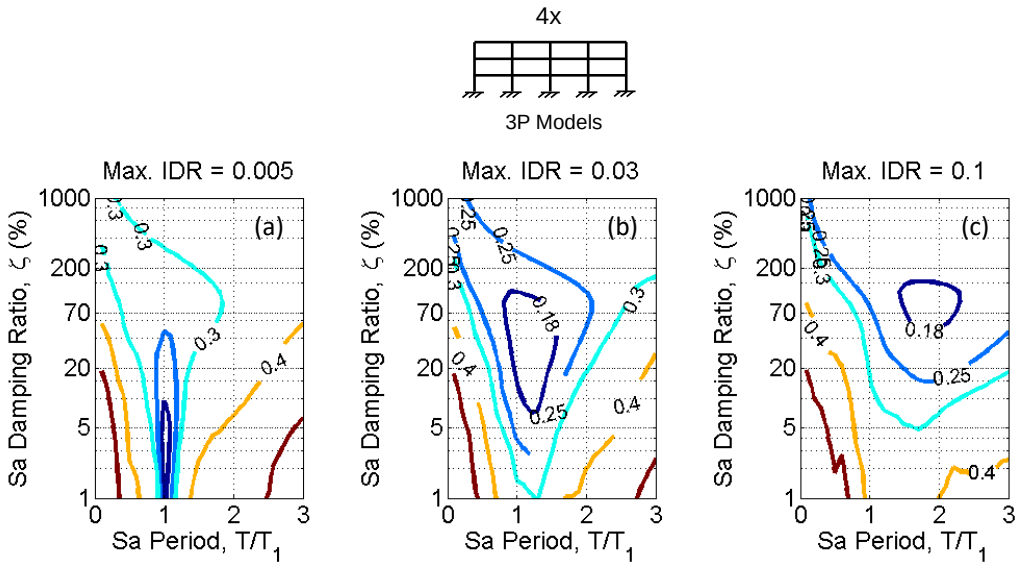

Figure 3.6: $\sigma_{\ln}$ of $Sa^{\zeta}(T)$ calculated for the 3P models with different values of ζ and T for (a) MIDR = 0.005, (b) MIDR = 0.03, and (c) MIDR = 0.01.

To succinctly show how the T and ζ values that yield low $\sigma_{\ln}$ change as MIDR increases, $\sigma_{\ln,\min}$ is defined as

$$\sigma_{\ln,\min} = \min_{T,\zeta} \sigma_{\ln}(T, \zeta) \tag{3.8}$$

for MIDRs ranging from 0.005 to 0.1. Then, to visualize the (T,ζ) pairs that produce the most efficient $Sa^{\zeta}(T)$ for the 3P models, Figure 3.7 shows a contour for each MIDR such that each contour encloses the set of (T,ζ) pairs for which $\sigma_{\ln} \leq 1.05\sigma_{\ln,\min}$. Each contour area thus represents a region of low $\sigma_{\ln}$, for which choosing any (T,ζ) pair in that region will achieve nearly the minimum possible $\sigma_{\ln}$ for the associated MIDR.

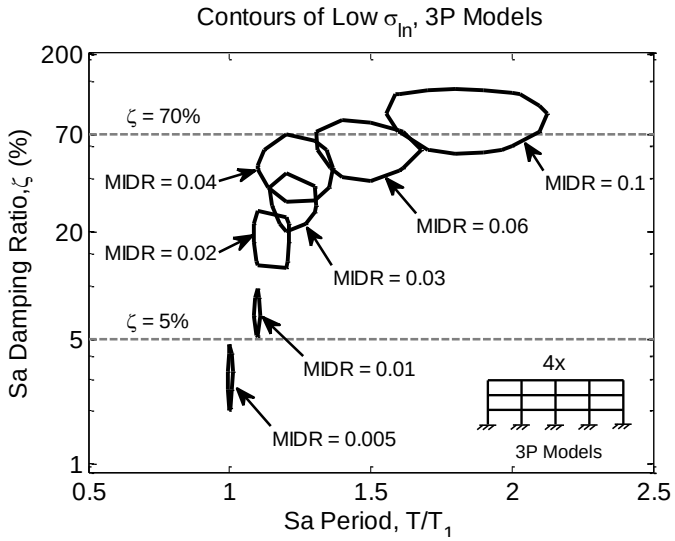

Figure 3.7: Contours representing $\sigma_{\ln} \leq 1.05\sigma_{\ln,\min}$ for each considered MIDR, ranging from 0.005 to 0.1. Results from the 3P models are shown here.

As seen in Figure 3.7, the regions of low $\sigma_{\ln}$ for the 3P models exhibit a clear trend as MIDR increases. For moderate drifts (MIDR = 0.005 and 0.01), the regions are very small and have ζ less than 10% with $T \approx T_1$. For large drifts (MIDR = 0.02, 0.03, and 0.04), the regions move upwards to ζ from 20% to 70% and become larger, indicating that many (T,ζ) pairs can yield low $\sigma_{\ln}$. For extremely large drifts, nearing global collapse (MIDR $\geq$ 0.06), the regions become even larger and expand to the right, indicating that a large range of ζ around 70% and periods around $1.5T_1$ to $2T_1$ will achieve low $\sigma_{\ln}$ at these drift levels.

The statistics from all building models are combined to develop the contours of low $\sigma_{\ln}$ in Figure 3.8. The two plots in Figure 3.8 show the regions of low $\sigma_{\ln}$ for MIDR = 0.03, MIDR = 0.06, MIDR = 0.1, and collapse for all eleven P models and all eleven B models. MIDRs lower than 0.03 are not included because higher-mode effects cause distortions in these contours when statistics from the 9- and 20-story models are included. The regions of low $\sigma_{\ln}$ for the P models all contain ζ = 70% at some T between T_1 and $2T_1$. As the EDP increases in severity, the associated contours become larger while moving upwards and to the right, indicating that longer T and larger ζ achieve lower $\sigma_{\ln}$. For the B models, most of the same observations hold true. However, for MIDR = 0.03 the contour of low $\sigma_{\ln}$ does not reach ζ = 70%. Furthermore, the contours for MIDR = 0.1 and collapse are not to the right of the contour for MIDR = 0.06, but are instead slightly to the left and bit larger. The results

from these plots imply that, when T is chosen appropriately, $Sa^{70\%}(T)$ is generally an efficient IM for predicting highly nonlinear response.

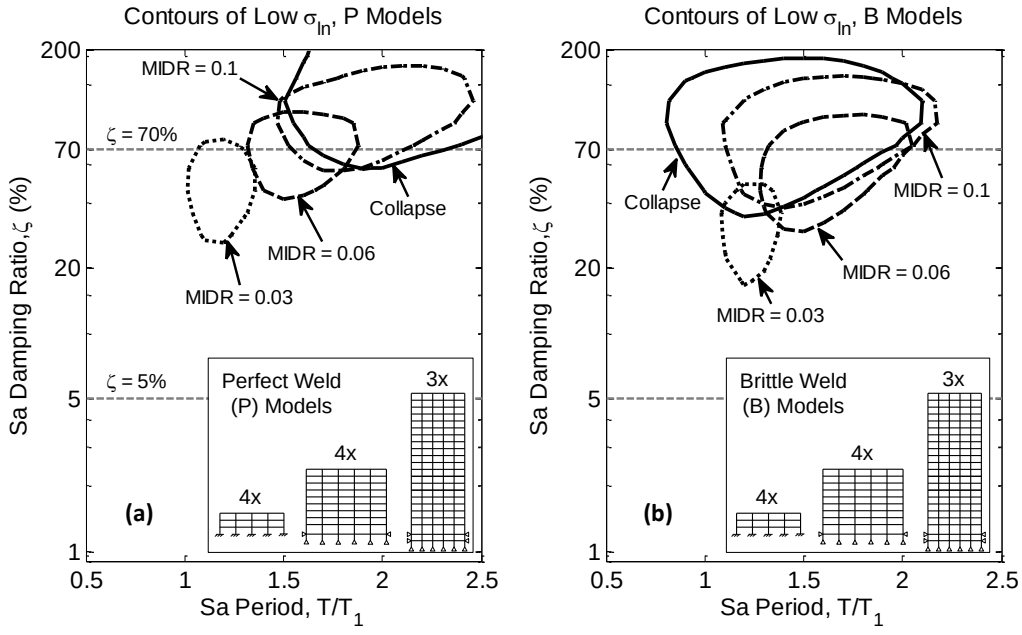

Figure 3.8: Contours representing $\sigma_{\ln} \leq 1.05\sigma_{\ln,\min}$ of $Sa^{\zeta}(T)$ for four EDPs: MIDR = 0.03, MIDR = 0.06, MIDR = 0.1, and collapse. Results from all of the P and B models are shown in (a) and (b), respectively.

Even though $Sa^{70\%}(T)$ is being investigated here, it should be noted that $Sa^{\zeta}(T)$ calculated with ζ slightly greater than and less than 70% also appear to have low $\sigma_{\ln}$, sometimes lower than $\sigma_{\ln}$ for ζ = 70%. Despite this, ζ = 70% is chosen as the focus of this study for three reasons. First, the difference in $\sigma_{\ln}$ at large drifts between $Sa^{70\%}(T)$ and, for example, $Sa^{50\%}(T)$ or $Sa^{100\%}(T)$ is generally small when compared $\sigma_{\ln}$ for $Sa^{5\%}(T)$. This means that, in general, as long as ζ is high enough, the particular value does not have a large effect on $\sigma_{\ln}$. Second, as previously observed, for nearly all considered highly nonlinear EDPs and building models, $Sa^{70\%}(T)$ has a low $\sigma_{\ln}$ for a range of T between T_1 and $2T_1$. So even though for a particular building model and EDP there may be a better choice for ζ that produces a lower $\sigma_{\ln}$, calculating $Sa^{\zeta}(T)$ with ζ = 70% will give a result that is close to the best for a wide range of building models and EDPs, indicating robustness. Lastly, as will be explained in Section 3.5, $Sa^{70\%}(T)$ is effectively equivalent to the peak acceleration of a record after it is filtered by a low-pass 2nd-order Butterworth filter, making it a special damping ratio independent of its application to building response.

This gives $Sa^{70\%}(T)$ a physical interpretation, which will be discussed further in Section 3.5.

Efficiency of $Sa^{70\%}(T)$ Compared to Other IMs

In Figures 3.9 and 3.10, $\sigma_{\ln}$ of $Sa^{70\%}(T_1)$ and $Sa^{70\%}(1.5T_1)$ are compared to that of other ground motion IMs, calculated based on the results from all models. The IMs compared to $Sa^{70\%}(T)$ are $Sa^{5\%}(T_1)$, $Sa^{5\%}(1.5T_1)$, $Sa^{20\%}(T_1)$, Sa_{avg}, Sd_i, and PGV. While PGV is a relatively simple IM, Sa_{avg} and Sd_i are the state-of-the-art in terms predicting highly nonlinear response. Sa_{avg} is the geometric mean $Sa^{5\%}(T)$ of a ground motion with T ranging from $0.2T_1$ to $3T_1$ calculated with a period increment of 0.01 seconds [35]. Sd_i is calculated in the same way as $Sd^{5\%}(T_1)$, where $Sd^{5\%}(T) = (1/\omega^2)Sa^{5\%}(T)$, except the simulated SDOF undergoes perfectly-plastic inelastic deformation when the displacement exceeds a specified yield point. The specified yield point is calculated based on each building's pushover curve according to Aslani and Miranda [49] and ATC-40 [43]. For a fair comparison, only the P models are considered for Sd_i, as Sd_i implicitly assumes that the building model is ductile and thus is not well-equipped to predict the response of a building model with brittle welds. $Sa^{5\%}(1.5T_1)$ is included because its calculation is a more standard method for accounting for period-lengthening. $Sa^{20\%}(T_1)$ is included because $\zeta = 20\%$ represents a more physically realistic level of damping that accounts for energy dissipation due to hysteresis during severe damage. Note that while PGV requires no information about the building model, the Sa-based IMs require the building period and Sd_i requires both the building period and the building's pushover curve.

Figures 3.9 and 3.10 show histograms of the IM values from which $\sigma_{\ln}$ is calculated for all P and all B models, respectively, for the considered IMs and considered EDPs: MIDR = 0.03, MIDR = 0.06, MIDR = 0.1, and collapse. In the histograms, the "geometric mean normalized logarithm" of each IM is plotted, defined here as $\ln(IM) - \mu[\ln(IM)]$, where $\mu[\ln(IM)]$ is calculated for each building model before combining the statistics with those of other models of the same model set. In every plot, each IM is ranked according to its corresponding $\sigma_{\ln}$, with the most efficient IMs at the top.

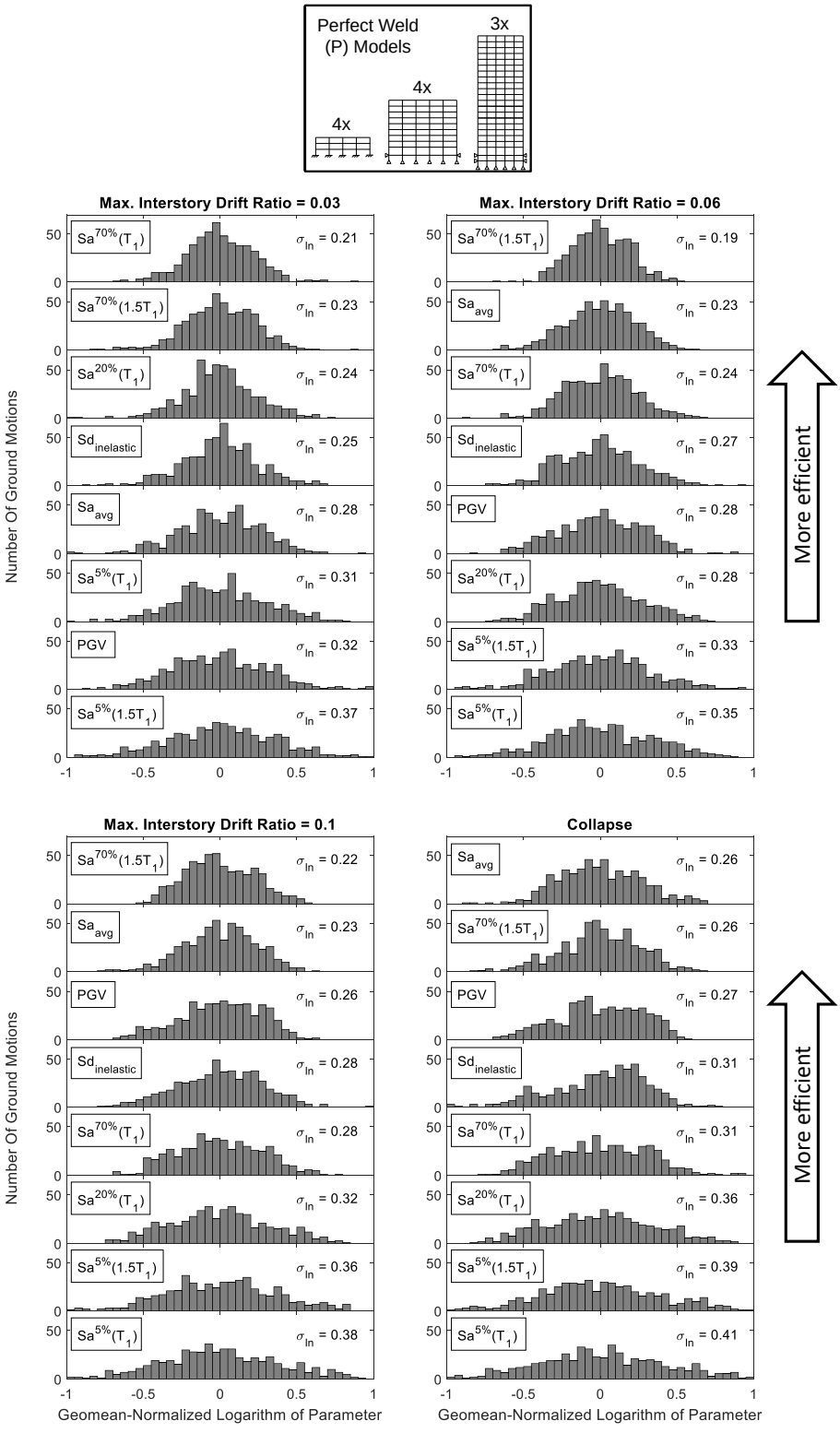

Figure 3.9: Histograms that demonstrate $\sigma_{\ln}$ for many IMs, calculated for all P models. IMs are ranked according to efficiency (low $\sigma_{\ln}$).

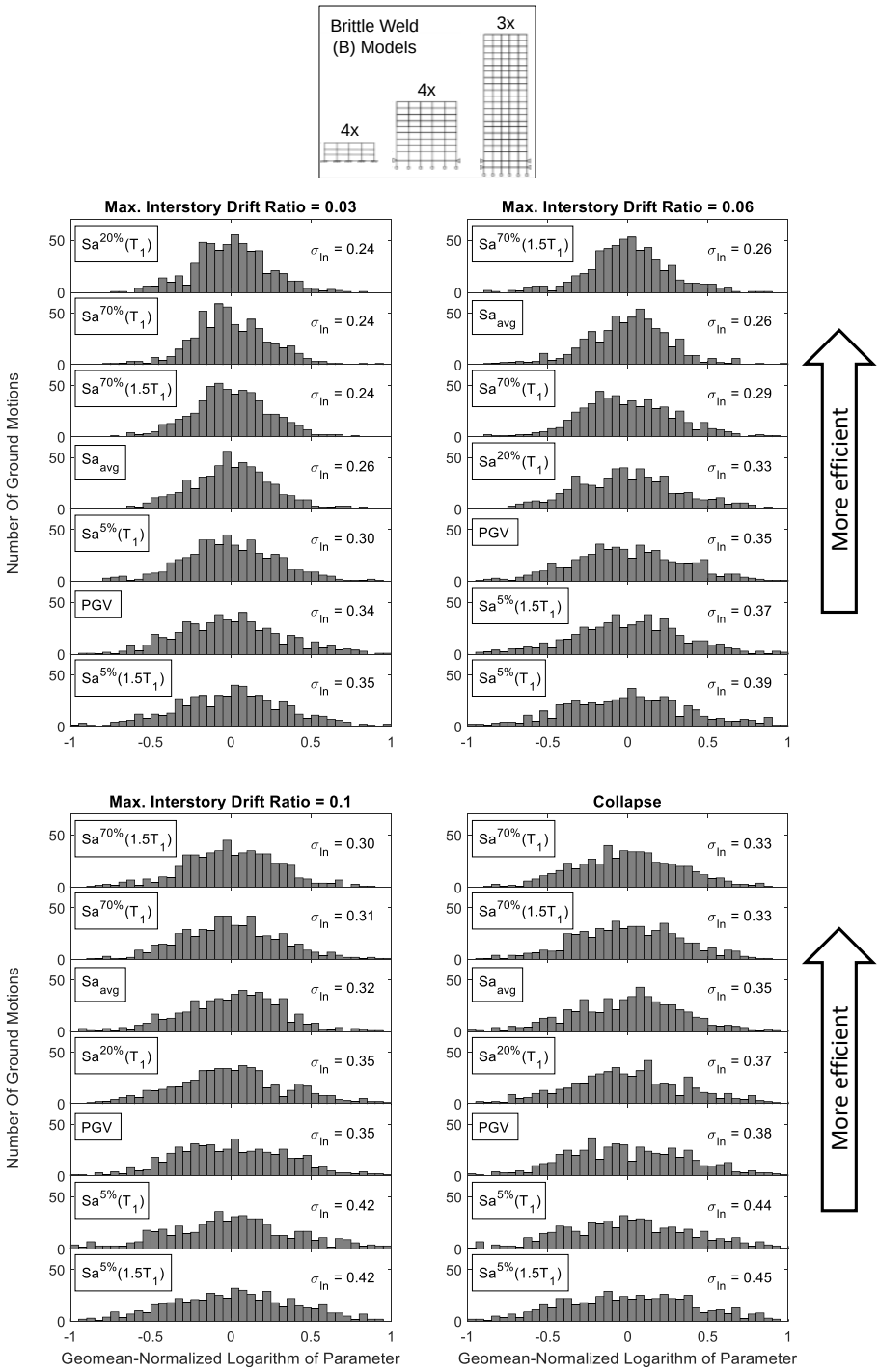

Figure 3.10: Histograms that demonstrate $\sigma_{\ln}$ for many IMs, calculated for all B models. IMs are ranked according to efficiency (low $\sigma_{\ln}$).

To further demonstrate how the efficiency of $Sa^{70\%}(T)$ compares to those of other

IMs, and how this changes with each set of building models, Tables 3.1-3.8 show $\sigma_{\ln}$ for all the IMs in Figures 3.9 and 3.10 plus $Sa^{70\%}(2T_1)$, $Sa^{5\%}(2T_1)$, PGA, and PGD. $\sigma_{\ln}$ is calculated for each set of P and B models for MIDR = 0.03, MIDR = 0.06, MIDR = 0.1, and collapse, denoted $\sigma_{\ln,0.03}$, $\sigma_{\ln,0.06}$, $\sigma_{\ln,0.1}$, and $\sigma_{\ln,\text{collapse}}$, respectively. In each table, the most efficient IM for each EDP is bolded. The statistics for the B models do not include Sd_i.

Table 3.1: $\sigma_{\ln}$ for 3P models. Minimum for each EDP is bolded

IM	$\sigma_{\ln,0.03}$	$\sigma_{\ln,0.06}$	$\sigma_{\ln,0.1}$	$\sigma_{\ln,\text{collapse}}$
PGA	0.42	0.44	0.48	0.52
PGV	0.31	0.27	0.24	0.26
PGD	0.75	0.67	0.61	0.55
$Sa^{5\%}(T_1)$	0.25	0.30	0.35	0.42
$Sa^{5\%}(1.5T_1)$	0.27	0.28	0.31	0.38
$Sa^{5\%}(2T_1)$	0.40	0.34	0.33	0.37
$Sa^{20\%}(T_1)$	0.17	0.24	0.31	0.37
$Sa^{70\%}(T_1)$	**0.16**	0.20	0.27	0.35
$Sa^{70\%}(1.5T_1)$	0.18	**0.15**	0.18	0.28
$Sa^{70\%}(2T_1)$	0.26	0.19	**0.17**	**0.24**
Sd_i	0.22	0.28	0.27	0.32
Sa_{avg}	0.20	0.19	0.21	0.26

Table 3.2: $\sigma_{\ln}$ for 9P models. Minimum for each EDP is bolded

IM	$\sigma_{\ln,0.03}$	$\sigma_{\ln,0.06}$	$\sigma_{\ln,0.1}$	$\sigma_{\ln,\text{collapse}}$
PGA	0.58	0.61	0.60	0.60
PGV	0.27	0.27	0.26	0.28
PGD	0.53	0.47	0.43	0.44
$Sa^{5\%}(T_1)$	0.35	0.38	0.40	0.41
$Sa^{5\%}(1.5T_1)$	0.41	0.34	0.37	0.39
$Sa^{5\%}(2T_1)$	0.52	0.44	0.41	0.41
$Sa^{20\%}(T_1)$	0.27	0.30	0.34	0.36
$Sa^{70\%}(T_1)$	**0.22**	0.24	0.29	0.30
$Sa^{70\%}(1.5T_1)$	0.24	**0.19**	0.23	0.25
$Sa^{70\%}(2T_1)$	0.29	0.21	**0.22**	0.25
Sd_i	0.27	0.27	0.28	0.31
Sa_{avg}	0.29	0.23	**0.22**	**0.23**

Table 3.3: $\sigma_{\ln}$ for 20P models. Minimum for each EDP is bolded

IM	$\sigma_{\ln,0.03}$	$\sigma_{\ln,0.06}$	$\sigma_{\ln,0.1}$	$\sigma_{\ln,\text{collapse}}$
PGA	0.71	0.65	0.63	0.62
PGV	0.38	0.30	0.30	0.30
PGD	0.45	0.38	0.40	0.41
$Sa^{5\%}(T_1)$	0.32	0.36	0.39	0.40
$Sa^{5\%}(1.5T_1)$	0.43	0.37	0.40	0.41
$Sa^{5\%}(2T_1)$	0.56	0.50	0.52	0.52
$Sa^{20\%}(T_1)$	0.26	0.29	0.32	0.33
$Sa^{70\%}(T_1)$	0.27	0.26	0.27	0.28
$Sa^{70\%}(1.5T_1)$	0.26	**0.22**	**0.25**	**0.26**
$Sa^{70\%}(2T_1)$	0.29	0.23	0.26	0.27
Sd_i	**0.25**	0.26	0.29	0.30
Sa_{avg}	0.34	0.27	0.29	0.29

Table 3.4: $\sigma_{\ln}$ for all P models. Minimum for each EDP is bolded

IM	$\sigma_{\ln,0.03}$	$\sigma_{\ln,0.06}$	$\sigma_{\ln,0.1}$	$\sigma_{\ln,\text{collapse}}$
PGA	0.57	0.56	0.56	0.57
PGV	0.32	0.28	0.26	0.27
PGD	0.60	0.53	0.49	0.47
$Sa^{5\%}(T_1)$	0.31	0.35	0.38	0.41
$Sa^{5\%}(1.5T_1)$	0.37	0.33	0.36	0.39
$Sa^{5\%}(2T_1)$	0.49	0.43	0.42	0.43
$Sa^{20\%}(T_1)$	0.24	0.28	0.32	0.36
$Sa^{70\%}(T_1)$	**0.21**	0.24	0.28	0.31
$Sa^{70\%}(1.5T_1)$	0.23	**0.19**	**0.22**	0.26
$Sa^{70\%}(2T_1)$	0.28	0.21	**0.22**	**0.25**
Sd_i	0.25	0.27	0.28	0.31
Sa_{avg}	0.28	0.23	0.23	0.26

Table 3.5: $\sigma_{\ln}$ for 3B models. Minimum for each EDP is bolded

IM	$\sigma_{\ln,0.03}$	$\sigma_{\ln,0.06}$	$\sigma_{\ln,0.1}$	$\sigma_{\ln,collapse}$
PGA	0.43	0.46	0.47	0.47
PGV	0.32	0.28	0.34	0.40
PGD	0.74	0.66	0.71	0.75
$Sa^{5\%}(T_1)$	0.25	0.33	0.36	0.40
$Sa^{5\%}(1.5T_1)$	0.24	0.26	0.33	0.40
$Sa^{5\%}(2T_1)$	0.36	0.34	0.44	0.50
$Sa^{20\%}(T_1)$	0.18	0.27	0.30	0.34
$Sa^{70\%}(T_1)$	**0.17**	0.22	0.27	**0.30**
$Sa^{70\%}(1.5T_1)$	0.18	**0.17**	**0.26**	0.32
$Sa^{70\%}(2T_1)$	0.25	0.20	0.29	0.36
Sa_{avg}	0.18	0.18	**0.26**	0.33

Table 3.6: $\sigma_{\ln}$ for 9B models. Minimum for each EDP is bolded

IM	$\sigma_{\ln,0.03}$	$\sigma_{\ln,0.06}$	$\sigma_{\ln,0.1}$	$\sigma_{\ln,collapse}$
PGA	0.59	0.62	0.59	0.57
PGV	0.28	0.31	0.31	0.31
PGD	0.54	0.50	0.53	0.55
$Sa^{5\%}(T_1)$	0.32	0.42	0.46	0.47
$Sa^{5\%}(1.5T_1)$	0.38	0.42	0.46	0.48
$Sa^{5\%}(2T_1)$	0.51	0.48	0.52	0.54
$Sa^{20\%}(T_1)$	0.25	0.35	0.38	0.39
$Sa^{70\%}(T_1)$	**0.23**	0.29	**0.31**	**0.32**
$Sa^{70\%}(1.5T_1)$	0.24	0.28	0.32	0.33
$Sa^{70\%}(2T_1)$	0.29	0.30	0.34	0.36
Sa_{avg}	0.27	**0.27**	0.32	0.34

Table 3.7: $\sigma_{\ln}$ for 20B models. Minimum for each EDP is bolded

IM	$\sigma_{\ln,0.03}$	$\sigma_{\ln,0.06}$	$\sigma_{\ln,0.1}$	$\sigma_{\ln,collapse}$
PGA	0.76	0.77	0.73	0.75
PGV	0.44	0.46	0.42	0.43
PGD	0.45	0.42	0.44	0.43
$Sa^{5\%}(T_1)$	0.32	0.41	0.43	0.45
$Sa^{5\%}(1.5T_1)$	0.42	0.41	0.46	0.47
$Sa^{5\%}(2T_1)$	0.57	0.54	0.58	0.58
$Sa^{20\%}(T_1)$	**0.28**	0.36	0.37	0.39
$Sa^{70\%}(T_1)$	0.32	0.37	0.36	0.37
$Sa^{70\%}(1.5T_1)$	0.30	**0.33**	**0.33**	**0.34**
$Sa^{70\%}(2T_1)$	0.32	**0.33**	**0.33**	**0.34**
Sa_{avg}	0.35	0.34	0.37	0.37

Table 3.8: $\sigma_{\ln}$ for all B models. Minimum for each EDP is bolded

IM	$\sigma_{\ln,0.03}$	$\sigma_{\ln,0.06}$	$\sigma_{\ln,0.1}$	$\sigma_{\ln,\text{collapse}}$
PGA	0.59	0.61	0.59	0.59
PGV	0.34	0.35	0.35	0.38
PGD	0.60	0.55	0.58	0.60
$Sa^{5\%}(T_1)$	0.30	0.39	0.42	0.44
$Sa^{5\%}(1.5T_1)$	0.35	0.37	0.42	0.45
$Sa^{5\%}(2T_1)$	0.48	0.45	0.51	0.54
$Sa^{20\%}(T_1)$	**0.24**	0.33	0.35	0.37
$Sa^{70\%}(T_1)$	**0.24**	0.29	0.31	**0.33**
$Sa^{70\%}(1.5T_1)$	**0.24**	**0.26**	**0.30**	**0.33**
$Sa^{70\%}(2T_1)$	0.28	0.27	0.32	0.35
Sa_{avg}	0.26	**0.26**	0.32	0.35

The results shown in Figures 3.9 and 3.10 and Tables 3.1-3.8 show that, compared to the other IMs, $Sa^{70\%}(1.5T_1)$ is either the most or nearly the most efficient IM for all models and considered EDPs. $Sa^{70\%}(T_1)$ is generally efficient for MIDR = 0.03, even when compared to $Sa^{70\%}(1.5T_1)$, but does not perform as well for more severe EDPs with the P models. $Sa^{70\%}(T_1)$ is also an efficient IM for all the considered EDPs for the 3B and 9B models. $Sa^{70\%}(2T_1)$ is sometimes slightly more efficient than $Sa^{70\%}(1.5T_1)$ for MIDR = 0.1 and collapse, but $Sa^{70\%}(1.5T_1)$ tends to have lower $\sigma_{\ln}$ over a wider range of building models and DMs. $Sa^{20\%}(T_1)$ has its best efficiency for MIDR = 0.03, but is only more efficient than $Sa^{70\%}(T_1)$ for the 20P and 20B models, and even then its $\sigma_{\ln,0.03}$ is only slightly lower than that of $Sa^{70\%}(T_1)$. Sa_{avg}, Sd_i, and PGV are more efficient than the standard $Sa^{5\%}(T_1)$ but do not consistently perform better than $Sa^{70\%}(T_1)$ at MIDR = 0.03 or $Sa^{70\%}(1.5T_1)$ at all EDPs. Of the three, Sa_{avg} is the closest to $Sa^{70\%}(1.5T_1)$ in terms of having low $\sigma_{\ln}$ for a broad range of EDPs. $Sa^{5\%}(T_1)$, $Sa^{5\%}(1.5T_1)$, and $Sa^{5\%}(2T_1)$ are the least efficient of the considered Sa-based IMs for almost all EDPs and sets of models, showing that they do not perform as well as the more advanced IMs when predicting highly nonlinear response. PGA and PGD are generally the least efficient of all the considered IMs. The only case in which one of them is comparably efficient to the other IMs is for the 20B model, for which PGD performs surprisingly well. Its value of $\sigma_{\ln,\text{collapse}}$ for the 20B model is lower than all the $Sa^{5\%}$-based IMs and is within about 25% of the most efficient IMs.

3.4 Sufficiency of $Sa^{70\%}(T)$

In this section, sufficiency of $Sa^{70\%}(1.5T_1)$ is measured with respect to earthquake magnitude (M), source-to-site Joyner-Boore distance (R_{JB}), and $\varepsilon(T_1)$. $\varepsilon(T_1)$ is calculated using the BA08 GMPEs [40]. The sufficiency of $Sa^{70\%}(1.5T_1)$ is presented instead of that of $Sa^{70\%}(T_1)$ or $Sa^{70\%}(2T_1)$ because it generally is the more efficient IM for the four EDPs representing highly nonlinear response: MIDR = 0.03, MIDR = 0.06, MIDR = 0.1, and collapse. Also, the sufficiency statistics of $Sa^{70\%}(T_1)$ and $Sa^{70\%}(2T_1)$ are generally similar to that of $Sa^{70\%}(1.5T_1)$. The sufficiency of $Sa^{70\%}(1.5T_1)$ is compared to that of $Sa^{5\%}(T_1)$ and Sa_{avg}. $Sa^{5\%}(T_1)$ is chosen because it is the most common IM in practice and Sa_{avg} is chosen because its efficiency for predicting highly nonlinear response is the closest to $Sa^{70\%}(1.5T_1)$ of all the considered non-$Sa^{70\%}(T)$ IMs.

To evaluate sufficiency, the framework implemented by Luco and Cornell [27] and Eads et al. [35] is used. For each building model, IM, EDP, and ground motion characteristic (M, R_{JB}, and $\varepsilon(T_1)$), a linear regression is performed of the following form:

$$\log(IM) = \beta_0 + \beta_1 \cdot x, \tag{3.9}$$

where $x = M, \log(R_{JB})$, or $\varepsilon(T_1)$. Each regression is performed on a set of 50 data points representing the IM values that induce the given EDP in the given building model for the set of 50 ground motions. If an IM is perfectly sufficient, then $\beta_1 = 0$ is expected, indicating no dependence of the IM values on the ground motion characteristic. For each linear regression, a hypothesis test is performed for which the null hypothesis is $\beta_1 = 0$ and the corresponding p-value is calculated. The p-value represents the probability that β_1 calculated from regression could be observed if the true value is $\beta_1 = 0$. A 5% significance level is used to judge sufficiency. That is, if the p-value for a regression is greater than 0.05, then the given IM is declared sufficient with respect to the given ground motion characteristic for the specific building model and EDP.

In addition to the p-value, the correlation coefficient, ρ, is calculated for each regression. For a given linear regression, $\rho = 1$ indicates a perfect, positive linear relationship (i.e. slope is positive), $\rho = -1$ indicates a perfect, negative linear relationship, and $\rho = 0$ indicates no linear relationship (i.e. slope is zero). As such, ρ close to zero indicates that sufficiency is likely while ρ far from zero indicates that sufficiency is unlikely. So for a given regression, if the p-value is small, then ρ is far from zero, and if the p-value is large, then ρ is close to zero. The p-value provides a

quantitative definition for sufficiency (i.e. 5% significance level) while ρ represents the nature of the correlation between the IM and ground motion characteristic (i.e. positive or negative correlation).

To demonstrate this procedure and how the p-value and ρ are obtained for a given regression, Figure 3.11 shows scatter plots of $\ln(IM)$ vs. M and $\ln(IM)$ vs. $\varepsilon(T_1)$ where IM is $Sa^{5\%}(T_1)$ and $Sa^{70\%}(1.5T_1)$ for MIDR = 0.06 for the 9P-94 model. In this example, $Sa^{5\%}(T_1)$ is insufficient with respect to $\varepsilon(T_1)$ for MIDR = 0.06 for the 9P-94 model because the p-value is less than 0.05. Note that that even though the p-value is only 0.02 for $Sa^{5\%}(T_1)$ with respect to $\varepsilon(T_1)$, there is significant scatter in the regression as indicated by the fact that $\rho = 0.32$, which is quite a bit less than 1.

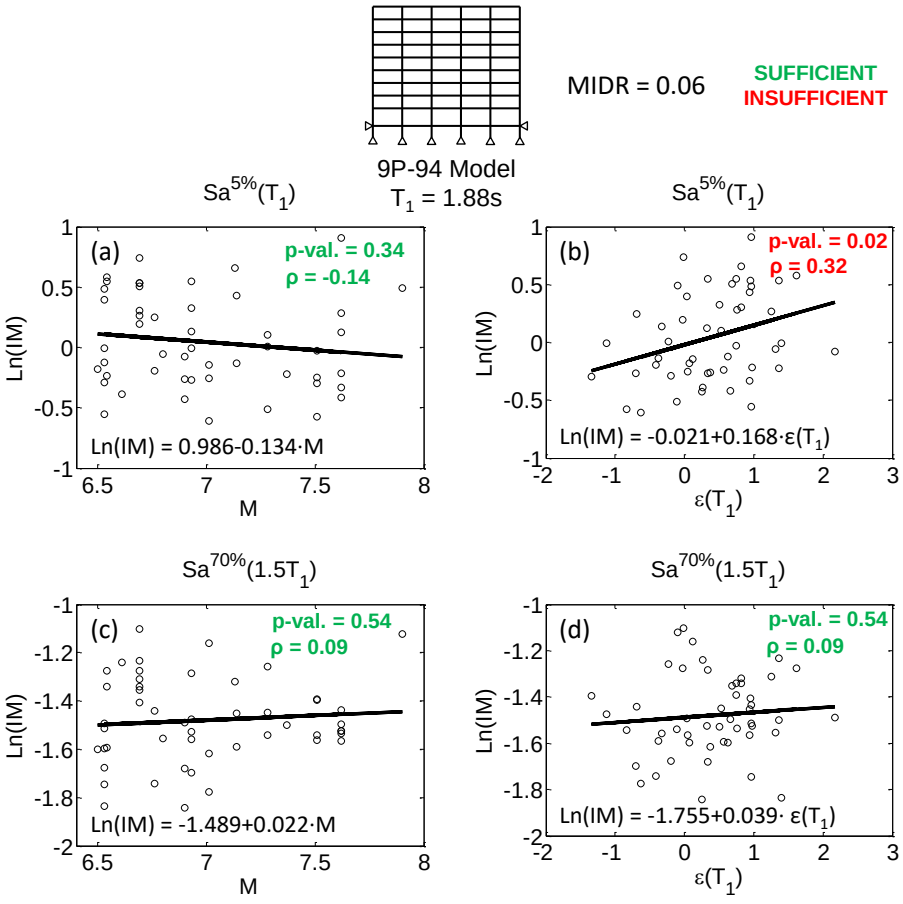

Figure 3.11: Demonstration of the data from which p-values and ρ for a given IM with respect to a given ground motion parameter are calculated for a given building model and EDP. In this example, p-values for $Sa^{5\%}(T_1)$ and $Sa^{70\%}(1.5T_1)$ are calculated with respect to M and $\varepsilon(T_1)$. The 9P-94 model and MIDR = 0.06 are considered. A p-value less than 0.05 indicates that the IM is insufficient.

For brevity, the p-value and ρ calculated for each regression are not shown here, but are tabulated in Tables B.1-B.18 in Appendix B. To summarize the p-values, Tables 3.9 and 3.10 show the percentage each of P and B models that are sufficient (i.e. p-value ≥ 0.05) for $Sa^{5\%}(T_1)$, $Sa^{70\%}(1.5T_1)$, and Sa_{avg} with respect to M, $\log(R_{JB})$, and $\varepsilon(T_1)$ for the four considered EDPs. Statistics for the four EDPs are combined in this table, so each percentage represents the fraction out of 44 total p-values (eleven building models and four EDPs). Note that by using a 5% significance level to define sufficiency, it is expected that about 5% of calculated p-values will be less than 0.05 if the IM is completely sufficient with respect to the considered ground motion parameter. That is, if an IM is completely sufficient, its expected reported value in Tables 3.9 and 3.10 would be 95%.

Table 3.9: Percentage of P models for which the p-value ≥ 0.05 for the four considered EDPs (MIDR = 0.03, MIDR = 0.06, MIDR = 0.1, and collapse). Calculated percentages consider 44 total responses (11 models, four EDPs)

	% of considered responses with p-value ≥ 0.05		
Parameter	$Sa^{5\%}(T_1)$	$Sa^{70\%}(1.5T_1)$	Sa_{avg}
M	95	93	73
$\log(R_{JB})$	98	95	82
$\varepsilon(T_1)$	5	77	48

Table 3.10: Percentage of B models for which the p-value ≥ 0.05 for the four considered EDPs (MIDR = 0.03, MIDR = 0.06, MIDR = 0.1, and collapse). Calculated percentages consider 44 total responses (11 models, four EDPs)

	% of considered responses with p-value ≥ 0.05		
Parameter	$Sa^{5\%}(T_1)$	$Sa^{70\%}(1.5T_1)$	Sa_{avg}
M	93	82	84
$\log(R_{JB})$	70	55	84
$\varepsilon(T_1)$	25	84	59

It appears that all three IMs are usually sufficient with respect to M, however, caution should be exercised when interpreting these results. As observed by Eads et al. [35], sufficiency with respect to M can be improperly classified by the p-value if the range of M values in the input ground motions is not large enough. In this study, M spans a range of $6.50 \leq M \leq 7.90$, so records from small magnitude events are not included. This may result in classifying IMs as sufficient with respect to M when this is not actually the case. For example, the results in Tables 3.9 and 3.10 show sufficiency of $Sa^{5\%}(T_1)$ with respect to M for all levels of highly nonlinear response, but others

(e.g. [27]) have found a slight dependence on M. It should be noted that some researchers *have* found $Sa^{5\%}(T_1)$ to be sufficient with respect to M for predicting highly nonlinear response (e.g. [32, 49–51]), so this is still being debated in the research community.

To further investigate the sufficiency of these IMs with respect to M, ρ is plotted as a function of T_1 for the P models and B models in Figures 3.12 and 3.13, respectively, for $Sa^{70\%}(1.5T_1)$, $Sa^{5\%}(T_1)$, and Sa_{avg}. Each data point represents a different building model, EDP, and IM. For models with $T_1 < 2.5$ s, the three IMs show similar trends in Figures 3.12 and 3.13, with $|\rho|$ less than 0.5 in every case. However, the three IMs differ for the P and B models with long T_1 (> 2.5 s). For these long-period models, the correlation coefficients corresponding to Sa_{avg} tend to be positive, the correlation coefficients corresponding to $Sa^{5\%}(T_1)$ tend to be negative, and the correlation coefficients corresponding to $Sa^{70\%}(1.5T_1)$ tend to be near zero. This implies that for the long-period models, ground motions from large-magnitude events need to have a higher value of Sa_{avg} to induce the same level of highly nonlinear response than ground motions from small-magnitude events. The opposite appears to be true with respect to $Sa^{5\%}(T_1)$. In comparison, the value of $Sa^{70\%}(1.5T_1)$ needed to induce highly nonlinear response in long-period models appears to be less correlated with M. Regardless, that none of the correlation coefficients are notably large (i.e. greater than 0.5 or less than -0.5) means that there is significant scatter in these regressions.

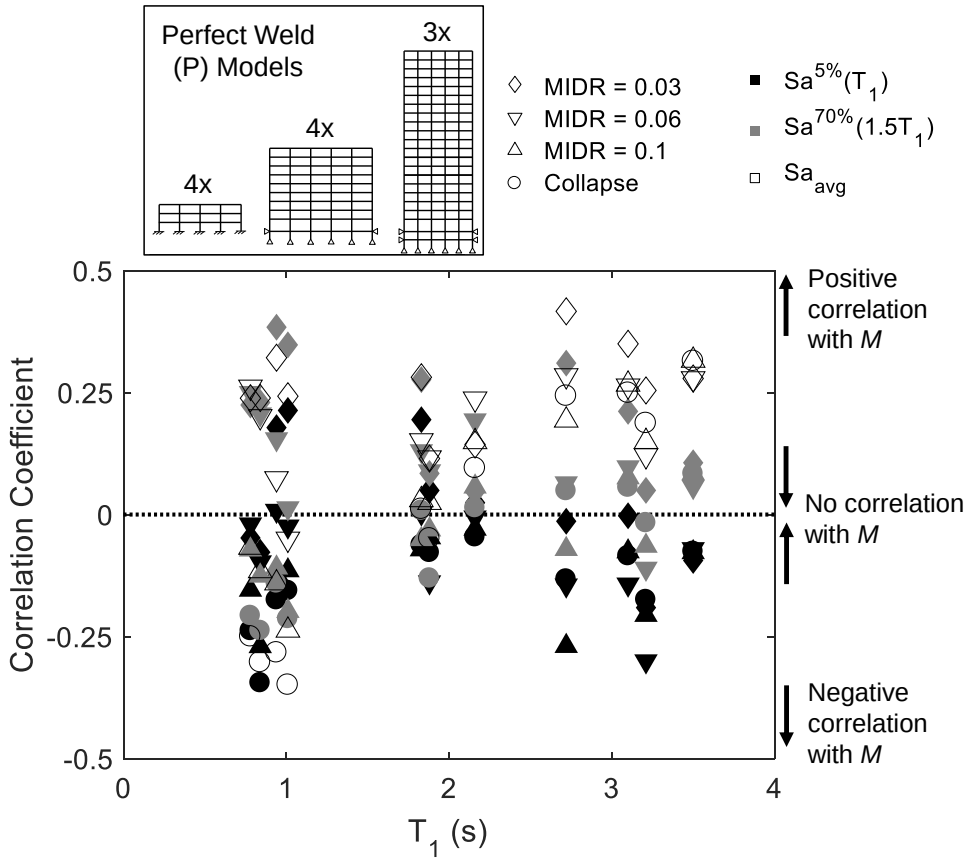

Figure 3.12: The correlation coefficients from testing sufficiency of $Sa^{5\%}(T_1)$, $Sa^{70\%}(T_1)$, and Sa_{avg} with respect to M for all P models and four EDPs: MIDR = 0.03, MIDR = 0.06, MIDR = 0.1, and collapse.

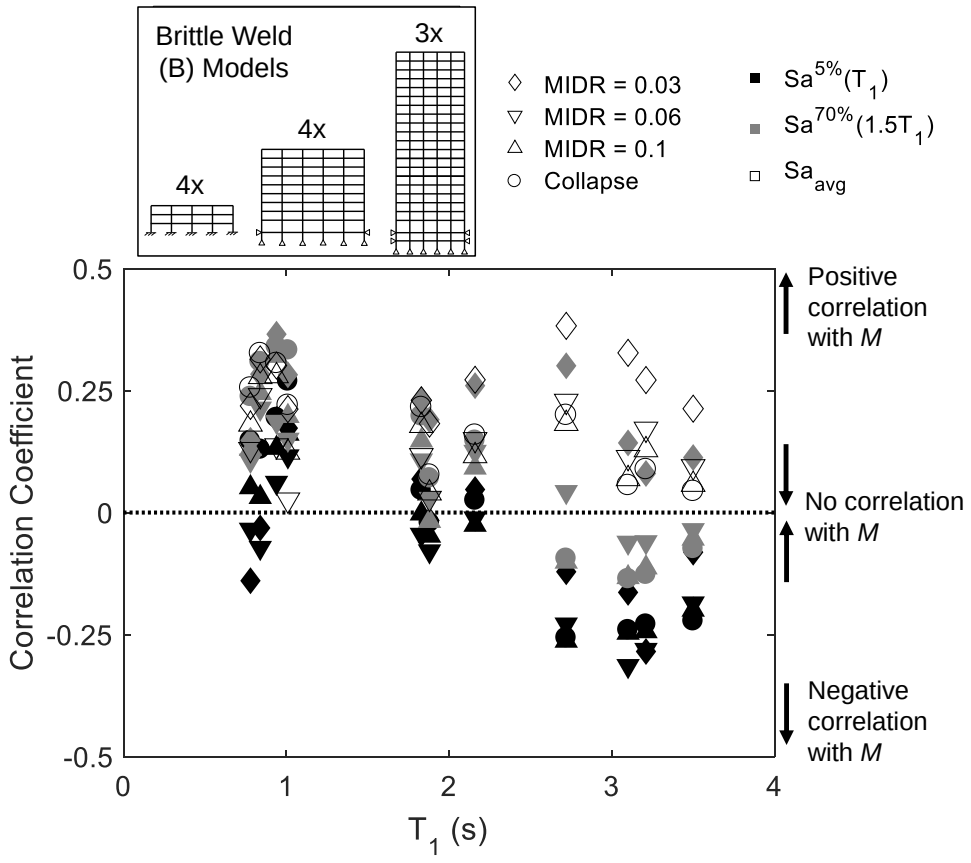

Figure 3.13: The correlation coefficients from testing sufficiency of $Sa^{5\%}(T_1)$, $Sa^{70\%}(T_1)$, and Sa_{avg} with respect to M for all B models and four EDPs: MIDR = 0.03, MIDR = 0.06, MIDR = 0.1, and collapse.

With respect to $\log(R_{JB})$, $Sa^{70\%}(1.5T_1)$ is usually sufficient, but is slightly less likely to be sufficient than $Sa^{5\%}(T_1)$ or Sa_{avg} for the B models. The correlation coefficients for $Sa^{70\%}(1.5T_1)$ with respect to $\log(R_{JB})$ for the B Models (see Table B.14) are usually less than zero. This indicates that, for a given value of $Sa^{70\%}(1.5T_1)$, a ground motion with small R_{JB} (i.e. a near-source record) is likely to induce a less severe response in a B model than a ground motion with large R_{JB} (i.e. not a near-source record). The same observation can be made about $Sa^{5\%}(T_1)$. For Sa_{avg}, ρ is usually negative for the 3B and 9B models but usually positive for the 20B models. There is not an obvious explanation for these observations, but since all the IMs are usually sufficient with respect to $\log(R_{JB})$ for all B models, it does not provide an obvious preference for one of the IMs over another. Sufficiency with respect to $\log(R_{JB})$ is also observed in most cases by Eads et al. [35] for $Sa^{5\%}(T_1)$ or Sa_{avg}.

While all three IMs are usually sufficient with respect to M and $\log(R_{JB})$ as measured

via the p-values, major differences arise with respect to $\varepsilon(T_1)$. Consistent with the observations of Eads et al. [35], $Sa^{5\%}(T_1)$ is rarely sufficient with respect to $\varepsilon(T_1)$, while Sa_{avg} is sufficient with respect to $\varepsilon(T_1)$ about half the time. Meanwhile, $Sa^{70\%}(1.5T_1)$ is sufficient in 77% of the considered responses for the P models and 84% of the considered responses for the B models. Thus, for both sets of models, the sufficiency of $Sa^{70\%}(1.5T_1)$ compares well to that of Sa_{avg} and both IMs are much more likely to be sufficient with respect to $\varepsilon(T_1)$ than $Sa^{5\%}(T_1)$.

To further demonstrate the trends in sufficiency with respect to $\varepsilon(T_1)$, Figures 3.14 and 3.15 plot the associated p-values as a function of T_1 of the P models and B models, respectively, for $Sa^{70\%}(1.5T_1)$, $Sa^{5\%}(T_1)$, and Sa_{avg}. Each data point represents a different building model, EDP, and IM. For all IMs and building models, the p-values generally decrease as T_1 gets larger. This means the considered IMs are less likely to be sufficient for long-period buildings. This may be because higher-mode response is more of a factor for taller buildings and the considered IMs do not capture short-period components of a ground motion as much as long-period components. Nonetheless, when the IM is $Sa^{70\%}(1.5T_1)$ for P and B models with $T_1 > 2.5$s, 63% of the considered responses are sufficient with respect to $\varepsilon(T_1)$. This is better than the corresponding values of 6% and 25% for $Sa^{5\%}(T_1)$ and Sa_{avg}, respectively. This implies that for taller buildings for which higher-mode response may be important, $Sa^{70\%}(1.5T_1)$ is more likely to be a sufficient IM for predicting highly nonlinear response than Sa_{avg} even though Sa_{avg} explicitly incorporates 5%-damped spectral acceleration values calculated with periods as low as $0.2T_1$.

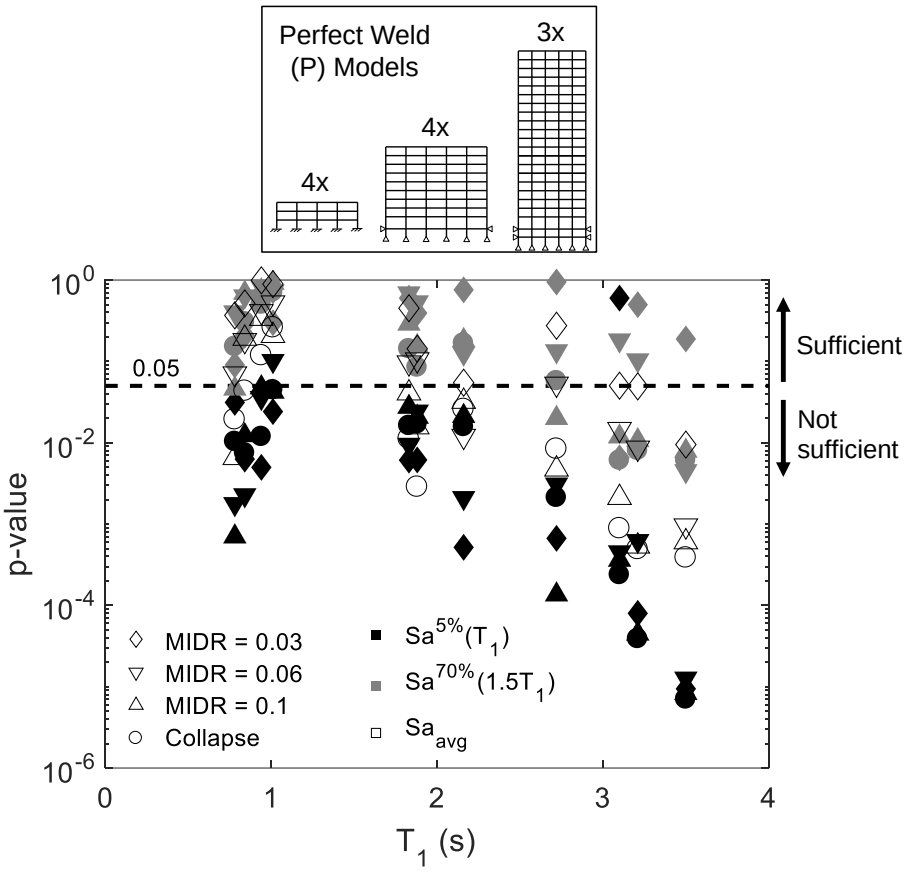

Figure 3.14: The p-values from testing sufficiency of $Sa^{5\%}(T_1)$, $Sa^{70\%}(T_1)$, and Sa_{avg} with respect to $\varepsilon(T_1)$ for all P models and four EDPs: MIDR = 0.03, MIDR = 0.06, MIDR = 0.1, and collapse.

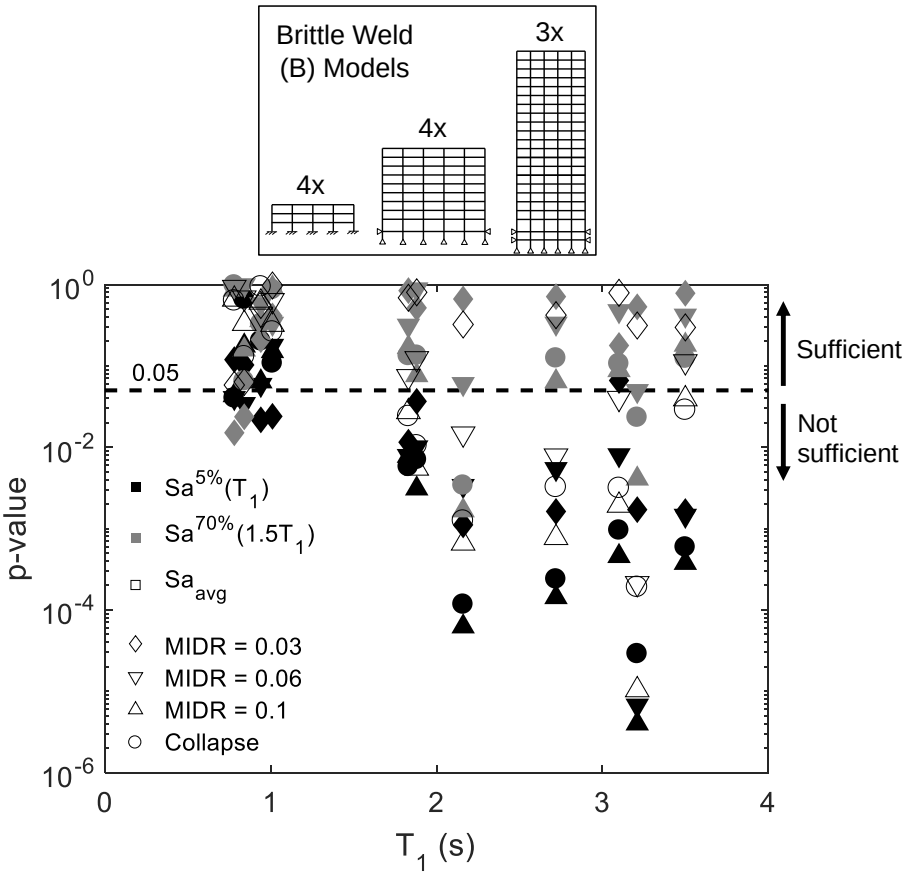

Figure 3.15: The p-values from testing sufficiency of $Sa^{5\%}(T_1)$, $Sa^{70\%}(T_1)$, and Sa_{avg} with respect to $\varepsilon(T_1)$ for all B models and four EDPs: MIDR = 0.03, MIDR = 0.06, MIDR = 0.1, and collapse.

3.5 Relation Between $Sa^{70\%}(T)$ and Base Shear

In Sections 3.3 and 3.4 it was shown that $Sa^{70\%}(1.5T_1)$ is an efficient and sufficient IM for predicting highly nonlinear response when compared to other common options. Furthermore, for MIDR = 0.03 in particular, $Sa^{70\%}(T_1)$ is highly efficient. In this section, $Sa^{70\%}(T)$ is demonstrated to be related to the base shear experienced by the building models during shaking. This provides a physical interpretation for $Sa^{70\%}(T)$ and a method for estimating how large $Sa^{70\%}(T)$ needs to be in a ground motion to induce highly nonlinear response. $Sa^{70\%}(T_1)$, $Sa^{70\%}(1.5T_1)$, and $Sa^{70\%}(2T_1)$ of the ground motions are compared to to $V_{\max}/M$ of the building models to determine if these comparisons can be used to predict highly nonlinear response.

Song and Heaton [52] predict collapse of a building model by directly comparing the given ground motion's peak filtered acceleration to $V_{\max}/M$, where M is the building model's seismic mass. In Song and Heaton's collapse prediction framework,

the filter is a low-pass Butterworth filter with a corner period of be cT_1, where c is some coefficient (usually between 1 and 2) dependent on the building model's global ductility, where a more ductile building will be assigned a larger value of c. The physical justification for this framework is that buildings tend to collapse due to long-period shaking and a building model's collapse capacity to long-period acceleration is approximated by $V_{\max}/M$. As alluded to in previous sections, when the filter is a low-pass Butterworth filter, the peak filtered acceleration with corner period T of a ground motion is approximately equal to $Sa^{70\%}(T)$ of that ground motion, so $Sa^{70\%}(T)$ can be interpreted as a measure of the long-period acceleration present in the ground motion, where the definition of "long-period" depends on the choice of T.

To replicate the framework of Song and Heaton, the sets of 50 scaled ground motions for each building model for which $Sa^{70\%}(T)$ first exceeds $V_{\max}/M$ is calculated for $T = T_1$, $1.5T_1$, and $2T_1$. The MIDR induced in the building model for each set of 50 scaled ground motions is found and these statistics are combined for each set of building models. From the combined statistics, the median MIDR and associated "pseudo-variability," $\hat{\sigma}_{\ln}$, is calculated for each set of models, where $\hat{\sigma}_{\ln}$ is one half the difference between the 84th and 16th percentile natural logarithms of the MIDRs. The median and $\hat{\sigma}_{\ln}$ values are used to estimate the geometric mean and $\sigma_{\ln}$ because some of these scaled ground motions induce collapse in the building models, which introduces values of infinite MIDR into the data set. The results are shown in Table 3.11. In some cases, more than 16% of scaled ground motions induce collapse, so $\hat{\sigma}_{\ln}$ is infinite. In these situations, $\hat{\sigma}_{\ln}$ is defined as the difference between the median and 16th percentile natural logarithms of the MIDRs and $\hat{\sigma}_{\ln}$ is indicated with an asterisk.

Table 3.11: Median and $\hat{\sigma}_{\ln}$ of MIDRs induced in each set of building models when $Sa^{70\%}(T) = V_{\max}/M$ for each building model.

	$T = T_1$		$T = 1.5T_1$		$T = 2T_1$	
Model Set	Median MIDR	$\hat{\sigma}_{\ln}$	Median MIDR	$\hat{\sigma}_{\ln}$	Median MIDR	$\hat{\sigma}_{\ln}$
3P	0.033	0.24	0.045	0.19	0.058	0.27
9P	0.027	0.18	0.041	0.20	0.061	0.24
20P	0.024	0.27	0.038	0.21	0.062	0.26*
3B	0.031	0.28	0.047	0.25*	0.074	0.39*
9B	0.023	0.23	0.036	0.27	0.063	0.35*
20B	0.022	0.41	0.033	0.40	collapse	-

* $\hat{\sigma}_{\ln}$ is calculated as difference between median and 16th percentile natural logarithm of the MIDRs because over 16% of responses are collapses.

The results in Table 3.11 show that if $Sa^{70\%}(T_1) = V_{\max}/M$, then median MIDRs of each set of models range from 0.022-0.033. If $Sa^{70\%}(1.5T_1) = V_{\max}/M$, then this range is 0.033-0.047, and if $Sa^{70\%}(2T_1) = V_{\max}/M$, then this range is 0.058 to collapse. Interestingly, the variations across sets of building models are not too large, although the median MIDRs tend to be slightly smaller for the taller buildings and the median response if $Sa^{70\%}(2T_1) = V_{\max}/M$ for the 20B models is "collapse," because the 20B models cannot withstand MIDRs much greater than 0.06 without collapsing. $\hat{\sigma}_{\ln}$ for the P models are smaller than those for the B models, which is to be expected because each B model has its weld fracture strain assigned according to a random distribution.

To demonstrate what these results mean for a particular model, the remainder of this section will focus on the 9P-94 model, MIDR = 0.03, and $Sa^{70\%}(T_1)$. For the 50 scaled ground motions that produce MIDR = 0.03 in the 9P-94 model, the 5%- and 70%-damped response spectra are shown in Figure 3.16 along with the pushover curve of the 9P-94 model. As would be expected given the results of Table 3.11, the geometric mean $Sa^{70\%}(T_1)$ is approximately equal to $V_{\max}/M$. This suggests that the the geometric mean used to generate $G[MIDR = 0.03|Sa^{70\%}(T_1)]$ could be estimated as $V_{\max}/M$ before performing nonlinear time history analysis.

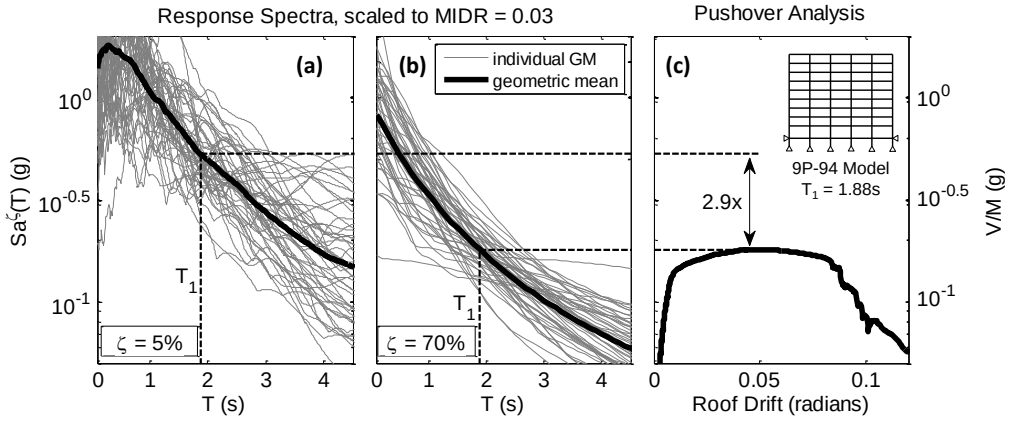

Figure 3.16: The (a) 5%-damped and (b) 70%-damped spectra of the set of 50 ground motions, each scaled to induce MIDR = 0.03 in the 9P-94 model and compared to the (c) pushover curve of the 9P-94 model.

Also note the relative scatter at T_1 in the two spectra in Figure 3.16. The compactness of $Sa^{70\%}(T_1)$ compared to $Sa^{5\%}(T_1)$ is a visual indicator that $Sa^{70\%}(T_1)$ is a more efficient IM for MIDR = 0.03, which was discussed in the Section 3.3. Furthermore, compared to the 5%-damped spectra, the 70%-damped spectra are much smoother with respect to T for individual ground motions, so small inaccuracies in estimating T_1 for a building model are less impactful when using $Sa^{70\%}(T_1)$ as the IM. $Sa^{70\%}(T)$ also has negative slope with respect to T for every individual ground motion. This results from the fact that $\zeta = \frac{1}{\sqrt{2}} \approx 70\%$ is the smallest value of ζ for which there is no resonance peak in the frequency response.

Recall that the original purpose of $Sa^{5\%}(T_1)$ was to approximate the base shear experienced by a building during shaking. As a building experiences highly nonlinear response, its base shear saturates at or near $V_{\max}$ and $Sa^{5\%}(T_1)$ becomes an overestimate. If it is assumed that the maximum base shear a building can experience during shaking is approximately $V_{\max}$, then it appears for MIDR = 0.03 that $Sa^{70\%}(T_1)$ could estimate the building's base shear during shaking.

To further clarify this point for a single ground motion, consider Figure 3.17. Shown here is the response of the 9P-94 model to the Chi-Chi TCU102-E ground motion, amplified (coincidentally by 1.00x) so that MIDR just exceeds 0.03. $\omega^2 u(t)$ is calculated according to Equation 3.3, where $\zeta = 5\%$ and 70%, $\omega = 2\pi/T_1$, and $\ddot{u}_g$ is the input ground motion. These plots are labeled $Sa^{5\%}(T_1)$ and $Sa^{70\%}(T_1)$ because the spectral accelerations are the maxima of these plots as a function of time. Also

plotted is the base shear (normalized by seismic mass) experienced by the building model and the IDR of the 5th story, which is the story at which the MIDR occurs.

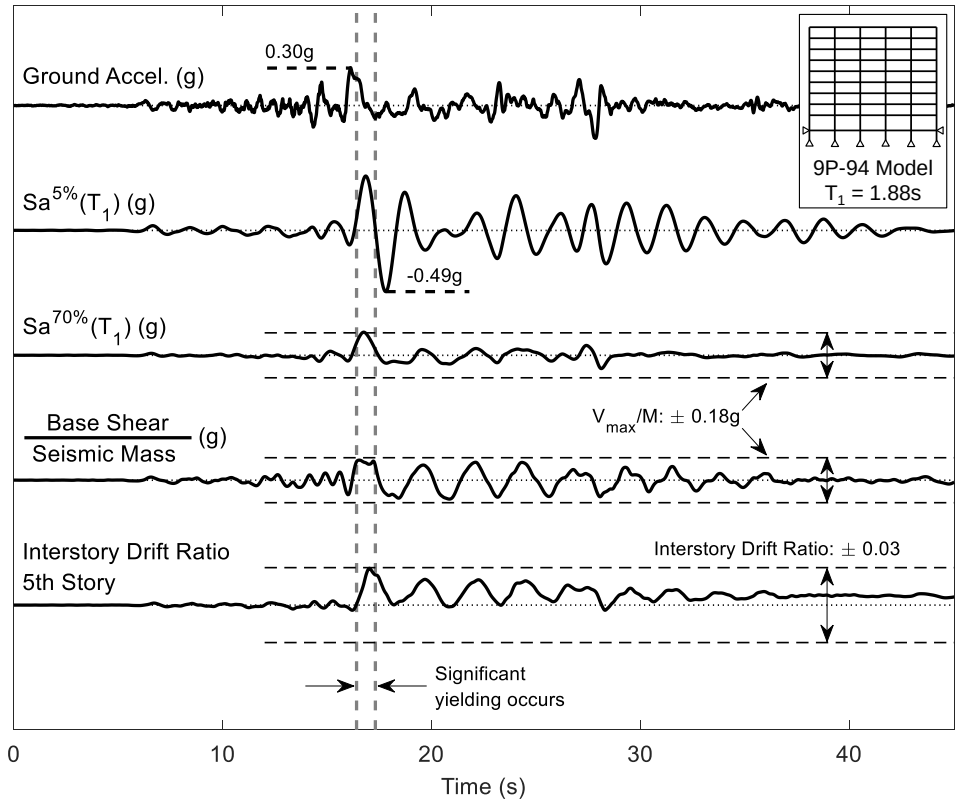

Figure 3.17: Response of the 9P-94 model to the 1999 Chi-Chi earthquake ground motion recorded at the TCU102 station in the EW direction scaled by 1.00x so that MIDR just exceeds 0.03. In this analysis, the MIDR occurs in the 5th story.

Several observations can be made about Figure 3.17. First, $Sa^{70\%}(T_1)$ is approximately equal to the normalized maximum base shear experienced by the building model during shaking. Furthermore, $Sa^{70\%}(T_1)$ occurs at about the same time as the maximum base shear and the maximum 5th-story IDR, but $Sa^{5\%}(T_1)$ occurs about a second later and in the opposite direction. Recall that $Sa^{5\%}(T_1)$ is meant to estimate the force experienced by the building during shaking, which in Figure 3.17 is expressed by the normalized base shear. $Sa^{5\%}(T_1)$ clearly overestimates the actual base shear experienced by the building, and this is further evident in Figure 3.16, which shows that the geometric mean $Sa^{5\%}(T_1)$ of scaled ground motions that induce MIDR = 0.03 is 2.9 times larger than $V_{\max}/M$ and the geometric mean $Sa^{70\%}(T_1)$. After the time interval of about one second during which most of the yielding occurs, the building experiences large oscillations of mostly free response. This free response

is reflected in the base shear and IDR plots, but is not seen as dramatically in the plot of the 70%-damped SDOF response. This indicates that in this case, $Sa^{70\%}(T_1)$ specifically measures the magnitude of the portion of the ground motion during which damage occurs. It is important to be cognizant of the fact that the observations made from Figure 3.17 are being made from a representative example. Most of the observed trends are common to other analyzed responses, but some outliers do exist, particularly for the 20-story models, for which response from higher-order modes can be significant.

It should be noted that the concept of approximating a nonlinear dynamic system with an equivalent linear SDOF that has a lengthened T and increased ζ for applications in earthquake engineering has been well-studied. A number of researchers have proposed different models (e.g. [53–56]), some of which are compiled and evaluated by Miranda and Ruiz-Garcia [57]. For these equivalent linear SDOFs, the goal is commonly to minimize the error between the the maximum displacement during excitation of some nonlinear SDOF and the maximum displacement during excitation of the equivalent linear SDOF. In this respect, the models evaluated by Miranda and Ruiz-Garcia [57] can be quite accurate on average, with errors usually less than 20%. The most accurate models assigned damping ratios to the equivalent SDOFs in the range of 10%-20%, which is much less than the SDOFs with $\zeta = 70\%$ considered in this section. One reason for this discrepancy is that the SDOFs with $\zeta = 70\%$ in this section are not meant to necessarily be "equivalent" linear SDOFs to the building models such that their maximum deformations are directly related. Instead, it is simply observed that if $Sa^{70\%}(T_1)$ of a ground motion exceeds $V_{\max}/M$ of the corresponding building model, this tends to be an indicator that highly nonlinear response will occur in the building model in response to the ground motion. Furthermore, some relationship is also observed in the time series of the responses of an SDOF with $\zeta = 70\%$ and a building model's nonlinear base shear, though more work should to be done to clarify the exact nature of this relationship.

This section has shown that if T is chosen properly, then $Sa^{70\%}(T)$ for a ground motion may be able to approximate the maximum base shear experienced by the building model if highly nonlinear response is expected. The demonstrated example with the 9P-94 model is only a representative example, but relatively low $\hat{\sigma}_{\ln}$ in Table 3.11 and the compactness of the 70%-damped spectra in Figure 3.16 means there is not dramatic variation in the observations between different models and ground motions. Following Table 3.11, one can make a rough prediction of the MIDR of a building

in response to a given ground motion by calculating $Sa^{70\%}(T_1)$, $Sa^{70\%}(1.5T_1)$, and $Sa^{70\%}(2T_1)$ and comparing these values to $V_{\max}/M$, which represents the model's base shear capacity. That is, the destructive power of a ground motion can be estimated before performing nonlinear dynamic analysis. As a note of caution, the precision of these response predictions should not be overestimated, as only a relatively small class of building models are considered in this study.

3.6 Ground Motion Scaling with $Sa^{70\%}(T)$

In most applications of ground motion IMs for structural analysis, the analyst defines a particular level of ground motion intensity using the IM (or IMs) to represent a specified seismic hazard. As a simple example, in order to check a building model's earthquake safety in maximum considered erathquake (MCE) shaking, an analyst may calculate the MCE-level $Sa^{5\%}(T_1)$ using seismic hazard analysis and apply input ground motions with this specified $Sa^{5\%}(T_1)$ to the building model. Even if all input ground motions have identical $Sa^{5\%}(T_1)$, the building responses will not be the same. Instead there will be a distribution of, for example, MIDRs that will have a corresponding variability $\sigma_{\ln}$. Note that, here, $\sigma_{\ln}$ represents the variability of MIDR values for a given IM. This is different than $\sigma_{\ln}$ in Section 3.3, which represents the variability of IM values for a given MIDR.

Huang et al. [58] provide a technical justification for the number of input ground motions, n, to use in analysis and found that

$$n = \left[\frac{\Phi^{-1}(1 - \alpha/2) \cdot \sigma_{\ln}}{\ln(1 + X)} \right]^2 \tag{3.10}$$

in order to estimate the median response to within a factor of $1 \pm X$ of the true median with $Z\%$ confidence, where Φ^{-1} is the inverse standardized normal distribution function and $\alpha = 1 - Z\%$. The relevance of Equation 3.10 that n is proportional to the square of $\sigma_{\ln}$, so choosing an efficient IM so that $\sigma_{\ln}$ is small can greatly reduce the number of ground motions required in analysis.

To demonstrate the utility of $Sa^{70\%}(T)$ as an IM with the goal of minimizing n, a median MIDR of 0.03 is targeted using four methods of modifying input ground motions: amplitude-scaling to a target $Sa^{5\%}(T_1)$, amplitude-scaling to a target $Sa^{70\%}(T_1)$, amplitude-scaling to a target Sa_{avg}, and spectrum-matching $Sa^{5\%}(T)$ from $0.2T_1$ to $1.5T_1$. MIDR = 0.03 is chosen as the target EDP because it approximately represents the response limit to MCE shaking. $Sa^{70\%}(T_1)$ is chosen instead of $Sa^{70\%}(1.5T_1)$ because it was shown to be particularly efficient for MIDR = 0.03 in

Section 3.3. For each P model, a target $Sa^{5\%}(T)$ spectrum and the target $Sa^{70\%}(T_1)$ is calculated from the geometric mean spectra of the 50 scaled ground motions for which MIDR = 0.03 is first exceeded (e.g. the geometric mean spectra in Figure 3.16 are the target spectra for the 9P-94 model). For the amplitude-scaling procedures, each of the original 50 ground motions is simply scaled so that their respective spectral ordinates match the target. This is done for each P model for each of the three amplitude-scaling procedures. Spectral-matching is performed for each P model using the computer program *rspMatch09* [59], which adds wavelets in the time domain to the original acceleration record. The period range of $0.2T_1$ to $1.5T_1$ is chosen to meet the requirements of Chapter 16 of ASCE 7-10 [20] for nonlinear time history analysis.

Following the aforementioned procedures, four sets of 50 modified ground motions are developed for each P model. As an example, response spectra of the four sets of modified ground motions developed for the 9P-94 model are shown in Figure 3.18.

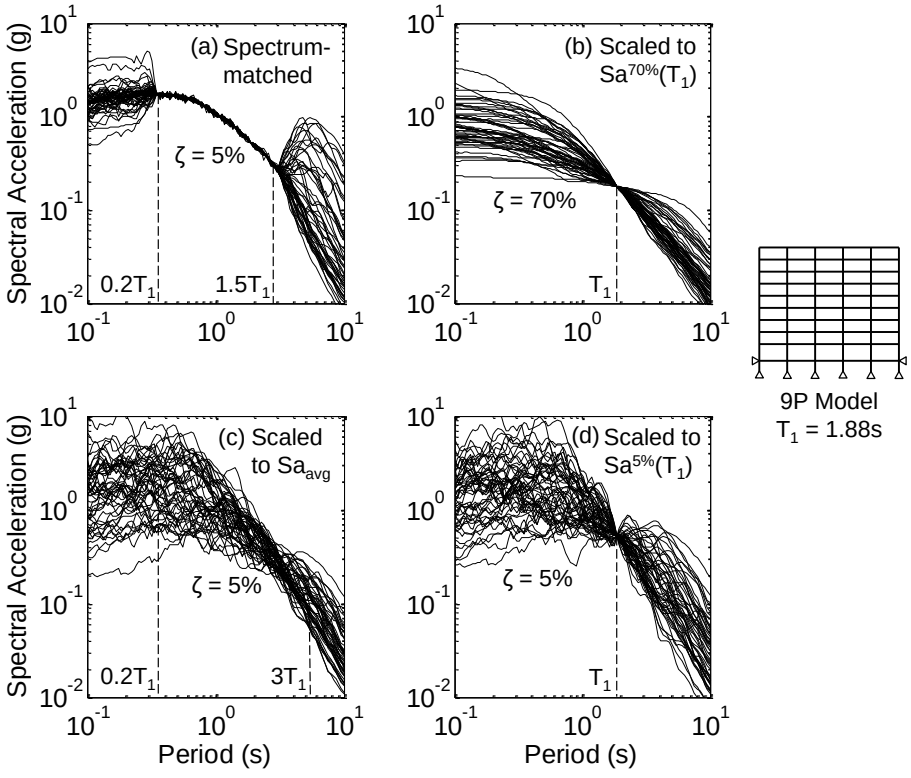

Figure 3.18: Response spectra of four sets of 50 ground motions modified in different ways to target MIDR = 0.03 for the 9P-94 model ($T_1 = 1.88s$): (a) spectrum-matched from $0.2T_1$ to $1.5T_1$, (b) amplitude-scaled to $Sa^{70\%}(T_1) = 0.18$ g, (c) amplitude-scaled to $Sa_{\text{avg}} = 0.32$ g, (d) amplitude-scaled to $Sa^{5\%}(T_1) = 0.53$ g.

Each set of ground motions is input into the corresponding building model to produce a set of MIDRs for each modification procedure. For each ground motion modification procedure, the MIDRs for all P models are combined to calculate $\hat{\sigma}_{\ln}$ in order to measure the efficiency of each procedure. As in Section 3.5, $\hat{\sigma}_{\ln}$ is used to approximate $\sigma_{\ln}$ because some of the responses result in collapse, yielding infinite $\sigma_{\ln}$. Based on the efficiency statistics previously calculated in Tables 3.1-3.4, it is expected that amplitude-scaling to $Sa^{70\%}(T_1)$ would have the lowest $\hat{\sigma}_{\ln}$ of the amplitude-scaling procedures, with Sa_{avg} close behind

The results are shown in Table 3.12 for the 3P, 9P, and 20P models. The statistics from all models are combined into an "All P" set to summarize the results. Not surprisingly, spectrum-matching is the most efficient modification procedure for all sets of building models. Of the amplitude-scaling procedures, using $Sa^{70\%}(T_1)$ as the target is either the most efficient or tied for the most efficient with Sa_{avg}. It also should not be surprising that amplitude-scaling to $Sa^{5\%}(T_1)$ is the least efficient of the considered procedures. There is slight variation in $\hat{\sigma}_{\ln}$ depending on the building height, but the only obvious trend is that $\hat{\sigma}_{\ln}$ is larger for the 20P models than for the 3P models regardless of the ground motion modification procedure. However, the relative efficiencies of the four procedures generally hold true for each of the 3P, 9P, and 20P models. To visualize these results, histograms of the MIDRs from all P models are shown in Figure 3.19.

Table 3.12: $\hat{\sigma}_{\ln}$ of MIDRs induced in the 3P, 9P, 20P, and all P models when the set of 50 ground motions is modified using four different techniques to target a median MIDR of 0.03 for each building model. For "All P", statistics from the 3P, 9P, and 20P models are combined.

	$\hat{\sigma}_{\ln}$ of MIDRs			
GM Modification Method	3P	9P	20P	All P
Spectrum-matched from $Sa^{5\%}(0.2T_1)$ to $Sa^{5\%}(1.5T_1)$	0.21	0.20	0.23	0.21
Amplitude-scaled to $Sa^{70\%}(T_1)$	0.24	0.20	0.25	0.23
Amplitude-scaled to Sa_{avg}	0.24	0.26	0.25	0.25
Amplitude-scaled to $Sa^{5\%}(T_1)$	0.26	0.32	0.31	0.29

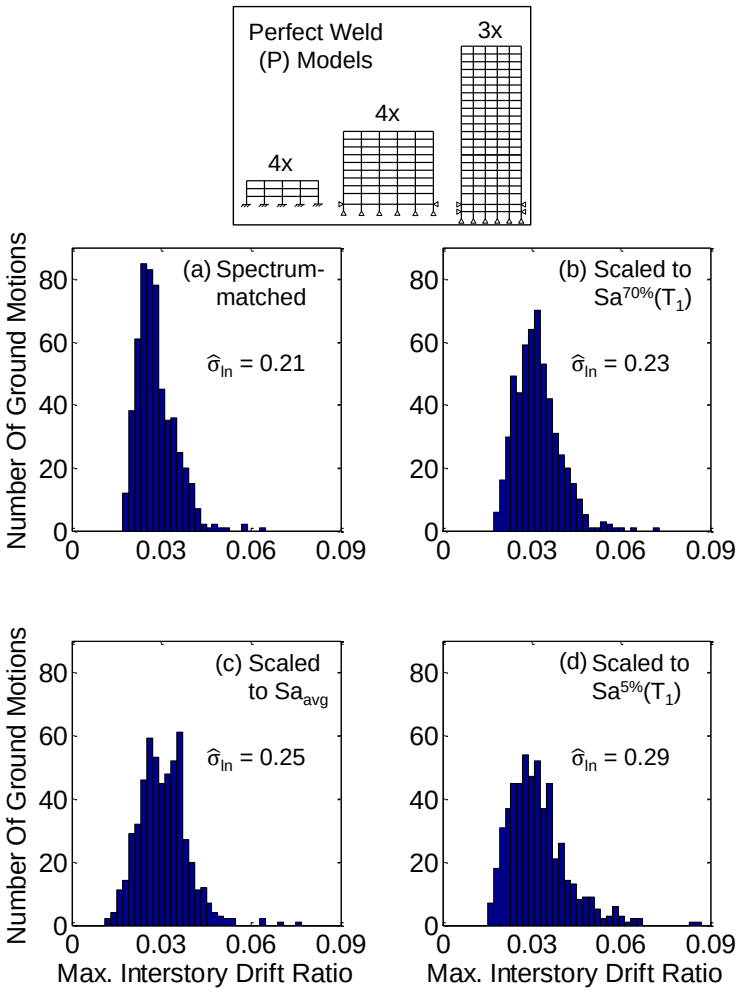

Figure 3.19: Histograms of MIDRs for all P models from which $\hat{\sigma}_{\ln}$ values are calculated (see Table 3.12). Each plot corresponds to eleven sets of 50 ground motions (one for each P model) that is (a) spectrum-matched from $0.2T_1$ to $1.5T_1$, (b) amplitude-scaled to $Sa^{70\%}(T_1)$, (c) amplitude-scaled to Sa_{avg}, (d) amplitude-scaled to $Sa^{5\%}(T_1)$.

The results imply that if efficiency is the only criterion so that n can be minimized, then spectrum-matching would be the best ground motion modification procedure to match a target hazard. In many cases, however, simple amplitude-scaling is preferred to spectrum-matching techniques. If amplitude-scaling is required or preferred, then scaling to match $Sa^{70\%}(T_1)$ would be the most efficient of the considered options.

3.7 $Sa^{70\%}(T)$ vs. Sa_{avg}

From the results shown in Tables 3.1-3.8, it is clear that the efficiencies of $Sa^{70\%}(1.5T_1)$ and Sa_{avg} for EDPs at or near collapse are relatively similar, though $Sa^{70\%}(1.5T_1)$ tends to be a bit more efficient. Sa_{avg} is also similar to $Sa^{70\%}(T)$ in terms of what it measures about a ground motion and this similarity necessitates further comment. These IMs are alike in that they both measure the "spectral shape" with an emphasis on long periods. Recall that Sa_{avg} for a ground motion is calculated by averaging its 5%-damped response spectrum from $0.2T_1$ to $3T_1$ with constant arithmetic spacing of 0.01 seconds. This averaging of the spectral content of a ground motion at many periods is similar to the low-pass filter interpretation of $Sa^{70\%}(T)$ and both IMs tend to give more weight to longer periods.

To demonstrate the long-period emphasis of Sa_{avg} and $Sa^{70\%}(T)$, consider the case in which the ground motion acceleration $\ddot{u}_g(t)$ is a simple harmonic with angular frequency ω_g and unit amplitude. As described in Section 3.1, the steady-state solution in this case is $u_{ss}(t) = U_{ss}\cos(\omega_g t + \delta)$, where δ is the phase difference between $u_{ss}(t)$ and $\ddot{u}_g(t)$ and U_{ss} is given by Equation 3.4. Plots of $\omega^2 U_{ss}$ vs. T_g/T are shown in Figure 3.20 for $\zeta = 5\%$ and $\zeta = 70\%$, where $T_g = 2\pi/\omega_g$. In the same figure, $(\omega_{\text{sdof}})^2 U_{ss}$ is plotted for $\zeta = 5\%$ with the SDOF period T_{sdof} ranging from $0.2T$ to $3T$ spaced arithmetically (0.1 second spacing) to represent the responses that are used to calculate Sa_{avg}. For these curves, $\omega_{\text{sdof}} = 2\pi/T_{\text{sdof}}$. The geometric mean of these 5%-damped spectra is plotted to approximately represent Sa_{avg}.

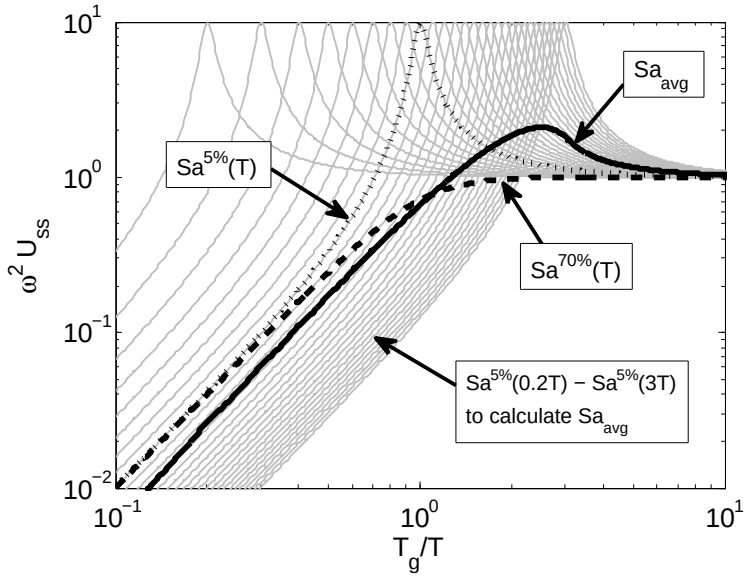

Figure 3.20: Steady-state response U_{ss} of SDOFs with period $T = 2\pi/\omega$ and $\zeta = 5\%$ and 70% to harmonic acceleration excitation with period T_g and unit amplitude. Also shown are steady state responses of SDOFs with periods ranging from $0.2T$ to $3T$ and $\zeta = 5\%$, whose geometric mean is used to calculate Sa_{avg}.

The purpose of Figure 3.20 is to show the degree to which different periods in a ground motion contribute to the calculations of $Sa^{5\%}(T)$, Sa_{avg}, and $Sa^{70\%}(T)$. The resonance peak in $Sa^{5\%}(T)$ around $T_g = T$ means that $Sa^{5\%}(T)$ for a ground motion is mostly a measure of a ground motion's spectral content around a period of T. In comparison to $Sa^{5\%}(T)$, the curve of Sa_{avg} has a wide peak around $T_g = 2.5T$, indicating that spectral content from a ground motion in the range of $1.5T$ to $3.5T$ is most important when calculating Sa_{avg}. This may be surprising because Sa_{avg} is calculated by averaging $Sa^{5\%}$ from $0.2T$ to $3T$.

In contrast to $Sa^{5\%}(T)$ and Sa_{avg}, $Sa^{70\%}(T)$ has no resonance peak. Instead, its corresponding steady-state response for $T_g < T$ increases until nearly reaching a value of one at $T_g = T$, which it approaches asymptotically for $T_g > T$. The interpretation here is that $Sa^{70\%}(T)$ is a measure of the long-period content in a ground motion with all long periods being given approximately equal weight, even for $T \to \infty$. This implies that spectral content in a ground motion cannot be too "long period" to affect building response. This may be surprising, but can be made clear by considering a pushover analysis. During pushover analysis, a slowly increasing lateral force is applied to the building model. This is usually done at least quasi-statically, but can also be done dynamically if the load is increased slowly enough. Lateral force

is equivalent to acceleration at the base of the structure, so a pushover analysis performed dynamically with a vertical load distribution proportional to the vertical mass distribution of the model is equivalent to the model's response to a slow acceleration ramp. This slow acceleration ramp can be expressed as a harmonic ground acceleration with period $T \rightarrow \infty$. Pushover analysis can be performed until the building collapses, which means a ground motion with infinitely long period can cause structural collapse, so long as the accelerations are large enough.

Obviously, real ground motions do not have spectral content at infinitely long periods, but the fact that a pushover analysis can cause collapse implies that spectral content in a ground motion is never "too long-period" to cause damage. However, in most recorded ground motions, the accelerations at periods much longer than those of civil structures are smaller than those at shorter periods. This is why, for example, current procedures for selecting and scaling ground motions to match a target spectrum only require hazard compatibility for periods up to $1.5T_1$ (e.g. ASCE 7-10 [20]) or $2T_1$ (e.g. ASCE 7-16 [60]). This may be sufficient in most cases because accelerations at very long periods are usually small, but anomalous ground motions with large accelerations at long periods (e.g. pulse-type motions) do occur and their destructive potential should not be underestimated, even if most of the spectral content is contained in periods much longer than T_1.

Another surprising observation from Figure 3.20 is that $Sa^{70\%}(T)$ gives relatively more weight to higher-order modes in its calculation than Sa_{avg}. This is clear from comparing their respective curves for $T_g \geq T$ (first-mode response if $T = T_1$) and $T_g < T$ (higher-order modes). For $T_g \geq T$, Sa_{avg} has a higher amplitude than $Sa^{70\%}(T)$, but for $T_g < T$ the opposite is observed. So even though Sa_{avg} explicitly accounts for periods as low as $0.2T$, short-period content in a ground motion will actually influence the value of $Sa^{70\%}(T)$ more than Sa_{avg}. This is due to arithmetic spacing when calculating Sa_{avg}.

This perhaps accounts for the results in Tables 3.1-3.3 regarding the relative efficiencies of $Sa^{70\%}(T_1)$ and Sa_{avg} in predicting collapse. For the 3P and 9P models (Tables 3.1 and 3.2), Sa_{avg} has a much lower $\sigma_{\ln,0.1}$ and $\sigma_{\ln,\text{collapse}}$ than $Sa^{70\%}(T_1)$. However, for the 20P models (Table 3.3), for which one would expect higher-order modes to be more influential, $Sa^{70\%}(T_1)$ has lower $\sigma_{\ln,0.1}$ and $\sigma_{\ln,\text{collapse}}$ than Sa_{avg}, indicating that it is more efficient for the taller building models. Though not explicitly shown in Figure 3.20, $Sa^{70\%}(1.5T_1)$ and $Sa^{70\%}(2T_1)$ also give more weight to higher-mode response than Sa_{avg}.

In application, the main advantage of Sa_{avg} over $Sa^{70\%}(T)$ is that GMPEs exist for $Sa^{5\%}(T)$ as do correlations between $Sa^{5\%}(T)$ values at different periods [61], so PSHA can be performed for Sa_{avg} relatively easily. Recently, direct GMPEs have also been developed for Sa_{avg} [62]. This means the full integral in Equation 3.1 can be calculated if the IM is Sa_{avg} because $\lambda[IM]$ can be generated. GMPEs for $Sa^{70\%}(T)$ do not yet exist, making its immediate use in application less feasible than Sa_{avg}. That said, this study has shown a couple advantages of $Sa^{70\%}(T)$. First, $Sa^{70\%}(T)$, and $Sa^{70\%}(1.5T)$ in particular, is generally slightly more efficient and sufficient than Sa_{avg} for a range of highly nonlinear EDPs. Second, the physical interpretation of $Sa^{70\%}(T)$ as a low-pass filter means the value for a ground motion may approximate the base shear experienced by the building model during shaking in order to make a prediction about the nonlinear response of the structure. In comparison, the value of Sa_{avg} does not have a physical meaning. Lastly, $Sa^{70\%}(T)$ measures the maximum response of an SDOF at a particular time during shaking, with most of the damage often occurring in the building model around this same time. Sa_{avg}, on other hand, is calculated as the geometric mean maximum response of many SDOFs with different T and their maxima can occur at different times during shaking. So although the near-term prospects for Sa_{avg} as an IM are more practical because GMPEs do not yet exist for $Sa^{70\%}(T)$, $Sa^{70\%}(T)$ shows promise as an improvement to Sa_{avg} in some ways and there is no theoretical barrier for generating GMPEs for new IMs, it is only a matter of computational time and effort.

It should be noted that only one definition for Sa_{avg} is used in this study, but others (e.g. [36, 37]) have used different definitions for average spectral acceleration that use different period ranges and spacings. Much like how different values of ζ and T can improve the performance of $Sa^{\zeta}(T)$ for a particular building model and EDP, different definitions of Sa_{avg} can improve its performance as measured via efficiency and sufficiency. As such, the results of this study should not be interpreted to imply that in all cases, $Sa^{70\%}(T)$ is a more sufficient and efficient IM than Sa_{avg}. That said, the results do show that these IMs are at least comparable and $Sa^{70\%}(T)$ should be considered as a useful IM when highly nonlinear response is expected.

3.8 Conclusions

As an IM for evaluating highly nonlinear response (MIDR ≥ 0.03) of the structures considered in this study, $Sa^{70\%}(1.5T_1)$ is generally efficient and sufficient and compares well to other considered IMs. For MIDR = 0.03 in particular, which is an applicable EDP in design because it is a common limit for MCE shaking, $Sa^{70\%}(T_1)$

is especially efficient. Beyond its relative efficiency and sufficiency, the equivalence of $Sa^{70\%}(T)$ to a low-pass Butterworth filter means it is a measure of the maximum long-period acceleration of a ground motion, where "long period" is defined as greater than T. This may justify a physical interpretation as an approximation of the base shear experienced by a building while it undergoes highly nonlinear response because the base shear due to strong shaking can be dominated by the long periods present in the input ground motion. This physical interpretation means the geometric mean $Sa^{70\%}(T)$ for use in $G[EDP|IM]$ can in some cases be estimated as $V_{\max}/M$ if the EDP represents highly nonlinear response and T is chosen appropriately. The effectiveness of $Sa^{70\%}(T)$ as an IM implies that spectral content in a ground motion cannot be too "long period" to have an effect on building response. Amplitude-scaling to $Sa^{70\%}(T)$ appears to be a relatively simple method for ground motion modification that yields variabilities of MIDRs nearly as small as those from spectrum matching if significant nonlinear response is expected. Sa_{avg} is similar to $Sa^{70\%}(T)$ in that they both measure the long-period content of a ground motion and both are relatively efficient and sufficient for highly nonlinear EDPs.

In terms of the application of $Sa^{70\%}(T)$ as an IM in practice for assessing collapse risk and/or the risk of highly nonlinear response, the missing piece from Equation 3.1 is $\lambda[Sa^{70\%}(T)]$, which requires a characterization of the seismic hazard. This characterization is not currently available and would require the generation of one or more GMPEs for $Sa^{70\%}(T)$ at many periods. As GMPEs for new IMs that characterize long-period shaking are developed, care should be taken before assuming a form for the statistical distributions because the statistics of long-period components in strong ground motions do not always follow the same statistics as short-period components [63]. Further confirmation on the utility of $Sa^{70\%}(T)$ when applied to lateral force-resisting systems other than steel moment frames (e.g. concrete shear walls) will also be needed before it can be applied in practice. Nonetheless, $Sa^{70\%}(T)$ shows promise as an IM for predicting highly nonlinear response.

Future Work

The results of this study motivate multiple directions of future research. The most obvious is the generation of GMPEs for $Sa^{70\%}(T)$, which would allow it to be used in practice to calculate collapse risk. Following research into Sa_{avg} as an IM, Kohrangi et al. [62] recently developed GMPEs so it can be used in practice. There is no reason this cannot be done for $Sa^{70\%}(T)$.

Another possible direction of future research would be to use $Sa^{70\%}(T)$ to measure the destructiveness of a "pulse" in a ground motion. Anderson and Bertero [64] found that nonlinear response is sensitive to pulse duration relative to T_1 and pulse acceleration relative to the seismic design coefficient, which is similar to comparing $Sa^{70\%}(T)$ to $V_{\max}/M$, as is done in this study. Mavroeidis et al. [65] also found that pulse duration was a key parameter to predicting nonlinear response and Malhotra [66] proposed the ratio PGV/PGA, which is often related to pulse duration, as a measurement of pulse destructiveness. Given that ground motions with pulses generally contain significant long-period energy, it is likely that $Sa^{70\%}(T)$ would be an effective measure of the destructiveness of a pulse.

Lastly, from a "big picture" perspective, it appears that if one disregards the criteria that IMs must have pre-existing GMPEs, there is a lot of room for investigation into IMs for predicting highly nonlinear response and collapse in addition to other EDPs. For example, this study does not consider peak floor acceleration (PFA) as an EDP, but this is a common predictor of non-structural damage (e.g. [25]). Furthermore, it is easy to imagine a procedure by which an "optimal" IM could be generated for a given EDP and a specific building model or class of building models by minimizing $\sigma_{\ln}$ over many different IMs. As an example, one could consider all IMs for which a frequency response function can be generated, such as in Figure 3.20. Then, over the infinite set of such possible IMs, the optimal IM could be generated using nonlinear minimization techniques. The problem with such an approach is that GMPEs only exist for a finite number of IMs, so an IM generated in this manner could not immediately be used in practice. However, as data processing techniques become computationally faster, one can also imagine creating a system that automatically calculates GMPEs for an IM input by a user, so long as the IM could be defined by a mapping from a ground motion record to a scalar. If such a system were to exist, researchers could quickly calculate the risk of collapse (or any EDP) using any IM of their choosing.

Chapter 4

EFFECTS OF LONG-PERIOD PROCESSING ON COLLAPSE PREDICTIONS

In this chapter, the the effects of long-period processing of ground motion records on structural response is investigated. Section 4.1 explains how long-period noise is removed from ground motion records and why it might be a problem if these processed records are used as input ground motions for nonlinear time history analysis because real long-period signal may be lost. Section 4.2 describes the different types of ground motions considered in this study: raw, tilt-corrected, and high-pass filtered. Section 4.3 describes the building models considered in this study. Section 4.4 examines the effects of processing input ground motions with high-pass acausal and causal filters, coming to the conclusion that high-pass acausal filters should be used because they have less of an effect on structural response. Section 4.5 summarizes the results of incremental dynamic analysis with all the considered ground motions and the 9-, 20-, and 55-story steel moment frame models with perfect welds. It is found that in some cases, applying high-pass filters to input ground motions can affect structural response, even if the cutoff period of the filter is much larger than the fundamental period of the building model. Section 4.6 looks into the results of incremental dynamic analysis with the seven of the strongest ground motion records and all of the considered building models. Section 4.7 summarizes the conclusions and limitations of this study while also suggesting some avenues of future work.

4.1 Introduction

The NGA-West2 database [67] of recorded and processed ground motions was developed in order to calculate ground motion prediction equations (GMPEs) for a variety of ground motion intensity measures (IMs). Although not explicitly created for structural analysis, the NGA-West2 database has also been used by engineers as a source of input ground motions for response history analysis of structural models. To remove long-period noise from raw recorded ground motions, each ground motion in the NGA-West2 database is high-pass filtered with a record-specific corner period. Long-period noise can include a tilt of the instrument during shaking, which introduces a static acceleration offset into the record that is not physically present in the true ground motion. For some applications (e.g. calculation of GMPEs

for peak ground acceleration), these high-pass filters do not affect the results of analysis when using ground motions from the NGA-West2 database. However, in other cases (e.g. estimating the collapse capacity of a building), the removal of long-period components from raw ground motions may have an impact.

For a large earthquake, near-fault ground displacement is predominantly described by the static offset, which can be as large as 10 meters [68]. However, in the displacement time series of ground motion records in the NGA-West2 database, there is no recognition of static offsets or permanent displacement offsets [69]. The explanation for this lies in the record processing methodology used by NGA-West2, which consists of a series of steps that include demeaning the raw record, correcting unrealistic trends, and acausal high-pass filtering [67]. Some researchers (e.g. [69, 70]) have concluded that removing static offsets from records does not affect a ground motion's response spectrum at periods that would be relevant in engineering, but others (e.g. [71]) have found that the removal of static offsets from ground motions can affect the nonlinear response of tall structures.

The removal of static offsets in processed near-source records has been recently recognized as an issue in the selection of ground motion time histories for the design of structures using nonlinear time history analysis if near-source shaking is a significant portion of the seismic hazard. The newly released 2017 version of the Los Angeles Tall Building Seismic Design Council (LATBSDC) alternate procedure for seismic design of tall buildings in Los Angeles [72] explicitly requires the addition of static offsets (described as "fling-steps") to input ground motions where such effects are anticipated. Burks and Baker [73] provide guidance for adding static offsets to processed ground motions for this purpose.

Applying high-pass filters to remove long-period noise from the raw record can have unintended consequences with regards to predicting structural response beyond removal of the static offset. For example, Boore and Akkar [74] and Burks and Baker [75] showed that high-pass acausal filters with corner periods that are too low can affect the inelastic displacement and collapse capacity, respectively, of nonlinear single-degree-of-freedom systems. To reflect the concerns associated with high-pass filters, the NGA-West2 flatfile reports a maximum useable period for each ground motion component. When selecting input ground motion records for the design of new buildings, it is common to only select records for which the maximum usable period is greater than $1.5T_1$, where T_1 is the fundamental period of the structure of interest [76]. In some cases, ensuring that periods up to $1.5T_1$ are preserved in

the ground motion is sufficient to accurately assess the ground motion's potential to cause collapse in a building model. However, some ground motions can have a substantial portion of their spectral content at long periods beyond $1.5T_1$, particularly those recorded in large-magnitude events or those that contain velocity pulses. It should be noted that the 2017 version of the LATBSDC alternate procedure [72] and the newly-released ASCE 7-16 [60] both require ground motions selected for nonlinear time history analysis to match the target spectrum at periods up to $2T_1$.

In this study, 26 ground motion records from seven large magnitude events are collected and processed in a manner that preserves the static offset. High-pass filters are applied to these records in order to evaluate the effects of filtering. Incremental dynamic analysis (IDA) is performed with each of these processed records on three mid- to high-rise steel moment frame (SMF) building models (9-, 20-, and 55-story) to evaluate the collapse capacity of each model to each ground motion and how this is affected by processing the records. Particular attention is paid to seven horizontal components that represent the particularly strong shaking. IDA is performed with all processed versions of these seven records for SMF models with perfect and brittle welds and for a simple model of a base-isolated building.

4.2 Ground Motions

This section summarizes the ground motions used in this study. These records were obtained and processed by Becky Roh and generously provided to the author for structural analysis. The text and figures of this section were created by both Becky Roh and the author. Some additional information about these ground motions can be found in Roh et al. [77].

Records

The ground motion records used in this study consist of ground motions from seven large earthquakes: (i) 2016 M7.8 Kaikōura, New Zealand; (ii) 2016 M7.0 Kumamoto, Japan; (iii) 2015 M7.8 Gorkha, Nepal; (iv) 2008 M7.9 Wenchuan, China; (v) 2002 M7.9 Denali, Alaska; (vi) 1999 M7.6 Chi-Chi, Taiwan; and (vii) 1992 M7.3 Landers, California. From these earthquakes, records from 26 stations are collected. The horizontal components are the focus of this study. The chosen records are from stations in regions with strong shaking, with instrumental intensity of IX and X+.

For earthquakes (i)-(iv), raw acceleration records are available from different strong motion databases. The following databases are used to collect the raw data: GeoNet for the Kaikōura earthquake; K-NET, KiK-net, and the Japan Meteorological Agency

(JMA) for the Kumamoto earthquake; the California Strong Motion Instrument Program (CSMIP) for the Gorkha earthquake; and the National Strong-Motion Observation Network System (NSMONS) of China for the Wenchuan earthquake.

For earthquakes (v)-(vii), raw acceleration records are not available. However, processed acceleration records with the static offsets preserved are accessible for the Chi-Chi and Landers earthquakes from Boore [70] and Chen [78], respectively. For the Denali earthquake, Ellsworth et al. [79] provide published ground displacements with the static offsets preserved, which are digitized to extract the time series. Filtered records from earthquakes (v)-(vii) with the static offsets removed are also available from the NGA-West2 database [67]. High-pass filter corner periods for these records were chosen individually for the NGA-West2 project with T_c as low as 10 seconds. These filtered records are combined with the processed records that preserve the static offsets through cross-fade filtering. Cross-fade filtering combines the high-frequency components of the filtered records with the low-frequency components of the records containing the static offsets. This gives the best representation of the "true" acceleration record.

Processing Methodology

For each horizontal ground motion record component from earthquakes (i)-(iv), for which raw, uncorrected records are available, three types of processed records are generated using the procedures outlined in Figure 4.1: a "raw" record, a "tilt-corrected" record, and several "filtered" records (with high-pass filters with different T_c). Raw, uncorrected records are not available from earthquakes (v)-(vii), so it is assumed that the cross-fade filtering procedure described in the previous section produces suitable tilt-corrected records. From these tilt-corrected records from earthquakes (v)-(vii), filtered records are generated in the same manner as those from earthquakes (i)-(iv). The remainder of this sub-section describes the processing methodology for the aforementioned three types of processed records.

In order to create a suitable "raw" record for structural analysis, the mean is removed from the uncorrected acceleration record so that any static offset present in the uncorrected record before shaking begins does not dominate structural response. The mean is removed from the entire record instead of the pre-event (before p-wave arrival) mean in order to be as naïve as possible when creating the raw record.

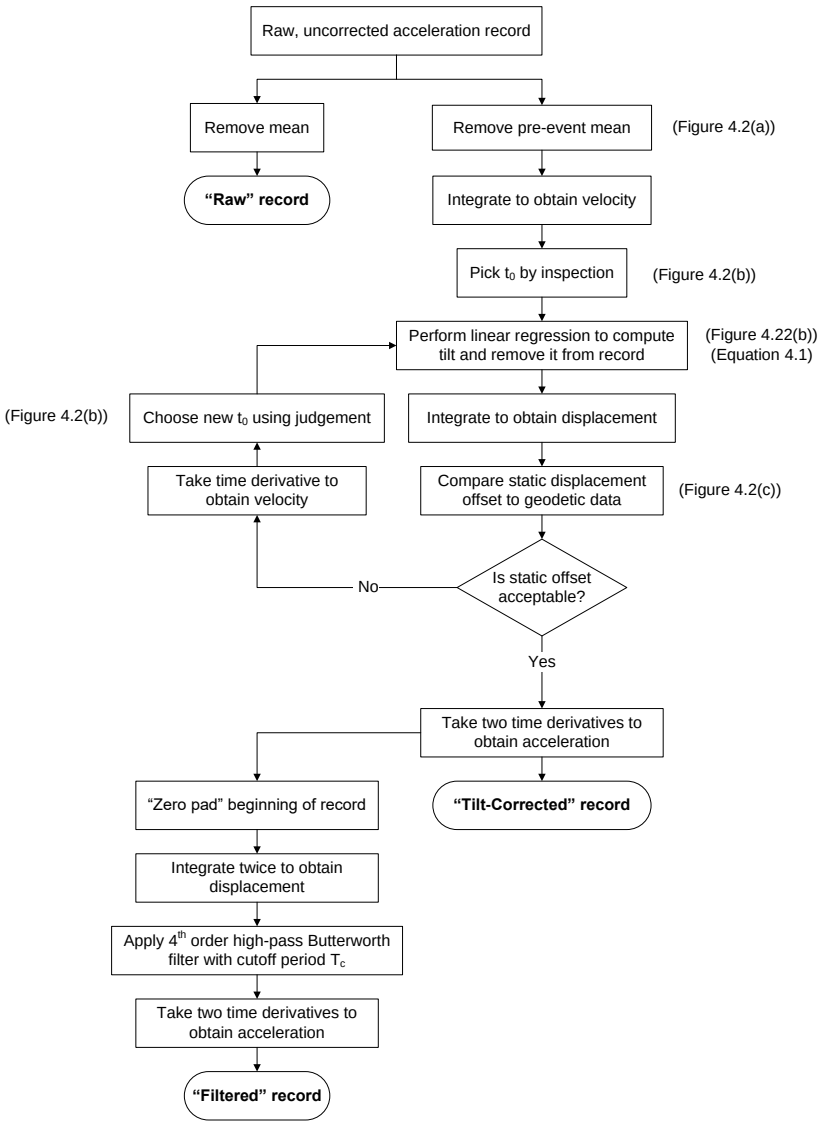

Figure 4.1: Flowchart detailing the procedure for obtaining raw, tilt-corrected, and filtered records from those recorded in earthquakes (i)-(iv), for which raw, uncorrected records are available.

The steps to produce the "tilt-corrected" record are plotted in greater detail in Figure 4.2. First, the pre-event mean (Figure 4.2(a)) is removed from the uncorrected acceleration record. This rids the record of static offsets present in the uncorrected record before shaking begins. The pre-event mean is removed instead of the mean from the entire record because the latter is contaminated by tilt effects during shaking. Then, from the velocity record, t_0 is identified by inspection, which is the time at which it is assumed the tilt occurs instantaneously. The tilt effects (Figure 4.2(b)) are corrected by removing a linear trend, $v_{\text{trend}}(t)$, in the velocity record. $v_{\text{trend}}(t)$ is

calculated by applying to the velocity record a least-squares regression of the form shown in Equation 4.1 [80]:

$$v_{\text{trend}}(t) = C_1(t - t_0) \cdot H(t - t_0) + C_2, \tag{4.1}$$

where C_1 and C_2 are the least-squares regression coefficients. Note that $C_1 = g \cdot \sin \bar{\theta}_0$ represents the horizontal acceleration removed from the record and attributed to tilt, where $\bar{\theta}_0$ is the calculated tilt angle whose effects are removed in this tilt correction process. Removal of $v_{\text{trend}}(t)$ from the velocity record typically results in a displacement time series that is stable and that preserves the static offset.

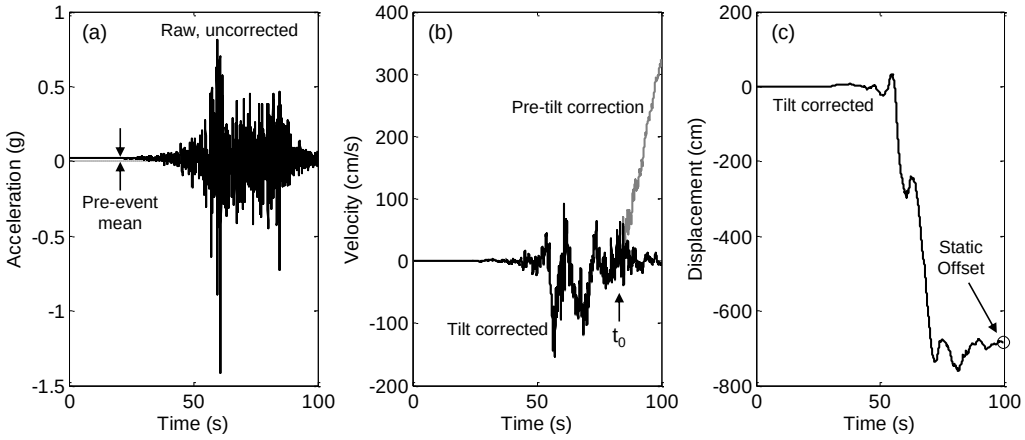

Figure 4.2: Steps for obtaining tilt-corrected record from raw, uncorrected record. In this example, the 2016 M7.8 Kaikōura KEKS NS record is processed. (a) Pre-event mean is removed from acceleration record. (b) Linear trend is removed from velocity record. (c) Final static offset in displacement record is checked to ensure stability and, if available, agree with geodetic data.

The value of t_0 will affect the static offset in the displacement record, so if observations of the static offsets are available for a record, t_0 is iteratively selected until the calculated static offset approximately matches the observed offset (Figure 4.2(c)). Observed static offsets are available from Hamling et al. [81] for the Kaikōura earthquake, Asano and Tomotaka [82] for the Kumamoto earthquake, Galetzka et al. [83] for the Gorkha earthquake, Lu et al. [84] for the Wenchuan earthquake, Ellsworth et al. [79] for the Denali earthquake, Boore [70] for the Chi-Chi earthquake, and Chen [78] for the Landers earthquake. If observations of the static offsets are not available for a particular record, the choice of t_0 is considered acceptable if it results

in a stable displacement time series. For each record, once a choice of t_0 is deemed acceptable, the resulting processed record is considered the "tilt-corrected" record.

After the ground motion is tilt-corrected, its tilt angle $\bar{\theta}_0$ can be calculated according to Equation 4.2:

$$\bar{\theta}_0 = \sin^{-1}\left(\frac{C_1}{g}\right). \tag{4.2}$$

Of the considered horizontal records, the tilt is always less than three degrees and usually less than one degree. Note that a tilt angle of one degree corresponds to 0.0175 g of horizontal acceleration.

To generate filtered records from the tilt-corrected records, acausal and causal 4th-order Butterworth high-pass filters are applied. The NGA-West2 project used acausal high-pass Butterworth filters, which is a change from the NGA-West1 project, for which causal Butterworth filtered records were preferred. Acausal filters were used in the NGA-West2 project because causal filters introduce phase distortions and were shown to affect measurements of spectral accelerations (e.g. [74]). In this study, acausal filters are implemented by first filtering the record in the forward time direction with a causal filter and then convolving the filtered record with a time-reversed copy of the same causal filter in order to remove the phase shifts. The acausal filter preserves the timing of the peak-to-peak values but removes the static offset and adds a precursory motion, usually leading to a reduction in the peak displacement of the record.

To produce the filtered records used in this study, data points of zero acceleration are applied to the beginning of the tilt-corrected record to satisfy zero initial conditions before filtering [85]. The "padded zeros" are not removed after filtering. After zero-padding, a Butterworth filter is applied to the displacement record. For each tilt-corrected record, twelve filtered records are generated by filtering the tilt-corrected record with a causal and an acausal 4th-order high-pass Butterworth filter with T_c = 10, 15, 20, 30, 40, and 60 seconds. For reference, in the NGA-West2 database, T_c = 10 seconds is used most frequently for $M > 6.0$ and $R_{JB} < 20$ km and $T_c = 33.33$ seconds is used most frequently for $M > 7.0$ and $R_{JB} < 20$ km [67, 69].

As an example, the raw and tilt-corrected displacement records from the KEKS station in the 2016 M7.8 Kaikōura earthquake in the NS direction are shown in Figure 4.3 along with the corresponding filtered records using acausal and causal filters with $T_c = 40$ seconds. The precursor introduced by the acausal filter before strong shaking begins is indicated.

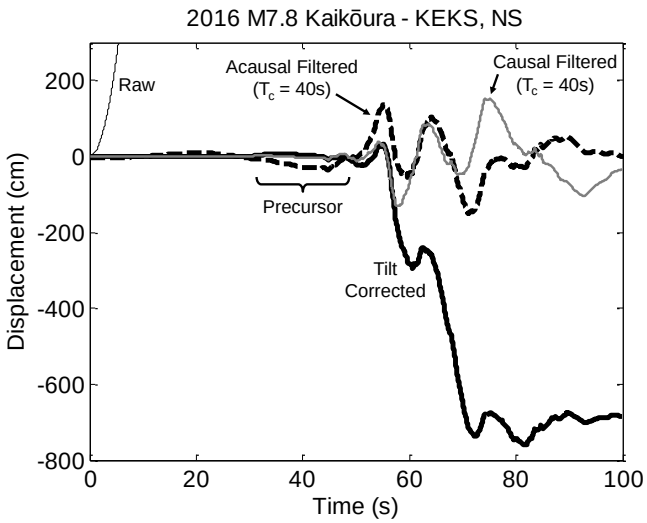

Figure 4.3: Example of raw, tilt-corrected, and filtered record. In this example, the 2016 M7.8 Kaikōura KEKS NS record is processed.

Processed Ground Motions

Information about each tilt-corrected ground motion record is shown in Table 4.1. For each record, there are two orthogonal horizontal directions. With two exceptions, the two horizontal components of every record are oriented arbitrarily (e.g. north-south and east-west directions) with no regard for fault geometry. The two exceptions are the 1992 M7.3 Landers LUC and 2002 M7.9 Denali PS10 records, both of which have one fault-parallel (FP) horizontal component and one fault-normal (FN) horizontal component. For every ground motion record, the reported PGA, PGV, PGD, and calculated tilt angle ($\bar{\theta}_0$) are the maximum of the two horizontal components. Note that for records from earthquakes (v)-(vii), no tilt angle can be calculated because the raw, uncorrected records are not available. For most records, R_{JB} is reported, but for some of the records from earthquakes (i) and (ii), information for R_{JB} is not yet available. For these records, the epicentral distance is reported and is marked with an asterisk.

Table 4.1: Details of every considered ground motion record. Reported values of PGA, PGV, PGD, and Tilt are the maximum of the two recorded horizontal directions and are calculated from the tilt-corrected records. For some records, R_{JB} is not available, so the epicentral distance is reported instead.

Earthquake	M	Station	R_{JB}	PGA (g)	PGV (cm/s)	PGD (cm)	Tilt (°)
2016 Kaikōura	7.8	CULC	15.6	0.27	29	75	0.62
		KEKS	3.0	1.97	269	867	1.54
		KIKS	0.7	0.51	160	304	1.83
		WDFS	8.5	2.51	210	816	1.23
		WIGC	18.0*	0.75	64	52	2.73
		WTMC	0.7	1.12	117	284	0.01
2016 Kumamoto	7.0	93048	0.6	0.79	264	186	0.58
		93051	0.5	0.84	178	105	0.48
		KMM001	5.0*	0.22	39	45	0.58
		KMM004	3.9*	0.35	82	74	0.12
		KMM005	5.6	0.54	69	115	0.55
		KMM007	3.5*	0.43	44	40	0.27
		KMM009	2.2*	0.79	38	41	0.19
		KMMH16	0.5	1.18	142	228	0.08
		OIT009	7.8*	0.73	78	102	0.11
2015 Gorkha	7.8	KATNP	0.1	0.16	112	246	0.02
2008 Wenchuan	7.9	AXT	9.8	0.29	31	105	0.04
		MZQ	0.8	0.82	136	213	0.07
		SFB	4.8	0.58	81	318	2.04
2002 Denali	7.9	PS10**	3.0	0.33	137	302	–
1999 Chi-Chi	7.6	TCU052	1.8	0.45	225	740	–
		TCU065	2.5	0.79	135	198	–
		TCU067	1.1	0.50	100	191	–
		TCU068	3.0	0.51	298	885	–
		TCU084	11.4	1.00	118	251	–
1992 Landers	7.3	LUC**	2.0	0.76	146	263	–

* Epicentral distance is reported because R_{JB} is not available.

** Two horizontal directions are oriented parallel and normal to the ruptured fault.

In most of the considered ground motion records, removing the pre-event mean acceleration and $v_{\text{trend}}(t)$ yields a stable displacement representation, even without applying a filter. The constant acceleration that is introduced into the unprocessed record by tilt effects is usually small in comparison to the peak accelerations of the record, so the differences between an unprocessed and tilt-corrected acceleration record are nearly imperceptible in the acceleration time series to the naked eye.

To demonstrate the differences between raw, tilt-corrected, filtered, and NGA-West2 records, Figure 4.4 shows the processed velocity and displacement time series for the 2016 M7.0 Kumamoto 93048 EW record, the 1992 M7.3 Landers LUC Fault-Normal (FN) record, and the 1999 M7.6 Chi-Chi TCU068 NS record. The filtered records are generated acausally with T_c = 10 and 40 seconds. The NGA-West2 versions of the Landers LUC FN and Chi-Chi TCU068 NS records are taken from the NGA-West2 database. For the Kumamoto 93048 EW record, a raw record is available and the tilt effects are clear in both the velocity and displacement time series.

The differences between the tilt-corrected records and the filtered and NGA-West2 records are most clear in the displacement time series. Compared to the tilt-corrected records, the filtered and NGA-West2 displacement time series contain precursors, as would be expected from acausal filtered records. Furthermore the peak displacements are always smaller in the filtered and NGA-West2 records than in the tilt-corrected records. The effects of filtering are not as obvious in the velocity time series except in the Chi-Chi TCU068 NS record, for which the acausal filtered record with T_c = 10 seconds has a significantly lower peak velocity than the other records.

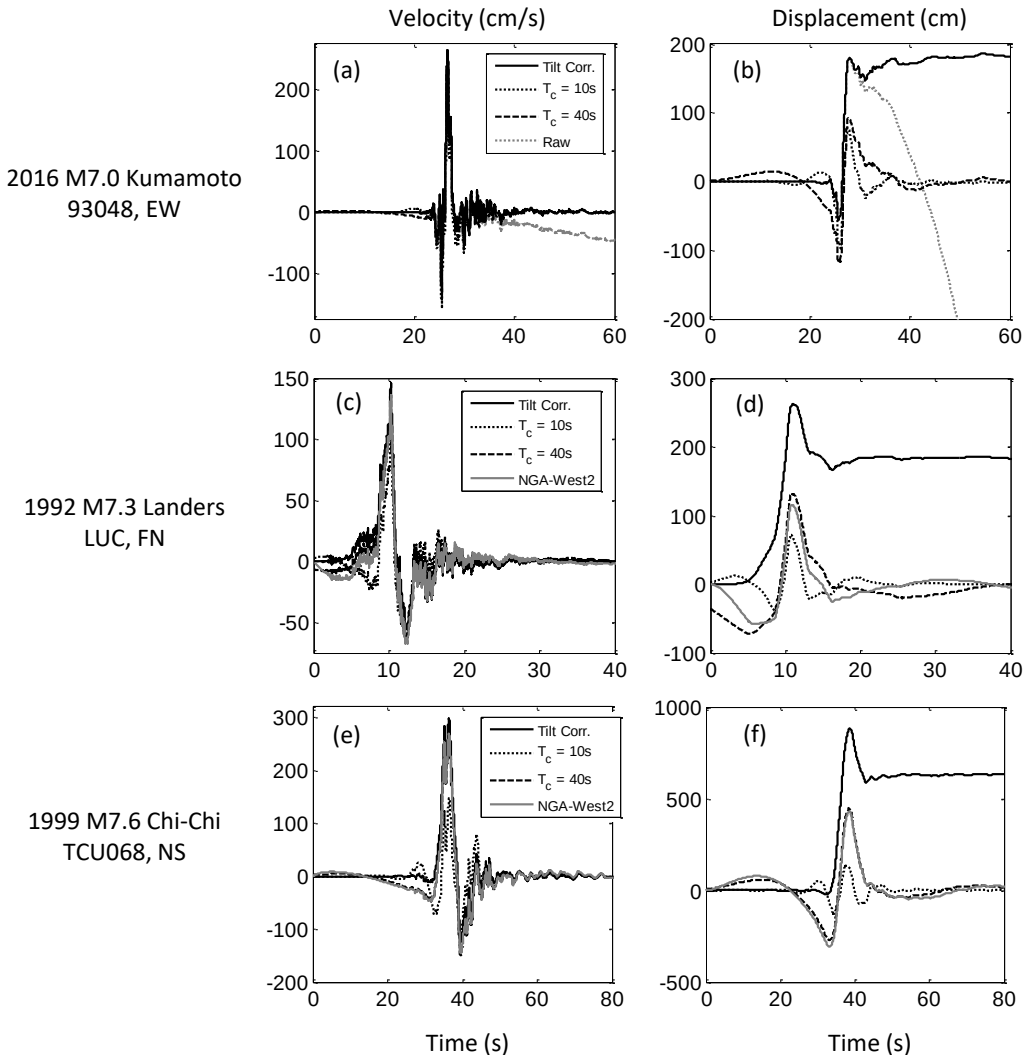

Figure 4.4: Examples of velocity and displacement series processed using different techniques. The filtered records (indicated by their respective T_c) are filtered acausally. An NGA-West2 record is not available for the Kumamoto 93048 EW record. Raw records are not available for the Landers LUC FN and Chi-Chi TCU068 NS records.

To further demonstrate the effects of the filters on the velocity of the records, Table 4.2 shows the PGV of one component of a record from each earthquake and compares the tilt-corrected PGV to the filtered PGV with various T_c. The records shown in Table 4.2 are those that have the largest PGV from each earthquake. Where available, the PGV from the record in the NGA-West2 database is shown for comparison.

Table 4.2: PGV of tilt-corrected and filtered records for ground motion records that have the highest PGV from each considered earthquake.

			PGV (cm/s)				
Earthquake	Station	Component	Tilt Corr.	T_c = 10s	T_c = 20s	T_c = 40s	NGA-West2
Kaikōura	KEKS	EW	269	213	232	235	–
Kumamoto	93048	EW	264	230	247	255	–
Gorkha	KATNP	EW	112	98	103	108	–
Wenchuan	MZQ	EW	136	89	117	129	–
Denali	PS10	FP	137	104	114	124	103[a]
Chi-Chi	TCU068	NS	298	147	230	265	269[b]
Landers	LUC	FN	146	113	128	137	136[c]

[a] T_c = 10 seconds and maximum usable period is 7.7 seconds.
[b] T_c = 50 seconds and maximum usable period is 40 seconds.
[c] No high-pass filter.

In every case, the PGV of the filtered record is less than that of the tilt-corrected record. For $T_c = 40$ seconds, the PGV is usually within about 10% of the tilt-corrected PGV. In the most extreme case, for the Chi-Chi TCU068 NS component, the $T_c = 10$ seconds filtered record has a PGV that is about 50% of the tilt-corrected PGV. The NGA-West2 records also have lower PGV than the tilt-corrected records. As should be expected, the discrepancy between the NGA-West2 PGV and the tilt-corrected PGV depends on the reported T_c from the NGA-West2 flatfile. Interestingly, the PGV of the tilt-corrected Landers LUC FN record is 7% larger than that of the NGA-West2 record even though no high-pass filter was applied to produce the NGA-West2 record. The discrepancy can be explained by the removal of a 6th-order polynomial from the displacement record after filtering in the NGA-West2 processing procedure. So even though the Landers LUC FN NGA-West2 record was not high-pass filtered, removing a 6th-order polynomial from the record removed enough of the signal for the PGV to be reduced by 7%.

4.3 Building Models

In order to quantify the effects of different ground motion processing techniques on structural response, incremental dynamic analysis (IDA) is performed with these ground motions on several different building models. Six steel moment frame models and one simple two-degrees-of-freedom (2DOF) model of a base-isolated building are considered. The six steel moment frame models are developed from three designs of steel moment frame buildings with heights of 9, 20, and 55 stories. For each design, two models are created, one with "perfect" (P) moment connections and one with pre-Northridge "brittle" (B) moment connections, for a total of six models. These models are described in Section 2.2 and denoted in this section 9P, 9B, 20P,

20B, 55P, and 55B to denote the height and connection type of each model. All models are based on steel moment frames designed according to the 1994 UBC. In this study, only a single realization of each B model is considered in order to isolate differences in responses to different ground motions to the ground motions themselves and not to different distributions of brittle welds in the model.

Pushover analysis is performed for each of the six building models considered in this study, calculated according to the dynamic procedure described in Section 2.2, except that the mass assigned to each story is not modified, so the vertical distribution of forces is proportional to the seismic mass of each story. Figure 4.5(a) shows the pushover curves for each building model. Each model is denoted first by the number of stories (9, 20, or 55) and then by the connection type (P or B). It may be surprising that the 55-story model has a higher base shear capacity than the 20-story model. This is in part due to its "tube" structural plan, with perimeter columns spaced only 8 feet apart in comparison to the 30- and 20-foot bays of the 9- and 20-story models, respectively. It is also due to the stringent wind load requirements that govern the design of most of the members of the 55-story model.

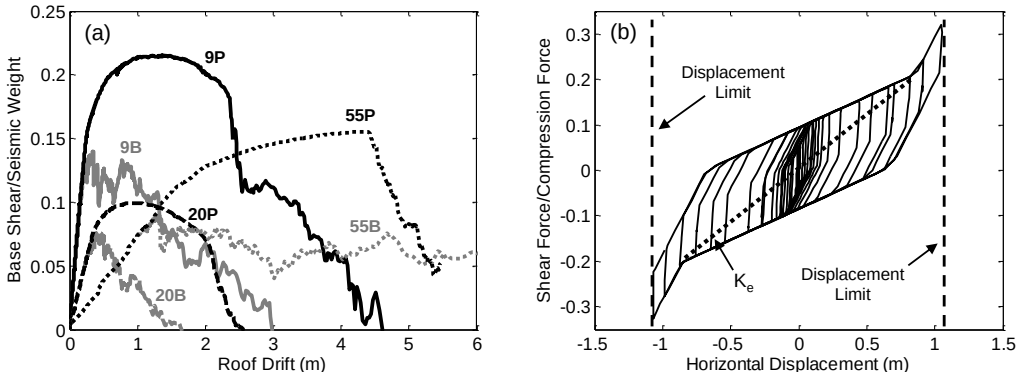

Figure 4.5: (a) Pushover curves of steel moment frame models. (b) Hysteretic behavior of isolator in 2DOF isolation system.

To represent a modern structure designed near a large fault whose seismic response may be affected by long-period shaking, a simple two-degrees-of-freedom (2DOF) model of a base-isolated building is developed using SAP2000 [86]. One of 69 isolators in the San Bernardino Justice Center, a 3-story podium and 12-story tower whose structural properties are summarized by Sarkisian et al. [87], is approximately modeled. The isolator is a triple concave-friction pendulum and is modeled using the Triple Friction Pendulum element in SAP2000. The properties for this element are

taken from Sarkisian et al. [87]. The force-displacement relationship for the isolation element, as calculated in SAP2000 during loading and unloading, is shown in Figure 4.5(b).

The superstructure is a linear single-degree-of-freedom element whose period is 1.01 seconds without the isolator. The effective stiffness (K_e) of the isolator is calculated from Figure 4.5(b), which approximates the stiffness of the isolator during strong shaking. This produces an effective period of 4.25 seconds for the complete 2DOF system. The maximum displacement of the isolator is 1.067 meters (42 inches), defined as the point at which both inner and outer stops in the isolator are impacted. This is the MCE (Maximum Considered Earthquake) maximum displacement limit in design (per Chapter 17 of ASCE 7-10 [20]) and analyses that produce isolator displacements exceeding this limit are not considered. This limit is used to define the "collapse capacity" for the model in this study, even though it does not imply collapse of the superstructure.

For the 9P, 20P, and 55P models, IDA is performed for each horizontal component of every considered ground motion. The two horizontal components of each record are treated as two individual ground motions (for a total of 52 considered record components) and vertical shaking is not considered. For a single model and ground motion, IDA is performed by multiplying the ground motion by a scale factor of 0.1 and performing nonlinear time history analysis in Frame-2d. This process is repeated by incrementing the scale factor by 0.1 for each successive analysis and is continued until the scaled ground motion causes collapse of the building model. In this paper, collapse of the steel moment frame models is defined to occur when a numerical instability arises in simulation. For each individual time history analysis in an IDA, the maximum roof drift and the maximum interstory drift ratio are recorded for post-processing. These results are presented in Sections 4.4 and 4.5. In Section 4.6, IDA is performed in the same manner for the 9B, 20B, and 55B models with all processed versions of the seven records with large PGV presented in Table 4.2. IDA is also performed for the isolator system model with these records in Section 4.6.

4.4 Acausal vs. Causal Filters

Similar to observations from previous researchers (e.g. ([74, 88]), the results of this study show that causal filters dramatically alter structural responses because they introduce phase distortions in the ground motion record. Shown in Figure 4.6 are the results of IDA for the 9P model with the Kaikōura KEKS NS ground

motion. For the Kaikōura KEKS NS record, Figure 4.6 plots the IDA curves for the tilt-corrected record, the record after it is high-pass filtered with a 4th-order *acausal* Butterworth filter with T_c = 40 seconds, and the record after it is high-pass filtered with a 4th-order *causal* Butterworth filter with T_c = 40 seconds.

For a typical IDA curve, the x-axis represents some measure of structural response (e.g. roof drift) and the y-axis represents some measure of the ground motion intensity (e.g. scale factor). Each curve represents a single ground motion and building model. The curve shows how the response of the building model changes as the intensity of the ground motion is increased. Eventually, when the ground motion's scale factor is large enough, the building model will collapse. This is indicated here by a roof drift that goes to infinity.

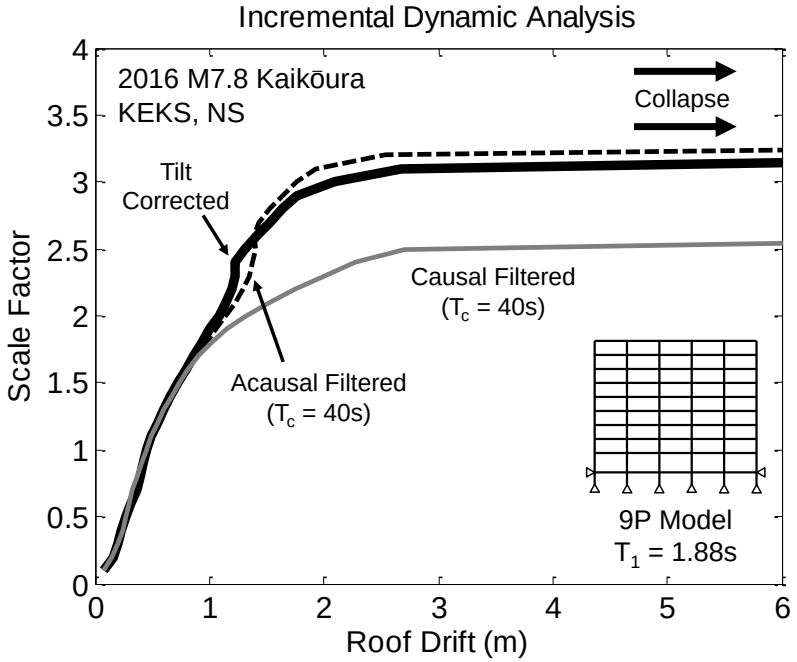

Figure 4.6: IDA curves of 9P model for the tilt-corrected Kaikōura KEKS NS ground motion record and its corresponding acausally and causally filtered records with T_c = 40 seconds.

With T_c = 40 seconds and T_1 = 1.88 seconds, one would assume that high-pass filtering the record should have a small or negligible effect on structural response. From Figure 4.6, it is clear that this essentially the case for the acausal filter but not for the causal filter. For brevity, only this one example is presented, but the observation that the causal T_c = 40 seconds filter affects nonlinear response but the acausal T_c = 40 seconds filter does not is consistent throughout most ground motions

and building models. As such, for all subsequent analyses, all "filtered" ground motions are processed with an *acausal* high-pass filter. *Causal* high-pass filters are no longer considered.

These results imply that the significant precursor created by filtering a record with an acausal high-pass filter does not have a significant effect on structural response. For example, Figure 4.3 shows the precursor in the displacement time series of the Kaikōura KEKS NS record that results from application of a high-pass 4th-order acausal Butterworth filter with T_c = 40 seconds. However, Figure 4.6 shows that this has a minimal effect on the response of the 9P model. This observation is consistent throughout most ground motions and building models

Also note that the acausal high-pass filter with T_c = 40 seconds reduces the PGD of the Kaikōura KEKS NS record by about 4x, as can be seen in Figure 4.3. This observation is also consistent throughout most ground motions. That nonlinear response is relatively unaffected by this drastic reduction in PGD implies that even though PGD may be an indicator of long-period shaking, more information than the absolute value of PGD is necessary to properly quantify the intensity of a ground motion with respect to its potential to induce nonlinear response in structures.

4.5 Scale Factor Ratios

From the results of IDA, the scale factor at which each of four engineering demand parameters (EDPs) is first elicited in each of the 9P, 20P, and 55P models is extracted for each ground motion. The four EDPs are maximum interstory drift ratio (MIDR) = 0.03, MIDR = 0.06, MIDR = 0.1, and collapse. For a given EDP, ground motion record, and building model, the scale factor ratio (SFR) for the record is defined as the scale factor needed to multiply by the record in order to induce the EDP divided by the scale factor needed to multiply by the corresponding tilt-corrected ground motion in order to induce the EDP:

$$SFR = \frac{\text{scale factor of processed (or raw) record to induce EDP}}{\text{scale factor of corresponding tilt-corrected record to induce EDP}}. \quad (4.3)$$

For example, for the 20P model and the Chi-Chi TCU084 NS ground motion record, MIDR = 0.06 is first achieved with a scale factor of 4.6 for the T_c = 10 seconds filtered record and with a scale factor of 4.3 for the tilt-corrected record. So in this example, SFR = 4.6/4.3 = 1.07.

Shown in Figures 4.7-4.10 are histograms of the SFR values corresponding to MIDR = 0.03, MIDR = 0.06, MIDR = 0.1, and collapse (denoted $SFR^{0.03}$, $SFR^{0.06}$, $SFR^{0.1}$,

and SFR^{col}), for the 9P, 20P, and 55P models for records filtered with T_c = 10, 20, and 40 seconds. For comparison, the SFR values for the raw records are shown for the ground motions for which raw records are available. If SFR = 1.00 for a filtered (or raw) record, then the collapse capacity of the structure is the same for the filtered (or raw) record as for the tilt-corrected record. The percent labeled in each plot is the height of the bar representing SFR approximately equal to 1.00. Each bar in the histograms has a width of 1/8.

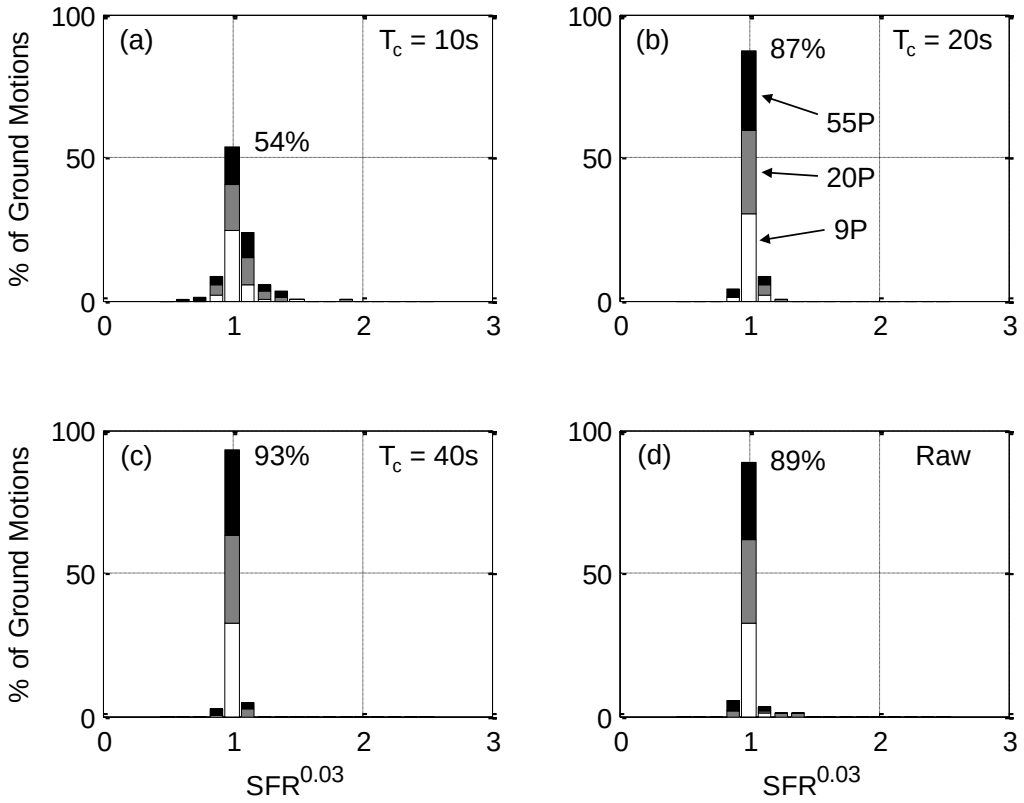

Figure 4.7: Histograms of $SFR^{0.03}$ for (a) filtered records with T_c = 10 seconds, (b) filtered records with T_c = 20 seconds, (c) filtered records with T_c = 40 seconds, and (d) raw records (where available). Each bar in the histograms has a width of 1/8 units.

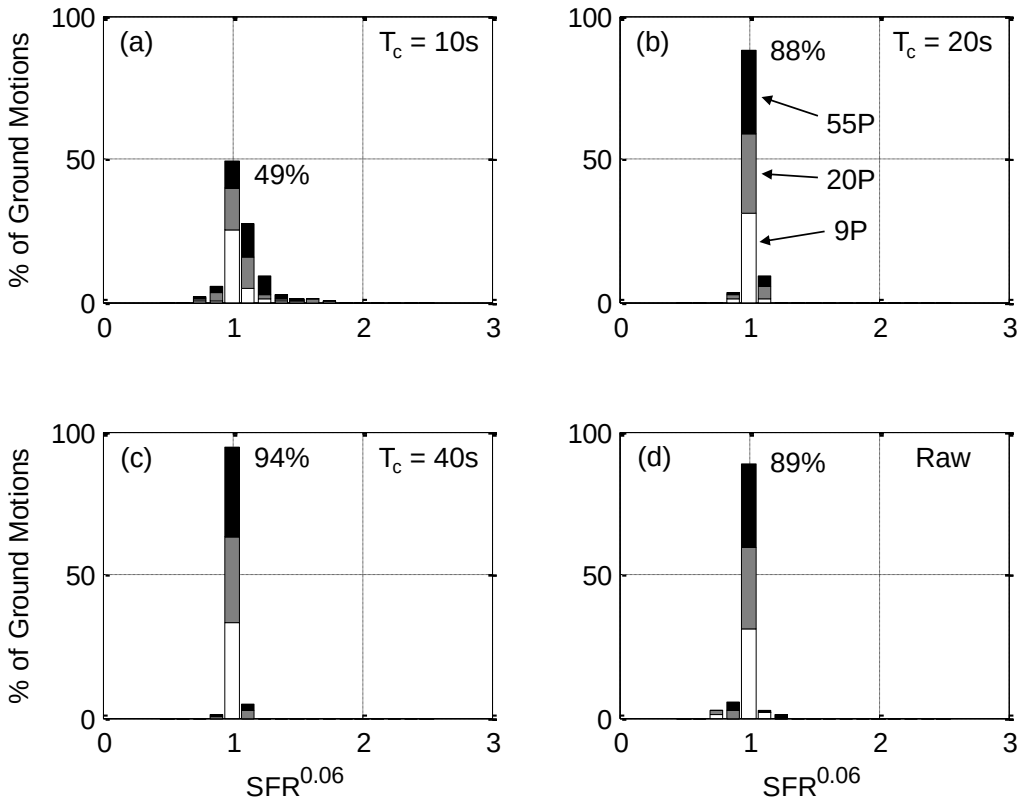

Figure 4.8: Histograms of $SFR^{0.06}$ for (a) filtered records with T_c = 10 seconds, (b) filtered records with T_c = 20 seconds, (c) filtered records with T_c = 40 seconds, and (d) raw records (where available). Each bar in the histograms has a width of 1/8 units.

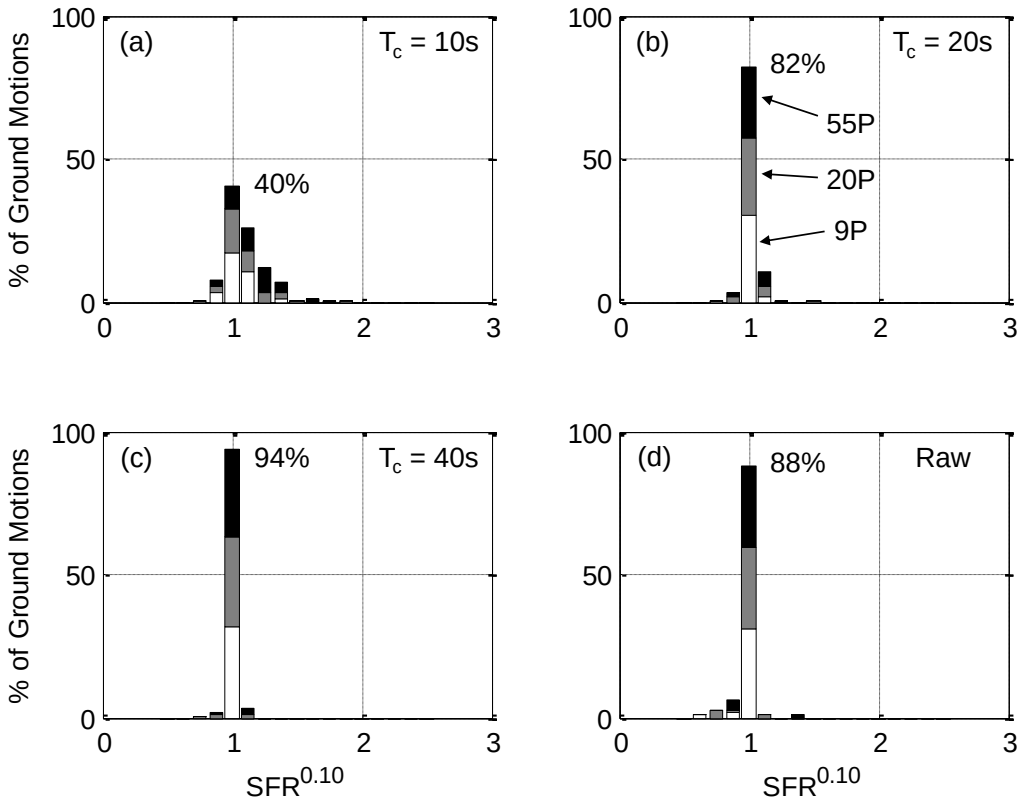

Figure 4.9: Histograms of $SFR^{0.10}$ for (a) filtered records with T_c = 10 seconds, (b) filtered records with T_c = 20 seconds, (c) filtered records with T_c = 40 seconds, and (d) raw records (where available). Each bar in the histograms has a width of 1/8 units.

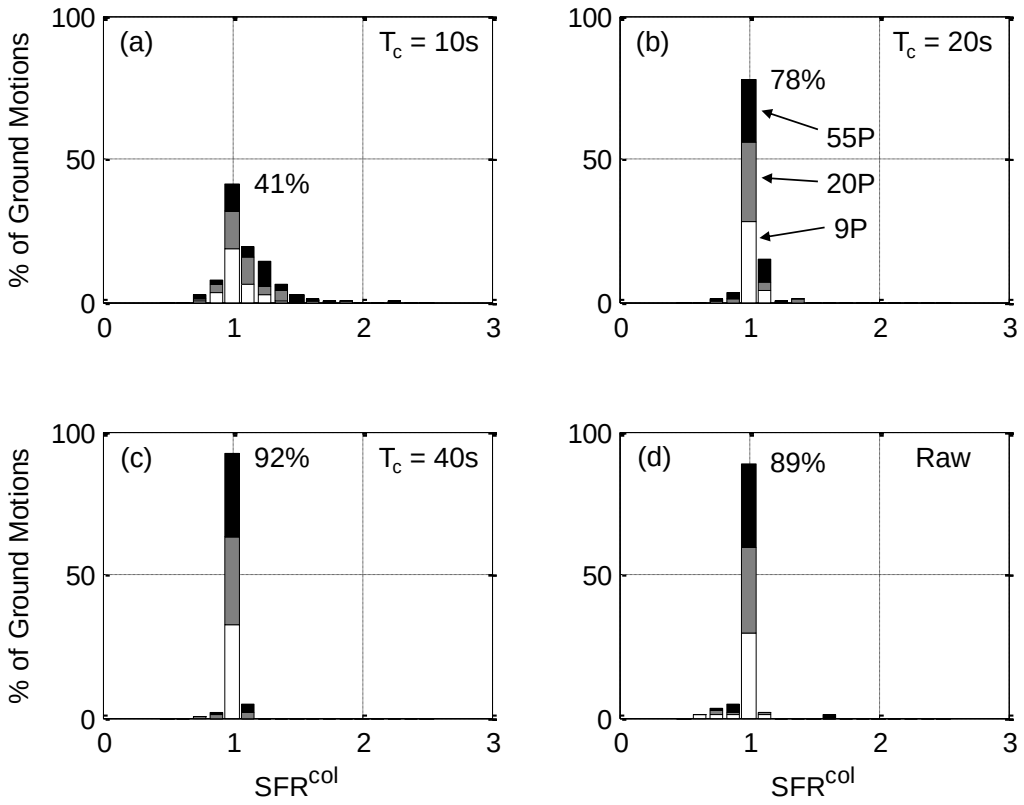

Figure 4.10: Histograms of SFR^{col} for (a) filtered records with T_c = 10 seconds, (b) filtered records with T_c = 20 seconds, (c) filtered records with T_c = 40 seconds, and (d) raw records (where available). Each bar in the histograms has a width of 1/8 units.

There are several interesting observations that can be made about Figures 4.7-4.10. First, as would be expected, as T_c increases, SFR for most of the records goes to 1.00. This makes sense because for a filter with larger T_c, more long-period motion remains in the record. It may be surprising, however, that for T_c = 10 seconds, only 41% of the records have SFR^{col} approximately equal to 1.00. In particular, there are a few records for which SFR^{col} for the 9P models is larger than 1.00 even though T_1 for the 9P model is 1.88 seconds, which would seem to be so much smaller than T_c = 10 seconds that the application of this filter would not affect the response of the 9P model. This is slightly less dramatic for less severe EDPs. For example, for T_c = 10 seconds, 54% of the records have $SFR^{0.03}$ approximately equal to 1.00 as opposed to 41% for SFR^{col}.

It may also be surprising that for most of the raw records, $SFR^{\text{col}} \approx 1.00$ despite the

presence of long-period noise in the raw records. In fact, these results imply that one may be better off estimating the collapse capacity of a building model using a raw record than using a record filtered with T_c = 10 or 20 seconds. This is also true for $SFR^{0.03}$, $SFR^{0.06}$, and $SFR^{0.1}$, though to a slightly lesser extent.

For a more comprehensive summary of the results, statistics of the SFR values for the 9P, 20P, and 55P models for all four considered EDPs are given in Tables 4.3 and 4.4. These statistics are meant to summarize corresponding histograms such as those in Figures 4.7-4.10. For each EDP and building model, SFR_{50} and SFR_{84} are reported, representing the median and 84th percentile SFR values, respectively. These values are calculated for filtered records with T_c = 10, 15, 20, 30, and 40 seconds. Results are not shown for the T_c = 60 seconds filter because they are very similar to those of the T_c = 40 seconds filter. For a given EDP and building model, the distribution of SFR values for filtered records tend to be skewed to be greater than 1.00, so that $SFR_{50} \geq 1$ in all cases. SFR_{16} is not shown because it is equal to 1.00 or nearly equal to 1.00 in every case.

For comparison, SFR_{50} and SFR_{84} are reported for the corresponding NGA-West2 records, where available. Note that only 14 of the 52 considered ground motion record components have corresponding NGA-West2 records. For further comparison, these statistics are also calculated for the corresponding raw records (available for 38 of 52 components). However, recall that the raw records contain long-period noise which can make ground motion records more destructive. As such, SFR values for the raw records tend to be skewed to be less than 1.00. So instead of reporting SFR_{84} (which is equal to 1.00 in almost all cases for the raw records), $1 + (1 - SFR_{16})$ is reported for the raw records. This allows for a more direct comparison to SFR_{84} for the filtered ground motions while still measuring the variability of the SFR values.

Table 4.3: SFR_{50} for the (a) 9P, (b) 20P, and (c) 55P models calculated based on results from all considered ground motion records.

(a) 9P	SFR_{50}						
EDP	T_c = 10s	15s	20s	30s	40s	NGA-West2	Raw
MIDR = 0.03	1.00	1.00	1.00	1.00	1.00	1.00	1.00
MIDR = 0.06	1.01	1.00	1.00	1.00	1.00	1.00	1.00
MIDR = 0.1	1.03	1.00	1.00	1.00	1.00	1.00	1.00
Collapse	1.02	1.00	1.00	1.00	1.00	1.00	1.00
(b) 20P							
MIDR = 0.03	1.03	1.00	1.00	1.00	1.00	1.00	1.00
MIDR = 0.06	1.06	1.00	1.00	1.00	1.00	1.00	1.00
MIDR = 0.1	1.05	1.00	1.00	1.00	1.00	1.02	1.00
Collapse	1.06	1.00	1.00	1.00	1.00	1.05	1.00
(c) 55P							
MIDR = 0.03	1.00	1.00	1.00	1.00	1.00	1.00	1.00
MIDR = 0.06	1.11	1.01	1.00	1.00	1.00	1.00	1.00
MIDR = 0.1	1.15	1.03	1.00	1.00	1.00	1.00	1.00
Collapse	1.20	1.03	1.02	1.00	1.00	1.00	1.00

Table 4.4: SFR_{84} for the (a) 9P, (b) 20P, and (c) 55P models calculated based on results from all considered ground motion records.

(a) 9P	SFR_{84}						
EDP	T_c = 10s	15s	20s	30s	40s	NGA-West2	Raw*
MIDR = 0.03	1.08	1.03	1.00	1.00	1.00	1.00	1.00
MIDR = 0.06	1.08	1.04	1.02	1.00	1.00	1.00	1.01
MIDR = 0.1	1.12	1.06	1.04	1.02	1.02	1.03	1.03
Collapse	1.14	1.07	1.06	1.03	1.02	1.05	1.02
(b) 20P							
MIDR = 0.03	1.15	1.07	1.04	1.00	1.00	1.09	1.01
MIDR = 0.06	1.17	1.09	1.05	1.03	1.01	1.22	1.05
MIDR = 0.1	1.21	1.09	1.05	1.02	1.01	1.47	1.04
Collapse	1.28	1.08	1.05	1.03	1.02	1.38	1.04
(c) 55P							
MIDR = 0.03	1.18	1.06	1.02	1.02	1.00	1.11	1.04
MIDR = 0.06	1.27	1.08	1.05	1.02	1.01	1.09	1.04
MIDR = 0.1	1.34	1.13	1.07	1.03	1.03	1.08	1.04
Collapse	1.44	1.17	1.09	1.07	1.03	1.12	1.02

* Reported values for raw records are $1 + (1 - SFR_{16})$.

Despite the fact that the distribution of SFR values for a given EDP and building model are neither normal nor lognormal, SFR_{50} and SFR_{84} provide insight into the

effects of the different filters on structural response. SFR_{50} measures how a "typical" record is affected by the filters while SFR_{84} indicates the presence of a few ground motion records that may be greatly affected by the filters. Of the filtered records, it is observed that three factors generally lead to larger SFR_{50} and SFR_{84}: more severe EDPs, taller building models, and filters with shorter corner periods. That these three factors lead to larger SFR values is not surprising. It would be expected that more severe EDPs would have higher SFR values because, as buildings experience more damage, their effective period lengthens and they become more vulnerable to long-period shaking. Similarly, tall building models have longer elastic periods, so it would be expected that for a given filter, the effects on a taller building's response would be more significant than that of a shorter building. Lastly, filters with shorter corner periods remove more of the original signal than filters with longer corner periods, so it makes sense that they would have more of an effect on structural response.

Except for T_c = 10 seconds, SFR_{50} is equal to 1.00 in almost all the cases presented in Table 4.3. This implies that for most ground motions, as long as T_c is at least 15 or 20 seconds, one can expect that structural response to the processed record will not be dramatically different to that of the true ground motion. However, SFR_{84} is significantly greater than 1.00 in many cases presented in Table 4.4 for T_c = 15 and 20 seconds. For example, for about 16% of the ground motions, the collapse capacity of the 20P model is at least 8% larger if the record is processed with T_c = 15 seconds as opposed to the tilt-corrected record. When combined with the observation that SFR_{50} values are almost always equal to 1.00, this means that although the structural responses are not usually affected by these filters in a significant way, there are some cases in which they can have an effect. One of these cases (response of 20P model to the Landers LUC FN record) is explored later in this section. It appears that if T_c = 40 seconds, the structural responses are basically unaffected, even judging from SFR_{84}.

The structural responses from the raw records are very similar to those of the tilt-corrected records. In every case, SFR_{50} equals 1.00 for the raw records. Qualitatively, the reported SFR_{84} values for the raw records (actually calculated as $1 + (1 - SFR_{16})$) are similar to those filtered with T_c = 30 seconds. This leads to the interesting conclusion that, at least for the considered ground motion records, applying a high-pass filter with $T_c < 30$ seconds to remove long-period noise can remove so much of the actual long-period motion in the record that the structural response from the raw

record is closer to the response from the true ground motion than the response from the filtered record.

The statistics from the NGA-West2 ground motions show some surprising behavior. Although, like the filtered ground motions, SFR_{50} equals 1.00 in most cases for the NGA-West2 records, SFR_{84} is often dramatically greater than 1.00, especially for the 20P model. These results are somewhat skewed by the fact that there are only 14 NGA-West2 records considered here, so SFR_{84} is controlled by the possibly anomalous results from the Denali PS10 and Landers LUC records. For the NGA-West2 versions of these records, the SFR values can be as large as 1.5. To investigate this further, the Landers LUC FN record is briefly analyzed, for which SFR^{col} for NGA-West2 record is 1.37 for the 20P model even though the NGA-West2 flatfile indicates that it is not high-pass filtered.

Figure 4.11 compares the NGA-West2 and tilt-corrected Landers LUC FN records and the corresponding IDA results for the 20P model. As discussed previously, the only difference that might be expected between these two records is a static offset in the displacement time series corresponding to a 6th-order polynomial fit that is removed as part of the NGA-West2 processing procedure. Figure 4.11(a) compares the displacement time series of the NGA-West2 and tilt-corrected Landers LUC FN records. These time series are also shown in Figure 4.4(d), but here the difference between the two records is explicitly plotted, which is virtually equivalent to a 6th-order polynomial fit to the tilt-corrected record. Figure 4.11(b) compares the 5%-damped acceleration response spectra of the two records and indicates T_1 for the 20P model, which is 3.50 seconds. Despite the obvious differences in the displacement time series, the two records have almost identical response spectra.

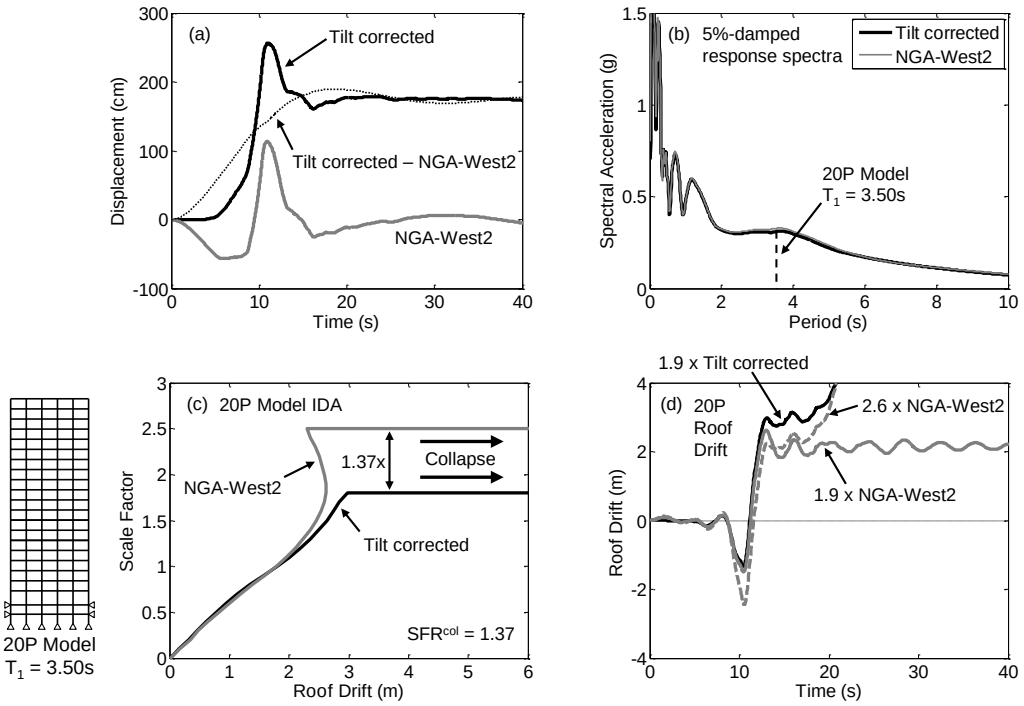

Figure 4.11: (a) Displacement time series of the Landers LUC FN tilt-corrected and NGA-West2 records. The difference between the two records is also shown. (b) Response spectra of the Landers LUC FN tilt-corrected and NGA-West2 records. (c) IDA curves when the Landers LUC FN tilt-corrected and NGA-West2 records are input into the 20P model, for which $T_1 = 3.50$ seconds. (d) Roof drift time histories of the 20P model in response to scaled versions of the Landers LUC FN tilt-corrected and NGA-West2 records.

Figure 4.11(c) compares the results of IDA between the NGA-West2 and tilt-corrected Landers LUC FN records. Despite the fact that the response spectra are nearly identical, the collapse capacities (i.e. the scale factor at which collapse first occurs) for the two records are notably different (by 37%). The responses are nearly identical for scale factors up to about one - it is only when the structure begins to experience highly nonlinear response that the results from the two records diverge. The large difference in the collapse capacities between the two records can be attributed to slightly different collapse mechanisms resulting from the two records. When collapse is induced by 1.9x the tilt-corrected record, large drifts in the structure are concentrated in stories 1-5. When collapse is induced by 2.6x the NGA-West2 record, large drifts are concentrated in stories 2-5. When 1.9x the NGA-West2 record is input into the 20P model, the structure nearly collapses with a mechanism in stories 1-5, but remains upright. As the scale factor is increased past 1.9 for the NGA-West2

record, the concentration of large drifts shifts from stories 1-5 to stories 2-5.

Figure 4.11(d) plots the roof drift over time of the 20P model in response to 1.9x the tilt-corrected record (which induces collapse), 2.6x the NGA-West2 record (which induces collapse), and 1.9x the NGA-West2 record (which does not induce collapse). It is evident that as the ground motions begins its pulse at about 10 seconds, the roof drift becomes large in the opposite direction, indicating that the base of the model is moving before the roof catches up. After 10 seconds, the roof of the model swings dramatically in the direction of the pulse and eventually the building collapses in this direction in response to 1.9x the tilt-corrected record and to 2.6x the NGA-West2 record. For 1.9x the NGA-West2 record, the roof does not swing quite as far in the direction of the pulse to induce collapse. For scale factors between 1.9x and 2.6x, response of the 20P model to the NGA-West2 record does not induce collapse because the initial roof drift that occurs around 10 seconds as the ground moves beneath the roof of the model causes enough yielding that the building does not swing as far in the direction of the pulse and thus does not collapse.

Interestingly, SFR^{col} for the $T_c = 40$ seconds filtered version of the Landers LUC FN record is 1.00 for the 20P model. Recall that for the filtered ground motions, filters are applied directly to the tilt-corrected ground motions. Thus, in the case of the Landers LUC FN record and the 20P model, removing a 6th-order polynomial fit to the tilt-corrected record has more of an effect on structural response than applying a high-pass filter with $T_c = 40$ seconds.

4.6 Results from Strongest Ground Motion Records

To demonstrate the aforementioned effects of high-pass filters for individual ground motions and building models, considered in this section are the ground motion record components from each earthquake that has the largest PGV: 2016 M7.8 Kaikōura WDFS EW, 2016 M7.0 Kumamoto 93048 EW, 2015 M7.8 Gorkha KATNP EW, 2008 M7.9 Wenchuan MZQ EW, 2002 M7.9 Denali PS10 Fault-Parallel (FP), 1999 M7.6 Chi-Chi TCU 068 NS, and 1992 M7.3 Landers LUC FN. These are denoted the "strongest" ground motion records. 5%-damped response spectra of the tilt-corrected versions of these records are shown in Figure 4.12 and compared to the MCE_R spectrum for a site in downtown Los Angeles (Latitude 34.05° N and Longitude -118.26° E) with Site Class C, for reference. The effects of the filters on PGV for these seven records were shown previously in Table 4.4. IDA is performed with these ground motions on the four building models not already analyzed in the previous

section (9B, 20B, 55B, and the isolation system) with the tilt-corrected and filtered versions of these records. Where available, IDA is also performed with the raw and NGA-West2 versions of these records.

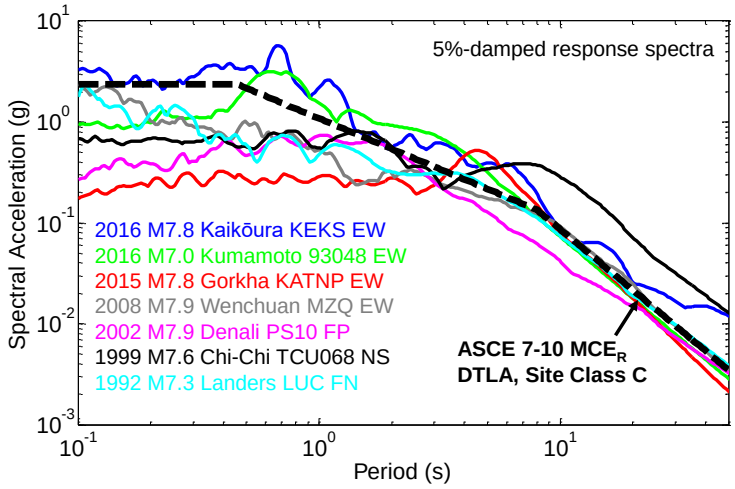

Figure 4.12: 5%-damped response spectra of tilt-corrected versions of the seven ground motion records considered in this section.

To summarize the results, $SF R^{\text{col}}$ is calculated for every available version of every ground motion. The results for the filtered records are shown in Figure 4.13 and the results for the raw and NGA-West2 records are shown in Tables 4.5 and 4.6, respectively. Recall that "collapse" is defined for the isolation system model to occur when the isolator reaches its displacement limit of 1.067 meters (42 inches), which does not necessarily mean the superstructure will experience collapse.

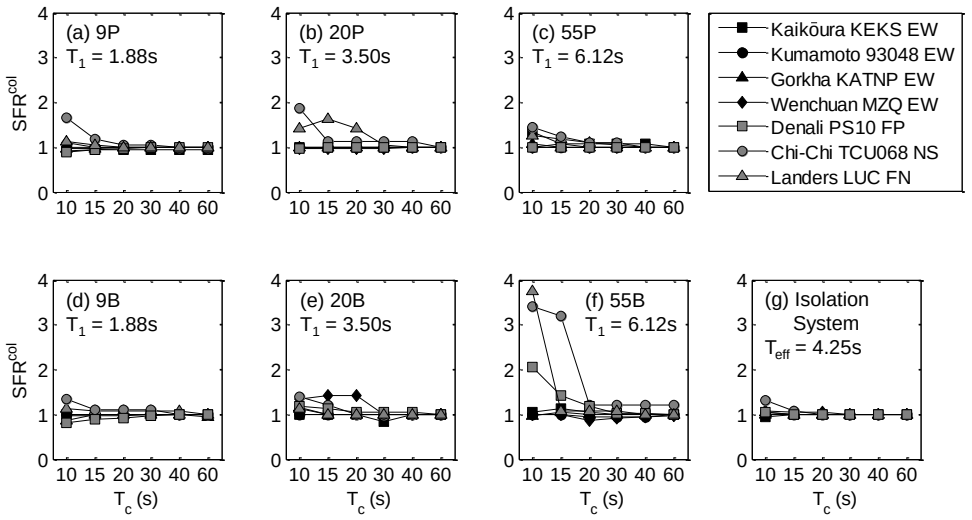

Figure 4.13: SFR^{col} values of all considered building models for the filtered versions of the strongest ground motion records with different T_c.

Table 4.5: SFR^{col} values of all considered building models for the strongest ground motion records for which corresponding raw records are available.

	SFR^{col} for raw records						
Record	9P	20P	55P	9B	20B	55B	Isolation System
Kaikōura KEKS EW	1.00	1.00	1.00	1.00	1.00	0.94	0.93
Kumamoto 93048 EW	1.00	1.00	1.00	1.00	1.00	1.00	1.00
Gorkha KATNP EW	1.00	1.00	1.00	0.93	1.00	1.04	1.00
Wenchuan MZQ EW	1.00	0.96	0.93	1.00	1.00	0.97	1.00

Table 4.6: SFR^{col} values of all considered building models for the strongest ground motion records for which corresponding NGA-West2 records are available.

	SFR^{col} for NGA-West2 records						
Record	9P	20P	55P	9B	20B	55B	Isolation System
Denali PS10 FP	0.90	1.00	1.02	0.82	1.06	1.76	1.04
Chi-Chi TCU068 NS	1.00	1.13	1.11	1.00	1.00	1.20	1.00
Landers LUC FN	0.96	1.37	1.09	1.00	1.00	1.08	0.94

Figure 4.13 shows that SFR^{col} is usually close to 1.00, but in some cases, particularly for $T_c = 10$ or 15 seconds, SFR^{col} can be significantly greater than 1.00. This is not surprising, as the same conclusions were drawn from Tables 4.3 and 4.4. Tables 4.5 and 4.6 also show the same trends as Tables 4.3 and 4.4 with regards to raw and NGA-West2 records. That is, SFR^{col} is always close to 1.00 for the raw records,

while SFR^{col} can vary greatly for the NGA-West2 records. For these seven strong ground motions, the 55B model appears to be the most susceptible to the effects of filtering input ground motions. This may be because the 55B model has the widest variety of different possible collapse mechanisms.

The response of the isolation system model does not seem to be significantly affected by high-pass filtering. This is probably because the effective period, $T_{\text{eff}} = 4.25$ seconds, of the isolation system model is calculated at its displacement limit, which is considered "collapse" for the purposes of this study. This means $T_{\text{eff}} = 4.25$ seconds is the upper limit of period lengthening. As such, spectral content in ground motions at periods longer than 4.25 seconds will not have a large effect on the isolation system model. It is therefore not surprising that the high-pass filters generally do not affect response because the smallest T_c is 10 seconds.

To take a closer look at how SFR^{col} varies by ground motion and building model, IDA curves for $T_c = 10$ seconds, $T_c = 20$ seconds, $T_c = 40$ seconds, and tilt-corrected versions of all seven ground motion records are shown in Figures 4.14-4.20 for all seven building models. For some of these records, such as the Kumamoto 93048 EW and Gorkha KATNP EW records, application of the high-pass filters has virtually no impact on structural response. However, for others, most dramatically the Chi-Chi TCU068 NS and Landers LUC FN records, the high-pass filters greatly affect structural response and the calculated collapse capacity.

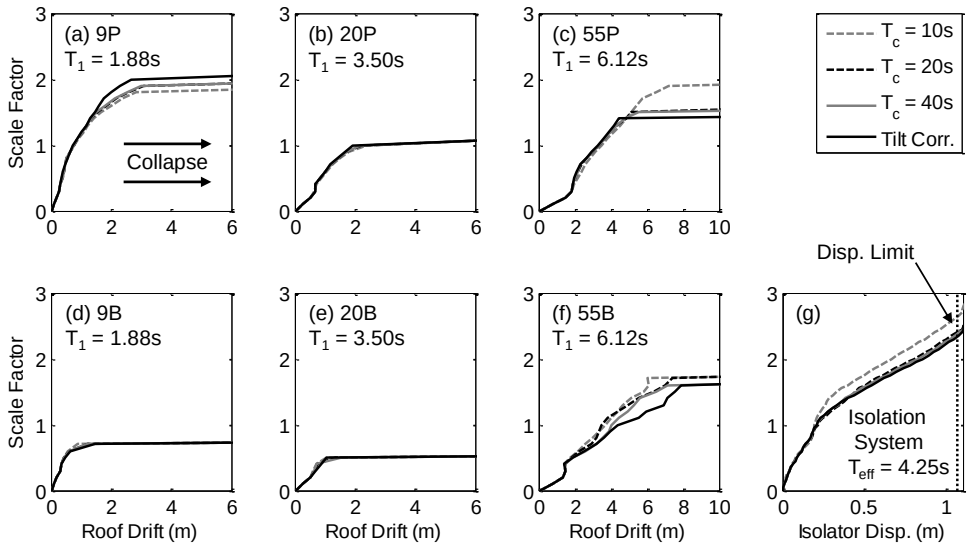

Figure 4.14: IDA curves of all considered building models for the tilt-corrected Kaikōura KEKS EW ground motion record and its filtered versions with T_c = 10, 20, and 40 seconds.

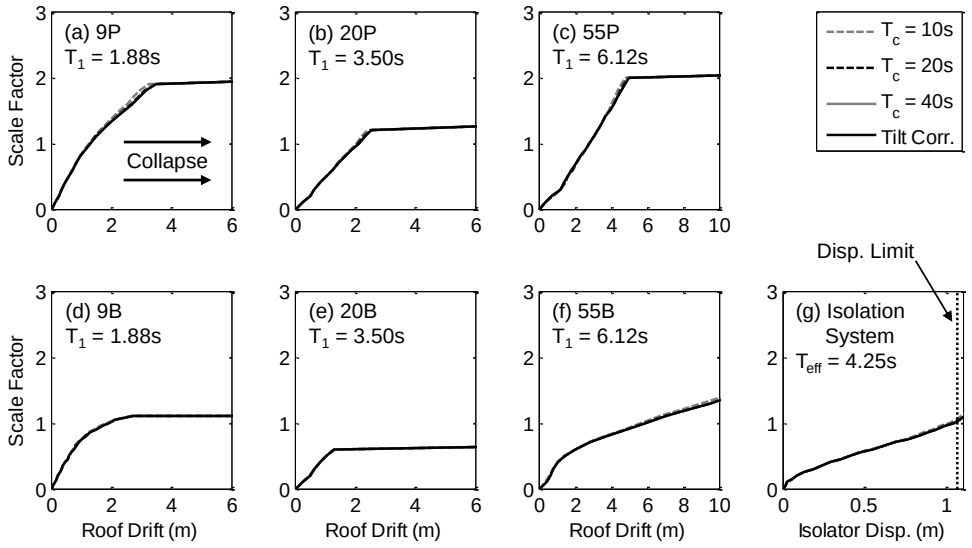

Figure 4.15: IDA curves of all considered building models for the tilt-corrected Kumamoto 93048 EW ground motion record and its filtered versions with T_c = 10, 20, and 40 seconds.

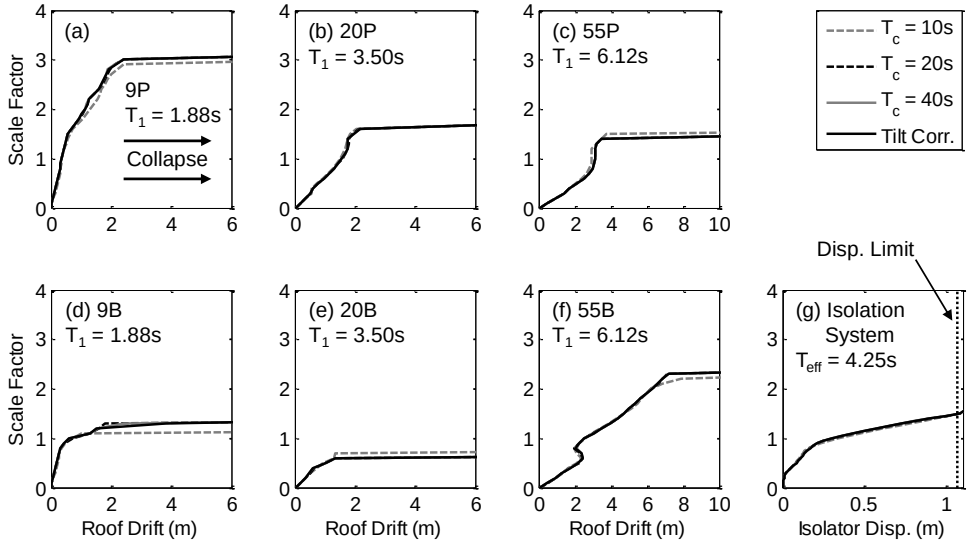

Figure 4.16: IDA curves of all considered building models for the tilt-corrected Gorkha KATNP EW ground motion record and its filtered versions with T_c = 10, 20, and 40 seconds.

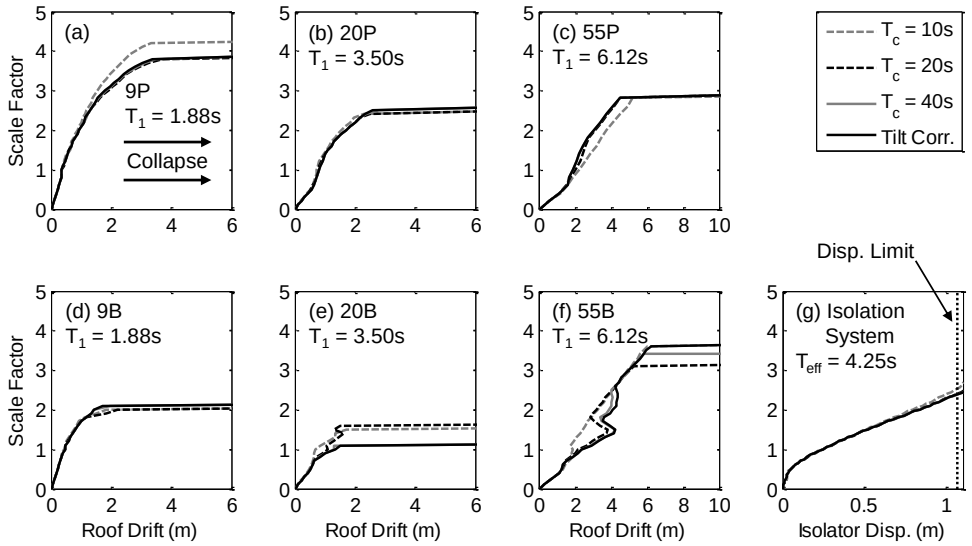

Figure 4.17: IDA curves of all considered building models for the tilt-corrected Wenchuan MZQ EW ground motion record and its filtered versions with T_c = 10, 20, and 40 seconds.

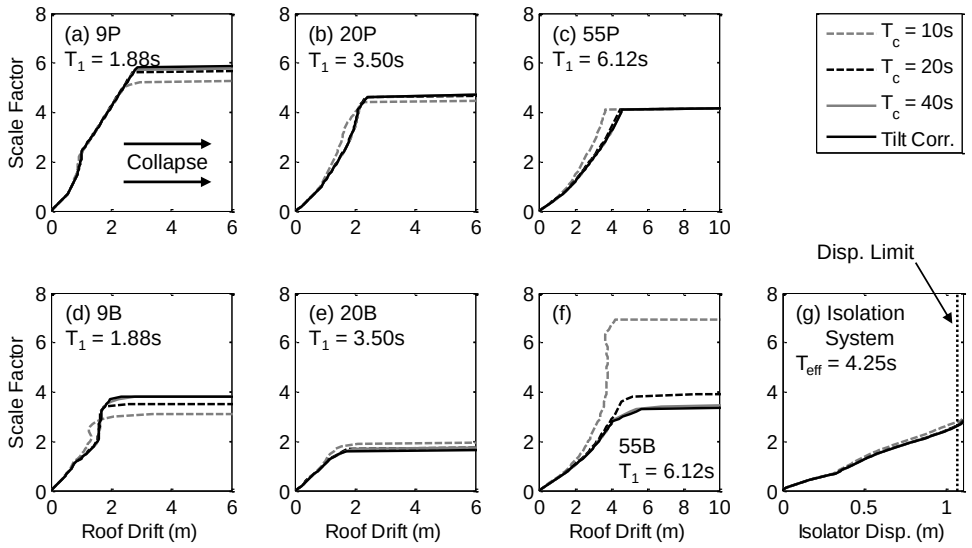

Figure 4.18: IDA curves of all considered building models for the tilt-corrected Denali PS10 FP ground motion record and its filtered versions with T_c = 10, 20, and 40 seconds.

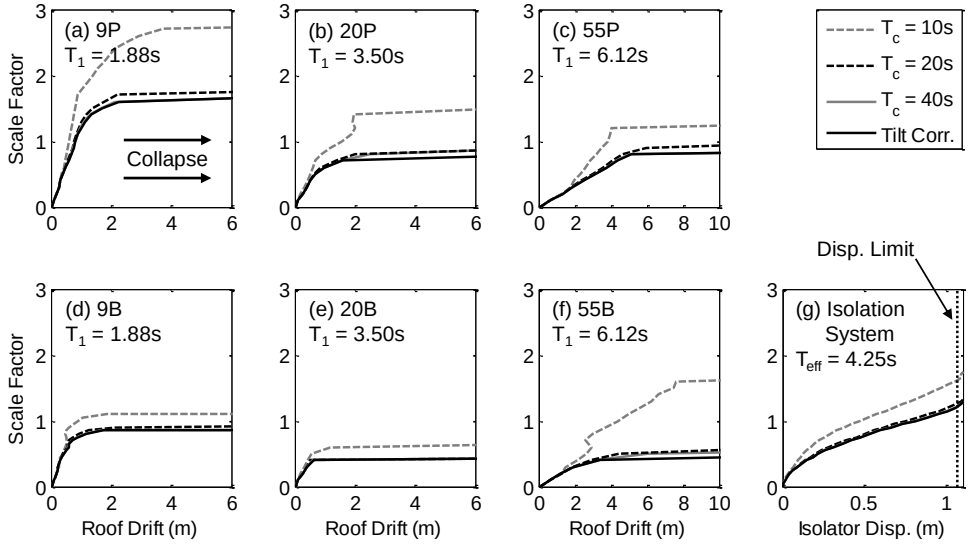

Figure 4.19: IDA curves of all considered building models for the tilt-corrected Chi-Chi TCU068 NS ground motion record and its filtered versions with T_c = 10, 20, and 40 seconds.

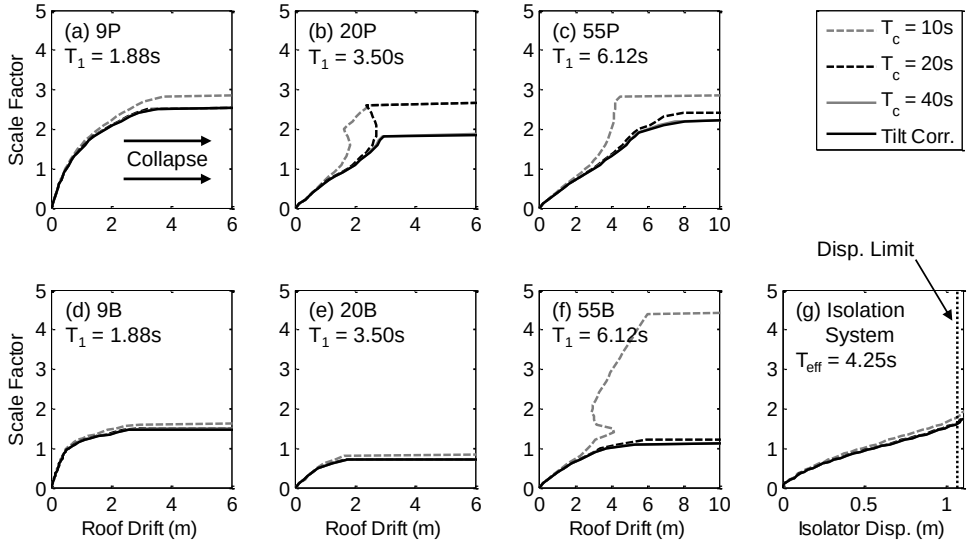

Figure 4.20: IDA curves of all considered building models for the tilt-corrected Landers LUC FN ground motion record and its filtered versions with T_c = 10, 20, and 40 seconds.

As evidenced by Figures 4.19 and 4.20, the high-pass filters can sometimes have a dramatic effect on the collapse capacity of the building models. The 55B model's collapse capacity for both the Chi-Chi TCU068 NS and Landers LUC FN records increases by more than 300% when a T_c = 10 seconds high-pass filter is applied, due to a phenomenon known as "severe hardening" [47] which is indicated by a negative slope in the IDA curve. Severe hardening occurs for the 55B model for both ground motions for the T_c = 10 seconds filtered versions but not in the tilt-corrected versions because its collapse mechanism is different for the T_c = 10 seconds filtered ground motion. For example, for the Landers LUC FN record, the tilt-corrected version first induces collapse in the 55B model with a scale factor of 1.2 and large drifts are concentrated in stories 25-45. The T_c = 10 seconds filtered version of the same record first induces collapse in the same model with a scale factor of 4.5 and large drifts are concentrated in stories 1-10. For reference, when the T_c = 10 seconds filtered version scaled by 1.2x, large drifts are concentrated in stories 30-45 in the 55B model, but the drifts are not quite large enough to induce collapse. As the scale factor is increased, the concentration of large drifts shifts to stories 1-10 and a much larger scale factor is needed to induce collapse.

In addition to the 55B model, this phenomenon is also seen to a lesser extent in the IDA curve of the 20P model for the Landers LUC FN record, which was discussed in

Section 4.5. These large values of SFR^{col} due to changes in collapse mechanisms are "unlucky" in a sense and are difficult to foresee, but it appears to be more likely to occur in taller buildings, for which there are more potential collapse mechanisms.

Another surprising observation is that the collapse capacities of the 9P and 9B models ($T_1 = 1.88$ seconds) to the Chi-Chi TCU068 NS record increase significantly (by more than 50% for the 9P model) after application of the filter with $T_c = 10$ seconds to the tilt-corrected ground motion (see Figures 4.19(a) and 4.19(d)). This is surprising because T_c is more than five times greater than T_1 in this case and most engineers would assume that removing long-period content at periods so much larger than T_1 would not affect building response. This observation occurs because the Chi-Chi TCU068 NS record contains significant long-period content not seen in any other record. The maximum of its velocity response spectrum occurs at about 8.6 seconds, which is quite close to $T_c = 10$ seconds, meaning the high-pass filter with $T_c = 10$ seconds is removing a significant portion of the true ground motion. This is also evident from Table 4.2, which shows that PGV for the tilt-corrected Chi-Chi TCU068 NS record (298 cm/s) is more than twice as large as that of the $T_c = 10$ seconds filtered version (147 cm/s).

It should be noted that the Chi-Chi TCU068 NS and Landers LUC FN records are outliers with regards to these observations. For the other records, application of these high-pass filters often causes some small changes in the IDA curves when the model is near collapse, but sometimes there are no changes observed. This is also clear from Figure 4.13, for which the largest values of SFR^{col} are usually from the Chi-Chi TCU068 NS and Landers LUC FN records (and in some cases the Denali PS10 FP record), while SFR^{col} for the other ground motion records are almost always close to one.

To see if these observations could be predicted from the elastic response spectra of the ground motion records, consider the Kumamoto 93048 EW, Gorkha KATNP EW, Chi-Chi TCU068 NS, and Landers LUC FN records. As can be seen from Figures 4.15 and 4.16, the IDA curves and collapse capacities of all considered building models are unchanged when the $T_c = 10$ seconds filter is applied to the tilt-corrected versions of the Kumamoto 93048 EW and Gorkha KATNP EW records. At the other extreme, it has been observed that the IDA curves and collapse capacities of many of the building models are changed dramatically when the $T_c = 10$ seconds filter is applied to the tilt-corrected versions of the Chi-Chi TCU068 NS, and Landers LUC FN records. The 5%-damped response spectra of tilt-corrected and $T_c = 10$ seconds

filtered versions of these four records are shown in Figure 4.21(a). The ratios of both versions of these spectra ("SA Ratio") for all four ground motions are shown in Figure 4.21(b).

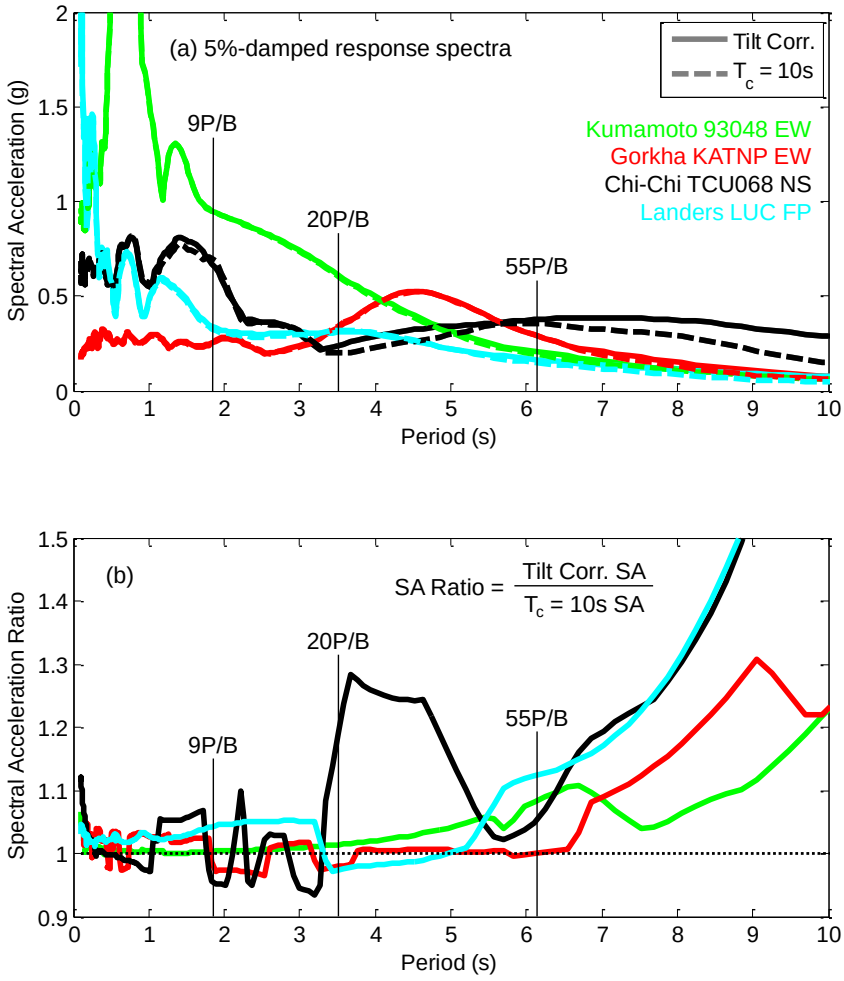

Figure 4.21: (a) 5%-damped response spectra of tilt-corrected and T_c = 10 seconds versions of the Kumamoto 93048 EW, Gorkha KATNP EW, Chi-Chi TCU068 NS, and Landers LUC FN records. (b) The ratio of the tilt-corrected 5%-damped response spectrum to the T_c = 10 seconds 5%-damped response spectrum for each of the aforementioned four records.

From Figure 4.21(b) it is clear that the response spectrum of the Chi-Chi TCU068 NS record is dramatically affected by the T_c = 10 seconds filter. At periods in the range of 3.5 to 5 seconds, the SA Ratio of the Chi-Chi TCU068 NS record is more than 1.2. This probably accounts for the effects in the nonlinear responses of the 9P model. From looking at these spectra, one could easily have predicted that applying

a $T_c = 10$ seconds filter to the tilt-corrected Chi-Chi TCU068 NS record would significantly change structural response of the considered models, perhaps even in the elastic range.

From examining Figure 4.21, the cause of the increased collapse capacity of the 20P model with respect to the Landers LUC FN record after applying the $T_c = 10$ seconds filter as seen in Figure 4.20(b) is less obvious, particularly when compared to the Kumamoto 93048 EW and Gorkha KATNP EW records, for which the $T_c = 10$ seconds filter has no effect on the structural response of the 20P model. The SA Ratio of the Landers LUC FN record does exceed 1.1 at periods of about 5.5 seconds and beyond, which could account for the observed effects. However, the SA Ratio of the Kumamoto 93048 EW record is nearly as large as that of the Landers LUC FN record for periods from 6 to 7 seconds and the SA Ratio of the Gorkha KATNP EW record is nearly as large as that of the Landers LUC FN record for periods larger than 7 seconds. It seems that examining how the high-pass filters affect elastic response spectra can in some cases make it obvious if the filters will affect nonlinear structural response (e.g. the Chi-Chi TCU068 NS record), but in other cases (e.g. the Landers LUC FN record), the elastic response spectra by themselves may not provide enough information.

4.7 Conclusions

This study shows that there are a number of cases in which applying high-pass filters to near-source ground motion records can affect the structural response to these records. Not surprisingly, these effects are most notable for more severe EDPs, models with longer T_1, and high-pass filters with shorter T_c. These effects are not always dramatic, but in some cases, the collapse capacity of a structure can change by over 50% if a high-pass filter is applied to a tilt-corrected record. When these effects are present, the collapse capacities of building models to filtered ground motions tend to be higher than to corresponding tilt-corrected ground motions. For $T_c \geq 40$ seconds, these observations become negligible for all considered building models and structural response is virtually identical to that of tilt-corrected records.

In practice, it is assumed that records selected from the NGA-West2 database are suitable for nonlinear time history analysis if the maximum usable period (0.8 times T_c) is greater than $1.5T_1$ or $2T_1$. The results of this study show that in some anomalous cases this limit is not sufficient. For the Chi-Chi TCU068 NS record, applying a high-pass filter with $T_c = 10$ seconds increases the collapse capacity of the 9P

model (T_1 = 1.88 seconds) by more than 50% because the Chi-Chi TCU068 NS record has significant long-period motion. For the Landers LUC FN record, for the 20P model (T_1 = 3.50 seconds), the NGA-West2 record yields a collapse capacity 37% times higher than the corresponding tilt-corrected record, despite the fact that the NGA-West2 record is not high-pass filtered. This discrepancy is caused by the removal of a 6th-order polynomial fit in the NGA-West2 processing procedure. In some cases (e.g. the Chi-Chi TCU068 NS record), these dramatic effects can be predicted from looking at changes in the elastic response spectrum, but in other cases (e.g. 20P response to the Landers LUC FN record), there may be no changes in the elastic response spectrum due to processing even though processing the record significantly affects nonlinear structural response

Interestingly, for the considered records, demeaned raw records yield structural analysis results more similar to the tilt-corrected records than to the records filtered with $T_c \leq 20$ seconds. This implies that applying high-pass filters with cutoff periods that are too low can remove so much of the true ground motion that one would be better off simply applying the raw ground motion record to a building model despite the presence of long-period noise. Of course, one can imagine a raw record whose signal is so distorted (e.g. 30° of tilt) that structural analysis will yield non-physical results, but in the cases analyzed in this study, calculated tilt was never more than 3°, and the collapse capacities of the considered building models were rarely affected.

Limitations and Future Work

This study considered a relatively small set of building models and a finite number of ground motion records. Some of the important conclusions made here only applied to a small number of the considered structural analyses, so extrapolating these trends to hold for a wide variety of ground motions and structures may be spurious. Furthermore, several assumptions were made in the modeling of these structures, most notably for the 55-story model. The 55-story model includes only a single perimeter frame and as such does not incorporate 3-D effects that would strengthen the structure, which was designed to take advantage of these effects. The isolation system model is also greatly simplified. As such, it is worth noting that the structural responses calculated in this study serve to compare to each other in order to evaluate the effects of ground motion processing, not necessarily to precisely predict how the structures will behave.

On the topic of using raw ground motion records as input ground motions for time

history analysis, further work is necessary to understand potential limitations. Even though the results of this study imply that using raw records does not present issues with regards to calculating the collapse capacity of a structure, using raw records with more long-period noise than those considered in this study may cause problems. A systematic evaluation of how tilt effects alter structural response with varying tilt angles would be useful. It should also be noted that this analysis does not consider the impact of tilt on drift calculations for a particular (scaled) record, but only the impacts on collapse capacity. Further work could be done to estimate how much drift tilt effects add to (or subtract from) the structure's response.

It would also be interesting to investigate the effects of removing a 6th-order polynomial fit from the displacement record, which is one of the steps in the NGA-West2 processing procedure. In this study, the NGA-West2 version of the Landers LUC FN record is not high-pass filtered, but the collapse capacity of the 20P model with respect to the NGA-West2 version is still much different to the tilt-corrected version. This can be attributed to removal of the 6th-order polynomial fit. A more comprehensive study would take tilt-corrected records and create versions for which a 6th-order polynomial fit is removed from displacement without any other processing. Differences in the structural response induced by these records would highlight the effects of this processing step.

Chapter 5

SENSITIVITY OF COLLAPSE RISK ESTIMATES OF STEEL MOMENT FRAMES TO DESIGN CRITERIA AND PROCEDURES

In this chapter, the collapse risk of steel moment frames designed based on different criteria and procedures are analyzed. A set of post-Northridge designs of steel moment frames are developed using different procedures and their collapse risks are compared to each other as well as to pre-Northridge steel moment frames. Section 5.1 motivates the study and provides an overview of past work on the topic of how design decisions affect collapse risk. Section 5.2 details the seismic design procedures considered in this study. It provides a summary of how seismic design loads have changed over time and describes the equivalent lateral force (ELF), response spectrum analysis (RSA) and performance-based design (PBD) procedures. Section 5.3 describes design considerations that are applied to all the post-Northridge designs developed in this study. Sections 5.4 and 5.5 detail the development of the ELF, RSA, and PBD post-Northridge designs. Section 5.6 provides information about Frame-2d models created for each of the post-Northridge designs that are used for collapse risk assessment. Section 5.7 explains the collapse risk assessment procedure and provides the results for each of the Frame-2d models of the post-Northridge designs. Models of pre-Northridge designs described in Chapter 2 are also considered, for comparison. In Section 5.8, four strong ground motion records from large magnitude events are considered and the collapse capacities of all pre- and post-Northridge models to these ground motions are calculated. Section 5.9 summarizes the conclusions and limitations of this study. It also suggests how this study could be expanded to include recent updates to design codes.

5.1 Introduction

In recent years, comprehensive procedures such as FEMA P-58 [25] have been developed to evaluate the seismic performance and risk of structures for which nonlinear finite element models can be created. However, on an urban scale for which there are hundreds or thousands of existing structures, these types of procedures may not be feasible because it would require the design plans of all relevant existing buildings and these plans are not easy to acquire. In lieu of structure-specific plans, archetypes of a class of structures are typically used. For example, in order to judge

the possibility of collapse of pre-Northridge steel moment frame high-rises in Los Angeles for the 2008 ShakeOut Scenario [89], a supplemental study by Krishnan and Muto [90] analyzed models of three archetype designs.

For steel moment frame (SMF) structures, it is common to classify designs as either pre- or post-Northridge because this only requires information about the design year. Sub-classes can also be created based on building height because this information is easy to obtain and can affect risk estimates. However, given the knowledge that a SMF is, for example, a 20-story post-Northridge design, it is not clear how accurately one could estimate its collapse risk without the actual design plans, as past research (e.g. [91]) has shown that the design of SMFs can vary significantly depending on design procedures. It is possible to incorporate design uncertainty into risk estimates as a form of modeling uncertainty and procedures for accounting for modeling uncertainty into risk calculations already exist (e.g. [92] and [93]), but this would require approximating the probability that a structure is designed with different criteria and understanding the effects of these criteria on structural performance.

Some work has been done to understand the sensitivity of the collapse risk of reinforced concrete (RC) moment frame structures to design criteria. In a comprehensive effort to quantify the seismic collapse risk of RC moment frame structures, Haselton and Deierlein [48] analyze the sensitivity of seismic collapse risk calculations to different design decisions and criteria (e.g. design base shear, drift limits, and column-beam strength ratio). Haselton and Deierlein [48] find that the design base shear and column-beam strength ratio matter much more than the drift limit in terms of effects on collapse risk of RC moment frame structures. For example, increasing the design base shear by 3x can decrease the collapse risk by about 10x and increasing the column-beam strength ratio by 3x can decrease the collapse risk by about 8x. To the knowledge of this author, similar efforts to quantify the effects of modern design criteria on collapse risk have not been performed with with steel moment frames (SMFs).

Furthermore, in recent years, performance-based design has become more prevalent, particularly for tall buildings. It is important to understand how structures designed using performance-based procedures that require nonlinear time history analysis compare to those designed using traditional "prescriptive" design procedures (e.g. Equivalent Lateral Force and Response Spectrum Analysis). Sattar [94] investigated how the seismic design requirements of ASCE 7 compare to the seismic assessment requirements of ASCE 41 for RC moment frames and found significant discrepancies

depending on the procedures used in both seismic design and in seismic assessment. Sattar [94] found that RC frames were most likely to pass collapse prevention evaluation per ASCE 41 if nonlinear dynamic procedures are followed (instead of linear static, linear dynamic, and nonlinear static procedures). However, how different design criteria affect collapse risk was not considered.

The goal of this study is to determine how the collapse risk of SMFs is affected by design procedure. In this study, a total of ten 9- and 20-story post-Northridge SMFs are designed according to Equivalent Lateral Force (ELF), Response Spectrum Analysis (RSA), and Performance Based Design (PBD) procedures. For ELF and RSA procedures, requirements from both ASCE 7-05 and ASCE 7-10 are considered, for comparison. All designs are developed with seismic loads calculated for a reference site in downtown Los Angeles (Latitude 34.05° N and Longitude -118.26° E) that is approximately the site of the recently constructed Wilshire Grand Tower. For the designs that use PBD procedures, site-specific spectra are required. In this study, actual site-specific spectra generated for the recent LA Live (LL) and Wilshire Grand (WG) projects in downtown Los Angeles are used for design. For each design, Frame-2d models are generated to perform collapse risk analysis. Results from incremental dynamic analysis (IDA) in Frame-2d are combined with PSHA at the reference site to estimate the collapse risk for each design. These results are compared to each other as well as to the pre-Northridge models of 9- and 20-story SMFs described in Chapter 2.

5.2 Overview of Seismic Design Procedures

Each local building authority in the United States determines which building code to adopt. Since the early-mid 2000s, most cities and states have adopted the International Building Code (IBC) with some (usually) small modifications. In this study, Los Angeles, California is the focus, with downtown Los Angeles being the site of interest. More specifically, the site of the recently constructed Wilshire Grand Tower (Latitude 34.05° N and Longitude -118.26° E) is used where more granular coordinates are required.

Historical Perspective

Prior to 2007, the Uniform Building Code (UBC) was adopted each code cycle by the California Building Code (CBC) with some (usually minor) amendments [95, 96]. The CBC is used by structural engineers to determine seismic design loads for structures in California. Each version of the UBC provides an equation to calculate

the design base shear, V, for use in seismic design. The 2007 CBC [97] adopted the 2006 International Building Code (IBC) [98], which references ASCE 7-05 [99] for the calculation of seismic design loads. Following its first edition in 1927, the UBC was updated approximately every three years, but not every update to the UBC made significant changes to seismic design requirements. The IBC is also updated approximately every three years. In this section, important updates to seismic design maps and to the equations for seismic base shear, V, in the UBC and ASCE 7, over time, that are relevant to Los Angeles will be summarized. In every version of the UBC and ASCE 7, V is proportional to W, the building weight. As such, V/W is reported in each case.

The first version of the UBC considered here is the 1946 UBC [100]. In this document, the design base shear is given by

$$V/W = ZC, \tag{5.1}$$

where Z depends on the geographical seismic "Zone" and $C = 0.02$ for stiff soils (most common designation) and $C = 0.04$ for soft soils. $Z = 1$ in Zone 1, $Z = 2$ in Zone 2, and $Z = 4$ in Zone 3. In the 1946 UBC, regions in California of high seismicity such as Los Angeles are Zone 3 and the rest of California is Zone 2. The 1946 UBC does not explicitly define a variable Z, but it is used here for consistency with later versions of the UBC. The seismic zone map in the 1946 UBC only encompasses the Western United States. "Stiff" soil is defined by the 1946 UBC to have a bearing capacity of more than 95.8 kPa (2,000 psf) and soil is classified "soft" otherwise.

Changes were made in the 1955 UBC [101] to the maps of seismic zones (to encompass the entire United States) and in the calculation of C. The 1955 UBC gives an equation for C that depends on the number of stories in the building, N:

$$C = \frac{0.15}{N + 4.5}. \tag{5.2}$$

The Z values were unchanged from previous versions of the UBC.

In the 1961 UBC [102], the seismic zone map remained unchanged from the 1955 UBC but major changes were made to the formula for V:

$$V/W = ZKC, \tag{5.3}$$

where K is a structure-specific factor (0.67 for moment frames) that reduces the design base shear if the structure is judged to have sufficient ductility. The coefficient

C is also calculated differently from the 1955 UBC, depending directly on the fundamental period of the structure, T:

$$C = \frac{0.05}{T^{1/3}}, \quad T \geq 0.1\text{s}. \tag{5.4}$$

Furthermore, the zone factor Z was re-calibrated so that $Z = 0.25$ in Zone 1, $Z = 0.5$ in Zone 2, and $Z = 1.0$ in Zone 3 in the 1961 UBC.

This remained unchanged until the 1976 UBC [103], which updated the seismic map and dramatically altered the design base shear equation:

$$V/W = ZIKCS. \tag{5.5}$$

In the 1976 UBC, an extra seismic zone was added and Z was again re-calibrated so that $Z = 0.1875$ in Zone 1, $Z = 0.375$ in Zone 2, $Z = 0.75$ in Zone 3, and $Z = 1.0$ in Zone 4. In the 1976 UBC, regions in California of high seismicity are Zone 4 and the rest of California is Zone 3. The 1976 UBC introduced the importance factor, I, which is equal to 1.0 for most structures, but can be as high as 1.5 for essential facilities (e.g. hospitals). The K value remained unchanged from previous versions of the UBC. The value of C took on a new form:

$$C = \frac{1}{15\sqrt{T}} \leq 0.12. \tag{5.6}$$

Another new value, S, was introduced in the 1976 UBC to represent soil effects:

$$\begin{aligned} &\text{If } \frac{T}{T_S} \leq 1.0, \quad S = 1.0 + \frac{T}{T_S} - 0.5\left[\frac{T}{T_S}\right]^2 \\ &\text{If } \frac{T}{T_S} > 1.0, \quad S = 1.2 + 0.6\frac{T}{T_S} - 0.3\left[\frac{T}{T_S}\right]^2, \end{aligned} \tag{5.7}$$

where T_S is the characteristic site period. In lieu of properly establishing T_S, the 1976 UBC permits S to be taken conservatively as 1.5.

The 1988 UBC [104] altered the seismic zone map for the final time and added another seismic zone, though these changes did not dramatically affect the zones in California. It also introduced significant changes to the calculation of V:

$$V/W = \frac{ZIC}{R_W}. \tag{5.8}$$

The 1988 UBC re-calibrated Z so that $Z = 0.075$ in Zone 1, $Z = 0.15$ in Zone 2A, $Z = 0.20$ in Zone 2B, $Z = 0.30$ in Zone 3, and $Z = 0.40$ in Zone 4. It replaced K

with R_W to represent ductility where $R_W = 12$ for special moment frame systems. The value for C was given a new form and the soil-related factor was embedded in the calculation of C:

$$C = \frac{1.25S}{T^{2/3}} \leq 2.75, \tag{5.9}$$

where S (ranging from 1.0 to 2.0) depends on the site's soil profile.

The final version of the UBC was the 1997 UBC [105], which not only changed the equation for V but also the framework for calculating V:

$$\begin{aligned} V/W &= \frac{C_v I}{RT} \\ &\leq \frac{2.5 C_a I}{R} \\ &\geq 0.11 C_a I \\ &\geq \frac{0.8 Z N_v I}{R} \quad \text{for Seismic Zone 4.} \end{aligned} \tag{5.10}$$

In Equation 5.10, C_v and C_a are two different seismic coefficients that vary as a function of seismic zone and soil profile type. For Zone 4, values of C_v range from $0.32N_v$ to $0.96N_v$ and values of C_a range from $0.32N_a$ to $0.44N_a$, where N_v and N_a are near-source factors that depend on the site's proximity to major faults. N_v ranges from 2.0 to 1.5 and N_a ranges from 1.0 to 1.5. The 1997 UBC also replaces R_W with R, which is equal to 8.5 for special moment frame systems. The seismic zone map for the 1997 UBC is the same as for the 1988 UBC.

The 1997 UBC remained the basis for the CBC until the 2007 CBC, which adopted the 2006 International Building Code (IBC). To define seismic design loads, the 2006 IBC referred to ASCE 7-05 [99], which provided a different method for calculating V when compared to the UBC:

$$V/W = C_s, \tag{5.11}$$

where

$$\begin{aligned} C_s &= \frac{S_{DS}}{R/I} \\ &\leq \frac{S_{D1}}{T(R/I)} \text{ for } T \leq T_L \\ &\leq \frac{S_{D1} T_L}{T^2(R/I)} \text{ for } T > T_L \\ &\geq 0.01 \\ &\geq \frac{0.5 S_1}{R/I} \text{ if } S_1 \geq 0.6\text{g}. \end{aligned} \tag{5.12}$$

If Equation 5.12, S_{DS} and S_{D1} are defined as

$$\begin{aligned} S_{DS} &= \frac{2}{3} S_{MS}, \\ S_{D1} &= \frac{2}{3} S_{M1}, \end{aligned} \tag{5.13}$$

where

$$\begin{aligned} S_{MS} &= F_a S_s, \\ S_{M1} &= F_v S_1, \end{aligned} \tag{5.14}$$

where F_a and F_v are site coefficients that mostly depend on site class, which is based on site soil properties. S_s and S_1 are mapped acceleration parameters that can also be found via an online tool provided by the USGS [106]. T_L in Equation 5.12 is the long-period transition period, whose value is geographically dependent. It is equal to either 8 or 12 seconds in most of California, so $T \leq T_L$ is true for the vast majority of structures. R provides the same function in ASCE 7-05 as in the 1997 UBC, but its value is equal to 8 (instead of 8.5) for special moment frame systems.

ASCE 7-05 was also adopted by the 2009 IBC and thus the 2010 CBC. The final update to seismic design loads considered in this study is ASCE 7-10 [20], which was adopted by the 2012 and 2015 IBC and the 2013 and 2016 CBC. The equation for V in ASCE 7-10 is almost the same as in ASCE 7-05 (Equation 5.12), but an extra constraint on C_s is provided:

$$C_s \geq 0.044 S_{DS} I_e, \tag{5.15}$$

where I_e is the importance factor (same as I in previous codes). Updates were also made to the mapped values of S_s and S_1.

To compare how the values of V/W have changed over time, these values are calculated for each of the presented building code versions based on the reference site in downtown Los Angeles (34.0498° N, -118.2601° E) for steel special moment frames. V/W is calculated as a function of building period, T, for every building code, with $T = 10N$ for the 1955 UBC. Where seismic zones are needed, the highest zone is selected. The site is assumed to be Site Class C according to ASCE 7-10 specifications (S_C for the 1997 UBC), which means V_{S30} is between 360 and 760 m/s (1,200 and 2,500 ft/s). This is approximately equivalent to soil type S_2 ($S = 1.2$) in the 1988 UBC. For the 1976 UBC, T_S is set to the minimum allowed value of 0.5 seconds and for the 1946 UBC, "stiff" soil is assumed. K, R_W, and R are assigned

according to the corresponding building code's designation for steel special moment frames. I is set to 1.0. For the 1997 UBC, soil profile type S_C and $Z = 0.4$ means $C_v = 0.56N_v$ and $C_a = 0.40N_a$. Assuming the site is between 5 and 10 kilometers from a seismic source type B (all faults other than those with maximum $M \geq 7.0$ and slip rate ≥ 5 mm/yr or those with maximum $M < 7.0$ and slip rate ≤ 2 mm/yr) yields $N_v = 1.1$ and $N_a = 1.0$. From the USGS online tool [106], according to the ASCE 7-05 maps, $S_{DS} = 1.42$ and $S_{D1} = 0.62$. According to the ASCE 7-10 maps, $S_{DS} = 1.58$ and $S_{D1} = 0.72$.

All these values result in the plots of V/W vs. T shown in Figure 5.1. The curve of V/W for the 1946 UBC is not plotted for $T > 1$ s because buildings taller than 13 stories or 150 feet were prohibited in Los Angeles until the 1950s and this height limit approximately corresponds to $T = 1$ s. For a fair comparison, all calculated values of V/W for the 1946, 1955, 1961, 1976, and 1994 UBC are divided by 0.7 because these codes assume Allowable Stress Design is used while the 1997 UBC, ASCE 7-05, and ASCE 7-10 assume Strength Design is used. A conversion factor of 0.7 between these two design methods is standard for seismic loads (e.g. Chapter 2 of ASCE 7-10).

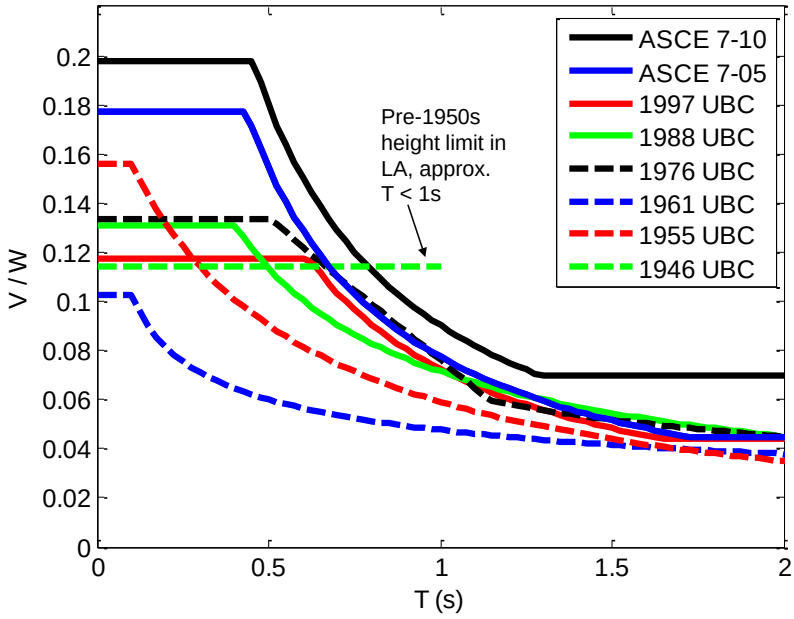

Figure 5.1: V/W vs. T in downtown Los Angeles with Site Class C for different building codes.

Figure 5.2 uses the same information from Figure 5.1 but plots V/W chronologically

for $T = 0.2$, 0.5, 1.0, and 2.0 seconds. In general, it appears that V/W has gradually increased over time. Furthermore, it appears that the dependence of V/W on T has become more pronounced over time. For example, in the 1961 UBC, V/W is proportional to $T^{-1/3}$ for non-short periods. This proportionality becomes $T^{-1/2}$ in the 1976 UBC, $T^{-2/3}$ in the 1988 UBC, and finally T^{-1} in the 1997 UBC.

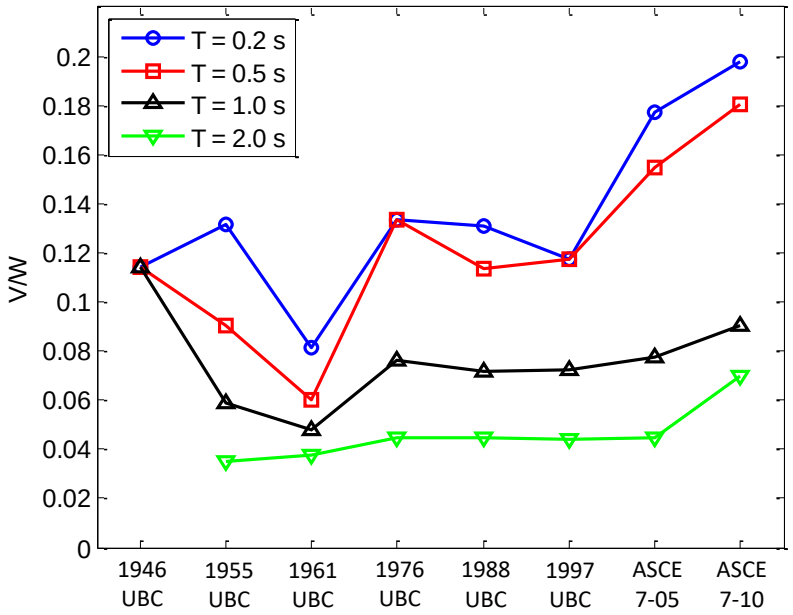

Figure 5.2: V/W as a function of building code year calculated for downtown Los Angeles with Site Class C with different values of T.

It should be noted that the above analysis has calculated the design base shear V that is used to ensure that structural members have sufficient strength to withstand seismic forces. However, the focus of this study is steel special moment frame structures and in most cases the design of beams in steel moment frames is governed by drift limits, not strength requirements [107]. To understand how the seismic design of steel moment frames has changed over time, it is thus important to also consider how drift limits have changed in the different building codes.

Seismic drift limits first appear in the 1976 UBC. Prior to this, some designers limited calculated seismic drifts to be within those used for wind loads but some designers did not consider seismic drift limits at all [19]. In the 1976 UBC, a seismic drift limit of $0.005K$ (0.0033 for moment frames) is specified, where the drift is calculated from application of the design base shear V. The 1988 UBC has a seismic drift limit of $0.04/R_W$ (0.0033 for moment frames) for buildings shorter than 65 feet (19.8 meters) and a drift limit of $0.03/R_W$ (0.0025 for moment frames) for taller

buildings. The 1988 UBC also allows the T used to compute V for the drift check to be calculated with no upper bound. This provision for T is contained in all future versions of the UBC and ASCE 7. The 1997 UBC specifies a seismic drift limit of $0.025/(0.7R)$ (0.0042 for moment frames) for buildings with $T < 0.7$ s and a drift limit of $0.020/(0.7R)$ (0.0034 for moment frames) for buildings with $T \geq 0.7$ s. ASCE 7-05 sets a seismic drift limit of $0.02/C_d$ (0.0036 for moment frames) for most structures, where $C_d = 5.5$ for special moment frame systems. ASCE 7-10 has the same seismic drift limit as ASCE 7-05 and includes an exception that the limit in Equation 5.15 does not need to be considered when calculating V for the drift check. Note that the drift limits for the 1997 UBC, ASCE 7-05, and ASCE 7-10 correspond to drifts calculated in response to seismic forces used for Strength Design while versions of the UBC before 1997 (i.e. 1994 and earlier) calculate drift in response to seismic forces used for Allowable Stress Design.

Current Procedures for Seismic Design

As described in the previous section, every local jurisdiction in California adopts the CBC with some (usually) minor modifications, which in turn adopts the most recent version of the IBC with some (usually) minor modifications. In this section, the seismic design procedures in the 2015 IBC [108] relevant to the design of steel special moment frame structures are briefly summarized. Local modifications are not considered here because they are not pertinent.

For design loads (i.e. seismic, wind, snow, etc.) and their combinations, the 2015 IBC references ASCE 7-10. ASCE 7-10 also describes specifications for structural models for analysis, prescribes drift and P-Δ stability limits, and defines acceptable structural analysis procedures. These procedures include the ELF procedure, the RSA procedure, and linear and nonlinear time history analysis (LTHA and NLTHA) procedures. Updates to ASCE 7 related to seismic loading usually consist of modifications to details in the seismic loading procedures as well as changes to the seismic design maps as new GMPEs and fault models result in updated hazard calculations and thus seismic design values.

For the design of steel members (i.e. beams, columns, braces, etc.) for strength from all types of loads, the 2015 IBC references AISC 360-10 [109]. AISC 360-10 provides equations to calculate the nominal strength of steel members that can be compared to the required strength of these members (calculated from structural analysis) to determine if the member sections are satisfactory. Updates to AISC 360

are not usually dramatic and changes are not often made that would significantly affect the design of special moment frames.

For the design of steel lateral-force resisting systems (i.e. moment frames, concentrically braced frames, etc.), the 2015 IBC references AISC 341-10 [110]. AISC 341-10 specifies the design procedures for steel members and connections specifically in seismic force resisting systems. For steel special moment frames, it contains requirements for strong-column/weak-beam criteria, panel zone strength, and moment connections. The design of moment connections is not considered in this study, but for completeness, it should be mentioned that AISC 358-10 [11] contains provisions for prequalified moment connections.

The aforementioned seismic design procedures are "prescriptive," meaning that if all the procedures and requirements are followed, it is implicitly assumed that the structure will perform satisfactorily in a seismic event. The "prescriptive" designation encompasses the strength procedures and the allowable stress procedures that are both allowed by ASCE 7-10. ASCE 7-10 also allows a third procedure that it calls "performance-based" which is not prescriptive. Performance-based seismic design is described in detail in the following sub-section.

Performance-Based Seismic Design

In recent years, performance-based seismic design procedures have become more common, particularly for tall and important structures. The principle of performance-based seismic design is that all new structures should achieve the same seismic "performance," judged in ASCE 7-10 by the collapse risk. ASCE 7-10 is calibrated such that every new standard building should have a probability of less than 1% of collapsing due to seismic loads in the next 50 years.

Different cities may have different requirements for performance-based design procedures and these can evolve over time. In this study, Los Angeles is the focus, so the guideline followed here will be that described in the 2014 version (with 2015 supplements) of the Los Angeles Tall Buildings Structural Design Council's alternate procedure for seismic analysis and design of tall buildings in Los Angeles [23]. This guideline will be referred to in this study as the "LATBSDC alternate procedure."

In 2017, a new version of the LATBSDC alternate procedure was developed and published [72], which includes several changes to procedures for selecting and scaling input ground motions. Because this version was published only recently, this study is based on the 2014 version (with 2015 supplements) of LATBSDC alternate

procedure. This sub-section summarizes the important features of the 2014 version of LATBSDC alternate procedure used in the design of buildings for this study. Significant changes in the 2017 version of the LATBSDC alternate procedure are summarized in Section 5.9.

Fundamentally, the LATBSDC alternate procedure provides checks for two performance goals: "serviceable" behavior in "frequent" ground motions and "low collapse probability" in "extremely rare" ground motions. "Serviceable" behavior approximately corresponds to Immediate Occupancy criteria and "low collapse probability" approximately corresponds to Collapse Prevention criteria. These performance criteria are defined in ASCE 41-13 [111]. A "frequent" ground motion is defined to have a 50% probability of exceedance in the next 30 years (50%/30-year ground motion) and an "extremely rare" ground motion is defined to be the Risk-Targeted Maximum Credible Earthquake (MCE_R) ground motion according to ASCE 7. MCE_R ground motion is defined in ASCE 7-10 to be the lesser of "Probabilistic" MCE_R ground motion and "Deterministic" MCE_R ground motion.

Probabilistic MCE_R ground motion is defined as the ground motion that would produce a 1% probability of collapse in 50 years given a standard collapse fragility. This standard collapse fragility is defined in ASCE 7-10 as a lognormal fragility with $\sigma_{\ln} = 0.6$ and a 10% probability of collapse given Probabilistic MCE_R ground motion. According to this definition, to calculate a site-specific Probabilistic MCE_R given a site-specific hazard curve, one would need to find the collapse fragility with $\sigma_{\ln} = 0.6$ that produces a 1% probability of collapse in 50 years and then from the fragility curve identify the spectral ordinate that implies a 10% probability of collapse in 50 years. This spectral ordinate is the MCE_R ground motion. In lieu of this relatively cumbersome procedure, ASCE 7 provides site-specific coefficients C_{RS} and C_{R1} at periods of 0.2 seconds and 1 second, respectively, that translate 2%/50-year (2,475-year return period) ground motion to MCE_R ground motion. These coefficients are approximately one in most regions in California but are closer to 0.8 in the Eastern United States and particularly near the New Madrid seismic zone. These coefficients are a function of the shape of the site-specific hazard curve. A site with a "flatter" hazard curve (i.e. hazard is dominated by large, rare events) will have a lower risk coefficient. This implies that Probabilistic MCE_R ground motions in the Eastern U.S. have a shorter return period, calculated by some to be around 2,000 years (e.g. [112]).

Deterministic MCE_R ground motion is defined as the maximum of 84th percentile

ground motions from characteristic earthquakes of all nearby faults. In practice, only in cases when the site is near a large fault is the Deterministic MCE_R ground motion usually less than the Probabilistic MCE_R ground motion. In these cases, the Deterministic MCE_R ground motion controls the MCE_R calculation. The Deterministic MCE_R ground motion thus provides an upper bound on the MCE_R calculation.

Typically, the 50%/30-year and MCE_R ground motions are calculated as response spectra and determined on a site-specific basis. Given these spectra, input ground motions can be generated for the corresponding "serviceability" and "collapse prevention" evaluations. For the serviceability (50%/30-year) evaluations, the LATBSDC alternate procedure permits using RSA with 2.5% damping or nonlinear time history analysis. For the collapse prevention (MCE_R) evaluations, nonlinear time history analysis is required. For the selection of input ground motions for nonlinear time history analysis, the LATBSDC alternate procedure defers to ASCE 7-10 for required procedures. ASCE 7-10 provides minimal quantitative guidance on this topic, requiring only that "[a]ppropriate ground motions shall be selected from events having magnitudes, fault distance, and source mechanisms that are consistent with those that control the maximum considered earthquake." Other references (e.g. [76, 113]) provide more guidance for selecting input ground motions, but these are not necessarily codified. The LATBSDC alternate procedure does require that ground motions should include near fault and directivity effects where applicable, but does not provide quantitative criteria. It should be noted that the newly released ASCE 7-16 [60] and 2017 version of the LATBSDC alternate procedure provides significantly more guidance on the selection of input ground motions. This is discussed in Section 5.9.

The LATBSDC alternate procedure requires at least three pairs of input ground motions for the serviceability evaluation (if time history analysis is performed) and at least seven pairs for the collapse prevention evaluation. To meet the requirements of ASCE 7-10, the LATBSDC alternate procedure allows amplitude-scaling or spectrum-matching procedures to modify the selected ground motions so that they match the hazard represented by the target spectrum. In amplitude-scaling, individual ground motions are simply multiplied by a scale factor. In the most common procedures for spectrum-matching, wavelets are iteratively added in the time domain until the response spectrum matches the target spectrum over some user-defined period range [59]. The LATBSDC alternate procedure also permits use of the conditional mean

spectrum (CMS) as the target spectrum for the input ground motions. Compared to the uniform hazard spectrum (UHS), which reports the spectral ordinate at each period that gives the same hazard (e.g. 2%-50/year), the CMS uses one period from the UHS as the "anchor," and computes the rest of the spectrum as the mean spectrum given the spectral ordinate at the anchor period [114].

For the service level evaluation, linear analysis is common, as the LATBSDC alternate procedure permits RSA. To meet serviceability criteria, the LATBSDC alternate procedure specifies a drift limit of 0.005 and refers to AISC 341 and AISC 360 for steel member acceptability criteria. It requires demand-to-capacity ratios of < 1.50 for deformation-controlled actions (e.g. beam rotations) and < 0.70 for force-controlled actions (e.g. compression in columns). If NLTHA is performed for the service level evaluation, the default acceptance criteria are those for Immediate Occupancy as defined in ASCE 41.

For the collapse-prevention evaluation, NLTHA is required in the LATBSDC alternate procedure. Acceptability criteria include demand-to-(expected)-capacity ratios of $< 2/3$ for critical force-controlled actions and 1.0 for non-critical force-controlled actions. For deformation-controlled actions, the default acceptance criteria are those for Collapse Prevention as defined in ASCE 41. From a suite of ground motions, the limit for mean peak transient drift is 0.03 and the limit for maximum (from one ground motion) peak transient drift is 0.045. Corresponding limits for residual drift are 0.01 and 0.015. It is also not permitted for any story to lose more than 20% of its initial strength during NLTHA.

5.3 General Design Considerations

In this study, a total of ten 9- and 20-story SMFs are designed with different procedures. Four 9-story SMFs are designed using ELF and RSA procedures according to ASCE 7-05 and ASCE 7-10. Two 9-story SMFs are designed using the performance-based procedures for tall buildings from the LATBSDC alternate procedure, which references ASCE 7-10 for the MCE_R definition. The LATSBSDC alternate procedure requires a site-specific hazard analysis, so geotechnical reports from two recently completed projects in downtown Los Angeles were obtained [115, 116] and their site-specific response spectra are used to generate two 9-story PBD designs. These two projects are named the "LA Live" and "Wilshire Grand" projects, so their corresponding reports are denoted as the "LL report" and the "WG report" respectively. Four 20-story SMFs are designed: two using RSA procedures according

to ASCE 7-05 and ASCE 7-10, and two using the LATSBDC alternate procedure with the two sets of obtained site-specific response spectra.

The geometry of the 9- and 20-story SMFs are the same as those used in previous chapters in this dissertation, which are based on designs from Gupta and Krawinkler [18]. The gravity members are not altered from those presented in Gupta and Krawinkler [18] so only the perimeter moment frames are designed in this study. The gravity loads are generally the same as those described by Gupta and Krawinkler [18]: a dead load of 4.60 kPa (96 psf) for typical floors, 3.97 kPa (83 psf) for the roof, 5.55 kPa (116 psf) for the roof penthouse, a cladding load of 1.20 kPa (25 psf), and a reduced live load of 0.96 kPa (20 psf) for every floor and the roof. For seismic mass calculations, only 4.12 kPa (86 psf) out of the total typical floor dead load is used to account for code provisions for partitions, which state that only 10 psf needs to be included in seismic mass calculations to account for partitions (as opposed to 20 psf for dead load calculations). This provision is incorporated in the dead load and seismic mass calculations by Gupta and Krawinkler [18] and is thus also included here. The seismic weights, W, of the 9- and 20-story SMFs are 88,340 kN (19,860 kips) and 108,540 kN (24,400 kips), respectively.

All members are designed using A922 steel with F_y = 50 ksi. Column and beam sizes in lower stories are never smaller than those in upper stories. An exception is made for the W14X22 beam sections in the basement of the 20-story SMFs, which are left unchanged from the designs in Gupta and Krawinkler [18]. W24 sections are used for all columns except for the exterior columns in the 20-story SMFs, which use HSS sections. Column splices are in the same locations as in Gupta and Krawinkler [18]. The smallest allowed beam section is W18X35, which is only relevant at the top story of the 20-story SMFs. This is to prevent dramatic differences in story stiffness between the 19th and 20th stories. Even though reduced beam section (RBS) connections are common in modern moment frames, beams with non-RBS beam connections are designed here so that the framework of Frame-2d does not need to be modified. All beam and column sections are required to be classified as seismically compact by AISC 341-10.

In practice, when panel zone doubler plates are required, it is sometimes more economical to increase the column size instead of adding doubler plates [107], but this criterion is not trivial to generalize and is often not considered in the design of archetype steel SMFs (e.g. Appendix D of [91]) for study by researchers. However, this consideration is important because increasing the column size instead of adding

a doubler plate can make the column-beam strength ratio much greater than one, thus increasing the overall ductility of the frame. As a compromise, for the SMFs designed in this study, if doubler plates thicker than 0.5x the column web are required, the column size is increased until the required doubler plate thickness is less than 0.5x the column web. This provides a simple criterion for avoiding columns sections that are much smaller than would be designed in practice without unrealistically over-designing them. The thicknesses of required doubler plates are rounded up to the nearest 1/8 of an inch.

In addition to seismic loads, wind loads are also considered. The downtown Los Angeles site has a basic wind speed of 38 m/s (85 mph) in ASCE 7-05 and 49 m/s (110 mph) in ASCE 7-10. Despite the change in basic wind speeds between the two codes, the end result is similar because ASCE 7-05 applies a factor of 1.6 to the wind load in the LFRD load combinations while ASCE 7-10 applies a factor of 1.0. The factored ASCE 7-10 wind loads are slightly larger than the factored ASCE 7-05 wind loads, but the difference is not as significant as the differences in the seismic loads. Exposure B is assumed when calculating the wind loads, which corresponds to an urban area. Further detail about the wind loads for each design are given in Appendix C. There are no codified limits for wind drifts, but the Commentary of Appendix C of ASCE 7-10 (and ASCE 7-05) suggests common drift limits of between 1/600 and 1/400 of either roof drift or story drift for serviceability wind loads. The Commentary of Appendix C of ASCE 7-10 suggests that serviceability wind loads should have a mean recurrence interval of 10-100 years, with the exact value selected based on engineering judgment. The Commentary of Appendix C of ASCE 7-05 provides a more concrete definition for serviceability wind loads: $0.7W$, where W is the unfactored design wind load. For simplicity, the latter definition for serviceability wind loads is used in this study and serviceability story drifts are limited to 1/400. Note that for strength design, the factored wind load is $1.6W$ in ASCE 7-05 but is $1.0W$ in ASCE 7-10. These are meant to be approximately equal, with W in ASCE 7-10 defined to be approximately 1.6 larger than W in ASCE 7-05. As such, for designs for which ASCE 7-10 is the applicable design code, serviceability wind loads are defined in this study to be $0.7W/1.6$.

With few exceptions, the design of beam sizes is governed by either seismic or wind drift requirements. The design of column sizes is usually governed by either strength requirements, column-beam strength ratio requirements, or panel zone requirements (i.e. ensuring required doubler plate thickness is less than 0.5 times the column web

thickness).

Table 5.1 summarizes the designs developed in this study. These designs are denoted by the number of stories (9 or 20), design procedure (ELF, RSA, or PBD), and year of ASCE 7 (05 or 10) or LL or WG report. So, for example, the 9-story SMF designed according to ASCE 7-05 using RSA procedures is denoted "9RSA-05." Descriptions of the design process and the member properties for the ELF and RSA designs are given in Section 5.4. The same information for the PBD designs is given in Section 5.5.

Table 5.1: Summary of post-Northridge designs.

Design	# of Stories	Design Procedure	Seismic Loads
9ELF-05	9	ELF	ASCE 7-05
9ELF-10	9	ELF	ASCE 7-10
9RSA-05	9	RSA	ASCE 7-05
9RSA-10	9	RSA	ASCE 7-10
9PBD-LL	9	PBD	LL report
9PBD-WG	9	PBD	WG report
20RSA-05	20	RSA	ASCE 7-05
20RSA-10	20	RSA	ASCE 7-10
20PBD-LL	20	PBD	LL report
20PBD-WG	20	PBD	WG report

5.4 ELF and RSA Designs

Seismic Loads

Four 9-story and two 20-story SMFs are designed according to ELF and RSA procedures from ASCE 7-05 and ASCE 7-10. The reference site of these designs is defined to be in downtown Los Angeles (34.05° N, -118.26° E) with Site Class C. The USGS online design map tool [106] is used to generate seismic design values, summarized in Table 5.2.

Table 5.2: Seismic design values (units of g) for Site Class C for reference site in downtown Los Angeles according to ASCE 7-05 and ASCE 7-10.

	S_S	S_1	S_{MS}	S_{M1}	S_{DS}	S_{D1}
ASCE 7-05	2.123	0.713	2.123	0.927	1.415	0.618
ASCE 7-10	2.372	0.833	2.372	1.083	1.581	0.721

For structures with more than two stories, ASCE 7-05 does not allow the ELF procedure for design if $3.5T_S > T$, where $T_s = S_{D1}/S_{DS}$ and T is the structure's fundamental period, in seconds. From the values in Table 5.2, $3.5T_S = 1.53$ for

ASCE 7-05, which is near what T may be for the 9-story SMFs and certainly less than T for the 20-story SMFs. ASCE 7-10 allows the ELF procedure for design if $3.5T_S < T$ or if the structure's height is less than 48.7 meters (160 feet). The 9-story SMFs have a height of 37.2 meters (122 feet) and the 20-story SMFs have a height of 80.8 meters (265 feet). Thus, the ELF procedure is not permitted for the 20-story SMFs for ASCE 7-05 or ASCE 7-10. The ELF procedure may be permitted for a 9-story SMF in ASCE 7-05 and is permitted for a 9-story SMF in ASCE 7-10. For completeness, two 9-story SMFs are designed according ASCE 7-05 and ASCE 7-10 using the ELF procedures, even though this may not be permitted in ASCE 7-05. The RSA procedure is permitted for all structures. As such, two 9-story SMFs (according to ASCE 7-05 and ASCE 7-10) and two 20-story SMFs (according to ASCE 7-05 and ASCE 7-10) are designed using RSA. Structural analysis models for these designs are created in ETABS [117]. These models are 3-D and incorporate seismic loading in both horizontal directions. Details about these models are available in Section D.1 of Appendix D.

In the ELF procedure, a static lateral force is applied to the structure to represent seismic loading. The design base shear, V, is calculated from the design values in Table 5.2. When calculating V, both ASCE 7-05 and ASCE 7-10 specify an upper bound on T of $C_u T_a$, where $C_u = 1.4$ if $S_{D1} \geq 0.4$ g and

$$T_a = C_t h_n^x, \tag{5.16}$$

where h_n is the height of the structure in feet, and C_t and x are 0.028 and 0.8, respectively, for SMFs. This results in an upper bound on T for the 9- and 20-story SMFs of 1.83 and 3.40 seconds, respectively. Using this upper bound as T, for ASCE 7-05, calculation of $V = C_s W$ for both the 9- and 20-story SMFs is governed by the requirement that $C_s \geq 0.5S_1/(R/I) = 0.045$. For ASCE 7-10, the requirement that $C_s \geq 0.044 S_{DS} I_e = 0.070$ controls the calculation of $V = C_s W$. It should be noted that ASCE 7-10 does not require $C_s \geq 0.044 S_{DS} I_e$ to be considered when performing the drift check using the ELF procedure. Instead, for ASCE 7-10 for the drift check, $C_s \geq 0.5S_1/(R/I_e) = 0.052$ controls the calculation of $V = C_s W$.

In the RSA procedure, the design response spectrum is extrapolated from the design values in Table 5.2 and RSA is performed using enough modes so that the combined modal mass participation is at least 90 percent of the actual mass in each orthogonal direction. Chapter 11 of ASCE 7 provides equations for calculation of the design response spectrum. These equations do not change from ASCE 7-05 to ASCE 7-10.

Based on the design values in Table 5.2, the design response spectra according to ASCE 7-05 and ASCE 7-10 are shown in Figure 5.3. Each of the four RSA designs is indicated according to its fundamental period, T_1 as calculated in ETABS using eigenvalue analysis.

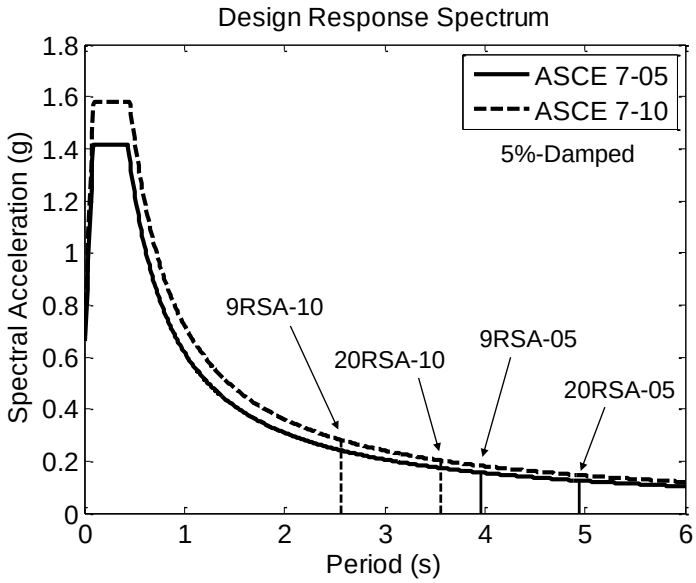

Figure 5.3: ASCE 7-05 and ASCE 7-10 design response spectra for reference site (34.045° N, -118.267° E).

When using RSA for strength design, both ASCE 7-05 and ASCE 7-10 require that the calculated member forces be amplified by $0.85V/V_t \geq 1$, where V_t is the modal base shear. For the SMF designs in this study, V_t is usually much less than V because the calculation of V is governed by a period-independent lower bound while V_t is calculated from Figure 5.3, which has no lower bound for long periods. So if the $0.85V/V_t$ amplification requirement did not exist, then if a design was altered to have smaller members, the design forces in RSA would become smaller because T_1 would increase. However, the existence of the $0.85V/V_t$ amplification requirement means that if T_1 is sufficiently long, altering a design to have smaller members does not reduce the design forces. Interestingly, this $0.85V/V_t$ amplification requirement does not apply to drifts in ASCE 7-05, but does apply to drifts in ASCE 7-10 with the stipulation that the V is calculated according to $C_s = 0.5S_1/(R/I_e)$ for ASCE 7-10.

Table 5.3 provides a summary of important seismic loading parameters for each design. In each case, T_1 is greater than C_uT_a, so C_uT_a is used as T to calculate V for every design. Note that since C_uT_a and T_1 for the 9ELF-05 design are greater than 1.53

seconds, the ELF procedure is actually not allowed according to ASCE 7-05 for the 9ELF-05 design. V_{strength} is the base shear used in each design for the strength checks. For the ELF designs, $V_{\text{strength}} = V$. For the RSA designs, $V_{\text{strength}} = 0.85V$ because of the requirement that calculated member forces be amplified by $0.85V/V_t \geq 1$ when using RSA. V_{strength} for the ASCE 7-10 designs is over 50% larger than that of the ASCE 7-05 designs due to the combined effects of the increased seismic design values (Table 5.2) and the lower limit for C_s of $0.44S_{DS}I_e$ in ASCE 7-10. Interestingly, V/W and V_{strength}/W are the same for the 9- and 20-story RSA designs for a given design code. This is because the calculation of V for all designs is governed by a period-independent lower bound.

V_{drift} is the base shear used in each design for the drift checks. For ELF design in ASCE 7-05, $V_{\text{drift}} = V_{\text{strength}} = V$. For ELF design in ASCE 7-10, drift checks do not need to incorporate the lower limit for C_s of $0.44S_{DS}I_e$, so the lower limit for C_s of $0.5S_1/(R/I_e)$ controls the calculation of V_{drift}. For RSA design in ASCE 7-10, V_{drift} is equal to 0.85 times V_{drift} from ELF design because the $0.85V/V_t$ amplification requirement applies to drifts in ASCE 7-10. For RSA design in ASCE 7-05, there is no lower bound for V_{drift}. As such, the V_{drift} values reported in Table 5.3 for the 9RSA-05 and 20RSA-05 designs (indicated with an asterisk) are the modal base shear values, V_t, calculated in ETABS. These values are significantly lower than V_{drift} for the other designs. Since drift requirements control design of most of the members, these differences in V_{drift} dramatically impact design.

Table 5.3: Seismic design parameters calculated for each design.

Design	C_uT_a (s)	T_1 (s)	V/W	V_{strength}/W	V_{drift}/W
9ELF-05	1.83	2.47	0.045	0.045	0.045
9ELF-10	1.83	2.26	0.070	0.070	0.052
9RSA-05	1.83	3.96	0.045	0.038	0.018*
9RSA-10	1.83	2.57	0.070	0.059	0.044
20RSA-05	3.40	4.94	0.045	0.038	0.014*
20RSA-10	3.40	3.56	0.070	0.059	0.044

* V_{drift} is defined as equal to the modal base shear, V_t.

It is worth noting that the values of T_1 calculated by eigenvalue analysis for the 9RSA-05 and 20RSA-05 designs are much larger than would be expected from steel moment frames of this height and are larger than the other post-Northridge SMF designs. As alluded to earlier, this is because there is no requirement in ASCE 7-05 for drifts calculated using RSA to be amplified by $0.85V/V_t$ even though this

requirement exists in ASCE 7-10. As noted by Gosh et al. [118], this requirement was added in ASCE 7-10 because "[t]here was general agreement within the Seismic Subcommittee of ASCE 7 that this was the intent all along and that this requirement is important for long-period structures." As such, it is very possible, if not likely, that practicing engineers designing SMFs according to ASCE 7-05 using RSA would have incorporated this requirement even though it is not specifically codified. Note that if this requirement was included in this study, the values of V_{drift}/W for the 9RSA-05 and 20RSA-05 designs would both be 0.038, more than double the values that are used here. The fact that practicing engineers may have incorporated this requirement in design even though it is not codified is not considered in this study, but this may be worth investigating in the future.

Section Properties

The section properties for each design are given in Tables 5.4-5.9.

Table 5.4: Member sizes of 9ELF-05 design.

	Column Section			Doubler Plate	
Story / Floor	Exterior	Interior	Beam Section	Exterior	Interior
9 / Roof	W24X103	W24X229	W21X44	0	0
8 / 9	W24X103	W24X229	W24X84	1/4	3/8
7 / 8	W24X176	W24X306	W27X102	1/8	3/8
6 / 7	W24X176	W24X306	W30X124	1/4	5/8
5 / 6	W24X176	W24X335	W30X124	1/4	1/2
4 / 5	W24X176	W24X335	W33X130	3/8	5/8
3 / 4	W24X207	W24X335	W33X130	1/4	5/8
2 / 3	W24X207	W24X335	W33X130	1/4	5/8
1 / 2	W24X250	W24X335	W33X130	0	5/8
-1 / 1	W24X250	W24X335	W33X130	0	5/8

Table 5.5: Member sizes of 9ELF-10 design.

	Column Section			Doubler Plate	
Story / Floor	Exterior	Interior	Beam Section	Exterior	Interior
9 / Roof	W24X103	W24X250	W21X50	0	0
8 / 9	W24X103	W24X250	W24X94	1/4	1/2
7 / 8	W24X176	W24X306	W30X108	1/8	3/8
6 / 7	W24X176	W24X306	W30X124	1/4	5/8
5 / 6	W24X207	W24X370	W33X131	1/4	5/8
4 / 5	W24X207	W24X370	W33X141	1/4	5/8
3 / 4	W24X250	W24X370	W33X152	1/8	3/4
2 / 3	W24X250	W24X370	W33X152	1/8	3/4
1 / 2	W24X279	W24X408	W33X152	0	1/2
-1 / 1	W24X279	W24X408	W33X152	0	1/2

Table 5.6: Member sizes of 9RSA-05 design.

	Column Section			Doubler Plate	
Story / Floor	Exterior	Interior	Beam Section	Exterior	Interior
9 / Roof	W24X62	W24X103	W18X40	0	1/8
8 / 9	W24X62	W24X103	W21X50	0	1/4
7 / 8	W24X76	W24X162	W24X55	0	1/4
6 / 7	W24X76	W24X162	W24X62	1/8	1/4
5 / 6	W24X94	W24X207	W24X76	1/8	3/8
4 / 5	W24X94	W24X207	W24X76	1/8	3/8
3 / 4	W24X131	W24X229	W24X84	1/8	3/8
2 / 3	W24X131	W24X229	W24X84	1/8	3/8
1 / 2	W24X162	W24X250	W27X94	1/8	1/2
-1 / 1	W24X162	W24X250	W27X94	1/8	1/2

Table 5.7: Member sizes of 9RSA-10 design.

	Column Section			Doubler Plate	
Story / Floor	Exterior	Interior	Beam Section	Exterior	Interior
9 / Roof	W24X94	W24X229	W21X50	0	0
8 / 9	W24X94	W24X229	W24X84	1/4	3/8
7 / 8	W24X146	W24X279	W27X102	1/4	1/2
6 / 7	W24X146	W24X279	W30X108	1/4	1/2
5 / 6	W24X162	W24X306	W30X108	1/4	3/8
4 / 5	W24X162	W24X306	W30X116	1/4	1/2
3 / 4	W24X192	W24X335	W33X130	1/4	5/8
2 / 3	W24X192	W24X335	W33X130	1/4	5/8
1 / 2	W24X207	W24X335	W33X130	1/4	5/8
-1 / 1	W24X207	W24X335	W33X130	1/4	5/8

Table 5.8: Member sizes of 20RSA-05 design.

	Column Section			Doubler Plate	
Story / Floor	Exterior	Interior	Beam Section	Exterior	Interior
20 / Roof	HSS10X10X3/4	W24X94	W18X35	0	1/8
19 / 20	HSS10X10X3/4	W24X94	W18X40	0	1/4
18 / 19	HSS12X12X7/8	W24X131	W21X44	0	1/8
17 / 18	HSS12X12X7/8	W24X131	W24X55	0	1/4
16 / 17	HSS14X14X1	W24X162	W24X55	0	1/4
15 / 16	HSS14X14X1	W24X162	W24X55	0	1/4
14 / 15	HSS14X14X1	W24X162	W24X62	0	1/4
13 / 14	HSS16X16X5/4	W24X207	W24X62	0	1/8
12 / 13	HSS16X16X5/4	W24X207	W24X62	0	1/8
11 / 12	HSS16X16X5/4	W24X207	W24X76	0	3/8
10 / 11	HSS16X16X3/2	W24X250	W24X76	0	1/4
9 / 10	HSS16X16X3/2	W24X250	W24X84	0	3/8
8 / 9	HSS16X16X3/2	W24X250	W24X94	0	1/2
7 / 8	HSS18X18X2	W24X250	W24X94	0	1/2
6 / 7	HSS18X18X2	W24X250	W27X94	0	1/2
5 / 6	HSS18X18X2	W24X250	W27X94	0	1/2
4 / 5	HSS18X18X2	W24X279	W27X94	0	3/8
3 / 4	HSS18X18X2	W24X279	W27X102	0	1/2
2 / 3	HSS18X18X2	W24X279	W27X102	0	1/2
1 / 2	HSS18X18X5/2	W24X279	W30X108	0	1/2
-1 / 1	HSS18X18X5/2	W24X279	W30X108	0	1/2
-2 / -1	HSS18X18X5/2	W24X279	W14X22	0	0

Table 5.9: Member sizes of 20RSA-10 design.

	Column Section			Doubler Plate	
Story / Floor	Exterior	Interior	Beam Section	Exterior	Interior
20 / Roof	HSS14X14X1	W24X162	W18X40	0	0
19 / 20	HSS14X14X1	W24X162	W24X62	0	1/4
18 / 19	HSS14X14X1	W24X250	W24X62	0	0
17 / 18	HSS14X14X1	W24X250	W24X94	0	1/2
16 / 17	HSS16X16X5/4	W24X306	W24X94	0	1/4
15 / 16	HSS16X16X5/4	W24X306	W27X94	0	1/4
14 / 15	HSS16X16X5/4	W24X306	W27X102	0	3/8
13 / 14	HSS16X16X3/2	W24X306	W30X108	0	3/8
12 / 13	HSS16X16X3/2	W24X306	W30X108	0	3/8
11 / 12	HSS16X16X3/2	W24X306	W30X116	0	1/2
10 / 11	HSS16X16X2	W24X335	W30X116	0	3/8
9 / 10	HSS18X18X2	W24X335	W30X116	0	3/8
8 / 9	HSS18X18X2	W24X335	W33X130	0	5/8
7 / 8	HSS18X18X5/2	W24X335	W33X130	0	5/8
6 / 7	HSS18X18X5/2	W24X335	W33X130	0	5/8
5 / 6	HSS18X18X5/2	W24X335	W33X130	0	5/8
4 / 5	HSS18X18X5/2	W24X370	W33X130	0	3/8
3 / 4	HSS18X18X5/2	W24X370	W33X141	0	5/8
2 / 3	HSS18X18X5/2	W24X370	W33X141	0	5/8
1 / 2	HSS20X20X3	W24X370	W33X141	0	5/8
-1 / 1	HSS20X20X3	W24X370	W33X141	0	5/8
-2 / -1	HSS20X20X3	W24X370	W14X22	0	0

The differences in the designs of the ASCE 7-05 and ASCE 7-10 SMFs are due to three important differences between the two codes. First, as is clear in Table 5.2, the design values in ASCE 7-10 are larger than those in ASCE 7-05. This leads to larger seismic loads in ASCE 7-10. Second, ASCE 7-10 has a lower limit for C_s of $0.44S_{DS}I_e$, which in this case governs the calculation of V. This limit is not included in ASCE 7-05. This limit does not need to be incorporated when calculating V for checking drift values so it only has an effect for checking the designs for strength. Lastly, in the RSA procedure, ASCE 7-10 requires that if V_t, the modal base shear, is less than $0.85C_sW$ where C_s is governed by the lower limit of $0.5S_1/(R/I_e)$, then the drifts calculated in RSA must be multiplied by $0.85C_sW/V_t$. This requirement is not included in ASCE 7-05. All of these changes result in the ASCE 7-10 designs having larger member sizes than the ASCE 7-05 designs, with the latter of the three changes being the most significant in this study.

Design Story Drifts

Due to the importance of drift requirements, the seismic drifts for each design are shown in Figures 5.4 and 5.5. In these plots, the drift at story x calculated by elastic analysis in ETABS is denoted Δ_{xe} and is multiplied by the deflection amplification factor C_d, which equals 5.5 for special SMFs, to produce the design story drift Δ_x, whose limit is 2% in both ASCE 7-05 and ASCE 7-10. It is clear from Figure 5.4 that seismic drift limits control design at almost every story. The drifts on the first story are less than required because of the design decision to require that beams at upper stories are smaller than beams at lower stories.

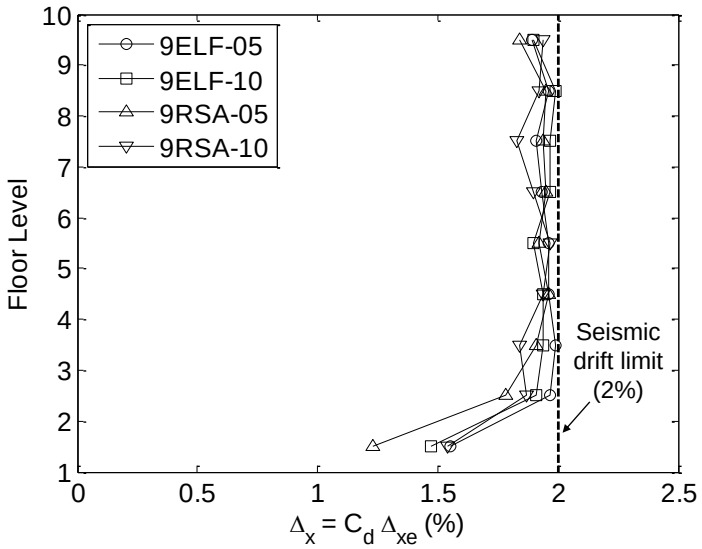

Figure 5.4: Design story drifts (Δ_x) calculated in response to seismic loads for 9ELF-05, 9ELF-10, 9RSA-05, and 9RSA-10 designs.

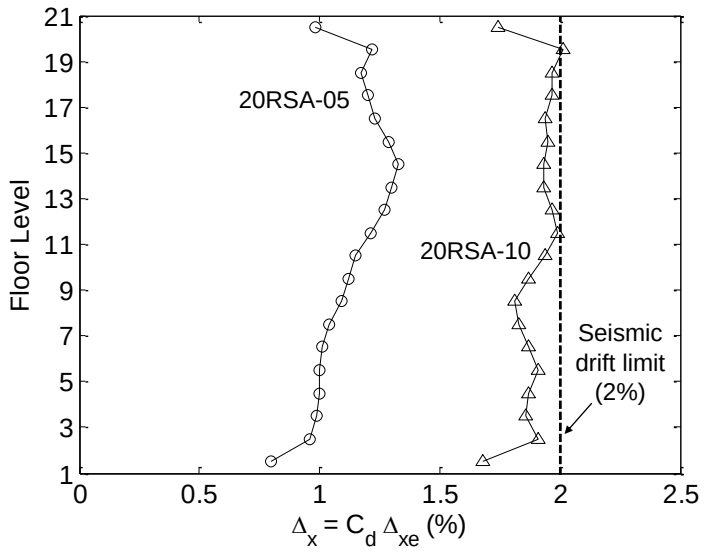

Figure 5.5: Design story drifts (Δ_x) calculated in response to seismic loads for 20RSA-05 and 20RSA-10 designs.

In Figure 5.5, it is clear that, like the 9-story SMF designs, the 20RSA-10 design is governed by seismic drift requirements at nearly every story. However, this is not the case for the 20RSA-05 design. Instead, for the 20RSA-05 design, wind drifts control design of the bottom half of the structure (Figure 5.6), while beam strength requirements for seismic loads govern design of beams in the remaining stories. Seismic drift requirements do not control the 20RSA-05 design because ASCE 7-05 does not require drifts calculated using the RSA procedure to be amplified by $0.85V/V_t$ like in ASCE 7-10. If this were required, the calculated drifts for the 20RSA-05 design would need to be amplified by nearly 3x, and would greatly exceed the specified limit of 2%.

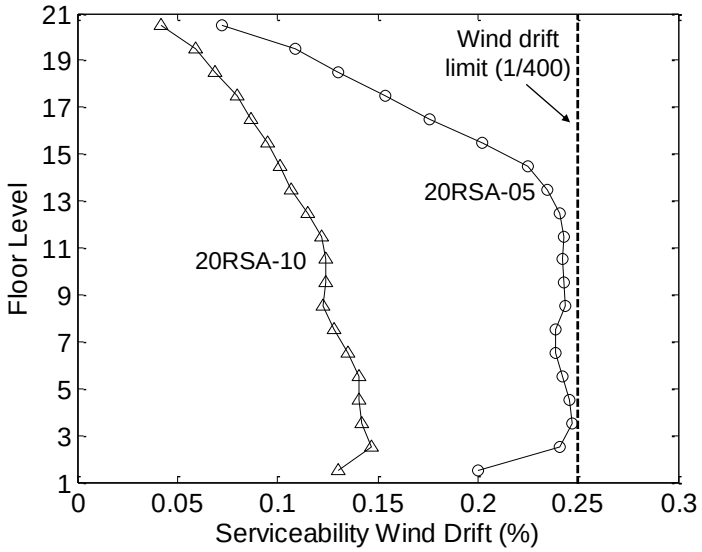

Figure 5.6: Serviceability drifts calculated in response to wind loads for 20RSA-05 and 20RSA-10 designs.

Additional design information for all designs presented in this section are available in Section E.1 of Appendix E.

5.5 Performance-Based Designs

A total of four SMFs (two 9-story and two 20-story) are designed using the LATBSDC alternate procedure to represent performance-based design (PBD). The LATBSDC alternate procedure requires site-specific response spectra at different hazard levels to define the seismic loads. This is normally done by a geotechnical engineering firm using proprietary procedures and is subjected to peer review. Instead of generating site-specific spectra from scratch for this study, site-specific spectra used in the performance-based designs of two high-rises (LA Live and Wilshire Grand towers) in downtown Los Angeles were obtained by the author. Two 9-story SMFs are designed using the LA Live (LL) site-specific spectra and Wilshire Grand (WG) site-specific spectra and two 20-story SMFs are designed using the LL and WG site-specific spectra. The LATBSDC alternate procedure was specifically developed for the design of tall buildings, which it defines to be those taller than 160 feet. This would classify the 20-story SMFs as "tall," but not the 9-story SMFs. However, the LATBSDC alternate procedure notes that "[n]othing in this document precludes its applicability to shorter buildings" [23]. So for comparison, 9-story SMFs are designed in addition to 20-story SMFs. The four SMF designs are denoted 9PBD-LL,

9PBD-WG, 20PBD-LL, and 20PBD-WG to indicate the number of stories (9 or 20), that performance based design is used (instead of ELF or RSA), and the geotechnical report from which the site-specific spectra are extracted (LL or WG).

Site-Specific Response Spectra

The first set of site-specific spectra used in this study for design are extracted from the geotechnical report prepared by GeoPentech [115] for the "LA Live" (LL) project in downtown Los Angeles, which includes a 55-story tower. The address of the site is 900 W. Olympic Blvd. (34.045° N, -118.267° E), which is approximately 850 meters from the reference site for this study. The obtained geotechnical report is dated January 23, 2007 and was obtained from the Los Angeles Department of Building and Safety. The report summarizes the probabilistic seismic hazard analysis (PSHA) procedures used to generate the site-specific spectra and tabulates site-specific 5%-damped spectral ordinates for periods up to 5 seconds in the Fault Normal (FN), Fault Parallel (FP), and Fault Average (FA) directions for 50%/30-year, 10%/50-year, and 2%/50-year seismic hazard levels. This report calculated the site-specific spectra using the average of three GMPEs published in 1997 by Abrahamson and Silva [119], Sadigh et al. [120], and Boore, Joyner, and Fumal [121].

The second set of site-specific spectra used in this study for design are extracted from the geotechnical report prepared by AMEC [116] for the "Wilshire Grand" (WG) project in downtown Los Angeles, which includes a 73-story tower. The address of the site is 655 S. Figueroa St. (34.050° N, -118.260° E), and is the location of the reference site for this study. The obtained geotechnical report is dated October 8, 2012 and was also obtained from the Los Angeles Department of Building and Safety. This report summarizes the PSHA procedures used to generate the site-specific spectra and tabulates site-specific 2%-, 5%-, and 10%-damped spectral ordinates for periods up to 10 seconds in the FN and FP directions for the 50%/30-year and MCE hazard levels. The MCE spectrum is taken as the minimum of the 2%/50-year probabilistic spectrum and MCE deterministic spectrum. According to this report, the deterministic spectrum is controlled by events on the Puente Hills fault (0 to 3 second), Newport-Inglewood fault (3-7.5 second), and Elsinore fault (beyond 7.5 second). In this report, the 2%-50-year probabilistic spectrum controls calculation of the MCE spectrum at all periods. This report calculated the site-specific spectra using the average of four GMPEs published in 2008 by Abrahamson and Silva [122], Boore and Atkinson [40], Campbell and Bozorgnia [123], and Chiou and Youngs [124].

The Service Level Earthquake (50%/30-year) and MCE (2%/50-year) spectra from these reports are shown in Figures 5.7 and 5.8. It should be noted that PSHA for both reports was conducted before the definition of MCE_R was codified in ASCE 7-10. As such, the MCE spectra correspond to 2%/50-year spectra instead of "1% probability of collapse in 50 years" spectra. As noted in Section 5.2, these spectra are probably similar in the Los Angeles region. In Figures 5.7 and 5.8, the spectra from the two geotechnical reports are denoted first by the project and second by the direction. So an FP spectrum from the LA Live project is denoted "LL-FP." For comparison, the MCE and MCE_R spectra calculated based on ASCE 7-05 and ASCE 7-10, respectively, for this study's reference site are also shown in Figure 5.8. The ASCE 7-05 MCE spectrum represents the shaking in the geometric mean direction while the ASCE 7-10 MCE_R spectrum represents shaking in the maximum direction. The difference between the geometric mean and maximum direction is approximated by a factor of 1.3 in the seismic design maps (e.g. Commentary to Chapter 11 Modifications in FEMA P-750 [125]). This distinction explains, in part, the differences between the ASCE 7-05 and ASCE 7-10 MCE and MCE_R spectra.

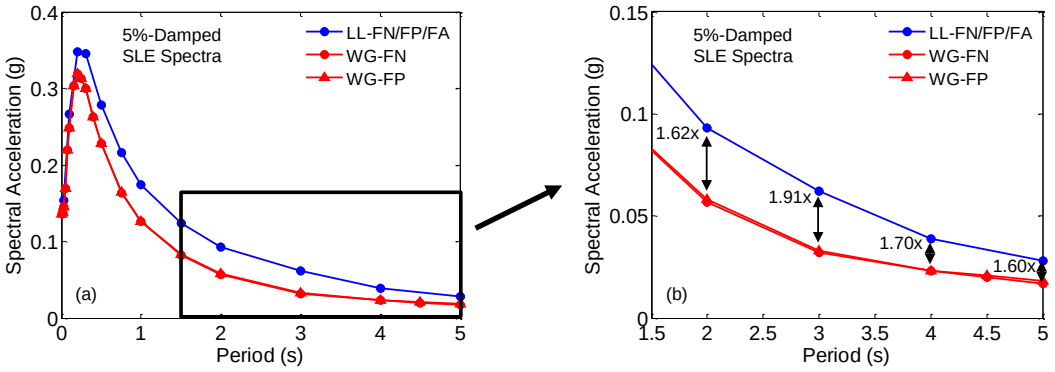

Figure 5.7: Service Level Earthquake (50%/30-year) 5%-damped response spectra taken from LL and WG reports.

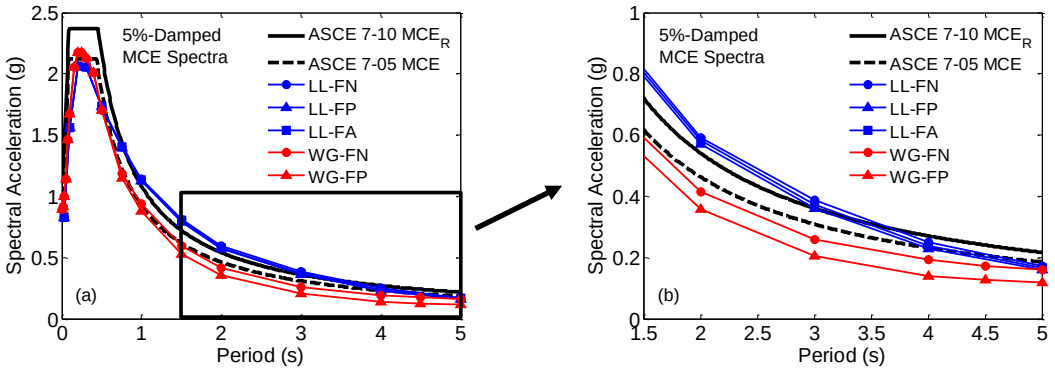

Figure 5.8: Maximum Considered Earthquake 5%-damped response spectra taken from LL and WG reports.

There are significant differences between the site-specific spectra for the LL project and the WG project that cannot be explained solely by the differences in location. The two sites are less than a kilometer apart and the S_1 values for the two sites as calculated per ASCE 7-10 using the USGS online map tool [106] are less than 3% apart, with the WG site actually having the larger value. As shown in Figure 5.7, the SLE spectral ordinates for periods of 2, 3, 4, and 5 seconds are larger in the LL project report by 60%-90%. The corresponding discrepancies in the MCE spectra for periods of 2, 3, and 4 are on the order of 40%-60% although for 5 seconds the discrepancy decreases to 36% and 8% in the FP and FN directions, respectively. For reference, as measured in ETABS via eigenvalue analysis, T_1 for the 9PBD-LL, 9PBD-WG, 20PBD-LL, and 20PBD-WG designs are 2.14, 3.75, 4.65, and 4.75 seconds, respectively.

The PSHA procedures in the two reports do not provide enough detail to explicitly see what factors cause the differences in the site-specific spectra, but at least part of the differences can be explained by the GMPEs used in the two reports. The LL project uses three GMPEs published in 1997 while the WG project uses four GMPEs published in 2008. Abrahamson and Silva, who published GMPEs in both 1997 and 2008, note in their 2008 report [122] when comparing the results of their 2008 GMPEs to their 1997 GMPEs that "[f]or M6, the models are similar, but for larger magnitudes, the current [2008] model leads to lower median ground motion at this short distance [R_{JB} = 1 km], reflecting the lower ground motions observed at short distances in recent large-magnitude earthquakes." Boore and Atkinson [40] make similar observations when comparing their 2008 GMPEs to the 1997 Boore,

Joyner, and Fumal GMPEs, which they denote "BJF97": "At all periods, the new equations predict significantly smaller motions than do the BJF97 equations for large magnitudes. This is probably the most important change in the new equations compared to the old equations. The difference in the predicted motions is particularly large for T = 1 s and M=7.5 (a factor of 2.4 at R_{JB} = 1 km)."

PBD Analysis Procedures

To demonstrate how the differences in site-specific spectra generated for the two reports manifest themselves in design, both sets of spectra are used for the design of SMFs using performance-based procedures. In this study, performance-based design procedures follow the guidelines of the 2014 version of the LATSBDC alternate procedure. In practice, it is unlikely that a project that follows the 2014 version of the LATBSDC alternate procedure would use the 1997 GMPEs to generate site-specific spectra, which are now considered out-of-date. However, in order to isolate the influence of design spectra on building design, this study considers both sets of design spectra in conjunction with the 2014 version of the LATSBDC alternate procedure, referred to in this study simply as the "LATSBSDC alternate procedure."

The LATBSDC alternate procedure requires an SLE evaluation and an MCE evaluation. For the SLE evaluation, RSA is permitted and is used in this study for design. The LATBSDC alternate procedure requires use of the 2.5%-damped 50%/30-year response spectrum for the SLE evaluation, but neither the LL or WG reports contain a 2.5%-damped 50%/30-year response spectrum. As such, the 5%-damped 50%/30-year response spectra from the two reports are used and a damping ratio of 2.5% is assigned to the structural model when performing RSA. The LATBSDC alternate procedure allows RSA to be performed using the geometric mean direction SLE response spectrum. In both the LL and WG reports, the FN and FP SLE spectra are virtually identical, so the directionality of the SLE spectrum is not significant in this case. For the sake of definiteness, the FA SLE spectrum is used for RSA for the LL designs and the FN SLE spectrum is used for RSA for the WG designs. The linear elastic structural models used for the SLE evaluations are created in ETABS in the same manner as the models developed in Section 5.4, with more information available in Section D.1 of Appendix D.

The MCE evaluation described in the LATBSDC alternate procedure requires nonlinear time history analysis with seven pairs of input ground motions. One set of input ground motions is generated for the 9PBD-LL and 20PBD-LL designs and

another set of input ground motions is generated for the 9PBD-WG and 20PBD-WG designs. Nonlinear time history analysis is performed using these input ground motions, with a structural model of each design, in PERFORM-3D [126]. These nonlinear models are created according to the recommendations in ATC 72-1 [127] for nonlinear analysis of steel moment frames. Information about these models are presented in Section D.2 of Appendix D.

A summary of the SLE and MCE evaluations performed in this section is provided in Table 5.10. Acceptability criteria that at least sometimes control design (i.e. drift limits and deformation-controlled criteria) are shown. None of the member sizes are controlled by requirements for force-controlled actions. No story is ever close to losing 20% of its initial strength. In a few cases, requirements for deformation-controlled actions in the MCE evaluation control design of the exterior column sizes at the base of the building due to plastic rotations at the base of these columns during MCE shaking. The remainder of the member sizes are controlled by drift limits and compatibility with special SMF requirements.

Table 5.10: Summary of relevant SLE and MCE evaluation procedures and acceptability criteria that are used in this section for design.

	SLE Evaluation	MCE Evaluation
Hazard Level	50%/30-year	2%/50-year
Analysis Procedure	RSA	NLTHA with 7 ground motions
Insterstory Drift Limit	0.005	0.03 mean, 0.045 max.
Deformation-Controlled Action Acceptability	D/C ratio < 1.5	CP criteria

Even though the LATBSDC alternate procedure specifies mean and maximum limits on residual interstory drift ratios of 0.01 and 0.015, respectively, these limits are not considered in this study for a few reasons. First, the Commentary to the LATBSDC alternate procedure notes that larger residual drifts can be acceptable in some special cases, such as specialized ground motion characerization. Given the selection of numerous near-source records in the suite of input ground motions, this criterion is perhaps satisfied in this study. Furthermore, in a recent study to determine suitable requirements for Chapter 16 of ASCE 7-16 [60], Jarrett et al. [128] recommend against requiring a formal check for residual drifts in collapse-prevention analysis

because a link is not found between high residual drifts and proximity to collapse. So residual drifts may not be a collapse prevention requirement in PBD in the near future. Lastly, Appendix C of FEMA P-58 [25] provides a comprehensive literature review of residual drift prediction, concluding that it is highly variable and sensitive to modeling assumptions when compared to other response parameters (e.g. MIDR). It also provides a simplified set of equations to predict the residual interstory story drift (Δ_r) from the maximum interstory drift (Δ), reproduced below:

$$\begin{aligned} \Delta_r &= 0 && \text{for } \Delta \leq \Delta_y, \\ \Delta_r &= 0.3(\Delta - \Delta_y) && \text{for } \Delta_y < \Delta < 4\Delta_y, \\ \Delta_r &= (\Delta - 3\Delta_y) && \text{for } \Delta \geq 4\Delta_y, \end{aligned} \tag{5.17}$$

where Δ_y is the interstory drift at yield. For a typical steel moment frame with a yield drift ratio of 0.01, calculating the residual drifts according to Equation 5.17 implies that if the maximum interstory drift limits (0.03 and 0.045) are satisfied, then the residual interstory drift limits (0.01 and 0.015) are also satisfied.

MCE Ground Motions

In this study, MCE input ground motions are selected from records in the NGA-West2 database [46] and are are modified to match the relevant target hazard spectrum using spectrum-matching procedures. The site-specific MCE uniform hazard spectra from the LL and WG reports are used as target spectra. Using a uniform hazard spectrum (UHS) instead of a conditional mean spectrum (CMS) is conservative and the LATBSDC alternate procedure allows use of the CMS. However, in this study, for simplicity, the UHS is the target spectrum. Two sets of seven pairs of input ground motions are generated for MCE evaluation: one set corresponding to the LL MCE spectra and one set corresponding to the WG MCE spectra. To further simplify the input ground motion selection and modification procedures, MCE evaluations for the 9PBD-LL and 20PBD-LL designs are performed using the same set of seven pairs of input ground motions. The 9PBD-WG and 20PBD-WG are also designed using the same input ground motions for MCE evaluation.

Input ground motions are required (per the LATBSDC alternate procedure) to be selected according to the guidance in ASCE 7-10, which states that "[a]ppropriate ground motions shall be selected from events having magnitudes, fault distance, and source mechanisms that are consistent with those that control the maximum considered earthquake" [20]. To identify these relevant characteristics it is necessary to disaggregate the hazard for the reference site. This can be done using OpenSHA

[129]. Disaggregation for 2%/50-year shaking is performed in OpenSHA using this study's reference site with V_{S30} = 350 m/s, the Boore and Atkinson 2008 GMPE [40], and the Mean UCERF3 model [130] with default settings of OpenSHA. V_{S30} = 350 m/s is chosen based on the estimated values for V_{S30} for sites in downtown Los Angeles used in similar studies by Haselton and Deierlein [48] (285 m/s) and Moehle et al. [131] (360 m/s) as well as the reported value (387 m/s) from the SCEC UGMS online tool [132], which cites Willis et al. [133] for its estimate of V_{S30}. V_{S30} = 350 m/s for the reference site appears to be a sufficient compromise for use in this study.

The results of PSHA indicate that approximately 15% of the hazard is from the San Andreas fault ($M \approx 8.0$, $R_{JB} \approx 55$ km) and most of the rest of the hazard is from nearby faults ($R_{JB} < 20$ km) for periods ranging from 2 to 5 seconds. For reference, the disaggregation graph for T = 5 s is shown in Figure 5.9. As a comparison, this disaggregation has a bit less hazard from long-distance events for longer periods when compared to the PSHA disaggregation performed for a similar site by Moehle et al. [131], but is generally similar.

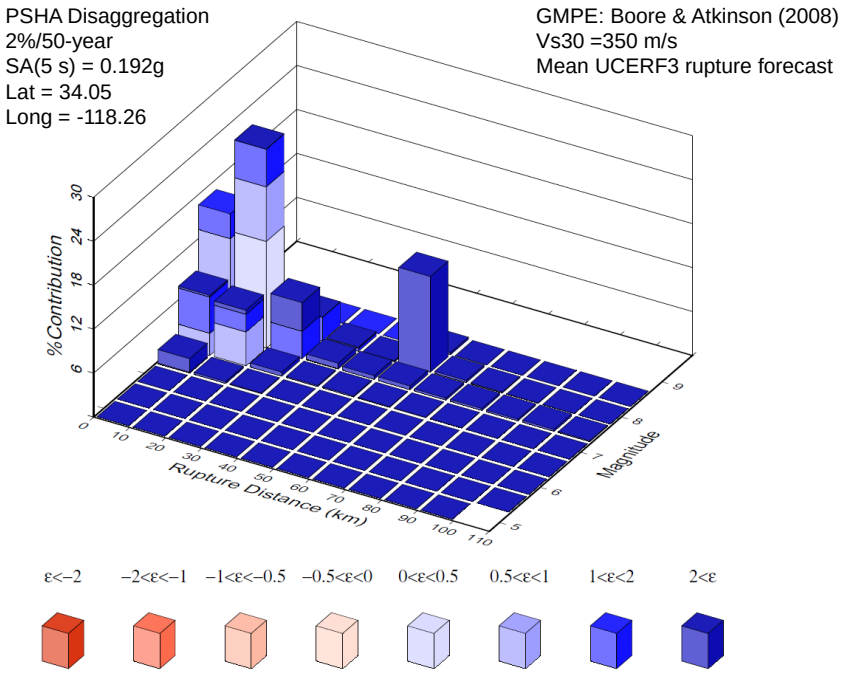

Figure 5.9: Disagreggation of 2%/50-year hazard of $Sa^{5\%}(T = 5s)$ for reference site (34.05° N, -118.26° E).

Based on the disaggregation results, of the seven input ground motions used for design, six are chosen from near-source (<10 km) records from events with M ranging

from 6.0 to 7.5 and one is chosen from long-distance (> 50 km) records from events with M ranging from 7.5 to 8.5. It should be noted that, since spectrum-matching is eventually used to modify the selection records, the proportion of records coming from different types of events is not particularly important in this study. One of the main reasons for selecting input records from sources similar to those controlling the hazard of the building site is to ensure that the spectral shape of the input ground motions are similar to what the building would be expected to experience. Since the spectral shape of each record is modified to match the target spectrum during spectrum-matching, selecting records based on event characteristics is not necessarily crucial. That said, the near-source record criteria is made strict (<10 km) in this study to encourage the selection of records with near-fault pulse motions because velocity pulses can be preserved after spectrum-matching (e.g. Section 4.3 of NIST GCR 11-917-15 [113]) and the presence of these pulses can amplify structural response (e.g. [3]). It should be acknowledged that more comprehensive guidelines such as those presented in Chapter 4 of NIST GCR 11-917-15 [113] are available for selecting and scaling ground motions for sites for which near-source ground motions are of concern. These guidelines include quantitative procedures for determining what fraction of input ground motions should contain a velocity pulse and how to properly orient the orthogonal pairs of input ground motions if they contain a velocity pulse. For simplicity, these guidelines are not considered in the selection of input ground motions in this study.

Based on the criteria stated above along with the requirement that the maximum usable period must be 7.1 seconds or greater (corresponding to $1.5T_1$, where T_1 = 4.75 seconds is the longest fundamental period of the considered designs), there are over 70 pairs of potential ground motion records that meet the near-source criteria ($R_{JB} < 10$ km and M between 6.0 and 7.5) in the NGA-West2 database. From these pairs, six are chosen based on the amplified fit of the square root of the sum of the squares (SRSS) spectrum to the target spectrum. For this purpose, the LL MCE target spectrum is defined as the reported FA MCE spectrum and the WG MCE target spectrum is defined as the geometric mean of the reported FP and FN MCE spectra. To measure the "amplified fit" of a pair of orthogonal ground motion records to a target spectrum, the SRSS spectrum of the pair is calculated and then amplified by a scale factor so that the "misfit" between the SRSS spectrum and the target spectrum for periods ranging from 2 to 5.5 seconds is minimized, where the misfit is defined as the squared error. The six records with the smallest misfit are selected, with the stipulation that no more than two records from a single event may be selected.

This admittedly arbitrary procedure for selecting ground motion records is based on the procedure for "Record Selection and Modification for Assessment Purposes" outlined by Moehle et al. [131]. There are not specific codified rules for record selection in ASCE 7-10 or the LATBSDC alternate procedure, but the procedure performed here reduces the required computational effort during spectrum-matching because the selected records already have a similar shape to the target spectrum. One pair of ground motion records is also chosen from the NGA-West2 database using the same procedure but with $R_{JB} > 50$ km and M between 7.5 and 8.5 to represent the hazard from long-distance events.

The seven ground motions selected based on the LL MCE target spectrum and the WG MCE target spectrum are given in Tables 5.11 and 5.12. Note that they share many of the same records in common. This is because the shape of the LL and WG MCE target spectra are relatively similar (despite the differences in amplitude) when compared to the high variability of spectral shapes of individual ground motion records. The record sequence number (RSN) for each record is its unique identifier in the NGA-West2 database. Of the selected LL MCE ground motions, three (RSNs 184, 779, and 802) are classified in Appendix C of NIST GCR 11-917-15 [113] as "pulse motions." Of the selected WG MCE ground motions, four (RSNs 143, 184, 285, and 208) are given the "pulse motion" designation.

Table 5.11: Selected ground motion records for nonlinear time history analysis of the 9PBD-LL and 20PBD-LL designs.

RSN	Event	Year	M_W	Station	R_{JB} (km)	Max. Usable T (s)
184	Imperial Valley	1979	6.53	H-EDA	5.09	34.8
779	Loma Prieta	1989	6.93	LGP	0.00	8.0
802	Loma Prieta	1989	6.93	STG	7.58	8.0
983	Northridge	1994	6.69	JGB	0.00	7.1
1044	Northridge	1994	6.69	NWH	3.16	8.3
1163	Kocaeli	1999	7.51	DHM	58.33	40.0
1611	Duzce	1999	7.14	1058	0.21	13.3

Table 5.12: Selected ground motion records for nonlinear time history analysis of the 9PBD-WG and 20PBD-WG designs.

RSN	Event	Year	M_W	Station	R_{JB} (km)	Max. Usable T (s)
143	Tabas	1978	7.35	TAB	1.79	8.0
184	Imperial Valley	1979	6.53	H-EDA	5.09	34.8
285	Irpina	1980	6.90	BAG	8.14	8.9
802	Loma Prieta	1989	6.93	STG	7.58	8.0
1044	Northridge	1994	6.69	NWH	3.16	8.3
1163	Kocaeli	1999	7.51	DHM	58.33	40.0
1611	Duzce	1999	7.14	1058	0.21	13.3

After the input ground motion records are selected, they must be modified to meet the requirements of ASCE 7-10 that "[e]ach pair of motions shall be scaled such that in the period range from $0.2T$ to $1.5T$, the average of the SRSS spectra from all horizontal component pairs does not fall below the corresponding ordinate of the response spectrum used in the design" [20]. In this study, spectrum-matching is used instead of the more simple (but conservative) amplitude-scaling. In the passage from ASCE 7-10, the "response spectrum used in the design" refers to the MCE_R spectrum, which is defined as the maximum-direction spectrum. ASCE 7-10 also stipulates that for near-source sites (within 5 km of the controlling fault), the FN and FP directions can be incorporated so long as the components of the selected record are rotated accordingly. These spectra are presented in the LL and WG reports, but for the designs in this study, the FN and FP directions are not specified with reference to the structure. As such, the near-source provisions in ASCE 7-10 are not considered here. Instead, each component of the input ground motions is spectrum-matched to the "geometric mean" MCE spectrum and then all pairs are scaled by the same factor until the average SRSS spectrum exceeds the MCE_R spectrum, defined as 1.3 times the geometric mean MCE spectrum. This "match-then-scale" procedure is approximately the same as that used to generate the input ground motions for the design of the San Bernardino Justice Center [134] and can be summarized as follows:

1. The "geometric mean" MCE spectrum is specified from the reported MCE LL and WG spectra for periods up to 7.5 seconds. The geometric mean MCE LL spectrum is taken as the MCE LL-FA spectrum and the geometric mean MCE WG spectrum is approximated as the geometric mean of the MCE WG-FN and WG-FP spectra. The spectral ordinate at 7.5 seconds of the geometric mean MCE-LL spectrum is extrapolated from the spectral ordinate at 5 seconds by

(conservatively) assuming the same spectral velocity at 7.5 seconds as at 5 seconds.

2. Each horizontal component of the seven selected ground motions is amplitude-scaled to the geometric mean MCE spectrum to minimize the squared error between the scaled ground motion component and the geometric mean MCE spectrum. Spectrum-matching of the ground motion time histories are performed to match to the geometric mean MCE spectrum using *rspMatch09* [59] in the period range from 0.1 seconds to 7.5 seconds.

3. For each pair of spectrum-matched horizontal ground motions, the SRSS spectrum is calculated. The mean SRSS spectrum is calculated from all seven SRSS spectra. Every ground motion component is scaled by the same amplification factor such that the mean SRSS spectrum exceeds 1.3 times the geometric mean MCE spectrum at all considered periods ranging from 0.1 seconds to 7.5 seconds. The results are the MCE ground motions.

Spectrum-matching is performed using *rspMatch09* [59], which iteratively adds wavelets to an acceleration time history until the record's response spectrum matches the target response spectrum at every considered period to within some threshold. In this study, a 5% mismatch is tolerated between the spectral ordinate of the matched ground motion's response spectrum and MCE geometric mean spectrum. For spectral matching, convergence is more easily achieved if the periods in the target spectrum (here, the MCE geometric mean spectrum) are closely spaced at short periods. As such, the MCE geometric mean spectrum for matching is interpolated linearly at 100 periods spaced logarithmically from 0.1 seconds to 7.5 seconds. In Step 3, when the spectrum-matched ground motions are amplified to 1.3 times the geometric mean MCE spectrum, only spectral ordinates at periods reported by the LL and WG reports are considered (in addition to the extrapolated value at 7.5 seconds for the geometric mean MCE-LL spectrum).

The final MCE-LL and MCE-WG ground motions used in design are shown in Figures 5.10 and 5.11, respectively. The N-S and E-W components are assigned randomly. As expected, the MCE-LL ground motions are more intense than the MCE-WG ground motions, which can be seen most obviously in the velocity records. Of the 14 components of MCE-LL ground motions, the average peak-to-peak velocity is 196 cm/s, with a maximum of 242 cm/s (N-S component of the 1994 M6.69 Northridge, Station NWH record). Of the 14 components of MCE-WG ground

motions, the average peak-to-peak velocity is 163 cm/s, with a maximum of 185 cm/s (E-W component of the 1989 M6.93 Loma Prieta, Station STG record). Qualitatively, the MCE ground motion time histories look similar to those used in the design of the San Bernardino Justice Center [134], though with slightly smaller amplitudes, owing to the close proximity of the San Bernardino Justice Center to the San Jacinto fault. Some components of the spectrum-matched MCE ground motions used in the San Bernardino Justice Center project have peak-to-peak velocities exceeding 300 cm/s. Note that the N-S component of the 1999 M7.14 Duzce, Station 1058 record matched to the WG spectrum (pink curve in Figure 5.11(e)) appears to end with non-zero velocity. This can happen as a result of the spectrum-matching procedure and is also seen in some MCE ground motion time histories used in the design of the San Bernardino Justice Center [134]. There do not appear to be any irregularities in nonlinear time history analysis with this ground motion so no manual adjustments are made to this record.

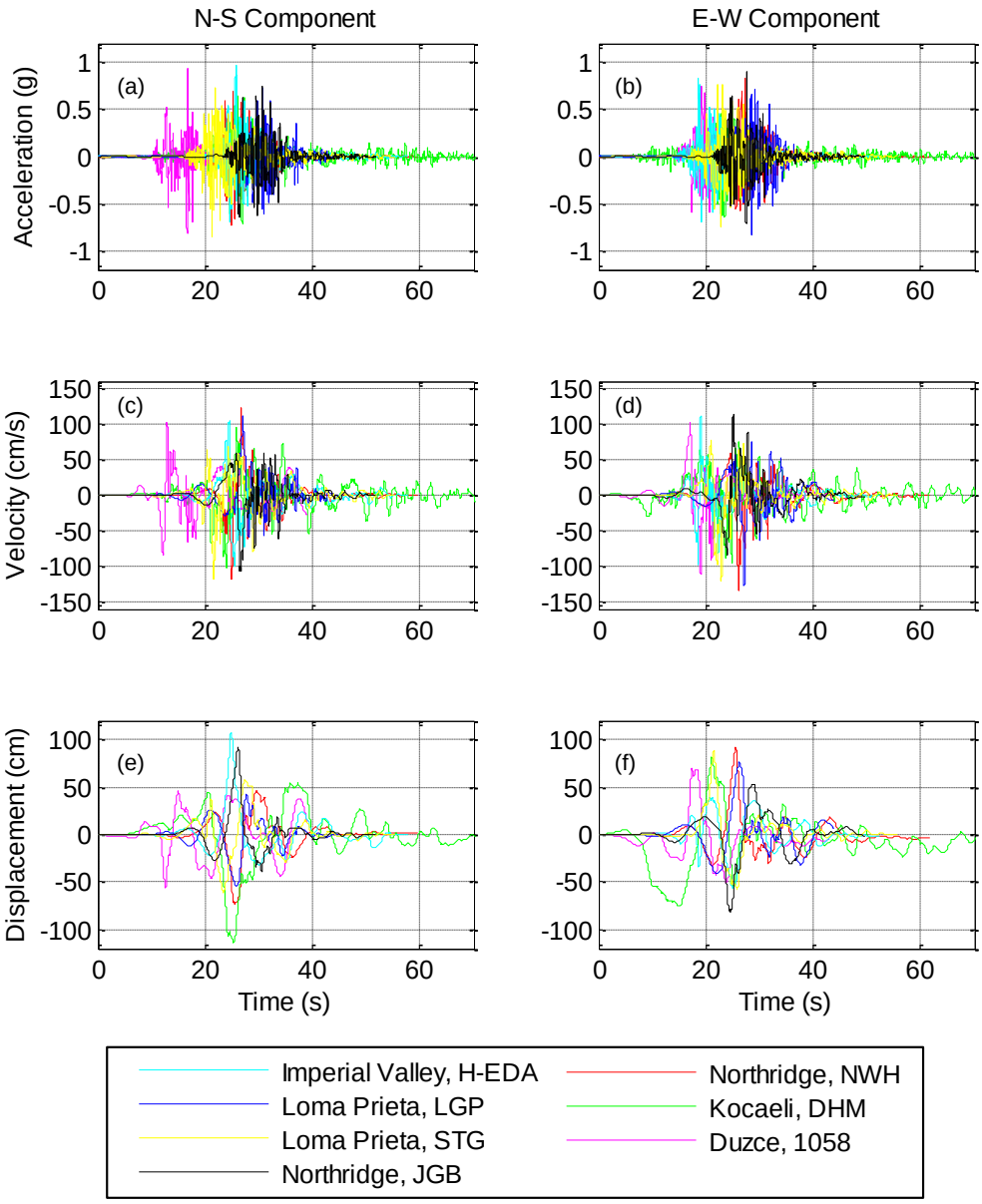

Figure 5.10: Spectrum-matched MCE time histories for nonlinear time history analysis of the 9PBD-LL and 20PBD-LL designs for collapse prevention evaluation.

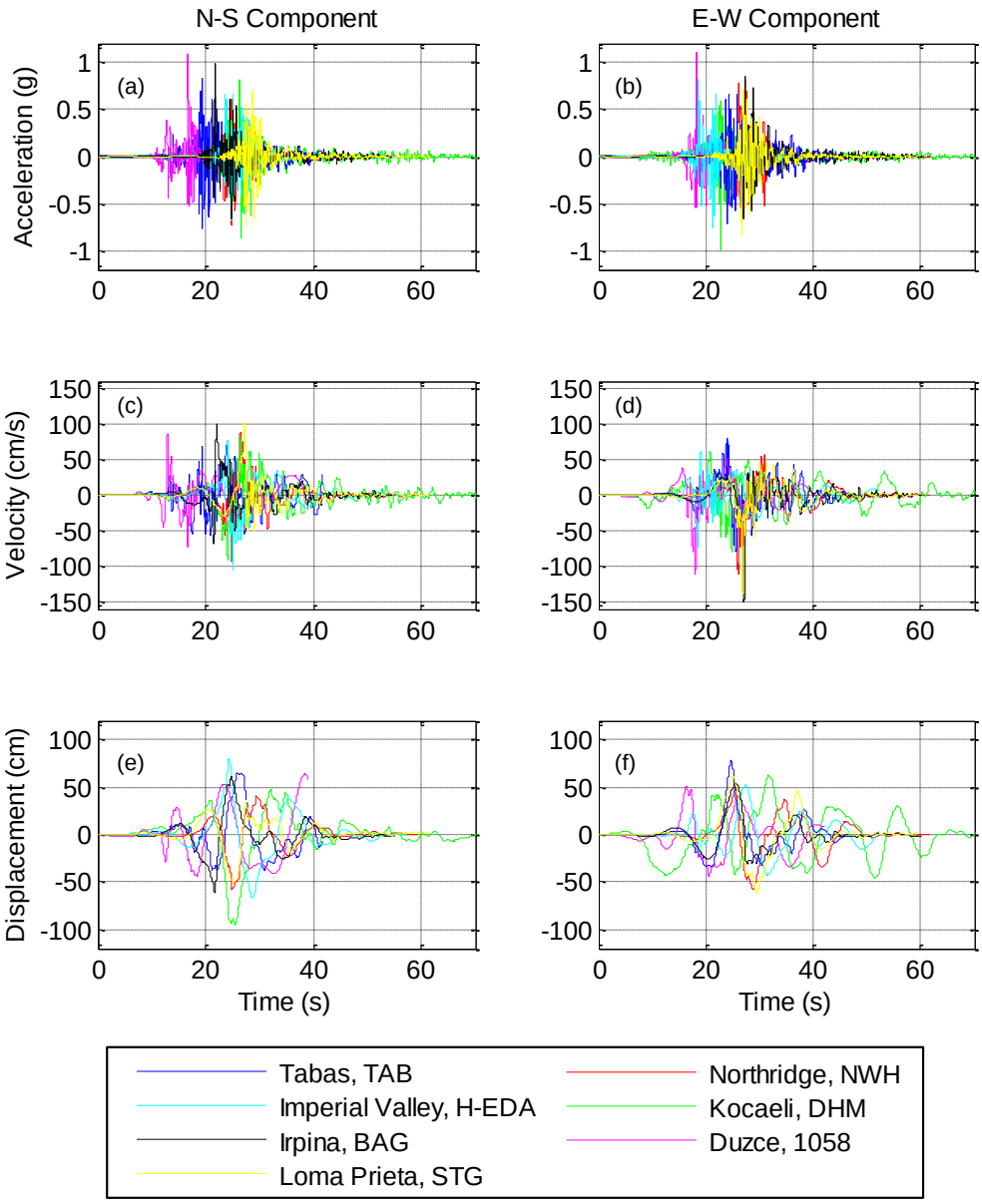

Figure 5.11: Spectrum-matched MCE time histories for nonlinear time history analysis of the 9PBD-WG and 20PBD-WG designs for collapse prevention evaluation.

SRSS response spectra of the MCE ground motions are shown in Figure 5.12 and compared to the relevant target spectrum (1.3 times the geometric mean MCE spectrum). These plots are shown to confirm that the response spectra of the MCE ground motions match the target spectrum. As would be expected, the mean SRSS response spectra for the LL and WG ground motions closely match the target spectra, so much so that the plots are nearly indistinguishable. The SRSS response spectra from each individual pair of ground motions are also shown, although these spectra

are barely visible.

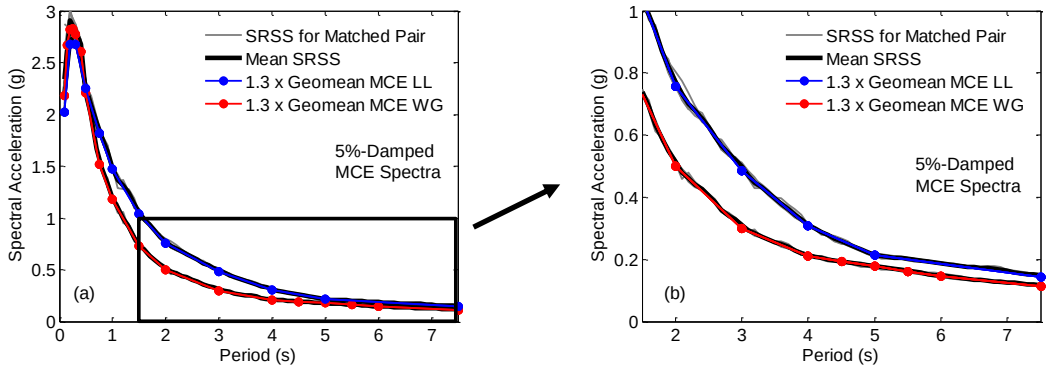

Figure 5.12: SRSS 5%-damped response spectra of spectrum-matched MCE time histories used in time history analysis of the 9PBD-LL, 20PBD-LL, 9PBD-WG, and 20PBD-WG designs for collapse prevention evaluation.

Section Properties

The section properties for each design are given in Tables 5.4-5.9.

Table 5.13: Member sizes of 9PBD-LL design.

	Column Section			Doubler Plate	
Story / Floor	Exterior	Interior	Beam Section	Exterior	Interior
9 / Roof	W24X131	W24X279	W24X55	0	0
8 / 9	W24X131	W24X279	W27X102	1/4	1/2
7 / 8	W24X176	W24X335	W30X116	1/4	3/8
6 / 7	W24X176	W24X335	W33X130	3/8	5/8
5 / 6	W24X207	W24X370	W33X130	1/4	3/8
4 / 5	W24X207	W24X370	W36X150	3/8	5/8
3 / 4	W24X250	W24X370	W36X150	1/8	5/8
2 / 3	W24X250	W24X370	W36X160	1/4	3/4
1 / 2	W24X306	W24X408	W36X160	0	5/8
-1 / 1	W24X306	W24X408	W36X160	0	5/8

Table 5.14: Member sizes of 9PBD-WG design.

	Column Section			Doubler Plate	
Story / Floor	Exterior	Interior	Beam Section	Exterior	Interior
9 / Roof	W24X76	W24X131	W21X44	0	1/8
8 / 9	W24X76	W24X131	W24X55	0	1/4
7 / 8	W24X94	W24X207	W24X76	1/8	3/8
6 / 7	W24X94	W24X207	W24X76	1/8	3/8
5 / 6	W24X103	W24X229	W24X84	1/4	3/8
4 / 5	W24X103	W24X229	W24X84	1/4	3/8
3 / 4	W24X131	W24X250	W24X84	1/8	3/8
2 / 3	W24X131	W24X250	W24X94	1/4	1/2
1 / 2	W24X146	W24X250	W24X94	1/4	1/2
-1 / 1	W24X146	W24X250	W24X94	1/4	1/2

Table 5.15: Member sizes of 20PBD-LL design.

	Column Section			Doubler Plate	
Story / Floor	Exterior	Interior	Beam Section	Exterior	Interior
20 / Roof	HSS10X10X3/4	W24X103	W18X35	0	1/8
19 / 20	HSS10X10X3/4	W24X103	W21X50	0	1/4
18 / 19	HSS12X12X7/8	W24X162	W21X50	0	1/8
17 / 18	HSS12X12X7/8	W24X162	W24X62	0	1/4
16 / 17	HSS14X14X1	W24X207	W24X76	0	3/8
15 / 16	HSS14X14X1	W24X207	W24X76	0	3/8
14 / 15	HSS14X14X1	W24X207	W24X76	0	3/8
13 / 14	HSS16X16X5/4	W24X229	W24X76	0	1/4
12 / 13	HSS16X16X5/4	W24X229	W24X76	0	1/4
11 / 12	HSS16X16X5/4	W24X229	W24X76	0	1/4
10 / 11	HSS16X16X5/4	W24X279	W24X84	0	1/8
9 / 10	HSS16X16X5/4	W24X279	W24X84	0	1/8
8 / 9	HSS16X16X5/4	W24X279	W27X94	0	3/8
7 / 8	HSS18X18X2	W24X279	W27X94	0	3/8
6 / 7	HSS18X18X2	W24X279	W27X94	0	3/8
5 / 6	HSS18X18X2	W24X279	W27X102	0	1/2
4 / 5	HSS18X18X2	W24X306	W27X102	0	3/8
3 / 4	HSS18X18X2	W24X306	W30X108	0	3/8
2 / 3	HSS18X18X2	W24X306	W30X108	0	3/8
1 / 2	HSS18X18X2	W24X306	W30X108	0	3/8
-1 / 1	HSS18X18X2	W24X306	W30X108	0	3/8
-2 / -1	HSS18X18X2	W24X306	W14X22	0	0

Table 5.16: Member sizes of 20PBD-WG design.

	Column Section			Doubler Plate	
Story / Floor	Exterior	Interior	Beam Section	Exterior	Interior
20 / Roof	HSS10X10X3/4	W24X84	W18X35	0	1/8
19 / 20	HSS10X10X3/4	W24X84	W18X35	0	1/8
18 / 19	HSS12X12X7/8	W24X131	W21X44	0	1/8
17 / 18	HSS12X12X7/8	W24X131	W24X55	0	1/4
16 / 17	HSS12X12X7/8	W24X162	W24X55	0	1/4
15 / 16	HSS12X12X7/8	W24X162	W24X62	0	1/4
14 / 15	HSS12X12X7/8	W24X162	W24X62	0	1/4
13 / 14	HSS16X16X5/4	W24X250	W24X62	0	0
12 / 13	HSS16X16X5/4	W24X250	W24X76	0	1/4
11 / 12	HSS16X16X5/4	W24X250	W24X84	0	1/4
10 / 11	HSS16X16X5/4	W24X279	W24X84	0	3/8
9 / 10	HSS16X16X5/4	W24X279	W24X84	0	3/8
8 / 9	HSS16X16X5/4	W24X279	W27X94	0	1/2
7 / 8	HSS18X18X2	W24X279	W27X94	0	3/8
6 / 7	HSS18X18X2	W24X279	W27X94	0	3/8
5 / 6	HSS18X18X2	W24X279	W27X102	0	1/2
4 / 5	HSS18X18X2	W24X306	W27X102	0	3/8
3 / 4	HSS18X18X2	W24X306	W30X108	0	3/8
2 / 3	HSS18X18X2	W24X306	W30X108	0	3/8
1 / 2	HSS18X18X2	W24X306	W30X108	0	3/8
-1 / 1	HSS18X18X2	W24X306	W30X108	0	3/8
-2 / -1	HSS18X18X2	W24X306	W14X22	0	0

The 9PBD-LL and 9PBD-WG designs are significantly different but the 20PBD-LL and 20PBD-WG designs are very similar. The difference in the 9PBD-LL and 9PBD-WG designs is, not surprisingly, due to the differences in the MCE and SLE spectra. The LL spectra are 40%-90% larger than the WG spectra in the range of periods from 2 to 4 seconds and T_1 (as measured via eigenvalue analysis in ETABS) is 2.14 seconds for the PBD-LL design and 3.75 seconds for the 9PBD-WG design. The PBD-LL design is controlled at all stories by drift limits in the SLE evaluation. The PBD-WG design is controlled in the first few stories by drift limits in the SLE evaulation and at the top stories by drift limits in the MCE evaluation. T_1 of the 9PBD-WG design is 75% larger than that of the 9PBD-LL design, which implies that the 9PBD-LL design is $1.75^2 \approx 3$ times stiffer than the 9PBD-WG design in a global sense.

This factor of three seems quite dramatic, but can be easily explained by the discrepancy in the SLE-LL and SLE-WG spectra. Let $SV_{1,LL}$ and $SV_{1,WG}$ be the

spectral velocities at $T = 1$ for the SLE-LL and SLE-WG spectra, respectively, let k_{LL} and k_{WG} be the first-mode effective stiffnesses of the 9PBD-LL and 9PBD-WG designs, respectively, and let T_{LL} and T_{WG} be the fundamental periods of the 9PBD-LL and 9PBD-WG designs, respectively. If it is assumed that the spectral velocity is approximately constant at the relatively long periods of T_{LL} and T_{WG}, then the SLE forces are proportional to $1/T$. Though not exactly the case here, if it is assumed that SLE drifts control design, one may make the approximation that

$$\frac{SV_{1,LL}/T_{LL}}{k_{LL}} = \frac{SV_{1,WG}/T_{WG}}{k_{WG}}. \tag{5.18}$$

Furthermore, if the first-mode effective mass of the 9PBD-LL and 9PBD-WG designs are the same, then

$$\frac{T_{WG}}{T_{LL}} = \sqrt{\frac{k_{LL}}{k_{WG}}}. \tag{5.19}$$

Inserting Equation 5.19 into Equation 5.18 and rearranging terms yields

$$\frac{SV_{1,LL}}{SV_{1,WG}} = \sqrt{\frac{k_{LL}}{k_{WG}}}, \tag{5.20}$$

or

$$k_{LL} = \left(\frac{SV_{1,LL}}{SV_{1,WG}}\right)^2 k_{WG}. \tag{5.21}$$

So under these conditions, one could estimate that the first-mode effective stiffness of the 9PBD-LL design would be greater than that of the 9PBD-WG design by a factor equal to the square of the ratio of the two spectra controlling the design. Assuming that the SLE-LL spectrum is 1.75 times larger than the SLE-WG spectrum (approximately the case in periods ranging from 2 to 5 seconds) leads to the estimation that the 9PBD-LL design is $1.75^2 \approx 3$ times stiffer than the 9PBD-WG design, which is approximately what is observed. That is, in the absence of other design considerations, differences in design spectra used for drift limit calculations can dramatically alter the final designs.

Despite these considerations, the 20PBD-LL and 20PBD-WG designs are identical in the first 10 stories and have nearly the same elastic periods calculated by eigenvalue analysis in ETABS (4.65 and 4.75 seconds, respectively). The first 10 stories are identical because the design of members at these levels is controlled by wind drift requirements, which are virtually the same for the two designs (the only difference comes from the fact that T_1 for the two designs are not exactly the same). Members in the top half of the structure are controlled by seismic drift requirements, so the

20PBD-LL design has larger members in the top half than the 20PBD-WG design as a result of the more severe seismic loading.

Design Story Drifts

The seismic drifts from the SLE and MCE evaluations in the N-S direction for each design are shown in Figures 5.13-5.16. The wind drifts in the N-S direction for the 20-story designs are shown in Figures 5.17. For brevity, drifts in the E-W direction are not shown, as E-W drifts are either similar to (for 9-story SMFs) or less than (for 20-story SMFs) those of the N-S direction due to the layout of the moment frames. In all cases, beam sizes are controlled by drift limits. In the MCE evaluation, collapse prevention (CP) criteria (according to ASCE 41-13 [111]) for seismically compact beams in special SMF permits plastic rotations of beams of up to $11\theta_y$, where θ_y is the beam's yield rotation. In the SMFs considered here, the geometry is highly regular and all of the lateral force resistance consists of moment frames. As such, during MCE shaking that induces beam yielding, the interstory story drift ratio in a given direction at a given story is approximately equal to the beam rotations of beams in that story. As calculated via ATC-72-1 [127], the minimum θ_y for any moment frame beam in any of the PBD SMF designs is 0.0065, though θ_y is much larger (often greater than 0.01) than this for most of the considered beam sections. In this extreme case, the CP limit is exceeded if plastic rotations in that beam exceed 0.072. However, the limit on interstory drift ratios for MCE evaluation is 0.03, less than half of 0.072. This drift limit is exceeded before the CP limit for beam yielding in every observed case, which is why beam sizes are all governed by drift limits.

As mentioned previously, beam sizes in the 9PBD-LL design are completely controlled by SLE drift requirements while beam sizes in the 9PBD-WG design are controlled by SLE drift limits at lower stories and MCE drift limits at higher stories. Beam sizes in the bottom half of both of the 20PBD designs are controlled by serviceability wind drift limits. Upper stories of the MCE-LL design are mostly controlled by SLE drift limits while the upper stories of the MCE-WG design are controlled by MCE drift limits.

Column sizes are for the most part controlled by column-beam strength ratio requirements or panel zone requirements (i.e. ensuring required doubler plate thickness is less than 0.5 times the column web thickness). The only exceptions are the exterior columns of the 9PBD designs. These columns experience large stresses in compression during MCE shaking as well as plastic rotations at the base. In such

situations, so long as the compression stresses are less than half of the column's nominal yield stress and the column section is seismically compact, plastic rotation is allowed at the column base according to the CP criteria of ASCE 41-13 up to a limit of

$$\theta_{\text{p,lim}} = 17(1 - \frac{5}{3}\frac{P}{P_{CL}})\theta_y, \tag{5.22}$$

where P is the axial force in the column and P_{CL} is the lower-bound axial capacity of the column. In the limiting case where $P/P_{CL} = 0.5$, which is nearly reached in all PBD designs for MCE evaluation, this leads to a plastic rotation limit of about $2.83\theta_y$, where θ_y is calculated according to ATC-72-1[127]. Consideration of column yielding at the base during MCE shaking is not as important for the 20PBD SMFs as for the 9PBD SMFs because during MCE shaking, plastic deformation is concentrated at the upper stories in the 20PBD SMFs with first-story interstory drift ratios never exceeding 1.25% (seen in Figures 5.15 and 5.16), while plastic deformation is more equally distributed during MCE shaking in the 9PBD SMFs, with first-story interstory drift ratios frequently exceeding 2% (seen in Figures 5.13 and 5.14).

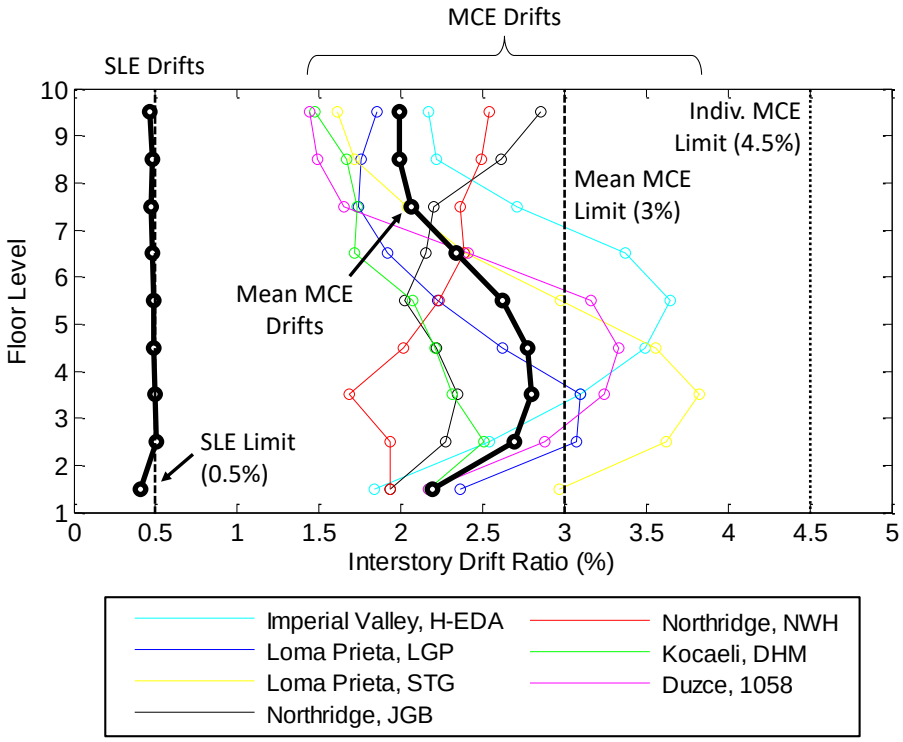

Figure 5.13: Maximum interstory drift ratios in the N-S direction of the 9PBD-LL design calculated for the service level evaluation (SLE drifts) and for the collapse prevention evaluation (MCE drifts).

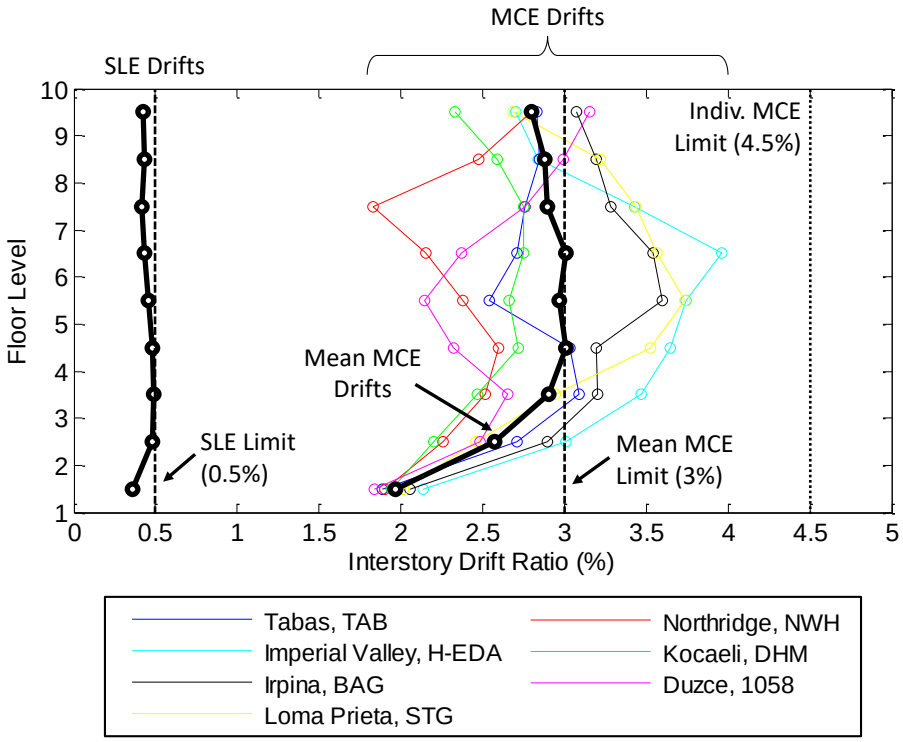

Figure 5.14: Maximum interstory drift ratios in the N-S direction of the 9PBD-WG design calculated for the service level evaluation (SLE drifts) and for the collapse prevention evaluation (MCE drifts).

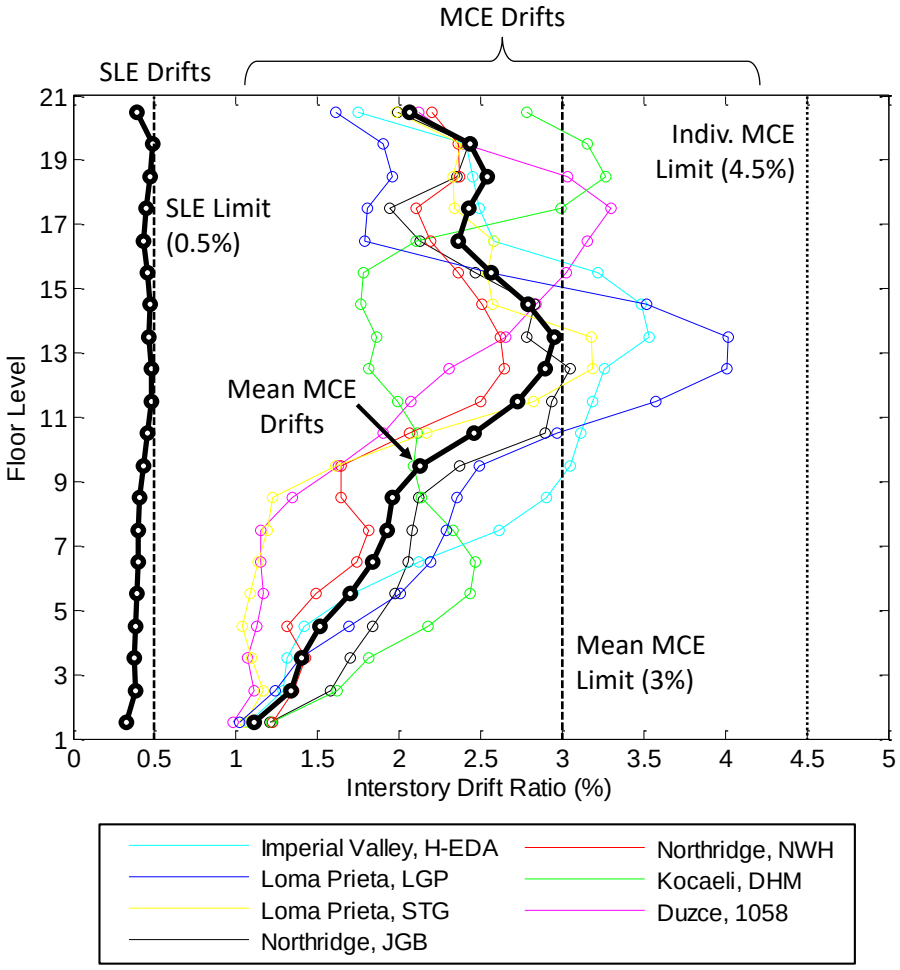

Figure 5.15: Maximum interstory drift ratios in the N-S direction of the 20PBD-LL design calculated for the service level evaluation (SLE drifts) and for the collapse prevention evaluation (MCE drifts).

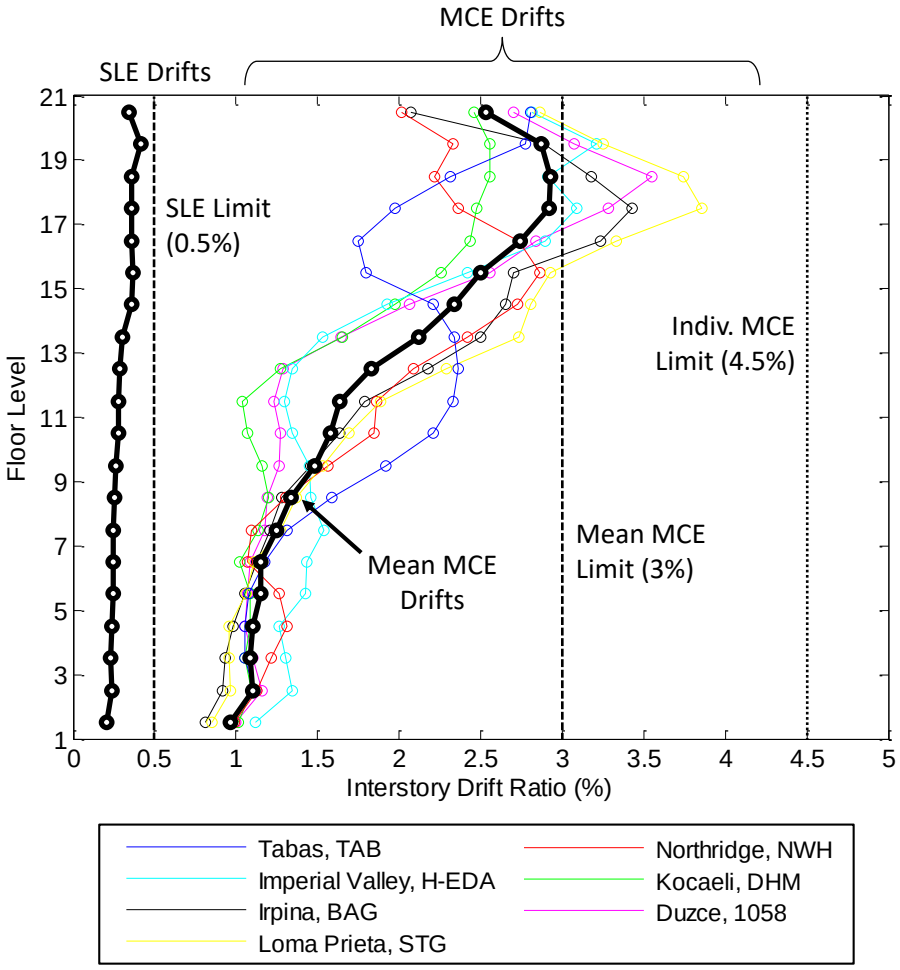

Figure 5.16: Maximum interstory drift ratios in the N-S direction of the 20PBD-WG design calculated for the service level evaluation (SLE drifts) and for the collapse prevention evaluation (MCE drifts).

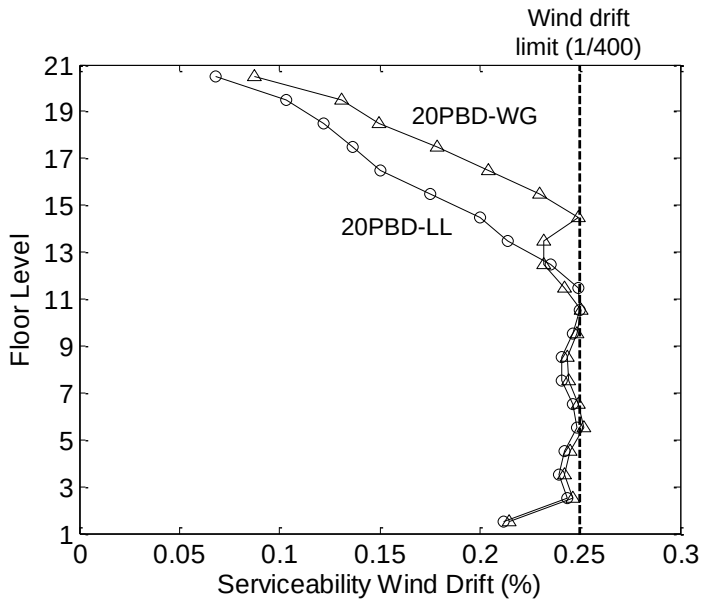

Figure 5.17: Serviceability drift ratios in the X direction calculated in response to wind loads for 20PBD-LL and 20PBD-WG designs.

Additional design information for all designs presented in this section are available in Section E.2 of Appendix E.

5.6 Building Models

For each of the ten designs described in Sections 5.4 and 5.5, Frame-2d models are created. These models have the same characteristics as the 9- and 20-story SMF models analyzed in Chapters 3 and 4 except properties for A992 steel are used for beams and columns (see Table 2.1). Brittle welds (i.e. B models) are not considered because all of these designs are based on design codes from well after the 1994 Northridge earthquake.

Pushover analysis is performed for each model using the procedure described in Section 2.2. Pushover curves for the six 9-story SMFs are shown in Figure 5.18(a) and pushover curves for the four 20-story SMFs are shown in Figure 5.18(b). The collapse mechanisms during pushover analysis are shown in Figure 5.19. Table 5.17 summarizes each model with its fundamental period T_1 and maximum base shear V_{max} calculated via pushover analysis. For the models corresponding to ELF and RSA designs, V_{max} is compared to V, $V_{strength}$ and V_{drift}, which are tabulated in Table 5.3.

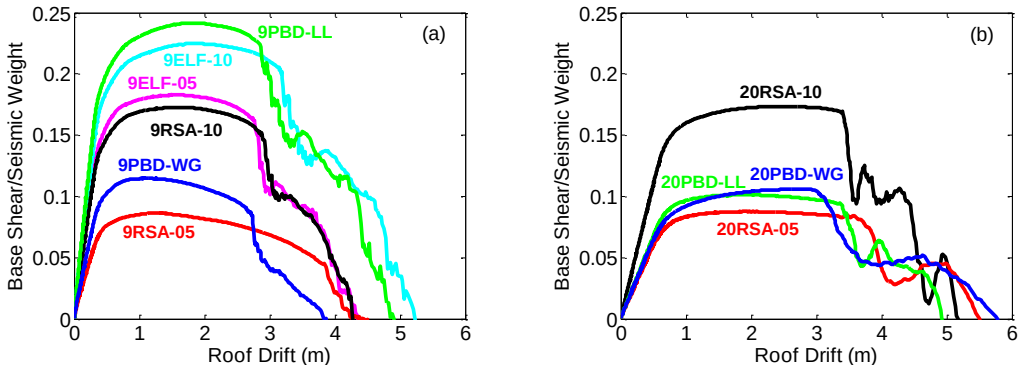

Figure 5.18: Pushover curves of Frame-2d models of (a) 9ELF-05, 9ELF-10, 9RSA-05, 9RSA-10, 9PBD-LL, and 9PBD-WG designs and of (b) 20RSA-05, 20RSA-10, 20PBD-LL, and 20PBD-WG designs.

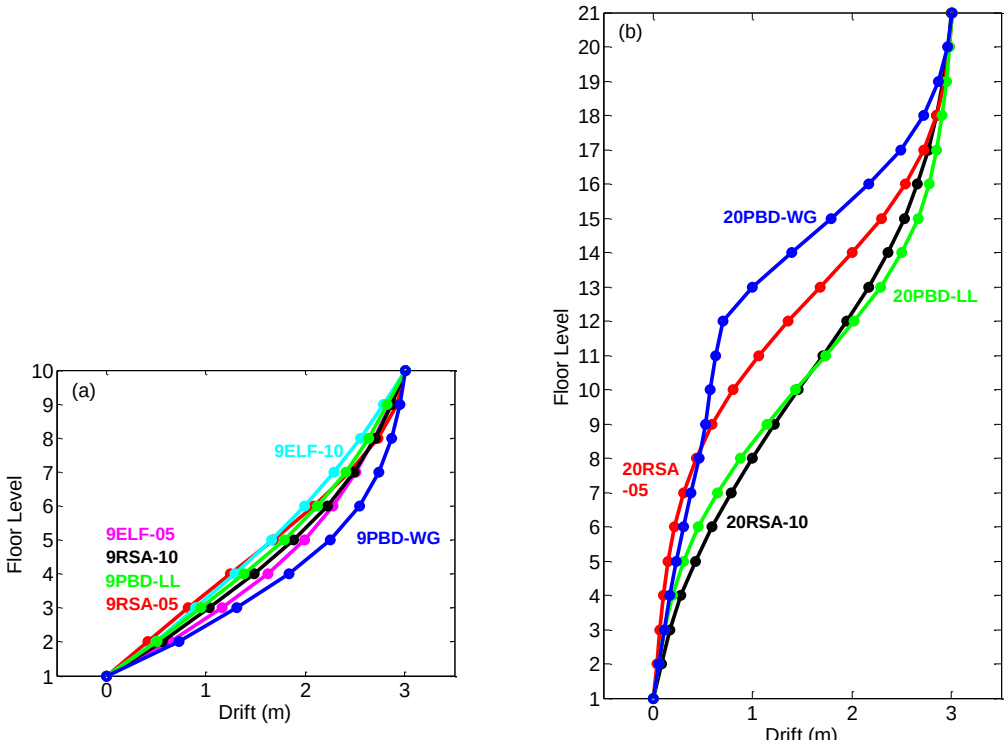

Figure 5.19: Drifts of each story during pushover analysis when the roof drift is 3 meters for Frame-2d models of the (a) 9ELF-05, 9ELF-10, 9RSA-05, 9RSA-10, 9PBD-LL, and 9PBD-WG designs and of the (b) 20RSA-05, 20RSA-10, 20PBD-LL, and 20PBD-WG designs.

Table 5.17: Basic properties (T_1 and V_{max}) of Frame-2d models. For the designs that follow ELF or RSA procedures, V_{max} is compared to V, $V_{strength}$, and V_{drift} from Table 5.3.

Design	T_1 (s)	V_{max}/W	V_{max}/V	$V_{max}/V_{strength}$	V_{max}/V_{drift}
9ELF-05	1.88	0.183	4.1	4.1	4.1
9ELF-10	1.76	0.225	3.2	3.2	4.3
9RSA-05	2.62	0.087	1.9	2.3	4.8
9RSA-10	1.93	0.173	2.5	2.9	3.9
9PBD-LL	1.67	0.242	–	–	–
9PBD-WG	2.30	0.115	–	–	–
20RSA-05	3.73	0.088	2.0	2.3	6.3
20RSA-10	2.77	0.174	2.5	2.9	4.0
20PBD-LL	3.49	0.101	–	–	–
20PBD-WG	3.55	0.106	–	–	–

There is significant variation in the ultimate pushover strength (V_{max}) of the 9-story SMFs, ranging from $V_{max}/W = 0.087$ for the 9RSA-05 design to $V_{max}/W = 0.242$ for the 9PBD-LL design, a difference of 2.8x. The 9PBD-LL model has an ultimate strength more than double that of the 9PBD-WG model, a difference that can be completely attributed to the differences in the SLE and MCE response spectra used for design. The long-period design spectral acceleration (S_{D1}) for the reference site increased about 16% from ASCE 7-05 to ASCE 7-10, which probably explains most of the difference in V_{max} between the 9ELF-05 and 9ELF-10 models, which vary by about 23%. This also contributed to the differences in V_{max} between the 9RSA-05 and 9RSA-10 models, but does not tell the full story, because V_{max} for the 9RSA-05 model is about half that of the 9RSA-10 model. Other than changes in design response spectra, the only considered difference in the design of the 9RSA-05 and 9RSA-10 SMFs is the stipulation in ASCE 7-10 (but not in ASCE 7-05) that drifts calculated using RSA be amplified according to the design base shear V. This is discussed in Section 5.4 and leads to the drastically different values of V_{drift} for the 9RSA-05 and 9RSA-10 designs seen in Table 5.3.

For the 20-story SMFs, V_{max} for the 20RSA-05, 20PBD-LL, and 20PBD-WG models are relatively similar, while that of the 20RSA-10 model is significantly larger than the others. The 20RSA-10 model has by far the largest V_{max} because it is the only 20-story SMF for which the design drifts need to be amplified according to the design base shear V. Interestingly, the 20RSA-10 and 9RSA-10 models have almost identical values of V_{max}/W. This can be attributed to the fact that the designs of both SMFs are controlled by drift and V_{drift}/W for both designs is identical (see

Table 5.3) because the calculation of V for both designs is governed by a lower limit independent of T, assigning both designs the same V_{drift}/W (and the same V_{strength}/W, though strength considerations do not govern design).

As discussed in Sections 5.4 and 5.5, the 20RSA-05, 20PBD-LL, and 20PBD-WG designs are governed by wind serviceability drift limits for the lower 10-15 stories. At the reference site, the calculated ASCE 7-05 wind loads are slightly lower than the ASCE 7-10 wind loads, which leads to the 20RSA-05 model having a lower ultimate strength than the 20PBD-LL and 20PBD-WG models, though by only about 15%. The 20PBD-LL and 20PBD-WG models are very similar in terms of T_1 and V_{max}, with the 20PBD-WG model actually having a larger ultimate strength even though the SLE and MCE spectra used in the 20PBD-LL design are significantly larger than those used in the 20PBD-WG design. This can, in part, be explained by the collapse mechanisms during pushover analysis, shown in Figure 5.19(b) for the 20-story models, which plots story drifts when the roof drift reaches 3 meters during pushover analysis. Recall from Section 5.5 that even though the bottom 10 stories of the 20PBD-LL and 20PBD-WG designs are identical because the lower stories are governed by wind, the upper stories of the 20PBD-LL design have larger sections than those of the 20PBD-WG design, since the design of the upper stories is governed by seismic drift limits. As such, deformation of the 20PBD-LL model during pushover analysis is spread over many stories spanning the lower-to-mid height (approximately stories 5-13) while deformation of the 20PBD-WG model during pushover analysis is concentrated in a few upper stories (approximately stories 12-16). So even though their pushover curves look very similar, the mechanisms by which the 20PBD-LL and 20PBD-WG models collapse during pushover analysis are very different.

One final observation from pushover analysis of these models is that for most of the ELF and RSA models, $V_{\text{max}}/V_{\text{drift}}$ is approximately equal to 4. It should not be surprising that these values are the same for most models because seismic drift limits controlled design in most cases. The only major outlier is the 20RSA-05 model, for which $V_{\text{max}}/V_{\text{drift}} = 6.3$, but this design was governed at most stories by serviceability wind drift limits. Another minor outlier is the 9RSA-05 model, for which $V_{\text{max}}/V_{\text{drift}} = 4.8$. This can possibly be attributed to the fact that the design of beams in the bottom two stories of the 9RSA-05 design is controlled by P-Δ stability requirements.

The value V_{max}/V, which represents overstrength, is typically reported for structural

models developed for research. Overstrength values calculated here in the range of 1.9 to 4.1 are consistent with the overstrength values calculated by other researchers for SMF models of similar heights (e.g. [9, 18, 19, 91]). The design overstrength factors (Ω_0) in both ASCE 7-05 and ASCE 7-10 for special SMFs are 3.0. Overstrength values greater than one occur for steel SMFs for a number of reasons. The two most important factors are probably the control of design by limits other than seismic strength (e.g. seismic or wind drift) and modeling considerations incorporated into the Frame-2d models that are not considered in design, such as using expected yield strength of steel instead of nominal and modeling strain hardening beyond the yield point.

In Section 5.7, collapse risk analysis is performed using the structural models presented in this section. To compare the results to pre-Northridge SMFs, the 9B-94, 9B-85, 9B-73wD, 9B-73noD, 20B-94, 20B-85, and 20B-73 models described in Section 2.2 and used in Chapter 3 are also analyzed. Compared to the models described in this section, the pre-Northridge SMF models have brittle welds and are designed based on the 1994, 1985, and 1973 UBC. Their pushover curves and deformation plots are shown in dashed lines in Figures 2.6 and 2.7. Their T_1 and V_{max} values are tabulated in Table 2.2.

5.7 Seismic Risk Assessment

The goal of seismic risk assessment for a given site, structural model, and EDP is to determine the probability of the structural model (located at the given site) experiencing response exceeding the EDP over some period of time. In this section, seismic risk assessment is performed for every SMF model described in Section 5.6 for the four EDPs described in Section 2.3 that can be interpreted as collapse limits depending on the application: MIDR = 0.03, MIDR = 0.06, MIDR = 0.1, and collapse. The reference site used for the design of these models (34.05° N, -118.26° E) is also used for seismic risk assessment.

The procedure for performing seismic risk assessment in this section is outlined as follows:

1. Perform probabilistic seismic hazard analysis (PSHA) at the reference site to compute seismic hazard curves for $Sa^{5\%}(T)$ for $T = 2$ and 3 seconds. Calculate the target $\varepsilon(T)$ for each period for 2%/50-year hazard.

2. Follow Method 2 of Haselton et al. [135] to calculate the fragility of each

building model to the four EDPs (MIDR = 0.03, MIDR = 0.06, MIDR = 0.1, and collapse) by performing incremental dynamic analysis with a set of ground motions. Calculate the fragility of each model with respect to $Sa^{5\%}(T)$ with and without adjustments for the target $\varepsilon(T)$ for $T = 2$ seconds for the 9-story SMFs and for $T = 3$ seconds for the 20-story SMFs.

3. Combine the results from PSHA for the reference site with the fragility for each model to compute the probability that each building model will exceed each EDP over a period of 50 years. For each EDP and building model, the risk is calculated with and without adjustments for the target $\varepsilon(T)$ and the results are compared.

Method 2 of Haselton et al. [135] recommends using T_1 as the spectral period when performing PSHA and calculating the model's fragility. However, in this study, this would require performing a separate PSHA for all 17 considered SMF models. In lieu of calculating a separate hazard curve for every model, a hazard curve is calculated for Sa with $T = 2$ seconds for use with the 9-story SMFs and a different hazard curve is calculated for Sa with $T = 3$ seconds for use with the 20-story SMFs. This approximation is common in studies for which seismic risk is calculated for many different building models (e.g. [48]). Spectral periods of 2 and 3 seconds are chosen for the 9- and 20-story SMFs, respectively, because they are the closest integer periods to the average T_1 of the 9- and 20-story SMF models, respectively. The calculated risk values vary slightly with the spectral period, so for completeness, results for all models are shown in Appendix F for spectral periods of 2, 3, 4, and 5 seconds.

The aforementioned steps and results are detailed in the following sub-sections.

Probabilistic Seismic Hazard Analysis (PSHA)

Probabilistic seismic hazard analysis (PSHA) is performed for the reference site (34.05° N, -118.26° E) using OpenSHA [129]. Properties for the site are similar to those assumed in the disaggregation analysis presented in Section 5.5. V_{S30} = 350 m/s is assumed for the site and the Mean UCERF3 model [130] with default settings is specified in OpenSHA. To account for differences in published GMPEs (i.e. epistemic uncertainty), hazard curves are calculated with four different GMPEs developed as part of the NGA-West1 project, denoted AS08 [122], BA08 [40], CB08 [123], and CY08 [124]. Additional site properties $V_{1.0}$, the depth to V_S = 1.0 km/s and $V_{2.5}$, the

depth to V_S = 2.5 km/s, are assumed to be 350 and 2100 meters, respectively. These values are calculated via the SCEC UGMS online tool [132].

Using these site properties and GMPEs, the seismic hazard curves shown in Figure 5.20 are generated for $Sa(T)$ with T = 2, 3, 4, and 5 seconds. The mean hazard curves calculated with the four GMPEs are used for risk assessment. Each seismic hazard curve plots the probability of exceeding the given spectral ordinate over a time period of 50 years. The recurrence interval of 50 years is somewhat arbitrary, but is chosen here so that the results of risk assessment can be compared to the ASCE 7-10 performance goal of a less than 1% probability of collapse in 50 years for typical new structures.

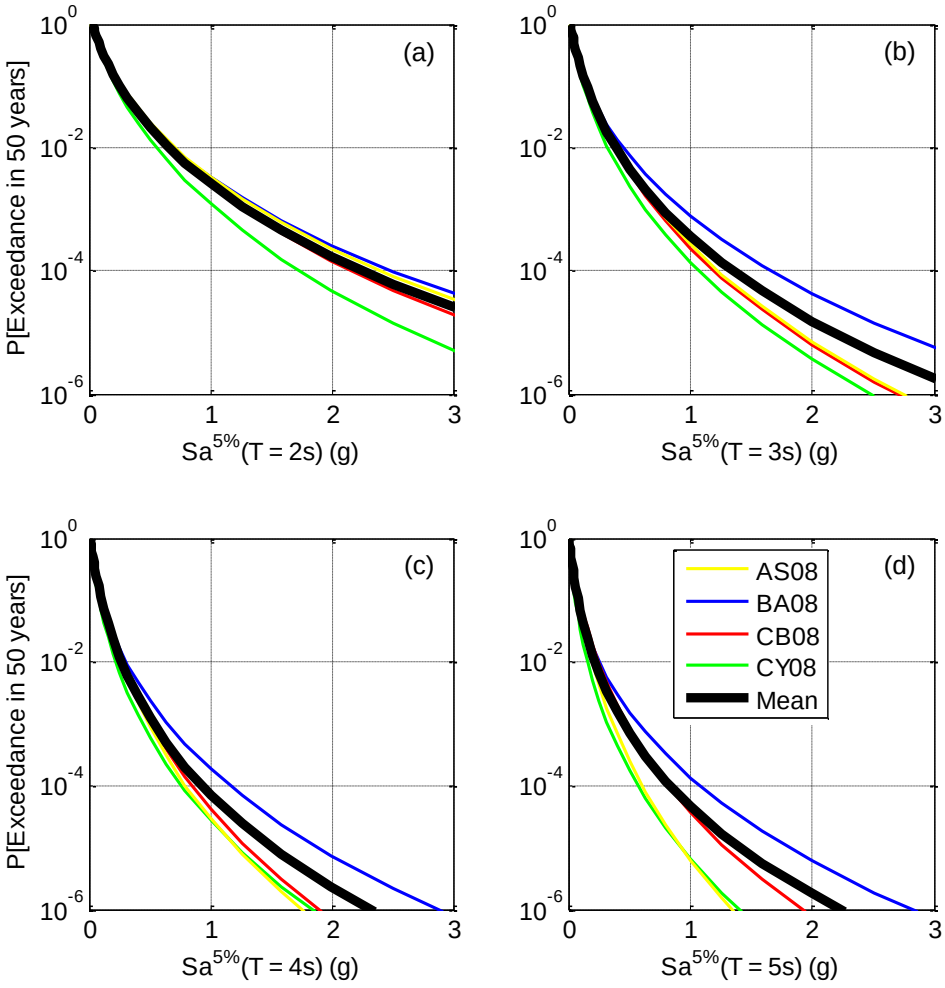

Figure 5.20: Seismic hazard curves for (a) $Sa^{5\%}(2s)$, (b) $Sa^{5\%}(3s)$, (c) $Sa^{5\%}(4s)$, and (d) $Sa^{5\%}(5s)$ calculated using OpenSHA [129] with estimated properties of the reference site (34.05° N, -118.26° E.)

Fragility Curves

The first step of Method 2 of Haselton et al. [135] is to select a set of "far-field" (defined as $R_{JB} > 10$ km) ground motions to be used as input ground motions for incremental dynamic analysis (IDA). In a case study, Haselton et al. use a set of 78 records, from which a smaller subset of 44 ground motions is used in the ATC-63 project [45] for IDA. This set of 44 ground motions is used here and is a subset of the 50 pairs of ground motions used in Chapter 3 and described in Section 3.2. The 5%-damped response spectra of these 44 ground motions are shown in Figure 5.21.

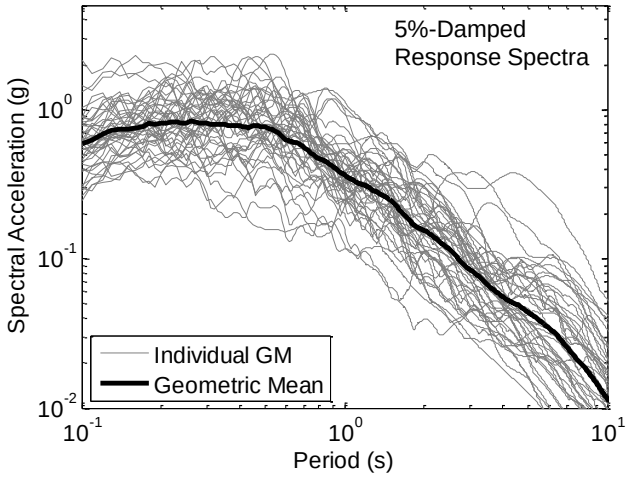

Figure 5.21: 5%-damped response spectra of the 44 "far field" ($R_{JB} > 10$ km) ground motion records selected for the ATC-63 project [45] that are used in this study as input ground motions for IDA.

The second step of Method 2 of Haselton et al. [135] is to perform IDA for each building model with the set of ground motions in order to calculate the fragility curve for all the considered EDPs for each building model. For each ground motion and building model, IDA is performed for this study with a scale factor increment of 0.1. For each analysis, the maximum interstory drift ratio (MIDR) is recorded. IDA is performed for each ground motion and building model until the model experiences collapse or until the ground motion is amplified by 15x. In the vast majority of cases, collapse occurs first. As described in Section 2.3, for each building model, fragility curves are generated with respect to four EDPs: MIDR = 0.03, MIDR = 0.06, MIDR = 0.1, and collapse. For each building model and EDP, a set of *Sa* values representing the amplified ground motions that induce the EDP in the model is generated from IDA. From these *Sa* values, the geometric mean ($\mu_{\ln}$) and lognormal

standard deviation ($\sigma_{\ln}$) are calculated. From $\mu_{\ln}$ and $\sigma_{\ln}$, the fragility curve can be calculated as the cumulative distribution function:

$$P[EDP|IM] = \frac{1}{2} + \frac{1}{2} \cdot \text{erf}\left[\frac{\ln(IM) - \ln(\mu_{\ln})}{\sqrt{2} \cdot \sigma_{\ln}}\right], \tag{5.23}$$

where erf[] is the error function. The corresponding probability distribution function is the derivative of the cumulative distribution function and is given by

$$G[EDP|IM] = \frac{1}{\sqrt{2\pi} \cdot IM \cdot \sigma_{\ln}} \cdot \exp\left[-\frac{(\ln(IM) - \ln(\mu_{\ln}))^2}{2{\sigma_{\ln}}^2}\right]. \tag{5.24}$$

Note that, assuming a lognormal distribution, $\mu_{\ln}$ and $\sigma_{\ln}$ completely characterize the fragility curve. These fragility curves are shown in Figure 5.22 for the 9-story SMFs designed in Sections 5.4 and 5.5 with MIDR = 0.06 and $Sa^{5\%}(2s)$.

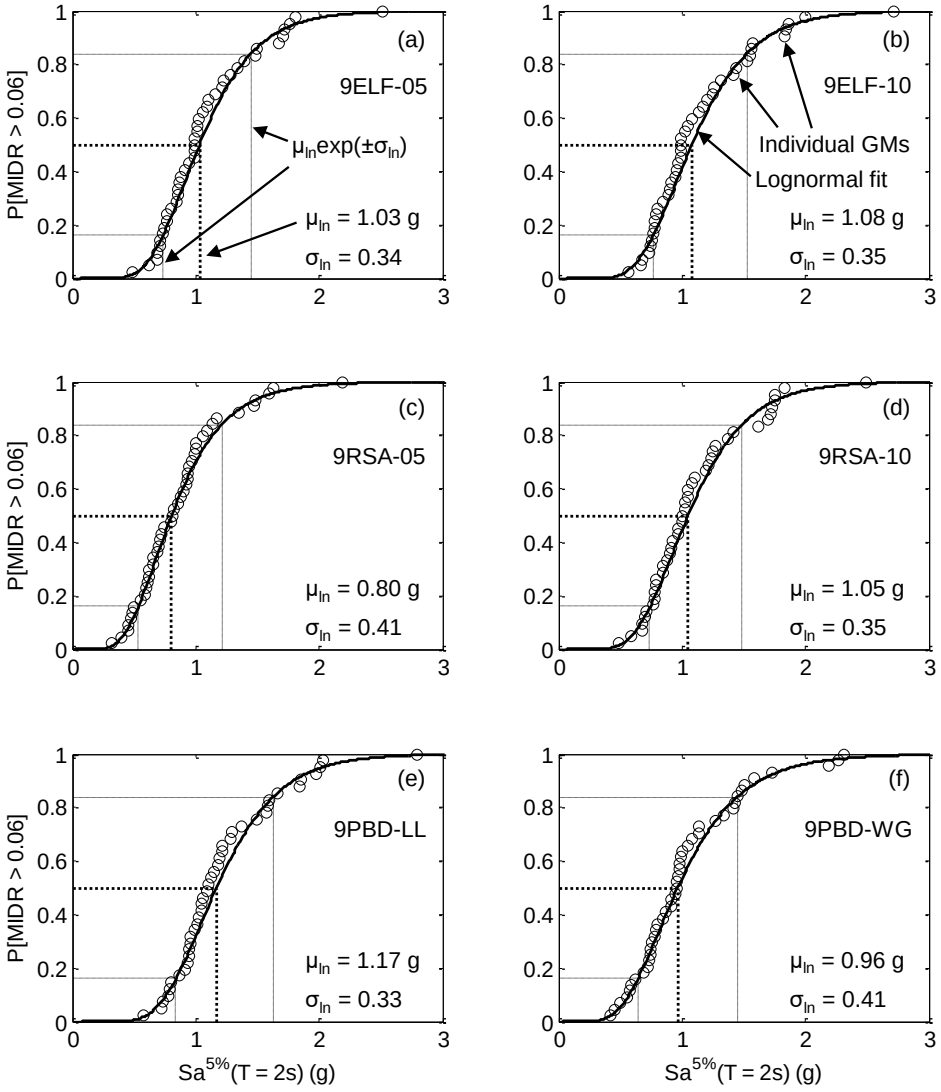

Figure 5.22: Fragility curves of the 9-story post-Northridge SMFs with MIDR = 0.06 as the EDP and $Sa^{5\%}(2s)$ as the IM.

The values of $\mu_{\ln}$ and $\sigma_{\ln}$ are computed for the six 9-story post-Northridge SMFs and the four 9-story pre-Northridge SMFs with four considered EDPs (MIDR = 0.03, MIDR = 0.06, MIDR = 0.1, and collapse) and $Sa^{5\%}(2s)$. These values are presented in Table 5.18. The same values are computed for the four 20-story post-Northridge SMFs and the three 20-story pre-Northridge SMFs with four considered EDPs (MIDR = 0.03, MIDR = 0.06, MIDR = 0.1, and collapse) and $Sa^{5\%}(3s)$. These values are presented in Table 5.19.

Table 5.18: The geometric mean ($\mu_{\ln}$) and lognormal standard deviation ($\sigma_{\ln}$) values of $Sa^{5\%}(2s)$ calculated for four different EDPs (MIDR = 0.03, MIDR = 0.06, MIDR = 0.1, and collapse) for the 9-story SMFs.

	Lognormal statistics of $Sa^{5\%}(T = 2s)$ for fragility curves							
	MIDR = 0.03		MIDR = 0.06		MIDR = 0.1		Collapse	
Model	$\mu_{\ln}(g)$	$\sigma_{\ln}$	$\mu_{\ln}(g)$	$\sigma_{\ln}$	$\mu_{\ln}(g)$	$\sigma_{\ln}$	$\mu_{\ln}(g)$	$\sigma_{\ln}$
9ELF-05	0.46	0.41	1.03	0.34	1.50	0.40	1.72	0.42
9ELF-10	0.47	0.44	1.08	0.35	1.63	0.39	1.89	0.38
9RSA-05	0.36	0.40	0.80	0.41	1.14	0.46	1.24	0.47
9RSA-10	0.47	0.41	1.05	0.35	1.55	0.43	1.75	0.44
9PBD-LL	0.54	0.38	1.17	0.33	1.69	0.39	1.91	0.39
9PBD-WG	0.42	0.37	0.96	0.41	1.31	0.46	1.46	0.46
9B-94	0.36	0.31	0.62	0.36	0.71	0.40	0.72	0.41
9B-85	0.36	0.35	0.60	0.44	0.68	0.46	0.71	0.47
9B-73wD	0.34	0.33	0.57	0.44	0.62	0.46	0.63	0.48
9B-73noD	0.36	0.35	0.59	0.44	0.63	0.46	0.66	0.46

Table 5.19: The geometric mean ($\mu_{\ln}$) and lognormal standard deviation ($\sigma_{\ln}$) values of $Sa^{5\%}(3s)$ calculated for four different EDPs (MIDR = 0.03, MIDR = 0.06, MIDR = 0.1, and collapse) for the 20-story SMFs.

	Lognormal statistics of $Sa^{5\%}(T = 3s)$ for fragility curves							
	MIDR = 0.03		MIDR = 0.06		MIDR = 0.1		Collapse	
Model	$\mu_{\ln}(g)$	$\sigma_{\ln}$	$\mu_{\ln}(g)$	$\sigma_{\ln}$	$\mu_{\ln}(g)$	$\sigma_{\ln}$	$\mu_{\ln}(g)$	$\sigma_{\ln}$
20RSA-05	0.31	0.35	0.65	0.42	0.78	0.43	0.80	0.43
20RSA-10	0.40	0.45	0.85	0.44	0.96	0.42	0.98	0.42
20PBD-LL	0.36	0.38	0.67	0.44	0.79	0.41	0.82	0.41
20PBD-WG	0.29	0.42	0.68	0.44	0.81	0.42	0.83	0.41
20B-94	0.22	0.39	0.33	0.45	0.34	0.43	0.36	0.41
20B-85	0.25	0.34	0.38	0.40	0.39	0.38	0.42	0.37
20B-73	0.16	0.29	0.36	0.45	0.43	0.43	0.45	0.43

In both tables, the pre-Northridge SMFs generally have much lower values of $\mu_{\ln}$ than the post-Northridge SMFs that are modeled in Frame-2d with perfect connections. This is not surprising, as this means the EDPs can be induced in the pre-Northridge models with less severe shaking than in the post-Northridge models. Furthermore, the values of $\mu_{\ln}$ for MIDR = 0.06, MIDR = 0.1, and collapse for the pre-Northridge models are very similar for a given model. This reflects the lack of ductility of the pre-Northridge models. That is, if a given level of shaking induces MIDR = 0.06 in a pre-Northridge model, it does not take a much higher level of shaking to induce

MIDR = 0.1 or collapse. This is particularly true for the 20-story pre-Northridge models.

Of the post-Northridge models, there is significant variation in the values of $\mu_{\ln}$ depending on the design. $\mu_{\ln}$ of the 9ELF-10 and 9PBD-LL models are 40%-50% greater than that of the 9RSA-05 model, depending on the EDP. $\mu_{\ln}$ of the 20RSA-10 model is up to 20% greater than $\mu_{\ln}$ of the other post-Northridge models. That the 9ELF-10, 9PBD-LL, and 20RSA-10 models are relatively "strong" (i.e. have larger collapse capacities than the other models) is not surprising, as these three models had the largest values of $V_{\max}/W$ as calculated via pushover analysis in Section 5.6.

As might be expected, the 20-story post-Northridge models appear to have less "global ductility" than the 9-story post-Northridge models. This can be seen in the difference in $\mu_{\ln}$ at MIDR = 0.1 and at collapse. For the 20-story SMFs, $\mu_{\ln}$ is nearly the same in both cases, indicating that if MIDR = 0.1 is induced in one of the post-Northridge SMFs, it does not take much more shaking to induce collapse. In comparison, there appears to be more capacity in the 9-story models to withstand drift ratios greater than 0.1 without collapsing, as indicated by the relatively large differences in $\mu_{\ln}$ at MIDR = 0.1 and at collapse.

There do not seem to be any noteworthy trends regarding $\sigma_{\ln}$. Regardless of the building model and EDP, $\sigma_{\ln}$ tends to be in the range of 0.35-0.5, with few exceptions.

The third step of Method 2 of Haselton et al. [135] is to determine the $\varepsilon(T)$ adjustment necessary for each building model and EDP. They suggest implementing linear regression between $\varepsilon(T)$ and the natural logarithm of the values of $Sa^{5\%}(T)$ at which the EDP is induced in the building model, here denoted $Sa^{5\%}_{EDP}(T)$. This regression can be expressed as

$$\ln\left[Sa^{5\%}_{EDP}(T)\right] = \beta_0 + \beta_1 \cdot \varepsilon(T) \tag{5.25}$$

or

$$Sa^{5\%}_{EDP}(T) = \exp\left[\beta_0 + \beta_1 \cdot \varepsilon(T)\right], \tag{5.26}$$

where β_0 and β_1 are the regression coefficients, specific to each building model and EDP pair. This is done by calculating $\varepsilon(T)$ for each ground motion according to BA08 [40] for T = 2 and 3 seconds.

The fourth step of Method 2 of Haselton et al. [135] is to calculate adjusted values of $\mu_{\ln}$ and $\sigma_{\ln}$, denoted $\mu^{\text{adj}}_{\ln}$ and $\sigma^{\text{adj}}_{\ln}$, for each building model and EDP according to the $\varepsilon(T)$ adjustment regression. This requires specifying a target $\varepsilon(T)$, $\varepsilon^*(T)$, that

represents the expected $\varepsilon(T)$ at the reference site. For regression, $\varepsilon(T)$ is calculated using BA08, so $\varepsilon^*(T)$ for the reference site is also calculated using BA08. This is done with OpenSHA using the same reference site parameters as in PSHA. From disaggregation for 2%/50-year hazard, the mean $\varepsilon(2s)$ and the mean $\varepsilon(3s)$ are both found to be equal to 1.24. Thus, for every considered building model and EDP, regression is performed with respect to $\varepsilon(T)$ and the regressed fit is evaulated at $\varepsilon^*(T) = 1.24$ to compute $\mu_{\ln}^{\text{adj}}$. $\sigma_{\ln}^{\text{adj}}$ is calculated as the residual between the fit and the data points.

Steps three and four of Method 2 of Haselton et al. [135] are shown visually in Figure 5.23 for the six 9-story SMFs designed in Sections 5.4 and 5.5 with MIDR = 0.06 and $Sa^{5\%}(2s)$. The exponential fits are calculated according to Equation 5.26.

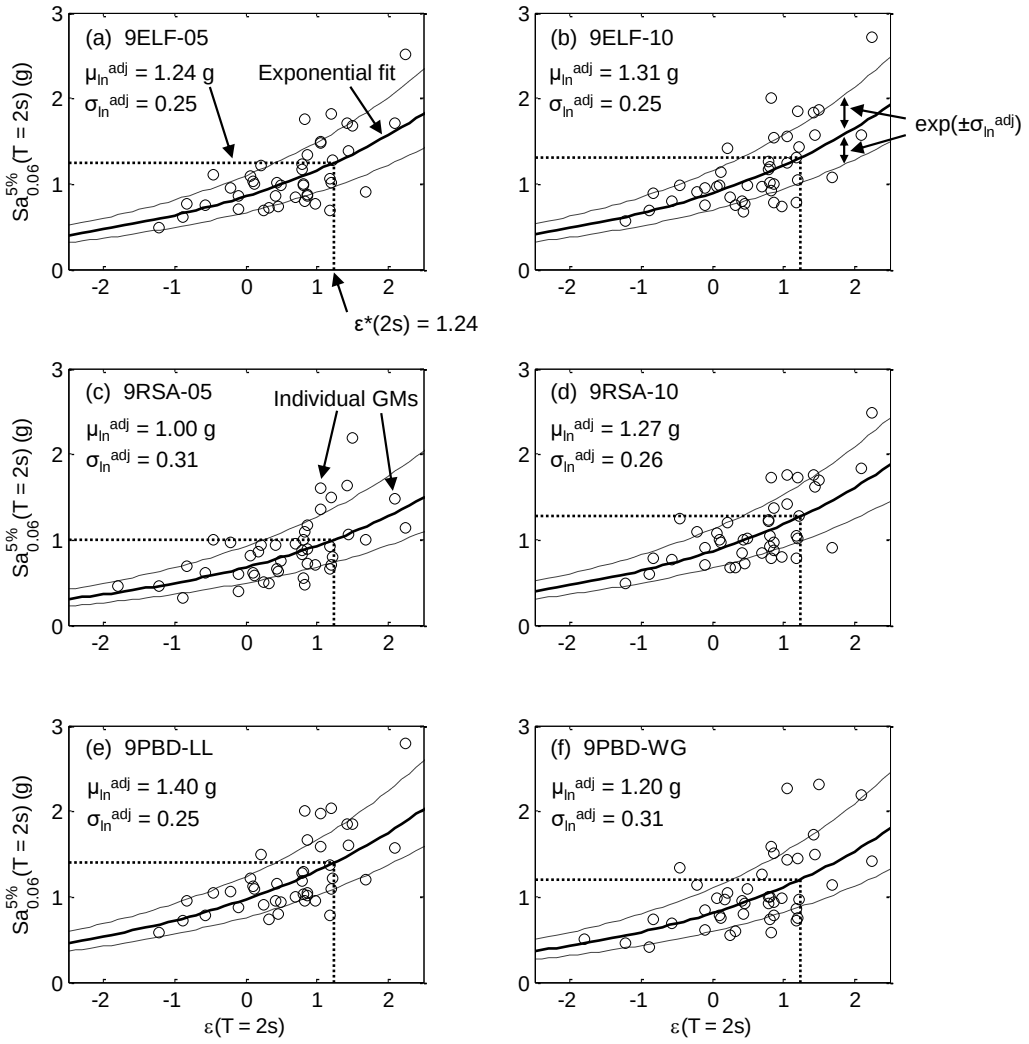

Figure 5.23: Adjustments of $\mu_{\ln}$ and $\sigma_{\ln}$ to $\mu_{\ln}^{\text{adj}}$ and $\sigma_{\ln}^{\text{adj}}$ to account for the target $\varepsilon^*(2s) = 1.24$ for the 9-story post-Northridge SMFs with MIDR = 0.06 as the EDP and $Sa^{5\%}(2s)$ as the IM. $Sa_{0.06}^{5\%}(2s)$ for a ground motion and building model is the value of $Sa^{5\%}(2s)$ that the ground motion has to be amplified to in order to induce MIDR = 0.06 in the building model.

Following the aforementioned procedure, the values of $\mu_{\ln}^{\text{adj}}$ and $\sigma_{\ln}^{\text{adj}}$ are computed for the six 9-story post-Northridge SMFs and the four 9-story pre-Northridge SMFs with four considered EDPs (MIDR = 0.03, MIDR = 0.06, MIDR = 0.1, and collapse) and $Sa^{5\%}(2s)$. These values are presented in Table 5.18. The same values are computed for the four 20-story post-Northridge SMFs and the three pre-Northidge 20-story SMFs with four considered EDPs (MIDR = 0.03, MIDR = 0.06, MIDR = 0.1, and collapse) and $Sa^{5\%}(3s)$. These values are presented in Table 5.19.

Table 5.20: The $\varepsilon(2s)$-adjusted geometric mean ($\mu_{\ln}^{\text{adj}}$) and lognormal standard deviation ($\sigma_{\ln}^{\text{adj}}$) values of $Sa^{5\%}(2s)$ calculated for four different EDPs (MIDR = 0.03, MIDR = 0.06, MIDR = 0.1, and collapse) for the 9-story SMFs.

	ε-adjusted lognormal statistics of $Sa^{5\%}(T = 2s)$ for fragility curves							
	MIDR = 0.03		MIDR = 0.06		MIDR = 0.1		Collapse	
Model	$\mu_{\ln}^{\text{adj}}(g)$	$\sigma_{\ln}^{\text{adj}}$	$\mu_{\ln}^{\text{adj}}(g)$	$\sigma_{\ln}^{\text{adj}}$	$\mu_{\ln}^{\text{adj}}(g)$	$\sigma_{\ln}^{\text{adj}}$	$\mu_{\ln}^{\text{adj}}(g)$	$\sigma_{\ln}^{\text{adj}}$
9ELF-05	0.56	0.32	1.24	0.25	1.83	0.28	2.06	0.31
9ELF-10	0.59	0.33	1.31	0.25	1.96	0.27	2.25	0.28
9RSA-05	0.45	0.29	1.00	0.31	1.42	0.37	1.55	0.37
9RSA-10	0.58	0.31	1.27	0.26	1.94	0.30	2.14	0.33
9PBD-LL	0.65	0.30	1.40	0.25	2.01	0.27	2.24	0.29
9PBD-WG	0.51	0.29	1.20	0.31	1.67	0.34	1.81	0.36
9B-94	0.41	0.26	0.75	0.28	0.89	0.29	0.91	0.29
9B-85	0.43	0.27	0.78	0.31	0.90	0.31	0.93	0.32
9B-73wD	0.40	0.27	0.72	0.32	0.79	0.35	0.84	0.34
9B-73noD	0.43	0.27	0.73	0.34	0.80	0.36	0.83	0.36

Table 5.21: The $\varepsilon(3s)$-adjusted geometric mean ($\mu_{\ln}^{\text{adj}}$) and lognormal standard deviation ($\sigma_{\ln}^{\text{adj}}$) values of $Sa^{5\%}(3s)$ calculated for four different EDPs (MIDR = 0.03, MIDR = 0.06, MIDR = 0.1, and collapse) for the 20-story SMFs.

	ε-adjusted lognormal statistics of $Sa^{5\%}(T = 3s)$ for fragility curves							
	MIDR = 0.03		MIDR = 0.06		MIDR = 0.1		Collapse	
Model	$\mu_{\ln}^{\text{adj}}(g)$	$\sigma_{\ln}^{\text{adj}}$	$\mu_{\ln}^{\text{adj}}(g)$	$\sigma_{\ln}^{\text{adj}}$	$\mu_{\ln}^{\text{adj}}(g)$	$\sigma_{\ln}^{\text{adj}}$	$\mu_{\ln}^{\text{adj}}(g)$	$\sigma_{\ln}^{\text{adj}}$
20RSA-05	0.37	0.32	0.86	0.31	1.00	0.34	1.05	0.33
20RSA-10	0.52	0.37	1.13	0.30	1.23	0.31	1.30	0.31
20PBD-LL	0.47	0.28	0.90	0.31	1.01	0.31	1.05	0.31
20PBD-WG	0.34	0.38	0.91	0.31	1.04	0.31	1.07	0.30
20B-94	0.26	0.34	0.43	0.37	0.44	0.35	0.45	0.34
20B-85	0.28	0.31	0.47	0.33	0.49	0.32	0.51	0.32
20B-73	0.17	0.29	0.40	0.43	0.53	0.37	0.57	0.36

In every case, $\mu_{\ln}^{\text{adj}}$ is larger than $\mu_{\ln}$ and $\sigma_{\ln}^{\text{adj}}$ is smaller than $\sigma_{\ln}$. The former observation is because $\varepsilon^*(T)$ is greater than the average $\varepsilon(T)$ for the ground motions in the input set and for every building model and EDP, $Sa_{EDP}^{5\%}(T)$ increases with $\varepsilon(T)$. This is a common result, as noted by Haselton et al. [135], and is due to the fact that the hazard of strong shaking (e.g. 2%/5-year) is usually dominated by shaking with positive $\varepsilon(T)$. Most ground motion records with positive $\varepsilon(T)$ have a "peak" in the response spectrum at T [34], so ground motions with positive $\varepsilon(T)$ tend to be less destructive than ground motions with the same $Sa^{5\%}(T)$ but with negative $\varepsilon(T)$.

It is also not surprising that $\sigma_{\ln}^{\text{adj}}$ is smaller than $\sigma_{\ln}$. This could be expected because, as shown in Chapter 3, $Sa^{5\%}(T)$ as an IM for highly nonlinear response is not sufficient with respect to $\varepsilon(T)$, so some of the variation in $Sa_{EDP}^{5\%}(T)$ can be directly attributed to the correlation with $\varepsilon(T)$. Removing this bias reduces the overall statistical variation of $Sa_{EDP}^{5\%}(T)$ and this manifests itself in the reduction of $\sigma_{\ln}$ to $\sigma_{\ln}^{\text{adj}}$.

Collapse Risk Calculations

Using the results from PSHA and the fragility curves for each building model and EDP, the seismic risk for each model and EDP can be assessed by computing the integral presented earlier in this dissertation in Equation 3.1, which is reproduced here, assuming that the IM is a non-negative scalar:

$$\lambda[EDP] = \int_0^\infty G[EDP|IM]\lambda[IM]dIM. \tag{5.27}$$

In this equation, $\lambda[EDP]$ is the mean frequency of a structure's response exceeding the EDP over some time interval (here 50 years), $G[EDP|IM]$ is the probability density function for a structure that relates the EDP to the IM, and $\lambda[IM]$ is the mean frequency of the IM being exceeded at the site of the structure over some time interval (here 50 years). In this study, for a given building model and EDP, $G[EDP|IM]$ is estimated as a lognormal distribution and is defined by $\mu_{\ln}$ and $\sigma_{\ln}$ (or $\mu_{\ln}^{\text{adj}}$ and $\sigma_{\ln}^{\text{adj}}$) according to Equation 5.24. $\lambda[IM]$ is equal to the hazard curves plotted in Figure 5.20. In this study, the mean hazard curve (among four GMPEs) is used. The hazard curve for $Sa^{5\%}(2s)$ (Figure 5.20(a)) is used for the 9-story models and the hazard curve for $Sa^{5\%}(3s)$ (Figure 5.20(b)) is used for the 20-story models.

The process of calculating risk is shown in Figures 5.24 (linear scale) and 5.25 (logarithmic scale) for the 9ELF-05 model with MIDR=0.06 as the EDP. In this calculation, $\mu_{\ln}^{\text{adj}}$ and $\sigma_{\ln}^{\text{adj}}$ are used to define $G[EDP|IM]$ to adjust for $\varepsilon(T = 2s)$. In this example, the IM is $Sa^{5\%}(2s)$. Shown in Figure 5.24(a) (and Figure 5.25(a)) are $G[EDP|IM]$ and $\lambda[IM]$ and shown in Figure 5.24(b) (and Figure 5.25(b)) is the product of $G[EDP|IM]$ and $\lambda[IM]$. Per Equation 5.27, the risk is calculated as the integral of this product of $G[EDP|IM]$ and $\lambda[IM]$.

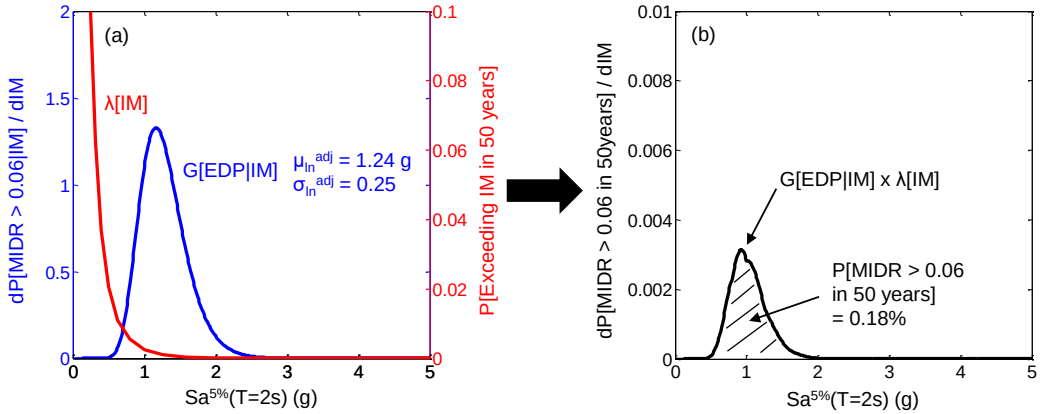

Figure 5.24: Visualization on a linear scale of how risk is calculated according to Equation 5.27. In this example, the $\varepsilon(2s)$-adjusted risk of exceeding MIDR = 0.06 is calculated for the 9ELF-05 model and the IM is $Sa^{5\%}(2s)$.

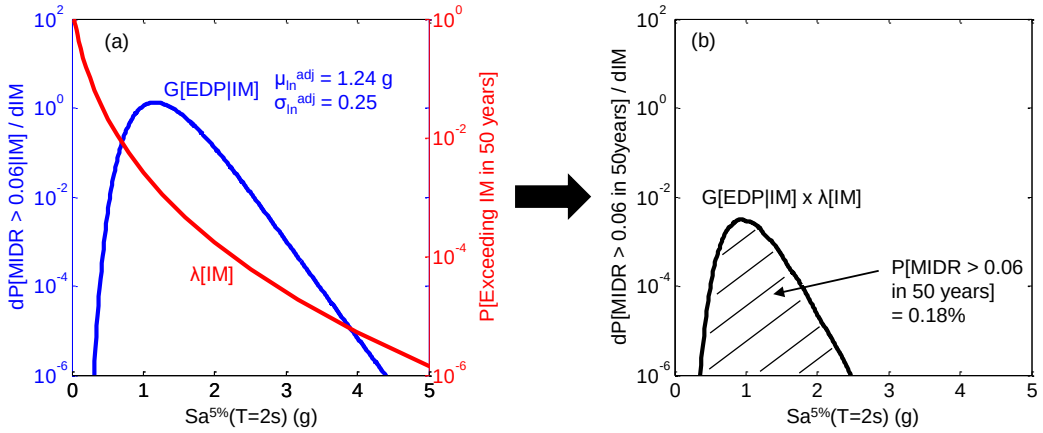

Figure 5.25: Visualization on a logarithmic scale of how risk is calculated according to Equation 5.27. Other than the logarithmic scale, this is the same as Figure 5.24.

The probability of exceeding each of the four considered EDPs is calculated for every building model in this manner. For comparison, this analysis is done with and without accounting for $\varepsilon(T)$. The results are shown for the 9-story models in Table 5.22 and for the 20-story models in Table 5.23. For a given building model and EDP, the column header "$Sa(2s)$" or "$Sa(3s)$" denotes that the risk is calculated using $Sa(2s)$ or $Sa(3s)$ as the IM without consideration for $\varepsilon(T)$. The column header "$+\varepsilon$" denotes that the risk is calculated by adjusting for $\varepsilon(2s)$ for the 9-story models or $\varepsilon(3s)$ for the 20-story models. The results for MIDR = 0.03 and collapse are shown

visually in Figures 5.26-5.29 and compared to the ASCE 7-10 collapse risk target of 1% in 50 years for new buildings.

Table 5.22: Computed risk with and without adjustments for $\varepsilon(2s)$ of the 9-story SMFs exceeding four EDPs (MIDR = 0.03, MIDR = 0.06, MIDR = 0.1, and collapse).

	Exceedance probability (%) in 50 years							
	MIDR = 0.03		MIDR = 0.06		MIDR = 0.1		Collapse	
Model	$Sa(2s)$	$+\varepsilon$	$Sa(2s)$	$+\varepsilon$	$Sa(2s)$	$+\varepsilon$	$Sa(2s)$	$+\varepsilon$
9ELF-05	3.99	2.15	0.42	0.18	0.16	0.05	0.11	0.04
9ELF-10	3.94	1.89	0.37	0.15	0.11	0.04	0.06	0.02
9RSA-05	6.43	3.41	1.02	0.43	0.45	0.17	0.36	0.12
9RSA-10	3.82	1.93	0.41	0.17	0.15	0.04	0.11	0.03
9PBD-LL	2.64	1.39	0.28	0.12	0.10	0.03	0.07	0.02
9PBD-WG	4.48	2.57	0.62	0.24	0.29	0.09	0.21	0.07
9B-94	5.88	4.09	1.79	0.94	1.40	0.58	1.33	0.54
9B-85	5.91	3.72	2.30	0.88	1.76	0.58	1.62	0.55
9B-73wD	6.55	4.38	2.59	1.10	2.24	0.92	2.17	0.75
9B-73noD	6.05	3.72	2.39	1.14	2.08	0.93	1.88	0.81

Table 5.23: Computed risk with and without adjustments for $\varepsilon(3s)$ of the 9-story SMFs exceeding four EDPs (MIDR = 0.03, MIDR = 0.06, MIDR = 0.1, and collapse).

	Exceedance probability (%) in 50 years							
	MIDR = 0.03		MIDR = 0.06		MIDR = 0.1		Collapse	
Model	$Sa(3s)$	$+\varepsilon$	$Sa(3s)$	$+\varepsilon$	$Sa(3s)$	$+\varepsilon$	$Sa(3s)$	$+\varepsilon$
20RSA-05	2.73	1.74	0.45	0.13	0.27	0.08	0.25	0.07
20RSA-10	1.80	0.73	0.21	0.05	0.13	0.03	0.13	0.03
20PBD-LL	2.02	0.82	0.45	0.11	0.24	0.07	0.21	0.06
20PBD-WG	3.53	2.29	0.42	0.10	0.23	0.06	0.21	0.06
20B-94	6.40	4.06	2.85	1.29	2.48	1.14	2.13	1.03
20B-85	4.37	3.23	1.85	0.89	1.64	0.80	1.35	0.71
20B-73	9.93	9.84	2.38	1.77	1.51	0.71	1.28	0.55

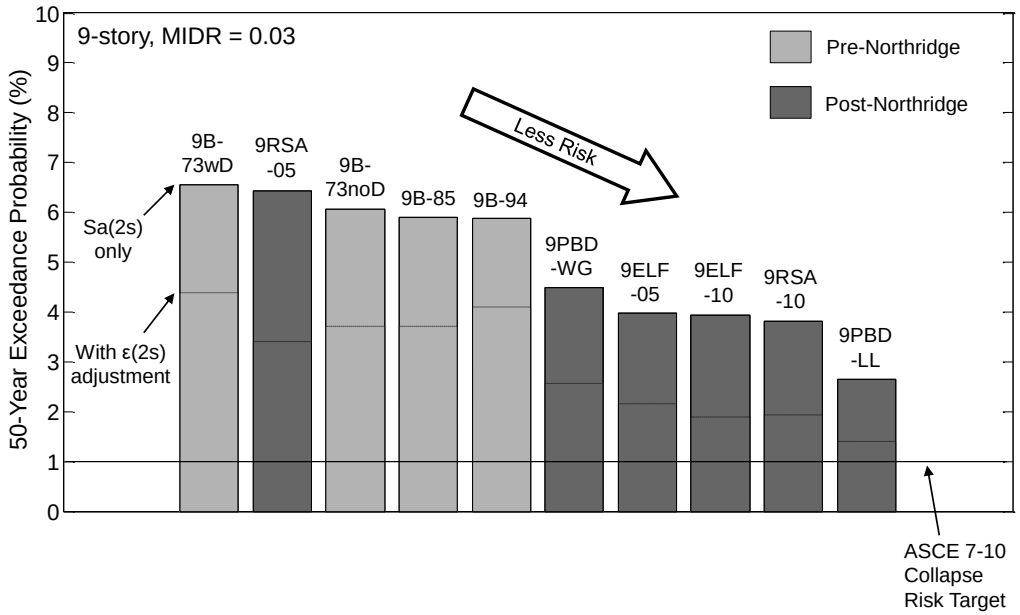

Figure 5.26: Computed risk with and without adjustments for $\varepsilon(2s)$ of the 9-story SMFs exceeding MIDR = 0.03.

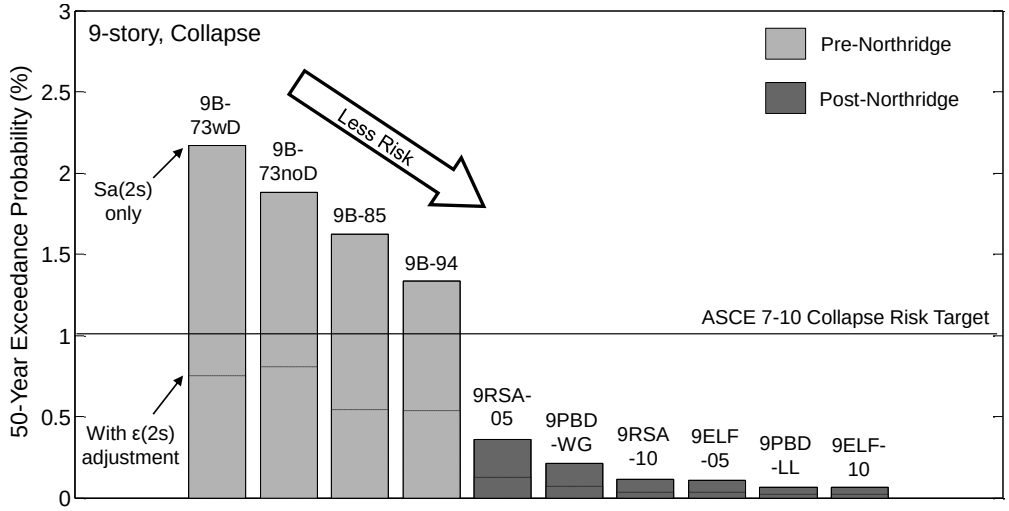

Figure 5.27: Computed risk with and without adjustments for $\varepsilon(2s)$ of collapse of the 9-story SMFs.

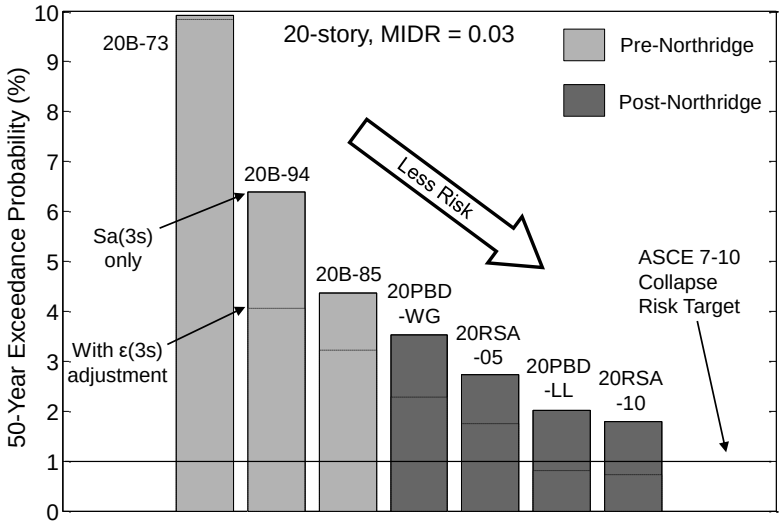

Figure 5.28: Computed risk with and without adjustments for $\varepsilon(3s)$ of the 20-story SMFs exceeding MIDR = 0.03.

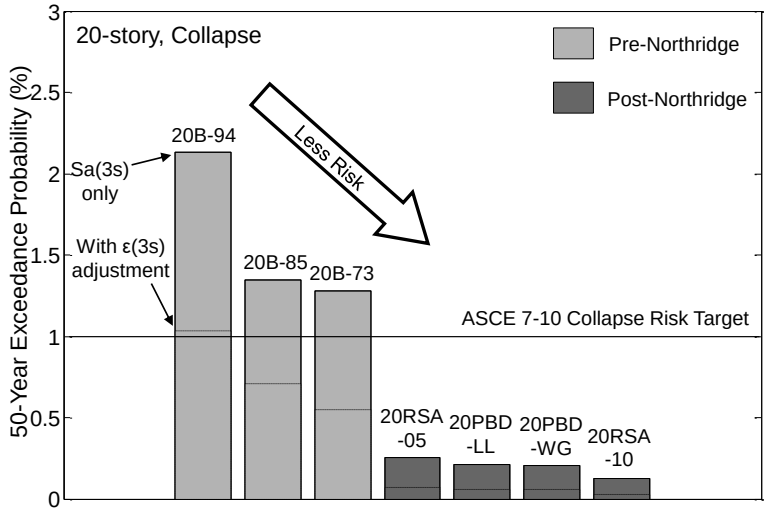

Figure 5.29: Computed risk with and without adjustments for $\varepsilon(3s)$ of collapse of the 20-story SMFs.

Most of the observations that can be made about these results could have been predicted from Tables 5.18-5.21. That is, the models for which $\mu_{\ln}$ and $\mu_{\ln}^{adj}$ are relatively high have lower probability of exceeding the corresponding EDPs. Of the 9-story post-Northridge models, the 9RSA-05 model tends to have the highest risk of highly nonlinear response, with the 9PBD-WG model close behind. Of the 20-story post-Northridge models, the 20RSA-10 model tends to have the lowest

risk of highly nonlinear response. The other post-Northridge models have relatively similar probabilities of exceeding the considered EDPs. The 9-story models generally have similar risk of highly nonlinear response as the 20-story models, though the 9RSA-05 model remains an outlier for its high risk. These general observations could also have been predicted by comparing $V_{\max}$ between the models as calculated via pushover analysis.

As expected, adjusting the risk calculations for $\varepsilon(T)$ decreases the risk estimates, a natural consequence of the previous observation that $\mu_{\ln}^{\text{adj}}$ is larger than $\mu_{\ln}$ in every case. Also, compared to the post-Northridge models, which are modeled with perfect (P) connections, the pre-Northridge B models have much higher risk of highly nonlinear response and collapse.

Many of these observations are not surprising, but what is interesting is the magnitude of the differences in risk among the different models. For example, the 9RSA-05 model has a collapse risk that is about 6x higher than that of the 9ELF-10 model, indicating that the 9RSA-05 model is six times more likely to collapse in the next 50 years. This is true whether or not risk estimates are adjusted to account for $\varepsilon(T)$. It should be noted that this example is an extreme case. Recall that the 9RSA-05 design was noted as an outlier in Section 5.4 as a result of the lack of a provision for scaling drifts when using RSA in ASCE 7-05 that was added into ASCE 7-10. As previously mentioned, practicing engineers may have used this provision despite the fact that it is not codified.The 9PBD-WG model has a collapse risk about 3x higher than the 9PBD-LL model. Since the designs of these models were developed identically except for the site-specific response spectra, all the difference in risk between these two models can be attributed to differences in the calculated site-specific response spectra for downtown Los Angeles in the LL and WG reports.

Variations in collapse risk among the 20-story models are moderate, as three of the four post-Northridge designs are mostly controlled by wind limits, which sets a lower bound for lateral force resistance independent of seismic design requirements. In the most extreme case for the 20-story models, the 20RSA-05 model has a $\varepsilon(T)$-adjusted collapse risk about 2.5x higher than that of the 20RSA-10 model while the 20B-73 model has a $\varepsilon(T)$-adjusted collapse risk about 8x higher than that of the 20RSA-05 model.

The differences in risk among models designed with different design codes are shown visually in Figure 5.30, which plots the $\varepsilon(T)$-adjusted risk of MIDR = 0.03 and collapse for all models except the PBD models as a function of design code. Results

from the PBD models are not shown because it would be misleading to assign them to a design code and, of the post-Northridge models, the extreme risk values tend to be from the ELF or RSA models. Note that the values plotted here are the same as shown in Tables 5.22 and 5.23. It is clear that the differences in risk between the pre-Northridge and post-Northridge models are more pronounced for collapse than for MIDR = 0.03. This is because the brittle connections incorporated in the pre-Northridge models serve to make these models more "brittle" in a global sense and this will have a more noticeable effect for more severe EDPs when compared to models that have perfect connections.

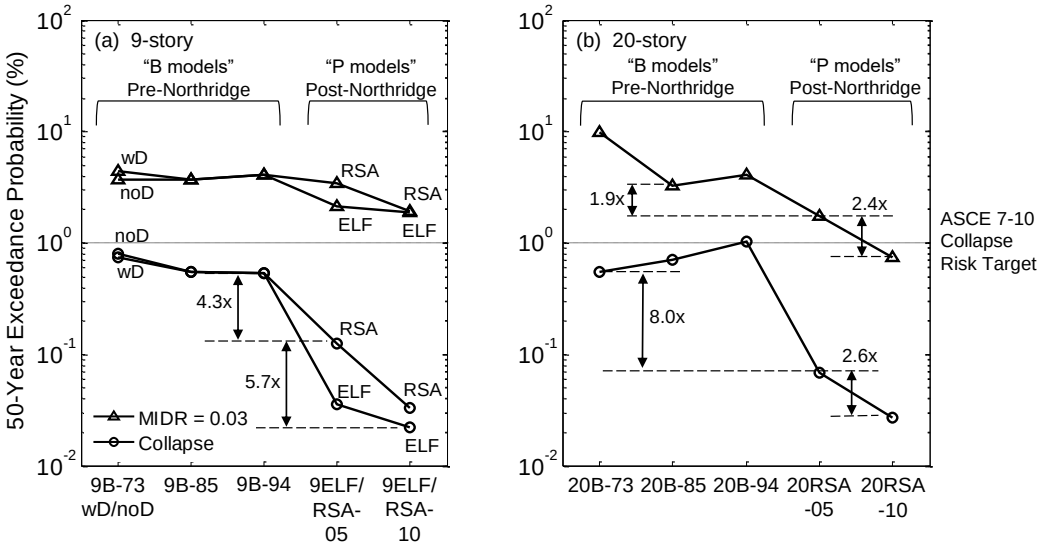

Figure 5.30: The $\varepsilon(T)$-adjusted risk of exceeding MIDR = 0.03 and collapse for the (a) 9-story and (b) 20-story SMFs designed according to ELF and RSA as a function of design code.

For a comprehensive demonstration of how risk varies with EDP for all models, risk is calculated with and without adjustments for $\varepsilon(T)$ for every model for EDPs ranging from MIDR = 0.005 to MIDR = 0.15 and these results are shown in Figures 5.31 for the 9-story models and 5.32 for the 20-story models. These plots demonstrate the trends for how risk varies with EDP and building model. Most notably, the differences in risk between the pre-Northridge and post-Northridge models are not visually clear until about MIDR = 0.05 for the 9-story models and about MIDR = 0.03 for the 20-story models. For large MIDRs, there is a signifcant chasm between the pre-Northridge and post-Northridge models. The variation in risk at large MIDRs for the 9-story post-Northridge models is also clear, particularly when compared

to the 20-story post-Northridge models. These plots also compare risk with and without adjustments for $\varepsilon(T)$, though adjusting for $\varepsilon(T)$ with $\varepsilon^*(T)$ calculated based on 2%/50-year ground motion is probably not valid for smaller MIDRs such as MIDR = 0.005. In any case, this adjustment has a significant effect on risk. However, note that for the post-Northridge models, the variation in design seems to have a comparable impact on risk as the $\varepsilon(T)$ adjustment.

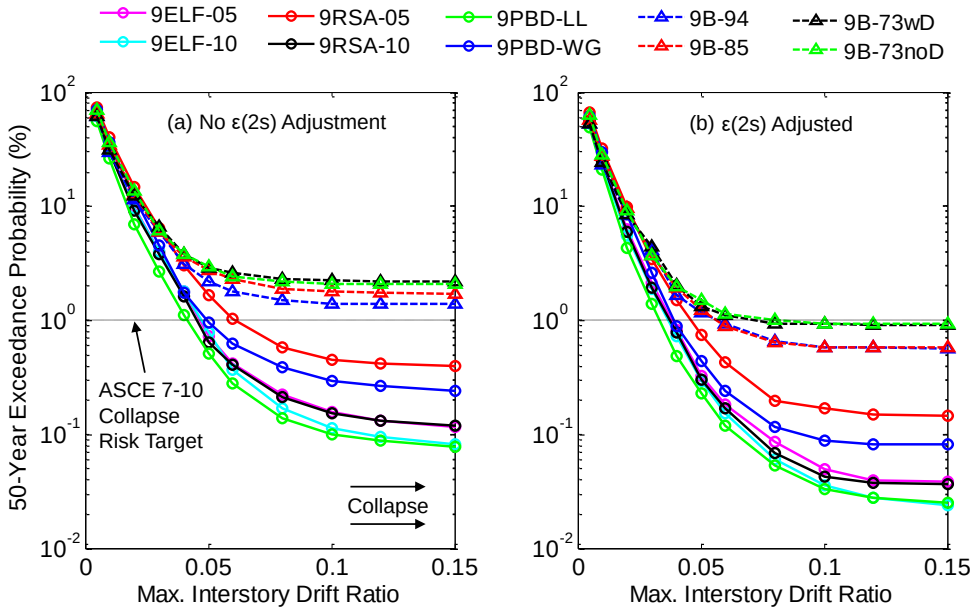

Figure 5.31: The risk of exceeding MIDRs ranging from 0.005 to 0.15 for the 9-story SMFs (a) without adjustments for $\varepsilon(2s)$ and (b) with adjustments for $\varepsilon(2s)$.

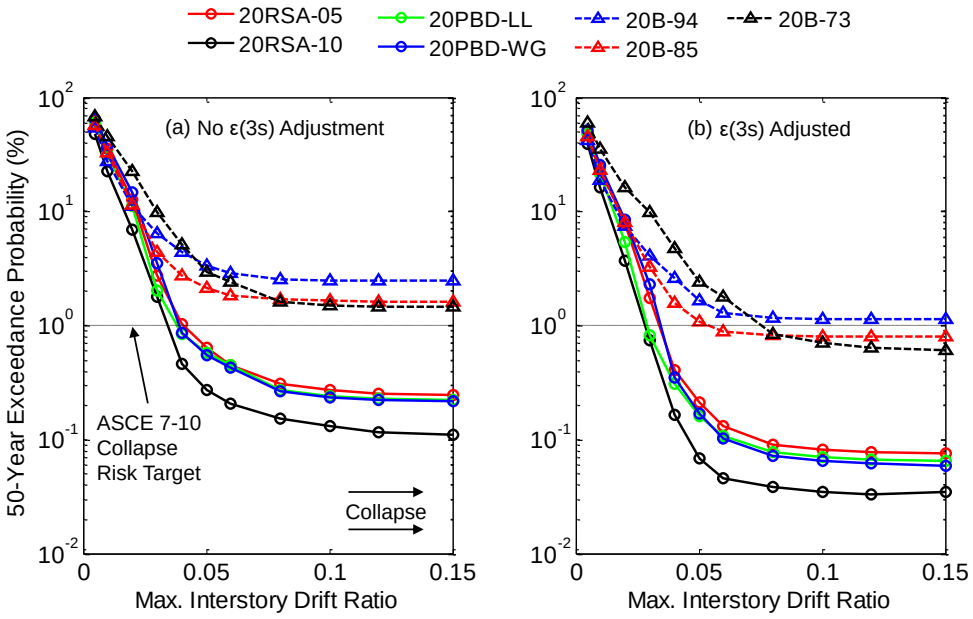

Figure 5.32: The risk of exceeding MIDRs ranging from 0.005 to 0.15 for the 20-story SMFs (a) without adjustments for $\varepsilon(3s)$ and (b) with adjustments for $\varepsilon(3s)$.

It should be noted that for all the post-Northridge models, the collapse risk is much less than 1% in 50 years, even if no adjustment is made for $\varepsilon(T)$. This implies that, despite the variability in risk estimates for different post-Northridge designs, all the models considered here satisfy the collapse risk target of 1% in 50 years, as specified by ASCE 7-10 for new buildings, by a large margin. For comparison, a comprehensive study of the collapse risk of reinforced concrete moment frame buildings by Haselton and Deierlein [48] found annual $\varepsilon(T)$-adjusted collapse probabilities of about 9×10^{-6} for modern 4-story reinforced concrete buildings conforming to ASCE 7-02, which, assuming a Poisson process for structural responses (e.g. [136]), is equivalent to approximately a 0.045% probability of collapse in 50 years. This is roughly the same collapse risk as is calculated for the post-Northridge models in this study, indicating that the large margin between the collapse risk of modern buildings and the ASCE 7-10 target is not unique to steel moment frames or to this study.

In fact, after accounting for $\varepsilon(T)$, most of the pre-Northridge models also meet 1% in 50-year collapse risk criterion of ASCE 7-10, which may be surprising. However, it is important to be cognizant of the modeling assumptions made here that may over-estimate the collapse capacity of these models. This includes not modeling cyclic degradation, local flange buckling, or column splice fracture. Furthermore,

the beams are not loaded within their spans, which may under-estimate the potential for local collapse of the pre-Northridge models.

5.8 Response to Strong Ground Motions

In this section, the SMF models analyzed in Section 5.7 are subjected to IDA with four strong ground motion records: 2016 M7.8 Kaikōura KEKS EW, 2016 M7.0 Kumamoto 93048 EW, 2015 M7.8 Gorkha KATNP EW, and 1999 M7.6 Chi-Chi TCU068 NS. Tilt-corrected versions of these records are used and their peak ground velocities are 269, 264, 112, and 298 cm/s, respectively. A description of the processing for these records is available in Chapter 4. These records are chosen because they all exceed the ASCE 7-10 MCE_R spectrum for downtown Los Angeles (calculated for Site Class C) for some range of periods, as shown in Figure 5.33.

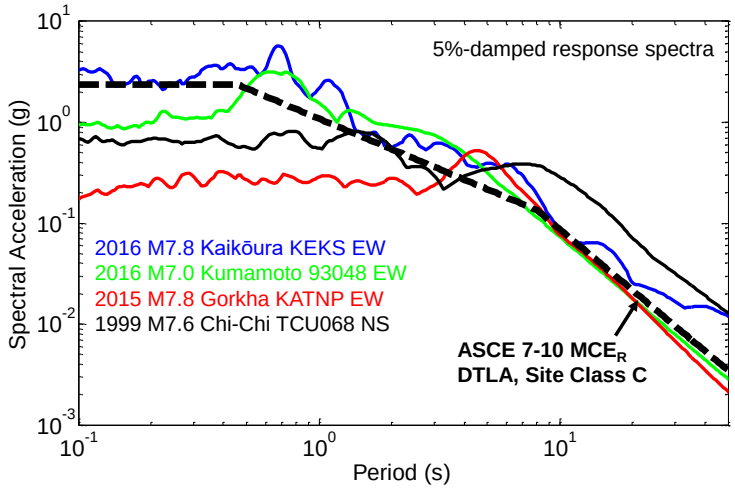

Figure 5.33: 5%-damped response spectra of four ground motion records considered in this section.

IDA is performed with each of these records for all of the pre-Northridge and post-Northridge 9- and 20-story models in order to calculate their collapse capacities. For each ground motion and building model, the scale factors are identified at which MIDR = 0.03, MIDR = 0.06, and collapse occur. The results are plotted as a function of "design code year" in Figures 5.34-5.36. As an example, the 9RSA-05 model has a "design code year" of 2005 because it is designed according to ASCE 7-05 and its scale factor is indicated with an "RSA" label in each plot. For the post-Northridge models, lines connect designs that use the same procedure (e.g. RSA) from different design code years. The color corresponding to each ground motion is the same as in Figure 5.33. The bold black line represents the median scale factor among the

four ground motions for each building model. Even though the performance-based designs do not necessarily align with a particular design code year, PBD-LL is plotted with a design year of 2005 because the GMPEs used to develop the site-specific spectra for the LL report are the same as used to create the design maps in ASCE 7-05 (the 2005 version of ASCE 7) and PBD-WG is plotted with a design year of 2010 because the GMPEs used to develop the site-specific spectra for the WG report are the same as used to create the design maps in ASCE 7-10 (the 2010 version of ASCE 7).

For the pre-Northridge designs, the results should be interpreted to generally represent pre-Northridge SMFs. That is, the year-to-year fluctuations between 1973, 1985, and 1994 should not be "over-interpreted" to imply differences in the design codes of these individual years. This is because the pre-Northridge designs considered in this study, as developed by Gupta and Krawinkler [18] and Lee and Foutch [19], are not necessarily designed using the same procedures. For example, Lee and Foutch consider the 1994 UBC designs to represent "upper bound" design and the 1985 designs to represent "lower bound" design based on how the design periods are calculated. The reader is referred to Lee and Foutch [19] for more details about these designs.

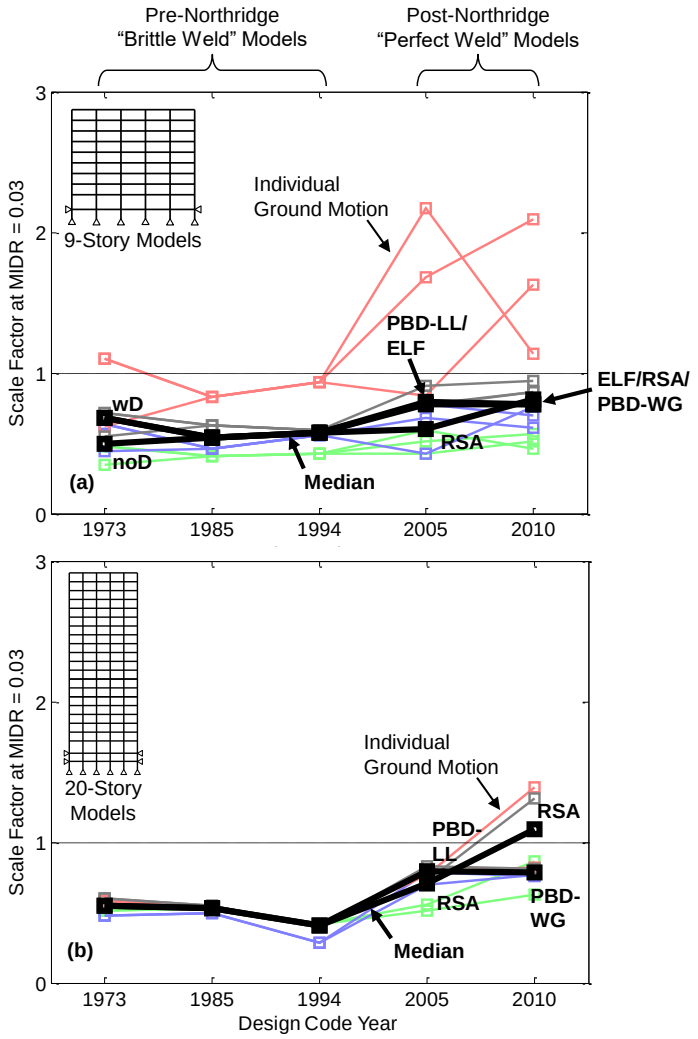

Figure 5.34: Scale factors at which MIDR = 0.03 is first induced in the 9- and 20-story pre-Northridge B models and post-Northridge P models in response to four strong ground motion records. The color for each individual ground motion corresponds to Figure 5.33.

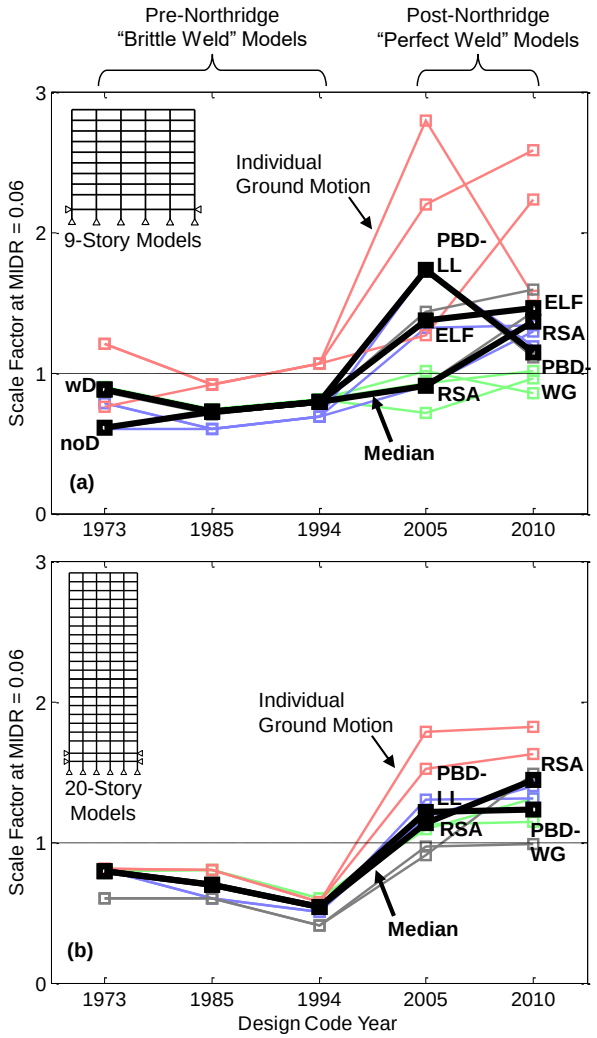

Figure 5.35: Scale factors at which MIDR = 0.06 is first induced in the 9- and 20-story pre-Northridge B models and post-Northridge P models in response to four strong ground motion records. The color for each individual ground motion corresponds to Figure 5.33.

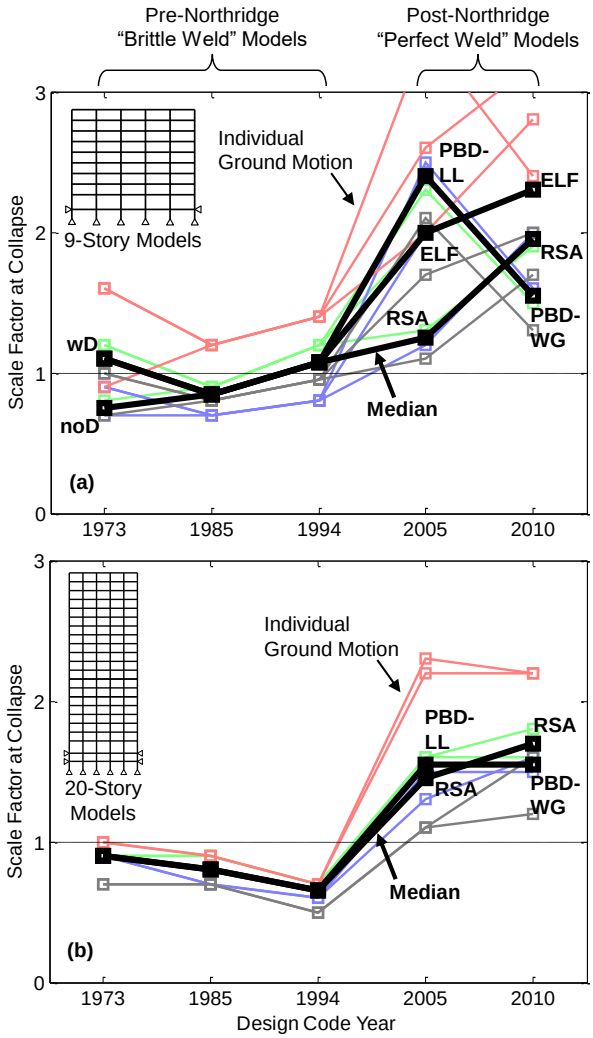

Figure 5.36: Scale factors at which collapse is first induced in the 9- and 20-story pre-Northridge B models and post-Northridge P models in response to four strong ground motion records. The color for each individual ground motion corresponds to Figure 5.33.

There are a number of interesting observations that can be made from these plots. For the more severe EDPs (i.e. MIDR = 0.06 and collapse), the pre-Northridge B models generally need a much lower scale factor to induce the EDP when compared to the post-Northridge P models. In fact, collapse first occurs in all of the 20-story pre-Northridge B models in response to all of the four ground motions with a scale factor of 1.0 or less, as can be seen in Figure 5.36. In contrast, none of the 9-story or 20-story post-Northridge P models experience collapse in response to any of the ground motions with a scale factor of 1.0. That is not to say that these strong ground motions do not induce significant damage in the post-Northidge P

models. As seen in Figure 5.34, most of the strong ground motions induce MIDR = 0.03 (the collapse-prevention limit in performance-based design) in most of the post-Northridge models with scale factors less than 1.0. The main exception is the response of the 9-story models to the Gorkha KATNP EW record (in red).

To demonstrate the effects of modeling brittle welds in the pre-Northridge models, Figure 5.37 shows the same data as Figure 5.36 except the pre-Northridge models are assigned perfect welds. That is, they are P models instead of B models. Interestingly, the collapse capacities (i.e. the scale factors that induce collapse) of the pre-Northridge P models are generally similar to those of the post-Northridge P models. This implies that the observation from Figure 5.36 that the pre-Northridge B models have significantly lower collapse capacities than the post-Northridge P models is predominantly due to modeling of brittle welds in the pre-Northridge B models and not due to differences between pre-Northridge and post-Northridge designs.

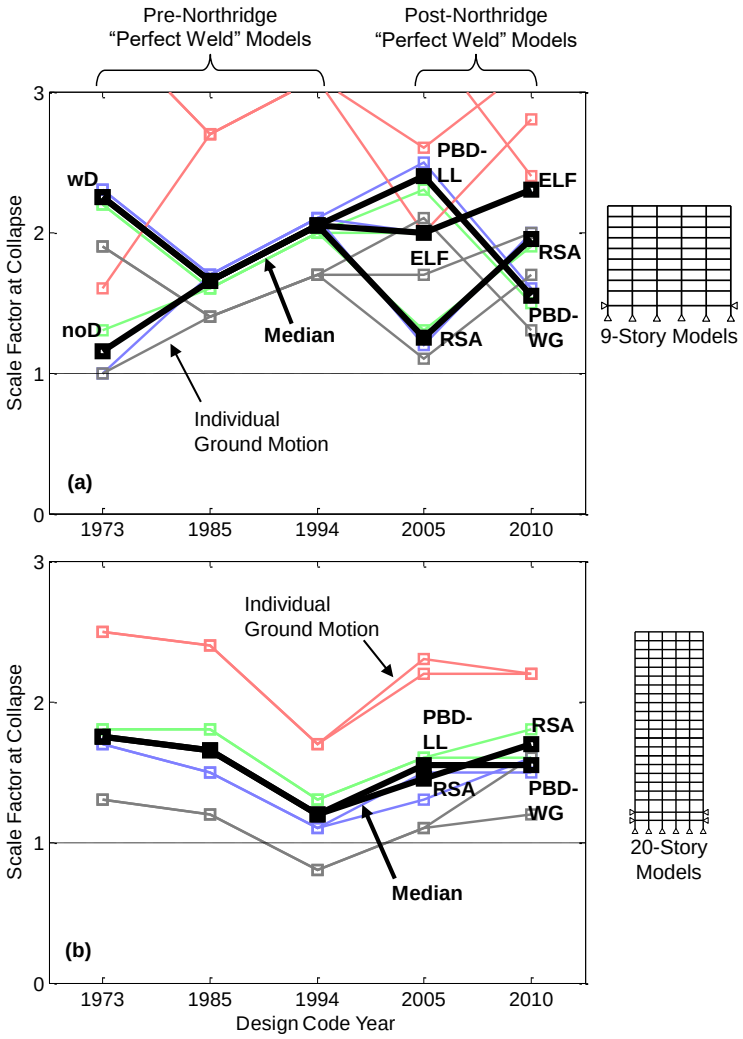

Figure 5.37: Scale factors at which collapse is first induced in the 9- and 20-story pre- and post-Northridge P models in response to four strong ground motion records. The color for each individual ground motion corresponds to Figure 5.33.

In summary, with a scale factor of 1.0 (i.e. the original records), the four strong ground motions considered in this section all induce collapse in the 20-story pre-Northridge B models and in many cases in the 9-story pre-Northridge B models. The post-Northridge P models are less susceptible to collapse, but these strong ground motions are still damaging, inducing drift ratios larger than 0.03 in many cases. The relative collapse vulnerability of the pre-Northridge B models is mostly due to the modeling of brittle pre-Northridge welds, as pre-Northridge P models have similar collapse capacities to the post-Northridge P models.

5.9 Conclusions

From a design perspective, several trends are observed that are not necessarily surprising. The design of beams in SMFs are generally controlled by drift limits (either seismic or wind). Design of columns are generally controlled by beam sizes, so, in effect, the drift limits generally control the design of the entire structure. Serviceability wind drift limits, as defined in this study, are not a factor in the design of the post-Northridge 9-story SMFs, but are a factor for three of the four post-Northridge 20-story SMFs, with the exception of the 20RSA-10 design.

Of the 9-story post-Northridge SMFs, the 9RSA-05 model (a noted outlier) has the highest collapse risk, followed by the 9PBD-WG model. Interestingly, the 9PBD-WG model has a collapse risk about 3x higher than that of the 9PBD-LL model. The only differences in the design processes of these two SMFs are the SLE and MCE response spectra used in their design from the LL and WG reports. To the best knowledge of the author, the main reason the response spectra in the LL and WG reports are different is that the LL report uses three 1997 GMPEs to generate their SLE and MCE response spectra while the WG uses four 2008 GMPEs to generate their SLE and MCE response spectra. If it is true that most of the differences between the LL and WG response spectra are due to the GMPEs, then results of this study indicate that the differences in these GMPEs manifest themselves in the collapse risk of 9-story SMFs designed according to response spectra generated by these GMPEs by up to a factor of 3.

Differences in collapse risk of the 20-story post-Northridge SMFs are not as drastic as those of the 9-story post-Northridge SMFs. This is due to serviceability wind drift limits, which control design of the first 10-15 stories of the 20RSA-05, 20PBD-LL, and 20PBD-WG designs. The collapse risk values of the models corresponding to these designs are relatively similar. The 20RSA-10 design is governed by seismic drift limits and its collapse risk is less than those of the other three 20-story post-Northridge SMFs by a factor of 2.6.

Not surprisingly, the pre-Northridge SMFs have significantly higher collapse risk than the post-Northridge SMFs – at least 4.3x higher for the 9-story SMFs and at least 8.0x higher for the 20-story SMFs. These differences become more dramatic for more severe EDPs.

In response to four strong ground motion records that all exceed the downtown Los Angeles MCE_R response spectrum for some range of periods, some of the 9-story and all of the 20-story pre-Northridge SMFs experience collapse. In constrast, none

of the post-Northridge SMFs collapse, though most are severely damaged (MIDR > 0.03). Differences between the pre- and post-Northridge SMFs are mostly due to the modeling of perfect (P) welds in the post-Northridge models as opposed to brittle (B) welds in the pre-Northridge models. Differences between the pre- and post-Northridge design codes do not appear to have as substantial of an effect on collapse capacity.

Limitations and Future Work

It is important to note the limitations of this study with regards to generalizations that can be made from the conclusions. The SMF designs do not necessarily represent existing structures for a variety of reasons. The designs are developed by the author (who is not a practicing engineer) based on existing literature on design practice, but still require engineering judgment and subjective design decisions. For example, the important provision in ASCE 7-10 that requires the amplification of RSA drifts by $0.85V/V_t$ may have been followed by designers designing according to ASCE 7-05 even though it is not a codified requirement. This study does not account for the fact that practicing engineers may use engineering judgment to not accept a design that appears to be an outlier.

Furthermore, the SMF models in this study are created with several simplifying assumptions that may have an effect on the collapse risk calculations. Cyclic degradation has been shown to be important to accurately simulate collapse (e.g. [14]), but is not incorporated in Frame-2d. Local flange buckling also cannot be modeled in Frame-2d. Other Frame-2d features such as soil-structure interaction and advanced damping modeling are not implemented in the models in this study, but may impact the accuracy of the collapse risk estimates.

Finally, the risk calculations are made with some simplifying assumptions. Method 2 of Haselton et al. [135] is used to calculate risk, which provides a method for accounting for $\varepsilon(T)$ with an arbitrary set of input ground motions. A more precise method to account for $\varepsilon(T)$ for risk assessment would be to select the set of input ground motions such that the $\varepsilon(T)$ value for every record is near $\varepsilon^*(T)$ as calculated via disaggregation. Furthermore, modeling uncertainty is not accounted for in this study. For example, the expected structural steel properties are implemented in the models. A more comprehensive risk assessment would consider the uncertainty of the nonlinear properties of structural steel, which would increase the collapse risk.

The results of this study could be formalized by suggesting a formulation for

incorporating design uncertainty into collapse risk assessments. Such procedures already exist for incorporating modeling uncertainty and the formulation for including design uncertainty would be similar. The difficulty is that probability distributions for modeling parameters (e.g. expected yield strength of steel) can be validated experimentally by testing a random distribution of structural steel members, but this cannot be done to generate probability distributions of design decisions. Hopefully, this study can provide a starting point for the variability that might be expected in designs for post-Northridge SMFs located at a given site.

The study presented in this chapter could be further expanded by incorporating designs corresponding to recent updates to ASCE 7 and the LATBSDC alternate procedure. The not-yet-developed 2019 CBC will probably adopt the 2018 IBC [137], which incorporates ASCE 7-16 [60]. Furthermore, the 2017 version of the LATBSDC alternate procedure [72] has recently been released and references ASCE 7-16 for the definition of MCE_R shaking as well as guidance for the selection and scaling of ground motion records.

The definition of MCE_R in ASCE 7-16 is unchanged from that of ASCE 7-10, although the seismic design values for the reference site of this study decrease slightly from those in ASCE 7-10 (see Table 5.2) to $S_{DS} = 1.572$ g and $S_{D1} = 0.652$ g. These values for ASCE 7-16 are between those of ASCE 7-05 and ASCE 7-10. The reductions in seismic design values are in part due to the changes in GMPEs from the NGA-West1 project (used to calculate seismic hazard maps in ASCE 7-10) to the NGA-West2 project (used to calculate seismic hazard maps in ASCE 7-16). Boore et al. [138] and Abrahamson et al. [139] both note that the 2014 versions of their GMPEs developed as part of the NGA-West2 project result in reduced median ground motion predictions from the 2008 versions of their GMPEs, particularly for smaller magnitude events. Another significant change in ASCE 7-16 is that, where required, responses calculated using the RSA procedure are required to be scaled up by V/V_t instead of $0.85V/V_t$. According to the Commentary, this change was made to reduce differences in buildings designed according to ELF and RSA procedures, a result that was observed in this study.

Compared to Chapter 16 of ASCE 7-10, Chapter 16 of ASCE 7-16 provides much more guidance for the selection and scaling of ground motion records for nonlinear time history analysis. It also requires 11 pairs of input ground motions (instead of 7 in ASCE 7-10) and that if spectral matching is used to modify ground motion records, then the target spectrum must be increased by 110%. The 2017 version of

the LATBSDC alternate procedure provides even more requirements for the selection and scaling of ground motions in addition to that of Chapter 16 of ASCE 7-16. Many of these requirements are relevant to sites that are near-source and/or have multiple sources of significant seismic hazard. These characteristics apply to most sites in Los Angeles. These additional requirements include ensuring that ground motions are selected with characteristics representing all sources contributing to at least 20% of the hazard, ground motion durations are reported, no less than five "pulse" or "non-pulse" ground motions are included if required, and a "fling step" (i.e. static offset) is added to the FN component of records where required.

BIBLIOGRAPHY

[1] Bonowitz, D., Durkin, M., Gates, W., Morden, M., and Youssef, N. *Surveys and Assessment of Damage to Buildings Affected by the Northridge Earthquake of January 17, 1994*. SAC 95-06. 1995.

[2] Hall, J. F. *Parameter study of the response of moment-resisting steel frame buildings to near-source ground motions*. 95-08. California Institute of Technology, Pasadena, CA.: Earthquake Engineering Research Laboratory, 1995.

[3] Hall, J. F., Heaton, T. H., Halling, M. W., and Wald, D. J. (1995). "Near-Source Ground Motion and its Effects on Flexible Buildings". *Earthquake Spectra*. **11**(4): 569–605.

[4] MacRae, G. A. *Parametric study on the effect of ground motion intensity and dynamic characteristics on seismic demands in steel moment resisting frames*. SAC/BD-99/01. 1999.

[5] FEMA (Federal Emergency Management Agency). *State of the Art Report on Past Performance of Steel Moment Frame Buildings in Earthquakes*. FEMA-355E. Washington, D.C., 2000.

[6] Challa, V. R. M. "Nonlinear seismic behavior of steel planar moment-resisting frames". PhD thesis. Pasadena, CA.: California Institute of Technology, 1992.

[7] Challa, V. R. M. and Hall, J. F. (1994). "Earthquake Collapse Analysis of Steel Frames". *Earthquake Engineering & Structural Dynamics*. **23**: 1199–1218.

[8] Hall, J. F. (1998). "Seismic response of steel moment frame buildings to near-source ground motions". *Earthquake Engineering & Structural Dynamics*. **27**: 1445–1464.

[9] Hall, J. F. *Seismic response of steel moment frame buildings to near-source ground motions*. 97-05. California Institute of Technology, Pasadena, CA.: Earthquake Engineering Research Laboratory, 1997.

[10] Bjornsson, A. B. "A Retrofitting Framework for Pre-Northridge Steel Moment-Frame Buildings". PhD thesis. Pasadena, CA.: California Institute of Technology, 2014.

[11] AISC. *Prequalified Connections for Special and Intermediate Steel Moment Frames for Seismic Applicaions, ANSI/AISC 358-10*. Chicago, IL., 2010.

[12] Krishnan, S. and Muto, M. (2012). "Mechanism of Collapse of Tall Steel Moment-Frame Buildings under Earthquake Excitation". *Journal of Structural Engineering*. **138**(11): 1361–1387.

[13] Hall, J. F. (2005). "Problems encountered from the use (or misuse) of

Rayleigh damping". *Earthquake Engineering and Structural Dynamics*. **121**: 1284–1291.

[14] Ibarra, L. F. and Krawinkler, H. *Global Collapse of Frame Structures Under Seismic Excitations*. 152. Stanford University, Stanford, CA.: John A. Blume Earthquake Engineering Center, 2005.

[15] NIST. *Soil-Structure Interaction for Building Structures*. NIST GCR 12-917-21. Gaithersburg, MD.: National Institute of Standards and Technology, 2012.

[16] Steel Shape Producers Council. *Statistical analysis of tensile data for wide flange structural shapes*. 1994.

[17] Arasaratnam, P., Sivakumaran, K. S., and Tait, M. J. (2011). "True Stress-True Strain Models for Structural Steel Elements". *ISRN Civil Engineering*.

[18] Gupta, A. and Krawinkler, H. *Seismic Demands for Performance Evaluation of Steel Moment Resisting Frame Structures*. 132. Stanford University, Stanford, CA.: John A. Blume Earthquake Engineering Center, 1999.

[19] Lee, K. and Foutch, D. *Performance Prediction and Evaluation of Steel Special Moment Frames for Seismic Loads*. SAC/BD-00/25. 2000.

[20] ASCE. *Minimum Design Loads for Buildings and Other Structures, ASCE/SEI 7-10*. Reston, VA.: American Society of Civil Engineers, 2010.

[21] Dizon, A. B. R. "A Hybrid-Parallel Framework for the Nonlinear Seismic Analysis of Very Tall Buildings". PhD thesis. Pasadena, CA.: California Institute of Technology, 2016.

[22] TBI Guidelines Working Group. *Guidelines for performance-based seismic design of tall buildings*. PEER 2010/05. Berkeley, CA.: Pacific Earthuake Engineering Research Center, 2010.

[23] LATBSDC (Los Angeles Tall Buildings Seismic Design Council). *An alternative procedure for seismic analysis and design of tall buildings located in the Los Angeles region, 2014 Edition with 2015 Supplements*. Los Angeles, CA., 2015.

[24] Eads, L. "Seismic collapse risk assessment of buildings: effects of intensity measure selection and computational approach". PhD thesis. Stanford, CA.: Stanford University, 2013.

[25] Federal Emergency Management Agency. *Seismic Performance Assessment of Buildings*. FEMA P-58. Washington, D.C., 2012.

[26] Moehle, J. and Deierlein, G. G. "A Framework Methodology for Performance-Based Earthquake Engineering". *Proceedings, 13th World Conference on Earthquake Engineering*. Vancouver, B.C., Canada, 2004.

[27] Luco, N. and Cornell, C. A. (2007). "Structure-Specific Scalar Intensity Measures for Near-Source and Ordinary Earthquake Ground Motions". *Earthquake Spectra*. **23**(2): 357–392.

[28] Masayoshi, N., Koshika, N., Kawano, K., Hirakawa, K., and Wada, A. (2012). "Performance-Based Seismic Design for High-Rise Buildings in Japan". *International Journal of High-Rise Buildings*. **1**(3): 155–167.

[29] Housner, G. W. (1941). "Calculating response of an oscillator to arbitrary ground motion". *Bulletin of the Seismological Society of America*. **31**: 143–149.

[30] Haviland, R. *A Study of the Uncertainties in the Fundamental Translational Periods and Damping Values for Rearl Buildings*. 5. Massachusetts Institute of Technology, Cambridge, Massachusetts: Evaluation of Seismic Safety of Buildings, 1976.

[31] ATC (Applied Technology Council). *Tentative Provisions for the Development of Seismic Regulations for Buildings*. ATC 3-06. Palo Alto, CA., 1978.

[32] Shome, N., Cornell, C. A., Bazzurro, P., and Carballo, J. E. (1998). "Earthquakes, records, and nonlinear responses". *Earthquake Spectra*. **14**(3): 469–500.

[33] Newmark, N. M. and Hall, W. J. *Earthquake Spectra and Design*. Chicago, IL., 1982.

[34] Haselton, C. B. and Baker, J. W. "Ground motion intensity measures for collapse capacity prediction: choice of optimal spectral period and effect of spectral shape". *Proceedings, 8th U.S. National Conference on Earthquake Engineering*. San Francisco, CA., 2006.

[35] Eads, L., Miranda, E., and Lignos, D. G. (2015). "Average spectral acceleration as an intensity measure for collapse risk assessment". *Earthquake Engineering & Structural Dynamics*. **44**(12): 2057–2073.

[36] Kazanti, A. K. and Vamvatsikos, D. (2015). "Intensity measure selection for vulnerability studies of building classes". *Earthquake Engineering & Structural Dynamics*. **44**(15): 2677–2694.

[37] Kohrangi, M., Bazzurro, P., and Vamvatsikos, D. (2016). "Vector and Scalar IMs in Structural Response Estimation, Part II: Building Demand Assessment". *Earthquake Spectra*. **32**(3): 1525–1543.

[38] Cordova, P. P., Deierlein, G. G., Mehanny, S. S. F., and Cornell, C. A. "Development of a two-parameter seismic intensity measure and probabilistic assessment procedure". *The Second US-Japan Workshop on Performance-Based Earthquake Engineering Methodology for Reinforced Concrete Building Structures*. Sapporo, Japan, 2000.

[39] Baker, J. W. and Cornell, C. A. (2005). "A vector-valued ground motion intensity measure consisting of spectral acceleration and epsilon". *Earthquake Engineering & Structural Dynamics*. **34**: 1193–1217.

[40] Boore, D. M. and Atkinson, G. M. (2008). "Ground-Motion Prediction Equations for the Average Horizontal Component of PGA, PGV, and 5%-Damped PSA at Spectral Periods between 0.01 s and 10.0 s". *Earthquake Spectra*. **24**(1): 99–138.

[41] Iwan, W. D. and Gates, N. C. (1979). "The Effective Period and Damping of a Class of Hysteretic Structures". *Earthquake Engineering and Structural Dynamics*. **7**: 199–211.

[42] Guyader, A. C. *A statistical approach to equivalent linearization with application to performance-based engineering*. 2004-04. California Institute of Technology, Pasadena, CA.: Earthquake Engineering Research Laboratory, 2004.

[43] ATC (Applied Technology Council). *Seismic Evaluation and Retrofit of Concrete Buildings*. ATC-40. Redwood City, CA., 1996.

[44] Akkar, S. and Ozen, O. (2005). "Effect of peak ground velocity on deformation demands for SDOF systems". *Earthquake Engineering & Structural Dynamics*. **34**: 1551–1571.

[45] FEMA (Federal Emergency Management Agency). *Quantification of Building Seismic Performance Factors*. FEMA P695. Washington, D.C., 2009.

[46] Pacific Earthquake Engineering Research Center. *PEER NGA-West2, Pacific Earthquake Research Center*. Berkeley, CA., available at http://peer.berkeley.edu/nga/. Last accessed 20 March, 2017. 2013.

[47] Vamvatsikos, D. and Cornell, C. A. (2002). "Incremental dynamic analysis". *Earthquake Engineering & Structural Dynamics*. **31**(3): 491–514.

[48] Haselton, C. B. and Deierlein, G. G. *Assessing Seismic Collapse Safety of Modern Reinforced Concrete Moment-Frame Buildings*. PEER 2007/08. Berkeley, CA.: Pacific Earthuake Engineering Research Center, 2008.

[49] Aslani, H. and Miranda, E. *Probabilistic Earthquake Loss Estimation and Loss Disaggregation in Buildings*. 157. Stanford University, Stanford, CA.: John A. Blume Earthquake Engineering Center, 2005.

[50] Tothong, P. and Cornell, C. A. (2006). "An Emperical Ground-Motion Attenuation Relation for Inelastic Spectral Displacement". *Bulletin of the Seismological Society of America*. **96**(6): 2146–2164.

[51] Bradley, B. A., Dhakal, R. P., MacRae, G. A., and Cubrinovski, M. (2010). "Prediction of spatially distributed seismic demands in specific structures: Ground motion and structural response". *Earthquake Engineering & Structural Dynamics*. **39**: 501–520.

[52] Song, S. and Heaton, T. H. "Predicting collapse of steel and reinforced-concrete frame buildings in different types of ground motions". *Proceedings, 15th World Conference on Earthquake Engineering*. Lisbon, Portugal, 2012.

[53] Iwan, W. D. (1980). "Estimating inelastic response spectra from elastic spectra". *Earthquake Engineering & Structural Dynamics*. **8**: 375–388.

[54] Rosenblueth, E. and Herrera, I. (1964). "On a kind of hysteretic damping". *Journal of Engineering Mechanics Division ASCE*. **90**: 37–48.

[55] Gulkan, P. and Sozen, M. (1974). "Inelastic response of reinforced concrete structures to earthquake motions". *ACI Journal*. **71**: 604–610.

[56] Kowalsky, M. J. "Displacement-based design-a methodology for seismic demand applied to RC bridge columns". MA thesis. La Jolla, CA.: University of California at San Diego, 1994.

[57] Miranda, E. and Ruiz-Garcia, J. (2002). "Evaluation of approximate methods to estimate maximum inelastic displacement demands". *Earthquake Engineering & Structural Dynamics*. **31**: 539–560.

[58] Huang, Y.-N., Whittaker, A. S., and Luco, N. *Performance Assessment of Convetional and Base-Isolated Nuclear Power Plants for Earthquake and Blast Loadings*. MCEER-08-0019. University at Buffalo, State University of New York, Buffalo, New York: Multidisciplinary Center for Earthquake Engineering Research, 2008.

[59] Al Atik, L. and Abrahamson, N. (2010). "An Improved Method for Nonstationary Spectral Matching". *Earthquake Spectra*. **26**(3): 601–617.

[60] ASCE. *Minimum Design Loads for Buildings and Other Structures, ASCE/SEI 7-16*. Reston, VA.: American Society of Civil Engineers, 2016.

[61] Baker, J. W. and Jayaram, N. (2008). "Correlation of spectral acceleration values from NGA ground motion models". *Earthquake Spectra*. **24**(1): 299–317.

[62] Kohrangi, M., Kotha, S. R., and Bazzurro, P. (2018). "Ground-motion models for average spectral acceleration in a period range: direct and indirect methods". *Bulletin of Earthquake Engineering*. **16**: 45–65.

[63] Yamada, M., Olsen, A. H., and Heaton, T. H. (2009). "Statistical Features of Short-Period and Long-Period Near-Source Ground Motions". *Bulletin of the Seismological Society of America*. **99**(6): 3264–3274.

[64] Anderson, J. C. and Bertero, V. V. (1987). "Uncertainties in Establishing Design Earthquakes". *Journal of Structural Engineering*. **113**(8): 1709–1724.

[65] Mavroeidis, G. P., Dong, G., and Papageorgiou, A. S. (2004). "Near-fault ground motions, and the response of elastic and inelastic single-degree-of-freedom (SDOF) systems". *Earthquake Engineering & Structural Dynamics*. **33**: 1023–1049.

[66] Malhotra, P. K. (1999). "Response of buildings to near-field pulse-like ground motions". *Earthquake Engineering & Structural Dynamics*. **28**: 1309–1326.

[67] Ancheta, T. D., Darragh, R. B., Stewart, J. P., Seyhan, E., Silva, W. J., Chiou, B. S.-J., Wooddell, K. E., Graves, J. W., Kottke, A. R., Boore, D. M., Kishida, T., and Donahue, J. L. (2014). "NGA-West2 Database". *Earthquake Spectra*. **30**(3): 989–1005.

[68] Ma, K.-F., Lee, C.-T., Tsai, Y.-B., Shin, T.-C., and Mori, J. (1999). "The Chi-Chi, Taiwan Earthquake: Large Surface Displacements on an Inland Thrust Fault". *EOS Transactions, American Geophysical Union*. **80**(50): 605–620.

[69] Kamai, R. and Abrahamson, N. (2015). "Are Near-Fault Fling Effects Captured in the New NGA West2 Ground Motion Models?" *Earthquake Spectra*. **31**(3): 1629–1645.

[70] Boore, D. M. (2001). "Effect of Baseline Corrections on Displacements and Response Spectra for Several Recordings of the 1999 Chi-Chi, Taiwan, Earthquake". *Bulletin of the Seismological Society of America*. **91**(5): 1199–1211.

[71] Ventura, C. E., Archila, M., Bebamzadeh, A., and Liam Finn, W. D. (2011). "Large coseismic displacements and tall buildings". *The Structural Design of Tall and Special Buildings*. **20**(S1): 85–99.

[72] LATBSDC (Los Angeles Tall Buildings Seismic Design Council). *An alternative procedure for seismic analysis and design of tall buildings located in the Los Angeles region, 2017*. Los Angeles, CA., 2017.

[73] Burks, L. S. and Baker, J. W. (2016). "A predictive model for fling-step in near-fault ground motiosn based on records and simulations". *Soil Dynamics and Earthquake Engineering*. **80**: 119–126.

[74] Boore, D. M. and Akkar, S. (2003). "Effect of causal and acausal filters on elastic and inelastic response spectra". *Earthquake Engineering & Structural Dynamics*. **32**: 1729–1748.

[75] Burks, L. S. and Baker, J. W. "Fling in Near-Fault Ground Motions and its Effect on Structural Collapse Capacity". *Proceedings, 10th U.S. National Conference on Earthquake Engineering*. Anchorage, AK., 2014.

[76] Haselton, C. B. *Evaluation of Ground Motion Selection and Modification Methods: Predicting Median Interstory Drift Response of Buildings*. PEER 2009/01. Berkeley, CA.: Pacific Earthuake Engineering Research Center, 2009.

[77] Roh, B., Buyco, K., and Heaton, T. H. "NGA High-Pass Filters Remove Important Real Signals; Simple Tilt Correction is Preferable". *Proceedings of the 11th National Conference in Earthquake Engineering*. Los Angeles, CA, 2018.

[78] Chen, X. "Near-Field Ground Motion from the Landers Earthquake". PhD thesis. Pasadena, CA.: California Institute of Technology, 1995.

[79] Ellsworth, W. L., Celebi, M., Evans, J. R., Jensen, E. G., Kayen, R., Metz, M. C., Nyman, D. J., Roddick, J. W., Spudich, P., and Stephens, C. D. (2004). "Near-Field Ground Motion of the 2002 Denali Fault, Alaska, Earthquake Recorded at Pump Station 10". *Earthquake Spectra*. **20**(3): 597–615.

[80] Yamada, M., Heaton, T. H., and Beck, J. (2007). "Real-Time Estimation of Fault Rupture Extent Using Near-Source versus Far-Source Classification". *Bulletin of the Seismological Society of America*. 97(6): 1890–1910.

[81] Hamling, I. J., Hreinsdóttir, S., Clark, K., Elliott, J., Liang, C., Fielding, E., Litchfield, N., Villamor, P., Wallace, L., Wright, T. J., D'Anastasio, E., Bannister, S., Burbidge, D., Denys, P., Gentle, P., Howarth, J., Mueller, C., Palmer, N., Pearson, C., Power, W., Barnes, P., Barrell, D. J. A., Van Dissen R. Langridge, R., Little, T., Nicol, A., Pettinga, J., Rowland, J., and Stirling, M. (2017). "Complex multifault rupture during the 2016 M_W 7.8 Kaikōura earthquake, New Zealand". *Science*. **349**: 1091–1095.

[82] Asano, A. and Tomotaka, I. (2016). "Source rupture process of the foreshock and mainshock in the 2016 Kumamoto earthquake sequence estimated from kinematic waveform inversion of strong motion data". *Earth, Planets and Space*. **78**: 147.

[83] Galetzka, J., Melgar, D., Genrich, J. F., Geng, J., Owen, S., Lindsey, E. O., Xu, X., Bock, Y., Avouac, J.-P., Adhikari, L. B., N., Upreti B., Pratt-Sitaula, B., Bhattarai, T. N., Sitaula, B. P., Moore, A., Hudnut, K. W., Szeliga, W., Normandeau, J., Fend, M., Flouzat, M., Bollinger, L., Shrestha, P., Koirala, B., Gautam, U., Bhatterai, M., Gupta, R., Kandel, T., Timsina, C., Sapkota, S. N., Rajaure, S., and Maharjan, N. (2015). "Slip pulse and resonance of the Kathmandu basin during the 2015 Gorkha earthquake, Nepal". *Science*. 349: 1091–1095.

[84] Lu, M., Li, X. J., An, X. W., and Zhao, J. X. (2010). "A Preliminary Study on the Near-Source Strong-Motion Characteristics of the Great 2008 Wenchuan Earthquake in China". *Bulletin of the Seismological Society of America*. **100**(5B): 2491–2507.

[85] Boore, D. M. (2005). "On Pads and Filters: Processing Strong-Motion Data". *Bulletin of the Seismological Society of America*. **88**(3): 745–750.

[86] Computers and Inc., Structures. *SAP2000 version 19, CSI Analysis Reference Manual*. Berkeley, CA., 2016.

[87] Sarkisian, M., Lee, P., Hu, L., Doo, C.-S., and Tsui, A. "Enhanced Seismic Performance of the New San Bernardino Justice Center". *Proceedings, SEAOC Convention*. Las Vegas, NV., 2011.

[88] Boore, D. M. and Bommer, J. J. (2005). "Processing of strong-motion accelerograms: needs, options, and consequences". *Soil Dynamics and Earthquake Engineering*. **25**: 93–115.

[89] Jones, L. M., Bernknopf, R., Cox, D., Goltz, J., Hudnut, K., Mileti, D., Perry, S., Ponti, D., Porter, K., Reichle, M., Seligson, H., Shoaf, K., Treiman, J., and Wein, A. *The ShakeOut Scenario*. USGS Open File Repor 2008-1150. Reston, VA., 2008.

[90] Krishnan, S. and Muto, M. *High-Rise Steel Buildings*. The ShakeOut Scneario, /textitSupplemental Study. Prepared for United States Geological Survey and California Geological Survey. Pasadena, CA., 2008.

[91] NIST. *Evaluation of the FEMA P-695 Methodology for Quantification of Building Seismic Performance Factors*. NIST GCR 10-917-8. Gaithersburg, MD.: National Institute of Standards and Technology, 2010.

[92] Zareian, F. and Krawinkler, H. (2007). "Assessment of probability of collapse and design for collapse safety". *Earthquake Engineering & Structural Dynamics*. **36**: 1901–1914.

[93] Liel, A. B., Haselton, C. B., Deierlein, G. G., and Baker, J. W. (2009). "Incorporating modeling uncertainties in the assessment of seismic collapse risk of buildings". *Structural Safety*. **31**: 197–211.

[94] Sattar, S. "Evaluating the Consistency Between Prescriptive and Performance-Based Seismic Design Approahces for Reinforced Concrete Moment Frames: ASCE 7 Versus ASCE 41". *Proceedings of the 2016 Annual Meeting of the Los Angeles Tall Buildings Structural Design Council*. Loc Angeles, CA., 2016.

[95] Gosh, S. K. (2002). "2001 California Building Code". *PCI Journal*. **47**(5): 102–104.

[96] Gosh, S. K. (2007). "2007 California Building Code". *PCI Journal*. **47**(4): 94–97.

[97] CBSC. *California Buildinc Code*. Falls Church, VA.: California Building Standards Commission, 2007.

[98] ICC. *International Building Code*. Falls Church, VA.: International Code Council, 2006.

[99] ASCE. *Minimum Design Loads for Buildings and Other Structures, including Supplement No. 1, ASCE/SEI 7-05*. Reston, VA.: American Society of Civil Engineers, 2006.

[100] PCBOC. *Uniform Building Code*. Los Angeles, CA.: Pacific Coast Building Officials Conference, 1946.

[101] PCBOC. *Uniform Building Code*. Los Angeles, CA.: Pacific Coast Building Officials Conference, 1955.

[102] ICBO. *Uniform Building Code*. Los Angeles, CA.: International Conference of Building Officials, 1961.

[103] ICBO. *Uniform Building Code*. Whittier, CA.: International Conference of Building Officials, 1976.

[104] ICBO. *Uniform Building Code*. Whittier, CA.: International Conference of Building Officials, 1988.

[105] ICBO. *Uniform Building Code*. Whittier, CA.: International Conference of Building Officials, 1997.

[106] United States Geological Survey (USGS). *USGS U.S. Seismic Design Maps*. Berkeley, CA., available at https://earthquake.usgs.gov/designmaps/us/application.php. Last accessed 5 April, 2018.

[107] NIST. *Seismic Design of Steel Special Moment Frames: A Guide for Practicing Engineers*. NIST GCR 09-917-3. Gaithersburg, MD.: National Institute of Standards and Technology, 2009.

[108] ICC. *International Building Code*. Falls Church, VA.: International Code Council, 2014.

[109] AISC. *Specification for Structural Steel Buildings, ANSI/AISC 360-10*. Chicago, IL., 2010.

[110] AISC. *Seismic Provisions for Structural Steel Buildings, ANSI/AISC 341-10*. Chicago, IL., 2010.

[111] American Society of Civil Engineers. *Seismic Evaluation and Retrofit of Existing Buildings, ASCE/SEI 41-13*. Reston, VA., 2013.

[112] Luco, N., Ellingwood, B. R., Hamburger, R. O., Hooper, J. D., Kimball, J. K., and Kircher, C. A. "Risk-targeted versus current seismic design maps for the conterminous United States". *SEAOC 2007 Convention Proceedings*. Squaw Creek, CA, 2007.

[113] NIST. *Selecting and Scaling Earthquake Ground Motions for Performing Response-History Analyses*. NIST GCR 11-917-15. Gaithersburg, MD.: National Institute of Standards and Technology, 2011.

[114] Baker, J. W. (2011). "Conditional Mean Spectrum: Tool for Ground-Motion Selection". *Journal of Structural Engineering*. **137**(3): 322–331.

[115] GeoPentech. *Geotechnical Investigation, LA Convention Center Hotel, Los Angeles, California*. 2007.

[116] AMEC. *Report of Geotechnical Consultation, Proposed Wilshire Grand Project*. 2012.

[117] Computers and Inc., Structures. *ETABS 2016, CSI Analysis Reference Manual*. Berkeley, CA., 2016.

[118] Gosh, S. K., Dowty, S., and Dasgupta, P. *Significan Changes to the Seismic Load Provisions of ASCE 7-10: An Illustrated Guide*. Reston, VA.: American Society of Civil Engineers, 2011.

[119] Abrahamson, N. A. and Silva, W. J. (1997). "Empirical Response Spectral Attenuation Relations for Shallow Crustal Earthquakes". *Seismological Research Letters*. **68**(1): 94–127.

[120] Sadigh, K., Chang, C. Y., Egan, J. A., Makdisi, F., and Youngs, R. R. (1997). "Attenuation Relationships for Shallow Crustal Earthquakes Based on California Strong motion Data". *Seismological Research Letters*. **68**(1): 180–189.

[121] Boore, D. M., Joyner, W. B., and Fumal, T. E. (1997). "Equations for Estimating Horiztonal Response Spectra and Peak Acceleration from Western and north American Earthquakes: A Summary of Recent Work". *Seismological Research Letters*. **68**(1): 128–153.

[122] Abrahamson, N. A. and Silva, W. J. (2008). "Summary of the Abrahamson & Silva NGA Ground-Motion Relations". *Earthquake Spectra*. **24**(1): 67–97.

[123] W., Campbell K. and Bozorgnia, Y. (2008). "NGA Ground Motion Model for Geometric Mean Horizontal Component of PGA, PGV, PGD and 5% Damped Linear Elastic Specra for Periods Ranging from 0.01 s to 10 s". *Earthquake Spectra*. **24**(1): 139–171.

[124] Chiou, B. S.-J. and Youngs, R. R. (2008). "An NGA Model for the Average Horizontal Component of Peak Ground Motion and Response Spectra". *Earthquake Spectra*. **24**(1): 173–215.

[125] FEMA (Federal Emergency Management Agency). *NEHRP Recommended Seismic Provisions*. FEMA P-750. Washington, D.C., 2009.

[126] Computers and Inc., Structures. *User Guide, PERFORM-3D, Version 5*. Berkeley, CA., 2011.

[127] ATC (Applied Technology Council). *Modeling and Acceptance Criteria for Seismic Design and Analysis for Tall Buildings*. PEER/ATC-72-1. Redwood City, CA., 2010.

[128] Jarrett, J. A., Zimmerman, R. B., Charney, F. A., and Jalalian, A. (2017). "Response-History Analysis for the Design of New Buildings in the NEHRP Provisions and ASCE/SEI 7 Standard: Part IV - A Study of Assumptions". *Earthquake Spectra*. **33**(2): 449–468.

[129] Field, E. H., Jordan, T. H., and Cornell, C. A. (2003). "OpenSHA: A Developing Community-modeling Environment for Seismic Hazard Analysis". *Seismological Research Letters*. **74**(4): 406–419.

[130] Field E. H. Arrowsmith, T. J., Biasi, G. P., Bird, P., Dawson, T. E., Felzer, K. R., Jackson, D. D., Johnson, K. M., Jordan, T. H., Madde, C., Michael, A. J., Milner, K. R., Page, M. T., Parsons, T., Bowers, P. M., Shaw, B. E., Thatcher, W. R., Weldon, R. J., and Zeng, Y. (2014). "Uniform California Earthquake Rupture Forecast, Version 3 (UCERF3) – The Time-Independent Model". *Bulletin of the Seismological Society of America*. **104**(3): 1122–1180.

[131] Moehle, J., Bozorgnia, Y., Jayaram, N., Jones, P., Rahnama, M., Shome, N., Tuna, Z., Wallace, J., Yang, T., and F., Zareian. *Case Studies of the Seismic Performance of Tall Buildings Designed by Alternative Means*. PEER 2011/05. Berkeley, CA.: Pacific Earthuake Engineering Research Center, 2011.

[132] Southern California Earthquake Center (SCEC) Committee for Utilization of Ground Motions Simulations (UGMS). *Site-Specific MCE_R & Design Response Spectra per Sect. 21.2, 21.3, 21.4 of ASCE 7-16*. Available at https://data2.scec.org/ugms-mcerGM-tool_v18.4/. Last accessed 10 April, 2018.

[133] Willis, C. J., Gutierrez, C. I., Perez, F. G., and Branum, D. M. (2015). "A Next Generation V_{S30} Map for California Based on Geology and Topography". *Bulletin of the Seismological Society of America*. **105**(6): 3083–3091.

[134] GeoPentech. *Geotechnical Investigation, New San Bernardino Courthouse, San Bernardino, California*. 2010.

[135] Haselton, C. B., Baker, J. W., Liel, A. B., and Geierlein, G. G. (2011). "Accounting for Ground-Motion Spectral Shape Characteristics in Structural Collapse Assessment through an Adjustment for Epsilon". *Journal of Structural Engineering*. **137**(3): 332–344.

[136] R. K. McGuire. *Seismic Hazard and Risk Analysis*. Oakland, CA.: Earthquake Engineering Research Institute, 2004.

[137] ICC. *International Building Code*. Falls Church, VA.: International Code Council, 2017.

[138] Boore, D. M., Stewart, J. P., Seyhan, E., and Atkinson, G. M. (2014). "NGA-West2 Equations for Predicting PGA, PGV, and 5% Damped PSA for Shallow Crustal Earthquakes". *Earthquake Spectra*. **30**(3): 1057–1085.

[139] Abrahamson, N. A., Silva, W. J., and Kamai, R. (2014). "Summary of the ASK14 Ground Motion Relation for Active Crustal Regions". *Earthquake Spectra*. **30**(3): 1025–1055.

Appendix A

DESIGN INFORMATION FOR 55-STORY MODEL

The 55-story Frame-2d model described in Chapter 2 for use in the study in Chapter 4 is based on a design by Dr. Abel Dizon, who generously provided the design information of a 55-story SMF according to the 1994 UBC for study in this dissertation. In this appendix, the design information provided by Dr. Dizon is presented. This design is similar to a 60-story SMF whose design is outlined in Chapter 8 of Dizon [21].

The plan view of a typical floor is shown in Figure A.1. The height of every story is 3.96 meters (13 feet) except the first story, which is 6.10 meters (20 feet). Column splices occur every two stories except for a column splice located after the first story. MF beams are designed to be the same for every two stories except the first story. Thus, the first story has unique column and beam assignments, then stories two and three have the same column and beam assignments. Similarly, stories four and five have the same column and beam assignments, and so on. Panel zone doubler plates are added automatically by Frame-2d to meet the 1994 UBC requirements, so doubler plates are not explicitly included here in design. The section properties of the exterior MF columns, interior MF columns, GF (gravity frame) columns, and MF beams are given in Table A.1. The "To story / floor" designation is meant to consolidate Table A.1, as every pair of stories and pair of floors (other than the first story and floor 2) shares identical section properties. That is, the section properties corresponding to "To story 5 / floor 6" represent the section properties for stories four and five, and floors five and six.

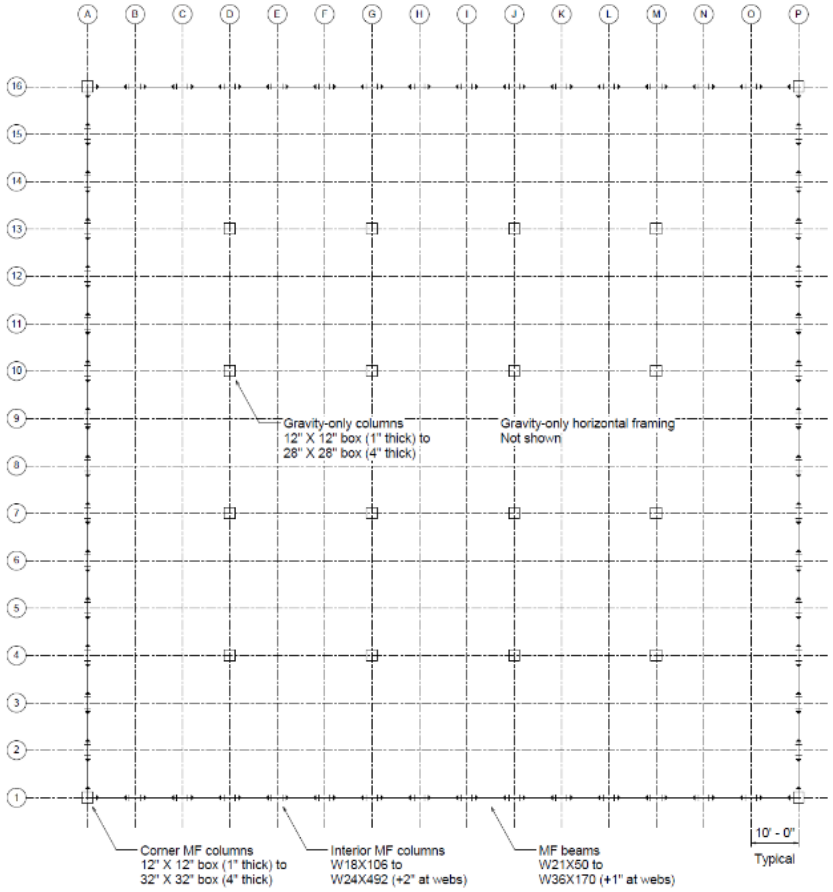

Figure A.1: Plan view of typical story for 55-story SMF design (image provided by Dr. Abel Dizon).

Table A.1: Member sizes of 55-story SMF design.

To story / floor	Column Section			MF Beam Section
	Corner MF	Interior MF	Gravity-only	
55 / Roof	HSS12X12X1	W18X106	HSS12X12X1	W21X50
53 / 54	HSS12X12X1	W18X106	HSS12X12X1	W21X50
51 / 52	HSS16X16X3/2	W18X119	HSS14X14X1	W21X55
49 / 50	HSS18X18X3/2	W18X130	HSS14X14X1	W24X62
47 / 48	HSS20X20X3/2	W21X132	HSS16X16X3/2	W24X68
45 / 46	HSS20X20X7/4	W21X147	HSS16X16X3/2	W24X76
43 / 44	HSS22X22X2	W21X166	HSS16X16X3/2	W24X84
41 / 42	HSS24X24X2	W21X182	HSS18X18X3/2	W27X84
39 / 40	HSS24X24X2	W21X1201	HSS18X18X3/2	W27X84
37 / 38	HSS24X24X5/2	W21X223	HSS18X18X3/2	W27X84
35 / 36	HSS24X24X5/2	W21X223	HSS20X20X3/2	W27X84
33 / 34	HSS26X26X5/2	W21X248	HSS20X20X7/4	W27X94
31 / 32	HSS26X26X5/2	W24X250	HSS22X22X7/4	W30X99
29 / 30	HSS28X28X5/2	W24X279	HSS22X22X7/4	W30X99
27 / 28	HSS28X28X5/2	W24X306	HSS22X22X7/4	W30X108
25 / 26	HSS28X28X5/2	W24X306	HSS22X22X2	W30X116
23 / 24	HSS28X28X5/2	W24X335	HSS24X24X2	W30X124
21 / 22	HSS28X28X5/2	W24X335	HSS24X24X2	W33X130
19 / 20	HSS28X28X5/2	W24X335	HSS26X26X2	W33X141
17 / 18	HSS28X28X5/2	W24X370	HSS26X26X2	W33X141
15 / 16	HSS28X28X5/2	W24X370	HSS28X28X2	W36X150
13 / 14	HSS28X28X3	W24X408	HSS28X28X2	W36X150
11 / 12	HSS28X28X3	W24X408	HSS28X28X2	W36X150
9 / 10	HSS28X28X7/2	W24X408	HSS28X28X2	W36X160
7 / 8	HSS28X28X4	W24X492	HSS28X28X5/2	W36X160
5 / 6	HSS30X30X4	W24X492	HSS28X28X5/2	W36X160
3 / 4	HSS30X30X4	W24X492	HSS28X28X5/2	W36X160
1 / 2	HSS32X32X4	W24X492[a]	HSS28X28X5/2	W36X170[b]

[a]Web thickened by 2".

[b]Web thickened by 1".

Appendix B

STATISTICS FROM REGRESSION FOR SUFFICIENCY

The results of regression in Section 3.4 are shown in Tables B.1-B.18. These tables show the p-value and ρ for every combination of SMF model, EDP, IM, and earthquake characteristic (M, R_{JB}, and $\varepsilon(T_1)$).

Table B.1: Calculated p-values and ρ from regression for all P models and EDPs to evaluate sufficiency of $Sa^{5\%}(T_1)$ with respect to M.

	MIDR = 0.03		MIDR = 0.06		MIDR = 0.1		Collapse	
Model	p-value	ρ	p-value	ρ	p-value	ρ	p-value	ρ
3P-94	0.74	-0.05	0.89	-0.02	0.28	-0.15	0.10	-0.24
3P-85	0.22	0.18	0.96	0.01	0.40	-0.12	0.22	-0.18
3P-73wD	0.59	-0.08	0.50	-0.10	0.06	-0.27	0.01	-0.34
3P-73noD	0.14	0.21	0.87	-0.02	0.43	-0.11	0.28	-0.16
9P-94	0.73	0.05	0.34	-0.14	0.75	-0.05	0.59	-0.08
9P-85	0.87	0.02	0.97	-0.01	0.84	-0.03	0.75	-0.05
9P-73wD	0.18	0.19	0.98	0.00	0.62	-0.07	0.67	-0.06
9P-73noD	0.92	-0.01	0.32	-0.14	0.06	-0.27	0.36	-0.13
20P-94	0.52	-0.09	0.63	-0.07	0.59	-0.08	0.60	-0.08
20P-85	0.18	-0.19	0.03	-0.30	0.15	-0.21	0.23	-0.17
20P-73	0.99	0.00	0.32	-0.14	0.60	-0.08	0.56	-0.08

Table B.2: Calculated p-values and ρ from regression for all P models and EDPs to evaluate sufficiency of $Sa^{70\%}(1.5T_1)$ with respect to M.

	MIDR = 0.03		MIDR = 0.06		MIDR = 0.1		Collapse	
Model	p-value	ρ	p-value	ρ	p-value	ρ	p-value	ρ
3P-94	0.12	0.22	0.08	0.25	0.62	-0.07	0.15	-0.21
3P-85	0.01	0.38	0.28	0.16	0.45	-0.11	0.33	-0.14
3P-73wD	0.11	0.23	0.15	0.21	0.38	-0.13	0.10	-0.24
3P-73noD	0.01	0.35	0.93	0.01	0.17	-0.20	0.14	-0.21
9P-94	0.56	0.08	0.54	0.09	0.83	-0.03	0.37	-0.13
9P-85	0.75	0.05	0.18	0.19	0.69	0.06	0.92	0.01
9P-73wD	0.05	0.28	0.37	0.13	0.73	-0.06	0.95	0.01
9P-73noD	0.03	0.31	0.66	0.06	0.62	-0.07	0.74	0.05
20P-94	0.46	0.11	0.69	0.06	0.56	0.08	0.56	0.08
20P-85	0.73	0.05	0.44	-0.11	0.66	-0.06	0.91	-0.02
20P-73	0.14	0.21	0.50	0.10	0.60	0.08	0.70	0.06

Table B.3: Calculated p-values and ρ from regression for all P models and EDPs to evaluate sufficiency of Sa_{avg} with respect to M.

	MIDR = 0.03		MIDR = 0.06		MIDR = 0.1		Collapse	
Model	p-value	ρ	p-value	ρ	p-value	ρ	p-value	ρ
3P-94	0.10	0.24	0.07	0.26	0.64	-0.07	0.08	-0.25
3P-85	0.02	0.32	0.61	0.07	0.33	-0.14	0.05	-0.28
3P-73wD	0.09	0.24	0.16	0.20	0.42	-0.12	0.03	-0.30
3P-73noD	0.09	0.24	0.73	-0.05	0.10	-0.24	0.01	-0.35
9P-94	0.43	0.11	0.42	0.12	0.87	0.02	0.73	-0.05
9P-85	0.32	0.14	0.10	0.24	0.30	0.15	0.51	0.10
9P-73wD	0.05	0.28	0.29	0.15	0.84	0.03	0.94	0.01
9P-73noD	0.00	0.42	0.04	0.28	0.18	0.19	0.09	0.24
20P-94	0.05	0.28	0.05	0.28	0.03	0.32	0.03	0.31
20P-85	0.07	0.25	0.40	0.12	0.30	0.15	0.19	0.19
20P-73	0.01	0.35	0.06	0.26	0.06	0.27	0.08	0.25

Table B.4: Calculated p-values and ρ from regression for all P models and EDPs to evaluate sufficiency of $Sa^{5\%}(T_1)$ with respect to $\log(R_{JB})$.

	MIDR = 0.03		MIDR = 0.06		MIDR = 0.1		Collapse	
Model	p-value	ρ	p-value	ρ	p-value	ρ	p-value	ρ
3P-94	0.26	-0.16	0.77	-0.04	0.69	-0.06	0.03	-0.31
3P-85	0.96	-0.01	0.84	-0.03	0.44	-0.11	0.71	-0.05
3P-73wD	0.86	-0.03	0.75	-0.05	0.55	-0.09	0.10	-0.23
3P-73noD	0.77	-0.04	0.99	0.00	0.41	-0.12	0.78	0.04
9P-94	0.37	-0.13	0.28	-0.16	0.38	-0.13	0.25	-0.17
9P-85	0.22	-0.18	0.35	-0.13	0.40	-0.12	0.07	-0.26
9P-73wD	0.18	-0.19	0.29	-0.15	0.28	-0.16	0.22	-0.18
9P-73noD	0.69	-0.06	0.92	0.02	0.61	-0.07	0.40	-0.12
20P-94	0.89	-0.02	0.46	-0.11	0.27	-0.16	0.25	-0.17
20P-85	0.68	0.06	0.51	-0.10	0.48	-0.10	0.44	-0.11
20P-73	0.36	-0.13	0.42	-0.12	0.32	-0.14	0.24	-0.17

Table B.5: Calculated p-values and ρ from regression for all P models and EDPs to evaluate sufficiency of $Sa^{70\%}(1.5T_1)$ with respect to $\log(R_{JB})$.

	MIDR = 0.03		MIDR = 0.06		MIDR = 0.1		Collapse	
Model	p-value	ρ	p-value	ρ	p-value	ρ	p-value	ρ
3P-94	0.29	-0.15	0.71	0.05	0.82	0.03	0.02	-0.33
3P-85	0.99	-0.00	0.63	0.07	0.33	-0.14	0.83	-0.03
3P-73wD	0.74	-0.05	0.79	-0.04	0.66	-0.06	0.17	-0.20
3P-73noD	0.39	-0.13	0.89	0.02	0.09	-0.24	0.81	0.03
9P-94	0.88	-0.02	0.22	-0.18	0.84	-0.03	0.66	-0.06
9P-85	0.02	-0.32	0.62	-0.07	0.91	0.02	0.24	-0.17
9P-73wD	0.15	-0.21	0.12	-0.23	0.62	-0.07	0.27	-0.16
9P-73noD	0.33	-0.14	0.45	0.11	0.63	-0.07	0.31	-0.15
20P-94	0.97	0.01	0.38	-0.13	0.53	-0.09	0.48	-0.10
20P-85	0.37	0.13	0.93	0.01	0.75	-0.05	0.64	-0.07
20P-73	0.66	-0.06	0.52	-0.09	0.41	-0.12	0.26	-0.16

Table B.6: Calculated p-values and ρ from regression for all P models and EDPs to evaluate sufficiency of Sa_{avg} with respect to $\log(R_{JB})$.

	MIDR = 0.03		MIDR = 0.06		MIDR = 0.1		Collapse	
Model	p-value	ρ	p-value	ρ	p-value	ρ	p-value	ρ
3P-94	0.70	0.06	0.04	0.29	0.12	0.22	0.25	-0.17
3P-85	0.22	0.18	0.05	0.28	0.49	0.10	1.00	0.00
3P-73wD	0.30	0.15	0.15	0.20	0.25	0.17	0.48	-0.10
3P-73noD	0.61	0.07	0.15	0.21	0.99	0.00	0.76	0.04
9P-94	0.32	0.14	0.36	0.13	0.30	0.15	0.46	0.11
9P-85	0.91	0.02	0.16	0.20	0.08	0.25	0.86	0.03
9P-73wD	0.83	-0.03	0.81	0.04	0.23	0.17	0.98	0.00
9P-73noD	0.11	0.23	0.01	0.39	0.05	0.28	0.18	0.19
20P-94	0.05	0.28	0.04	0.30	0.10	0.24	0.12	0.22
20P-85	0.00	0.41	0.02	0.33	0.05	0.28	0.09	0.24
20P-73	0.21	0.18	0.07	0.26	0.10	0.23	0.18	0.19

Table B.7: Calculated p-values and ρ from regression for all P models and EDPs to evaluate sufficiency of $Sa^{5\%}(T_1)$ with respect to $\varepsilon(T_1)$.

	MIDR = 0.03		MIDR = 0.06		MIDR = 0.1		Collapse	
Model	p-value	ρ	p-value	ρ	p-value	ρ	p-value	ρ
3P-94	0.03	0.30	0.00	0.43	0.00	0.46	0.01	0.36
3P-85	0.00	0.39	0.04	0.30	0.05	0.28	0.01	0.35
3P-73wD	0.01	0.38	0.00	0.42	0.01	0.35	0.01	0.37
3P-73noD	0.02	0.32	0.10	0.23	0.04	0.29	0.04	0.29
9P-94	0.01	0.38	0.02	0.32	0.02	0.33	0.02	0.34
9P-85	0.00	0.47	0.00	0.42	0.02	0.33	0.02	0.34
9P-73wD	0.01	0.38	0.01	0.36	0.03	0.31	0.02	0.34
9P-73noD	0.00	0.47	0.00	0.41	0.00	0.51	0.00	0.42
20P-94	0.00	0.58	0.00	0.57	0.00	0.58	0.00	0.59
20P-85	0.00	0.53	0.00	0.47	0.00	0.54	0.00	0.55
20P-73	0.60	0.08	0.00	0.48	0.00	0.48	0.00	0.50

Table B.8: Calculated p-values and ρ from regression for all P models and EDPs to evaluate sufficiency of $Sa^{70\%}(1.5T_1)$ with respect to $\varepsilon(T_1)$.

	MIDR = 0.03		MIDR = 0.06		MIDR = 0.1		Collapse	
Model	p-value	ρ	p-value	ρ	p-value	ρ	p-value	ρ
3P-94	0.09	-0.24	0.40	0.12	0.05	0.28	0.15	0.21
3P-85	0.61	-0.07	0.84	-0.03	0.74	-0.05	0.50	0.10
3P-73wD	0.21	-0.18	0.63	0.07	0.69	0.06	0.31	0.15
3P-73noD	0.30	-0.15	0.73	-0.05	0.92	0.02	0.71	0.05
9P-94	0.39	0.12	0.54	0.09	0.15	0.20	0.08	0.25
9P-85	0.76	0.04	0.13	0.22	0.18	0.19	0.17	0.20
9P-73wD	0.60	0.08	0.69	0.06	0.29	0.15	0.14	0.21
9P-73noD	0.95	-0.01	0.13	0.21	0.02	0.33	0.06	0.27
20P-94	0.19	0.19	0.00	0.40	0.01	0.37	0.01	0.38
20P-85	0.50	0.10	0.10	0.23	0.01	0.36	0.01	0.37
20P-73	0.01	-0.38	0.18	0.19	0.01	0.35	0.01	0.38

Table B.9: Calculated p-values and ρ from regression for all P models and EDPs to evaluate sufficiency of Sa_{avg} with respect to $\varepsilon(T_1)$.

	MIDR = 0.03		MIDR = 0.06		MIDR = 0.1		Collapse	
Model	p-value	ρ	p-value	ρ	p-value	ρ	p-value	ρ
3P-94	0.37	-0.13	0.07	0.26	0.01	0.38	0.02	0.33
3P-85	0.99	0.00	0.41	0.12	0.34	0.14	0.12	0.22
3P-73wD	0.52	-0.09	0.18	0.19	0.19	0.19	0.04	0.29
3P-73noD	0.89	-0.02	0.53	0.09	0.21	0.18	0.26	0.16
9P-94	0.14	0.21	0.10	0.23	0.02	0.34	0.00	0.41
9P-85	0.05	0.27	0.01	0.35	0.03	0.30	0.03	0.32
9P-73wD	0.45	0.11	0.10	0.24	0.04	0.29	0.01	0.36
9P-73noD	0.27	0.16	0.05	0.28	0.00	0.39	0.01	0.37
20P-94	0.01	0.36	0.00	0.45	0.00	0.47	0.00	0.48
20P-85	0.05	0.28	0.01	0.37	0.00	0.47	0.00	0.48
20P-73	0.05	-0.28	0.01	0.34	0.00	0.42	0.00	0.46

Table B.10: Calculated p-values and ρ from regression for all B models and EDPs to evaluate sufficiency of $Sa^{5\%}(T_1)$ with respect to M.

	MIDR = 0.03		MIDR = 0.06		MIDR = 0.1		Collapse	
Model	p-value	ρ	p-value	ρ	p-value	ρ	p-value	ρ
3B-94	0.33	-0.14	0.81	-0.03	0.72	0.05	0.31	0.15
3B-85	0.18	0.19	0.67	0.06	0.36	0.13	0.18	0.19
3B-73wD	0.83	-0.03	0.62	-0.07	0.83	0.03	0.37	0.13
3B-73noD	0.23	0.17	0.42	0.12	0.26	0.16	0.06	0.27
9B-94	0.91	-0.02	0.59	-0.08	0.74	-0.05	0.89	-0.02
9B-85	0.74	0.05	0.94	-0.01	0.86	-0.03	0.86	0.03
9B-73wD	0.64	0.07	0.76	-0.05	0.99	-0.00	0.75	0.05
9B-73noD	0.40	-0.12	0.11	-0.23	0.06	-0.26	0.07	-0.26
20B-94	0.57	-0.08	0.20	-0.19	0.16	-0.20	0.12	-0.22
20B-85	0.04	-0.28	0.05	-0.28	0.09	-0.24	0.11	-0.23
20B-73	0.26	-0.16	0.03	-0.31	0.08	-0.25	0.09	-0.24

Table B.11: Calculated p-values and ρ from regression for all B models and EDPs to evaluate sufficiency of $Sa^{70\%}(1.5T_1)$ with respect to M.

	MIDR = 0.03		MIDR = 0.06		MIDR = 0.1		Collapse	
Model	p-value	ρ	p-value	ρ	p-value	ρ	p-value	ρ
3B-94	0.31	0.15	0.46	0.11	0.37	0.13	0.10	0.24
3B-85	0.01	0.37	0.19	0.19	0.02	0.32	0.02	0.34
3B-73wD	0.05	0.28	0.14	0.21	0.09	0.24	0.03	0.31
3B-73noD	0.05	0.28	0.30	0.15	0.17	0.20	0.02	0.33
9B-94	0.19	0.19	0.84	0.03	0.90	-0.02	0.63	0.07
9B-85	0.07	0.26	0.39	0.12	0.53	0.09	0.31	0.15
9B-73wD	0.11	0.23	0.46	0.11	0.31	0.15	0.17	0.20
9B-73noD	0.03	0.30	0.77	0.04	0.48	-0.10	0.52	-0.09
20B-94	0.44	0.11	0.81	-0.04	0.71	-0.05	0.61	-0.07
20B-85	0.58	0.08	0.68	-0.06	0.44	-0.11	0.38	-0.13
20B-73	0.32	0.14	0.67	-0.06	0.36	-0.13	0.35	-0.14

Table B.12: Calculated p-values and ρ from regression for all B models and EDPs to evaluate sufficiency of Sa_{avg} with respect to M.

	MIDR = 0.03		MIDR = 0.06		MIDR = 0.1		Collapse	
Model	p-value	ρ	p-value	ρ	p-value	ρ	p-value	ρ
3B-94	0.13	0.22	0.37	0.13	0.21	0.18	0.07	0.26
3B-85	0.03	0.30	0.34	0.14	0.05	0.28	0.03	0.31
3B-73wD	0.03	0.31	0.09	0.24	0.05	0.28	0.02	0.33
3B-73noD	0.14	0.21	0.86	0.03	0.39	0.12	0.12	0.22
9B-94	0.21	0.18	0.84	0.03	0.78	0.04	0.59	0.08
9B-85	0.06	0.27	0.30	0.15	0.42	0.12	0.27	0.16
9B-73wD	0.11	0.23	0.42	0.12	0.22	0.18	0.13	0.22
9B-73noD	0.01	0.38	0.11	0.23	0.21	0.18	0.16	0.20
20B-94	0.14	0.21	0.51	0.09	0.69	0.06	0.76	0.04
20B-85	0.06	0.27	0.23	0.17	0.37	0.13	0.54	0.09
20B-73	0.02	0.33	0.43	0.11	0.63	0.07	0.70	0.06

Table B.13: Calculated p-values and ρ from regression for all B models and EDPs to evaluate sufficiency of $Sa^{5\%}(T_1)$ with respect to $\log(R_{JB})$.

	MIDR = 0.03		MIDR = 0.06		MIDR = 0.1		Collapse	
Model	p-value	ρ	p-value	ρ	p-value	ρ	p-value	ρ
3B-94	0.12	-0.22	0.43	-0.12	0.06	-0.27	0.14	-0.21
3B-85	0.49	-0.10	0.09	-0.24	0.01	-0.34	0.01	-0.38
3B-73wD	0.31	-0.15	0.27	-0.16	0.04	-0.30	0.01	-0.34
3B-73noD	0.42	-0.12	0.13	-0.22	0.07	-0.26	0.08	-0.25
9B-94	0.35	-0.13	0.17	-0.20	0.03	-0.32	0.01	-0.38
9B-85	0.19	-0.19	0.08	-0.25	0.06	-0.27	0.05	-0.28
9B-73wD	0.15	-0.21	0.12	-0.22	0.03	-0.31	0.03	-0.31
9B-73noD	0.33	-0.14	0.36	-0.13	0.64	-0.07	0.61	-0.07
20B-94	0.01	0.35	0.00	0.46	0.00	0.40	0.00	0.41
20B-85	0.05	-0.27	0.40	-0.12	0.19	-0.19	0.22	-0.18
20B-73	0.06	-0.27	0.10	-0.24	0.09	-0.24	0.12	-0.23

Table B.14: Calculated p-values and ρ from regression for all B models and EDPs to evaluate sufficiency of $Sa^{70\%}(1.5T_1)$ with respect to $\log(R_{JB})$.

	MIDR = 0.03		MIDR = 0.06		MIDR = 0.1		Collapse	
Model	p-value	ρ	p-value	ρ	p-value	ρ	p-value	ρ
3B-94	0.24	-0.17	0.44	-0.11	0.02	-0.33	0.06	-0.27
3B-85	0.49	-0.10	0.01	-0.34	0.00	-0.46	0.00	-0.45
3B-73wD	0.18	-0.19	0.33	-0.14	0.06	-0.27	0.06	-0.27
3B-73noD	0.12	-0.22	0.01	-0.35	0.03	-0.30	0.03	-0.30
9B-94	0.42	-0.12	0.22	-0.18	0.01	-0.38	0.00	-0.43
9B-85	0.12	-0.22	0.03	-0.31	0.03	-0.31	0.03	-0.30
9B-73wD	0.19	-0.19	0.16	-0.20	0.02	-0.33	0.02	-0.32
9B-73noD	0.53	-0.09	0.55	-0.09	0.44	-0.11	0.44	-0.11
20B-94	0.01	0.37	0.00	0.53	0.00	0.52	0.00	0.52
20B-85	0.86	-0.03	0.07	-0.26	0.03	-0.31	0.08	-0.25
20B-73	0.80	-0.04	0.52	-0.09	0.04	-0.30	0.05	-0.27

Table B.15: Calculated p-values and ρ from regression for all B models and EDPs to evaluate sufficiency of Sa_{avg} with respect to $\log(R_{JB})$.

	MIDR = 0.03		MIDR = 0.06		MIDR = 0.1		Collapse	
Model	p-value	ρ	p-value	ρ	p-value	ρ	p-value	ρ
3B-94	0.85	0.03	0.51	0.09	0.17	-0.20	0.18	-0.19
3B-85	0.45	0.11	0.62	-0.07	0.10	-0.24	0.03	-0.32
3B-73wD	0.98	-0.00	0.90	-0.02	0.20	-0.18	0.14	-0.21
3B-73noD	0.94	0.01	0.77	-0.04	0.42	-0.12	0.20	-0.19
9B-94	0.57	0.08	0.79	-0.04	0.09	-0.24	0.06	-0.27
9B-85	0.90	0.02	0.50	-0.10	0.35	-0.14	0.36	-0.13
9B-73wD	0.96	-0.01	0.69	-0.06	0.17	-0.20	0.16	-0.20
9B-73noD	0.17	0.20	0.04	0.29	0.09	0.24	0.10	0.23
20B-94	0.00	0.53	0.00	0.66	0.00	0.60	0.00	0.63
20B-85	0.02	0.32	0.15	0.21	0.49	0.10	0.52	0.09
20B-73	0.17	0.20	0.30	0.15	0.71	0.05	0.68	0.06

Table B.16: Calculated p-values and ρ from regression for all B models and EDPs to evaluate sufficiency of $Sa^{5\%}(T_1)$ with respect to $\varepsilon(T_1)$.

	MIDR = 0.03		MIDR = 0.06		MIDR = 0.1		Collapse	
Model	p-value	ρ	p-value	ρ	p-value	ρ	p-value	ρ
3B-94	0.12	0.22	0.04	0.29	0.04	0.29	0.04	0.29
3B-85	0.02	0.32	0.06	0.27	0.06	0.26	0.20	0.18
3B-73wD	0.10	0.23	0.03	0.30	0.18	0.19	0.66	0.06
3B-73noD	0.02	0.32	0.18	0.19	0.15	0.21	0.11	0.23
9B-94	0.04	0.30	0.01	0.36	0.00	0.41	0.01	0.38
9B-85	0.00	0.45	0.00	0.41	0.00	0.54	0.00	0.52
9B-73wD	0.01	0.35	0.01	0.37	0.01	0.37	0.01	0.39
9B-73noD	0.00	0.43	0.01	0.39	0.00	0.51	0.00	0.50
20B-94	0.00	0.43	0.00	0.44	0.00	0.48	0.00	0.47
20B-85	0.00	0.43	0.00	0.59	0.00	0.60	0.00	0.55
20B-73	0.07	0.26	0.01	0.37	0.00	0.48	0.00	0.45

Table B.17: Calculated p-values and ρ from regression for all B models and EDPs to evaluate sufficiency of $Sa^{70\%}(1.5T_1)$ with respect to $\varepsilon(T_1)$.

	MIDR = 0.03		MIDR = 0.06		MIDR = 0.1		Collapse	
Model	p-value	ρ	p-value	ρ	p-value	ρ	p-value	ρ
3B-94	0.02	-0.34	0.94	-0.01	0.86	-0.03	0.98	0.00
3B-85	0.21	-0.18	0.58	-0.08	0.36	-0.13	0.33	-0.14
3B-73wD	0.02	-0.32	0.99	-0.00	0.16	-0.20	0.07	-0.26
3B-73noD	0.41	-0.12	0.33	-0.14	0.92	-0.02	0.87	0.02
9B-94	0.52	-0.09	0.88	0.02	0.08	0.25	0.13	0.21
9B-85	0.66	-0.06	0.06	0.27	0.00	0.43	0.00	0.41
9B-73wD	0.84	-0.03	0.31	0.15	0.17	0.20	0.13	0.22
9B-73noD	0.71	-0.05	0.33	0.14	0.06	0.26	0.12	0.22
20B-94	0.78	-0.04	0.42	0.12	0.18	0.19	0.12	0.22
20B-85	0.53	-0.09	0.05	0.28	0.00	0.40	0.02	0.32
20B-73	0.18	-0.19	0.47	0.10	0.09	0.24	0.11	0.23

Table B.18: Calculated p-values and ρ from regression for all B models and EDPs to evaluate sufficiency of Sa_{avg} with respect to $\varepsilon(T_1)$.

	MIDR = 0.03		MIDR = 0.06		MIDR = 0.1		Collapse	
Model	p-value	ρ	p-value	ρ	p-value	ρ	p-value	ρ
3B-94	0.06	-0.27	0.93	0.01	0.66	0.06	0.63	0.07
3B-85	0.56	-0.08	0.43	0.11	0.60	0.08	0.94	-0.01
3B-73wD	0.06	-0.26	0.69	0.06	0.33	-0.14	0.13	-0.22
3B-73noD	0.97	-0.00	0.64	0.07	0.32	0.14	0.26	0.16
9B-94	0.80	0.04	0.12	0.22	0.01	0.39	0.01	0.36
9B-85	0.32	0.14	0.01	0.34	0.00	0.47	0.00	0.44
9B-73wD	0.69	0.06	0.07	0.25	0.03	0.31	0.02	0.32
9B-73noD	0.42	0.12	0.01	0.37	0.00	0.46	0.00	0.41
20B-94	0.30	0.15	0.11	0.23	0.04	0.29	0.03	0.31
20B-85	0.31	0.15	0.00	0.50	0.00	0.58	0.00	0.50
20B-73	0.79	-0.04	0.04	0.29	0.00	0.43	0.00	0.41

Appendix C

ASCE 7-05 AND ASCE 7-10 WIND LOADS

Design of the post-Northridge SMFs incorporate wind checks for strength and serviceability drifts. The wind loads for use in the LRFD load combinations are shown for the 9-story SMFs in Table C.1 and for the 20-story SMFs in Table C.2. These are calculated from the design wind pressures tributary to each floor. The basic wind speed at the reference site is 38 m/s (85 mph) for ASCE 7-05 and (49 m/s) 110 mph for ASCE 7-10. The PBD designs use the ASCE 7-10 wind loads. For all designs, the Exposure category is assumed to be Exposure B; the wind directionality factor, K_d, is assumed to be 0.85; the topographic factor, K_{zt}, is assumed to be 1.0; the internal pressure coefficient, GC_{pi} is assumed to be ±0.18; and the external pressure coefficients C_p are assumed to be 0.8 in the windward direction and -0.5 in the leeward direction. In the relevant LFRD load combinations, there is a load factor of 1.6 on W in ASCE 7-05 and a load factor of 1.0 on W in ASCE 7-10. The changes in basic wind speed between ASCE 7-05 and ASCE 7-10 do not have a significant effect on design because the load factors are also changed. The factored wind loads of ASCE 7-05 would be slightly lower than the factored wind loads of ASCE 7-10 at the reference site for the same structure. Small deviations in the wind loads for a given design code seen in Tables C.1 and C.2 are due to differences in T_1 for the SMFs. The values of T_1 calculated via eigenvalue analysis in ETABS are used to calculate the wind loads for each design. Note that the elastic drifts calculated in response to the factored wind loads are reduced by a factor of $1.6/0.7$ for comparison to the serviceability wind drift limits.

Table C.1: Factored LRFD wind loads (1.6W for ASCE 7-05 and W for ASCE 7-10) used in the design of 9-story post-Northridge SMFs.

	Factored LRFD Wind Load (kN)					
Floor	9ELF-05	9ELF-10	9RSA-05	9RSA-10	9PBD-LL	9PBD-WG
Roof	131	141	143	144	139	159
9	256	276	280	282	272	311
8	250	270	274	276	266	305
7	244	263	267	270	259	297
6	238	256	259	262	252	289
5	230	247	251	254	244	279
4	221	238	241	243	234	268
3	209	225	228	231	222	254
2	231	249	252	254	245	281

Table C.2: Factored LRFD wind loads (1.6W for ASCE 7-05 and W for ASCE 7-10) used in the design of 20-story post-Northridge SMFs.

	Factored LRFD Wind Load (kN)			
Floor	20RSA-05	20RSA-10	20PBD-LL	20PBD-WG
Roof	148	152	164	166
20	293	302	325	329
19	290	299	322	326
18	287	296	319	323
17	284	293	316	320
16	281	290	312	316
15	278	287	309	313
14	274	284	305	309
13	271	280	301	305
12	267	276	297	301
11	263	272	293	296
10	259	267	288	291
9	254	262	282	286
8	250	258	277	281
7	244	252	271	274
6	238	245	264	267
5	231	238	256	259
4	222	230	247	250
3	212	219	235	238
2	236	243	262	265

Appendix D

ETABS AND PERFORM-3D MODELS

In Chapter 5, ten SMFs are designed using different design criteria and procedures. In analysis for design, elastic finite element models of all ten SMFs are created in ETABS [117]. Four of the SMFs are designed using performance-based procedures, which necessitate nonlinear time history analysis. In addition to the linear finite element models in ETABS, nonlinear finite element models of these four SMFs are developed in PERFORM-3D [126].

D.1 ETABS Models

General Modeling Considerations

A linear ETABS model is created for every post-Northridge SMF design. Like the Frame-2d models, the 9-story models have a pinned basement level and the 20-story models have two pinned basement levels. Each story is constrained to have a rigid diaphragm. The model consists of linear beam, column, and panel zone elements, assigned section properties according to the relevant design. Perimeter beam elements attached to columns with moment connections are assigned rigid end offsets to account for panel zone elements. Gravity beams and sub-beams are assigned pinned connections and loaded with gravity loads. An isometric view of the ETABS model of the 20RSA-05 design is shown in Figure D.1.

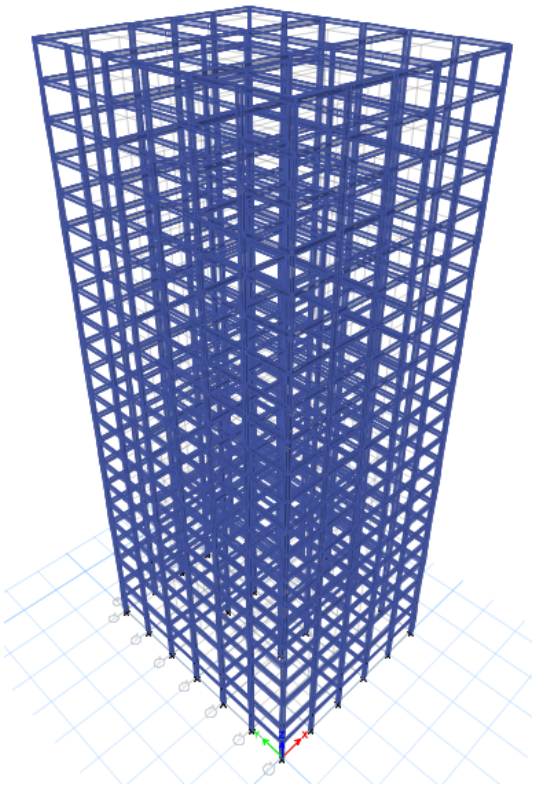

Figure D.1: Isometric view of ETABS model of the 20RSA-05 design.

Gravity loads and seismic masses are assigned according to Gupta and Krawinkler [18]. The dead load on a typical floor is 4.60 kPa (90 psf), on the roof is 3.97 kPa (83 psf), and below the roof penthouse is 5.55 kPa (116 psf). The cladding load is 1.20 kPa (25 psf) and the reduced live load (for each floor and for the roof) is 0.96 kPa (20 psf). For mass calculations, the floor dead load is 4.12 kPa (86 psf). For the 9-story SMFs, the seismic mass of the roof is 1,067 tonnes (73.1 kips $\cdot$ s^2/ft), the seismic masses of floors 3 to 9 are 990 tonnes (67.9 kips $\cdot$ s^2/ft), and the seismic mass of floor 2 is 1,008 tonnes (69.0 kips $\cdot$ s^2/ft). For the 20-story SMFs, the seismic mass of the roof is 585 tonnes (40.1 kips $\cdot$ s^2/ft), the seismic masses of floors 3 to 20 are 551 tonnes (37.8 kips $\cdot$ s^2/ft), and the seismic mass of floor 2 is 564 tonnes (38.6 kips $\cdot$ s^2/ft). Gravity loads are applied to beams and sub-beams oriented in the NS direction according to their tributary area. Seismic masses are lumped at each story. The seismic weight, W, of the 9-story models is 88,340 kN (19,860 kips) and of the 20-story models is 108,540 kN (24,400 kips).

ELF Procedure

The design period, T, for the 9ELF-05 and 9ELF-10 designs is 1.83 seconds in both cases (see Table 5.3) and the design lateral forces are applied according to the vertical distribution specified in ASCE 7-05 and ASCE 7-10. The lateral seismic force applied at each story in addition to the story shears are shown in Table D.1. These forces are applied using a linear static load case. Note from Table 5.3 that V_{drift} and V_{strength} are the same for the 9ELF-05 design but not for the 9ELF-10 design. The values shown in Table D.1 correspond to V_{strength} for both designs. Diaphragm eccentricity of 5% is assumed when calculating the demands. The loads are applied in both horizontal directions and demands are calculated according to $1.0E_x$+$0.3E_y$.

Table D.1: Vertical distribution of seismic design forces and shears for 9ELF-05 and 9ELF-10 designs.

	Seismic Design Force (kN)		Seismic Design Shear (kN)	
Floor / Story	9ELF-05	9ELF-10	9ELF-05	9ELF-10
Roof / 9	1,033	1,612	1,033	1,612
9 / 8	794	1,239	1,828	2,851
8 / 7	643	1,003	2,471	3,854
7 / 6	505	787	2,976	4,641
6 / 5	380	593	3,356	5,234
5 / 4	270	421	3,626	5,655
4 / 3	175	274	3,801	5,928
3 / 2	98	153	3,899	6,081
2 / 1	40	63	3,939	6,144

RSA Procedure

For RSA, the Response Spectrum load case is applied in ETABS with the design response spectrum of ASCE7-05 or ASCE 7-10 (see Figure 5.3), depending on the design. 5% modal damping is applied in this analysis and diaphragm eccentricity of 5% is assumed when calculating the demands. A total of 12 modes are calculated for RSA, which is more than enough for 90% mass participation in each of the horizontal directions. Modal responses are combined using the Complete Quadratic Combination (CQC) method. RSA is performed in both horizontal directions and demands are calculated according to $1.0E_x$+$0.3E_y$. The story shears in the N-S direction divided by R (8 for SMFs) calculated via RSA are shown in Table D.2 for the 9-story and 20-story designs. Where specified by ASCE 7-05 or ASCE 7-10, calculated demands are scaled by $0.85V/V_t$, where V_t is the calculated base shear from RSA.

Table D.2: Story shears in the N-S direction divided by R (8 for SMFs) calculated via RSA for 9RSA-05, 9RSA-10, 20RSA-05, and 20RSA-10 designs.

	RSA Story Shears (kN)			
Story	9RSA-05	9RSA-10	20RSA-05	20RSA-10
20	–	–	313	483
19	–	–	483	755
18	–	–	577	919
17	–	–	668	1,065
16	–	–	754	1,204
15	–	–	821	1,322
14	–	–	876	1,423
13	–	–	934	1,520
12	–	–	991	1,615
11	–	–	1,039	1,702
10	–	–	1,084	1,781
9	606	962	1,134	1,861
8	750	1,324	1,189	1,946
7	922	1,589	1,240	2,028
6	1,046	1,850	1,282	2,099
5	1,154	2,072	1,320	2,163
4	1,278	2,259	1,367	2,233
3	1,348	2,423	1,426	2,319
2	1,462	2,634	1,485	2,408
1	1,614	2,849	1,525	2,473

Service Level Evaluation

For SLE checks of the PBD designs, the Response Spectrum load case is applied in ETABS with the design response spectrum given in the LL or WG report (see Figure 5.7), depending on the design. Per the LATBSDC alternate procedure, 2.5% modal damping is applied in this analysis. Modal responses are combined using the Complete Quadratic Combination (CQC) method. RSA is performed in both horizontal directions and demands are calculated according to $1.0E_x$+$0.3E_y$. A total of 12 modes are calculated for RSA. The story shears in the N-S direction calculated via RSA are shown in Table D.3 for the 9-story and 20-story designs.

Table D.3: Story shears in the N-S direction calculated via RSA for SLE checks of the 9PBD-LL, 9PBD-WG, 20PBD-LL, and 20PBD-WG designs.

	RSA Story Shears for SLE Checks (kN)			
Story	9PBD-LL	9PBD-WG	20PBD-LL	20PBD-WG
20	–	–	856	611
19	–	–	1,348	904
18	–	–	1,651	1,032
17	–	–	1,833	1,156
16	–	–	2,023	1,268
15	–	–	2,172	1,341
14	–	–	2,278	1,401
13	–	–	2,373	1,470
12	–	–	2,472	1,541
11	–	–	2,565	1,600
10	–	–	2,652	1,653
9	2,362	1,054	2,753	1,718
8	3,545	1,302	2,877	1,798
7	4,446	1,502	3,011	1,877
6	5,223	1,678	3,139	1,946
5	5,893	1,786	3,266	2,016
4	6,508	1,937	3,409	2,106
3	7,053	2,041	3,575	2,224
2	7,568	2,222	3,736	2,345
1	7,986	2,500	3,847	2,430

D.2 PERFORM-3D Models

General Modeling Considerations

Nonlinear PERFORM-3D models are created for the 9PBD-LL, 9PBD-WG, 20PBD-LL, and 20PBD-WG designs in order to perform nonlinear time history analysis, which is necessary for the MCE checks. These models have the same boundary conditions, diaphragm constraints, releases, and seismic masses as the corresponding ETABS models. The gravity loads are the same but they are applied directly to columns instead of to beams and sub-beams because sub-beams are not modeled in PERFORM-3D. $P-\Delta$ effects are incorporated. Beam, column, and panel zone elements are assigned nonlinear properties, which are detailed in the remainder of this section. An isometric view of the PERFORM-3D model of the 20PBD-LL design is shown in D.2.

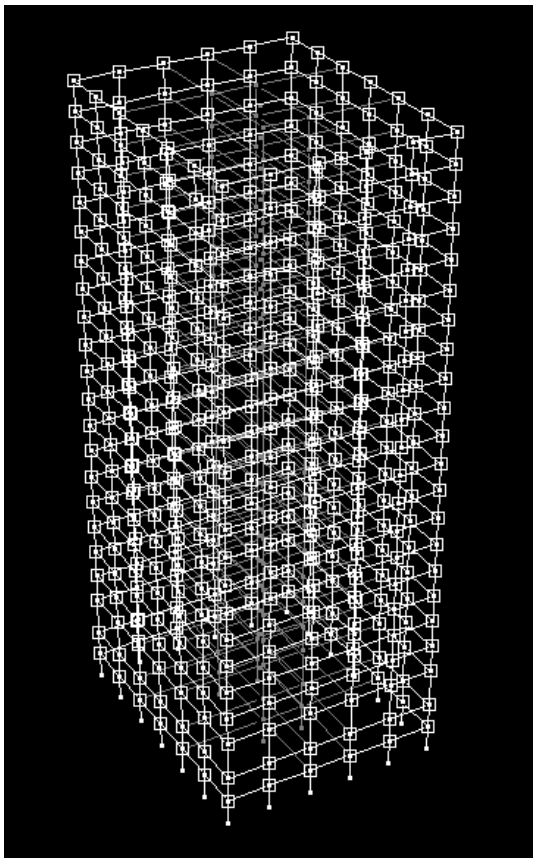

Figure D.2: Isometric view of PERFORM-3D model of the 20PBD-LL design.

Beam Elements

Beams included in the perimeter moment frames are expected to experience non-linear behavior during MCE shaking. The "FEMA Beam" inelastic component is implemented in PERFORM-3D to model this behavior. The backbone curve of the moment-rotation relation for this component is shown in Figure D.3. In PERFORM-3D, each FEMA Beam element is uniquely defined by FU (maximum moment), DL (rotation at which strain softening begins), and DR (rotation at which the residual moment is reached). These values are calculated for each beam size according to ATC-72-1 [127] for non-RBS beams. The value of FR/FU (residual moment as fraction of maximum moment) is set to 0.28 for every FEMA Beam element, as specified by ATC-72-1. Cyclic degradation is not modeled explicitly, so the backbone curve is modified per requirements of ATC-72-1 and the LATBSDC alternate procedure [23].

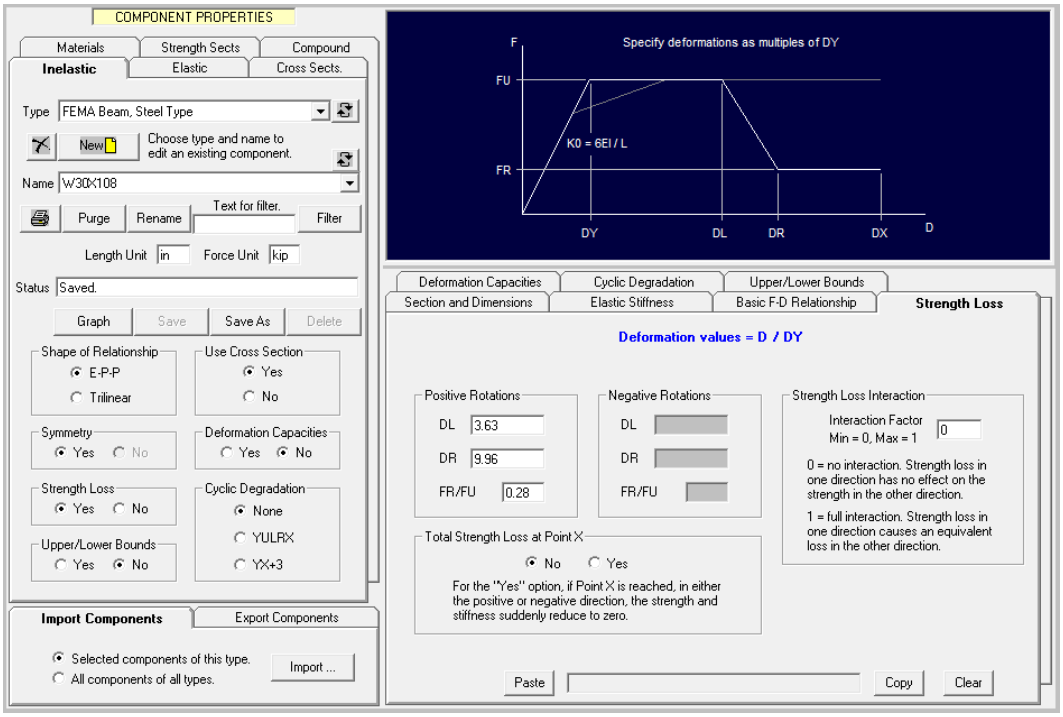

Figure D.3: Backbone curve definition of FEMA Beam component in PERFORM-3D. In this example, strength loss entries for a W30X108 beam is shown.

Column Elements

Nonlinear behavior is generally not expected in moment frame columns during MCE shaking, but plastic rotations at the base of first-story columns can occur. To be conservative, the "FEMA Column" inelastic component is implemented in PERFORM-3D to model all perimeter moment frame columns. ATC-72-1 does not provide much guidance for modeling steel moment frame columns, but does suggest that it is crucial to model P-M-M interaction. The default settings for P-M-M interaction are specified in PERFORM-3D, with the yield surface shown in Figure D.4. Beyond yield, behavior is elastic-perfectly-plastic. The yield axial force (PU) in tension and compression is specified as

$$PU = R_y F_y A, \tag{D.1}$$

as suggested by ASCE 41-13, where $R_y = 1.1$ and $F_y = 345$ MPa (50 ksi) for A992 steel and A is the cross-section area. The yield moment in bending in the strong and weak axes are specified to be the same as for beams according to ATC-72-1. Additional details about the FEMA Column element are available in the PERFORM-3D manual [126].

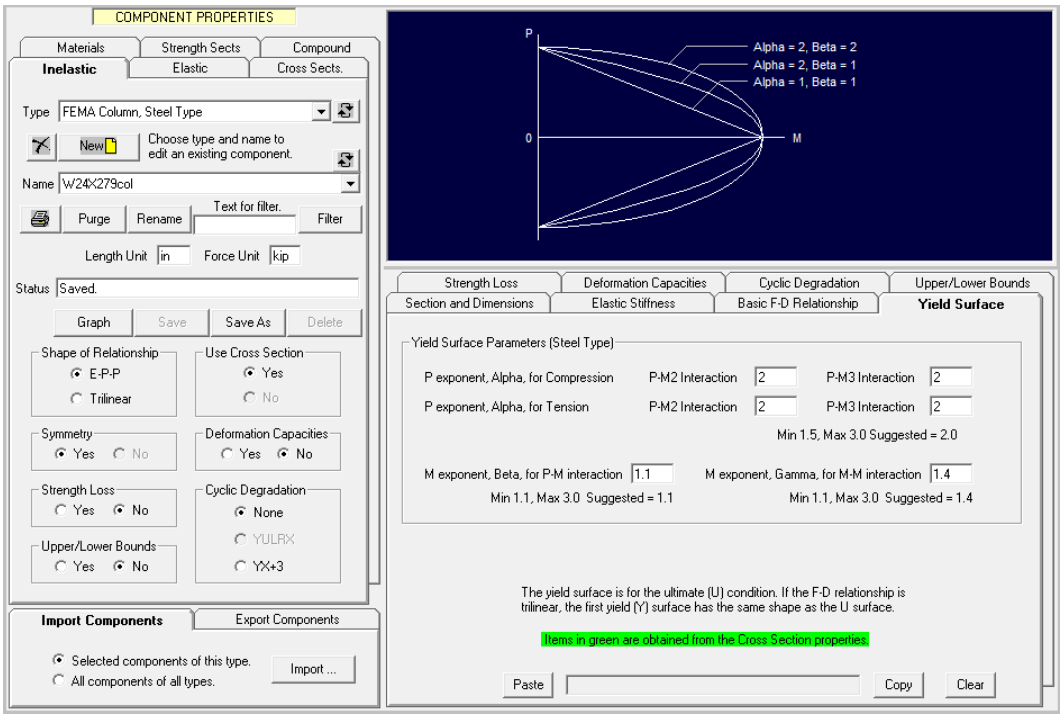

Figure D.4: P-M-M interaction yield surface definition of FEMA Column component in PERFORM-3D. In this example, the default yield surface parameters are shown.

The panel zone of each column is modeled with a nonlinear element according to the default trilinear element in PERFORM-3D, although no panel zone element is observed to yield during any of the MCE nonlinear time history analyses. Further information about the default panel zone element in PERFORM-3D is available in the PERFORM-3D manual [126].

Appendix E

DESIGN INFORMATION FOR POST-NORTHRIDGE MODELS

In this appendix, design information is provided for the post-Northridge designs created in Chapter 5. It should be noted that results from wind load combinations are not shown here. Wind load combinations only controlled the design of members through serviceability drift requirements, which were reported where relevant in Sections 5.4 and 5.5. As such, D/C ratios from wind load combinations are not reported here.

E.1 ELF and RSA Designs

Tables E.1-5.9 show demand-capacity ratios (D/C ratios) and column-beam strength ratios (SC/WB ratios) for the 9ELF-05, 9ELF-10, 9RSA-05, 9RSA-10, 20RSA-05, and 20RSA-10 designs. In each table, a single value is given per floor. The reported value is the largest D/C ratio and the smallest SC/WB ratio per floor. D/C ratios greater than 1.0 and SC/WB ratios less than 1.0 are not permitted. The reported values are calculated from the two LRFD seismic load cases:

$$\begin{aligned} 1.2D + 1.0E + L \\ 0.9D + 1.0E. \end{aligned} \tag{E.1}$$

ASCE 7-05 and ASCE 7-10 are followed for the application of seismic loads. ETABS models created for each design according to Section D.1 of Appendix D are used to calculate demands. AISC 360-10 is followed to compute LRFD D/C ratios from the calculated demands and AISC 341-10 is followed to compute SC/WB ratios. Note that the relevant equations in AISC 341 and AISC 360 do not change from their 2005 versions to their 2010 versions. Per AISC 341-10, axial forces in columns to calculate D/C ratios are calculated from the amplified seismic load, which is multiplied by the overstrength factor, Ω_0, which equals 3.0 for SMFs.

D/C ratios for beams rarely control design. Beam sizes are usually governed by drift requirements. The only exception is the 20RSA-05 design, for which beam design in the upper stories is controlled by D/C ratios. D/C ratios for columns sometimes control design. If they do, it is usually at lower stories and/or for the exterior columns. SC/WB ratios frequently control design of columns.

Table E.1: Demand-capacity ratios (D/C ratios) and column-beam strength ratios (SC/WB ratios) for the 9ELF-05 design.

	D/C Ratio			SC/WB Ratio	
Story / Floor	Ext. Column	Int. Column	Beam	Exterior	Interior
9 / Roof	0.17	0.13	0.43	2.19	2.65
8 / 9	0.22	0.18	0.39	1.81	2.22
7 / 8	0.19	0.19	0.38	1.80	1.86
6 / 7	0.23	0.22	0.38	1.69	1.56
5 / 6	0.38	0.24	0.39	1.58	1.59
4 / 5	0.47	0.35	0.40	1.28	1.41
3 / 4	0.48	0.40	0.41	1.32	1.34
2 / 3	0.55	0.47	0.41	1.35	1.28
1 / 2	0.91	0.79	0.39	1.34	1.21
-1 / 1	0.81	0.71	0.13	1.31	1.10

Table E.2: Demand-capacity ratios (D/C ratios) and column-beam strength ratios (SC/WB ratios) for the 9ELF-10 design.

	D/C Ratio			SC/WB Ratio	
Story / Floor	Beam	Ext. Column	Int. Column	Exterior	Interior
9 / Roof	0.30	0.15	0.51	1.88	2.54
8 / 9	0.36	0.22	0.48	1.56	2.15
7 / 8	0.27	0.25	0.51	1.53	1.70
6 / 7	0.44	0.31	0.50	1.60	1.53
5 / 6	0.47	0.30	0.50	1.29	1.31
4 / 5	0.57	0.42	0.51	1.29	1.31
3 / 4	0.57	0.48	0.51	1.24	1.39
2 / 3	0.66	0.56	0.51	1.28	1.21
1 / 2	0.86	0.71	0.48	1.26	1.14
-1 / 1	0.73	0.57	0.14	1.29	1.19

Table E.3: Demand-capacity ratios (D/C ratios) and column-beam strength ratios (SC/WB ratios) for the 9RSA-05 design.

	D/C Ratio			SC/WB Ratio	
Story / Floor	Ext. Column	Int. Column	Beam	Exterior	Interior
9 / Roof	0.51	0.38	0.66	1.40	1.29
8 / 9	0.58	0.46	0.76	1.90	1.76
7 / 8	0.60	0.38	0.80	1.65	1.84
6 / 7	0.53	0.77	0.73	1.50	1.94
5 / 6	0.71	0.50	0.74	1.20	1.63
4 / 5	0.81	0.57	0.76	1.24	1.77
3 / 4	0.71	0.59	0.74	1.34	1.59
2 / 3	0.82	0.71	0.72	1.56	1.59
1 / 2	0.92	0.85	0.64	1.37	1.28
-1 / 1	0.82	0.71	0.22	1.47	1.29

Table E.4: Demand-capacity ratios (D/C ratios) and column-beam strength ratios (SC/WB ratios) for the 9RSA-10 design.

	D/C Ratio			SC/WB Ratio	
Story / Floor	Ext. Column	Int. Column	Beam	Exterior	Interior
9 / Roof	0.34	0.20	0.54	1.69	2.30
8 / 9	0.38	0.27	0.51	1.59	2.20
7 / 8	0.32	0.26	0.50	1.46	1.74
6 / 7	0.48	0.31	0.51	1.52	1.63
5 / 6	0.52	0.39	0.54	1.49	1.65
4 / 5	0.63	0.47	0.54	1.34	1.52
3 / 4	0.61	0.47	0.53	1.11	1.24
2 / 3	0.71	0.54	0.54	1.13	1.25
1 / 2	0.95	0.78	0.53	1.07	1.18
-1 / 1	0.80	0.62	0.17	1.05	1.12

Table E.5: Demand-capacity ratios (D/C ratios) and column-beam strength ratios (SC/WB ratios) for the 20RSA-05 design.

	D/C Ratio			SC/WB Ratio	
Story / Floor	Ext. Column	Int. Column	Beam	Exterior	Interior
20 / Roof	0.44	0.28	0.55	1.10	1.34
19 / 20	0.51	0.39	0.73	1.75	2.20
18 / 19	0.59	0.39	0.80	1.81	2.12
17 / 18	0.66	0.50	0.79	1.56	1.73
16 / 17	0.60	0.46	0.86	1.91	1.89
15 / 16	0.70	0.54	0.91	2.26	2.06
14 / 15	0.76	0.60	0.88	1.85	1.72
13 / 14	0.61	0.52	0.92	2.42	1.95
12 / 13	0.69	0.59	0.93	2.98	2.20
11 / 12	0.75	0.62	0.83	2.15	1.62
10 / 11	0.71	0.56	0.83	2.27	1.79
9 / 10	0.78	0.59	0.78	2.12	1.76
8 / 9	0.81	0.63	0.73	1.74	1.50
7 / 8	0.64	0.66	0.75	2.41	1.45
6 / 7	0.67	0.67	0.77	2.83	1.28
5 / 6	0.71	0.70	0.75	2.69	1.24
4 / 5	0.75	0.66	0.75	2.55	1.31
3 / 4	0.79	0.68	0.72	2.19	1.27
2 / 3	0.84	0.73	0.71	2.05	1.23
1 / 2	0.93	0.87	0.69	2.02	1.05
-1 / 1	0.68	0.65	0.25	3.18	1.02

Table E.6: Demand-capacity ratios (D/C ratios) and column-beam strength ratios (SC/WB ratios) for the 20RSA-10 design.

	D/C Ratio			SC/WB Ratio	
Story / Floor	Ext. Column	Int. Column	Beam	Exterior	Interior
20 / Roof	0.26	0.18	0.49	2.46	2.14
19 / 20	0.36	0.26	0.58	2.41	2.15
18 / 19	0.47	0.27	0.67	2.27	2.71
17 / 18	0.56	0.29	0.59	1.29	1.97
16 / 17	0.52	0.28	0.62	1.62	2.15
15 / 16	0.59	0.31	0.65	1.79	2.14
14 / 15	0.68	0.35	0.64	1.53	1.90
13 / 14	0.67	0.44	0.63	1.41	1.62
12 / 13	0.74	0.49	0.64	1.46	1.57
11 / 12	0.79	0.53	0.63	1.23	1.40
10 / 11	0.62	0.50	0.64	1.67	1.44
9 / 10	0.69	0.56	0.65	2.11	1.50
8 / 9	0.73	0.57	0.59	1.60	1.18
7 / 8	0.68	0.59	0.61	1.73	1.15
6 / 7	0.72	0.62	0.63	1.85	1.12
5 / 6	0.78	0.63	0.64	1.73	1.09
4 / 5	0.83	0.61	0.64	1.60	1.15
3 / 4	0.89	0.62	0.61	1.34	1.10
2 / 3	0.93	0.66	0.62	1.20	1.08
1 / 2	0.97	0.80	0.67	1.62	1.05
-1 / 1	0.71	0.56	0.26	2.98	1.04

Table E.7 shows the ratio of the $P-\Delta$ stability coefficient (θ) to its limit, $\theta_{\max}$, at each story for the 9ELF-05, 9ELF-10, 9RSA-05, 9RSA-10, 20RSA-05, and 20RSA-10 designs. Both θ and $\theta_{\max}$ are computed according to ASCE 7-10 and using story forces calculated in ETABS. The calculation of $\theta_{\max}$ requires the shear capacity of each story. To estimate this, the procedure outlined by NIST GCR 09-917-3 [107] is used. This requirement controls 9RSA-05 beam design at lower stories, but is not a controlling factor for any other designs. Note that a ratio of 1.01 is reported for the second story of the 9RSA-05 design. Since this ratio is within 1% of the limit, it is deemed acceptable by the author, but this is a subjective design decision.

Table E.7: Ratio of the $P-\Delta$ stability coefficient (θ) to its limit (θ_{max}) for all six ELF and RSA designs.

	θ/θ_{max} Ratio					
Story	9ELF-05	9ELF-10	9RSA-05	9RSA-10	20RSA-05	20RSA-10
20	–	–	–	–	0.15	0.08
19	–	–	–	–	0.30	0.13
18	–	–	–	–	0.34	0.15
17	–	–	–	–	0.39	0.18
16	–	–	–	–	0.50	0.19
15	–	–	–	–	0.59	0.21
14	–	–	–	–	0.67	0.23
13	–	–	–	–	0.75	0.24
12	–	–	–	–	0.71	0.26
11	–	–	–	–	0.67	0.28
10	–	–	–	–	0.66	0.29
9	0.19	0.13	0.31	0.12	0.62	0.29
8	0.19	0.16	0.53	0.18	0.62	0.29
7	0.21	0.18	0.68	0.22	0.60	0.30
6	0.23	0.20	0.74	0.27	0.60	0.32
5	0.26	0.22	0.81	0.31	0.63	0.34
4	0.29	0.25	0.94	0.34	0.64	0.34
3	0.32	0.28	1.01	0.35	0.64	0.35
2	0.36	0.30	0.96	0.37	0.62	0.36
1	0.32	0.26	0.94	0.45	0.70	0.46

E.2 PBD Designs

The PBD designs require an SLE check and an MCE check. The SLE check is done using RSA in ETABS while the MCE check requires nonlinear time history analysis, which is done in PERFORM-3D. The ETABS models are described in Section D.1 of Appendix D while the PERFORM-3D models are described in Section D.2 of Appendix D.

Tables E.8-E.11 show D/C ratios for SLE checks of the 9PBD-LL, 9PBD-WG, 20PBD-LL, and 20PBD-WG designs as well as SC/WB ratios. In each table, a single value is given per floor. The reported value is the largest D/C ratio and the smallest SC/WB ratio per floor. For the D/C ratios, the LATBSDC alternate procedure is followed the for the application of seismic loads using RSA, with the response spectra taken from the in the LL and WG reports. D/C ratios are calculated and checked according to the LATBSDC alternate procedure, which permits D/C ratios up to 1.5 for deformation-controlled actions and up to 0.7 for force-controlled actions. For SMFs, flexural yielding of beams and P-M-M yielding at base columns

are considered deformation-controlled actions while axial forces in columns are considered force-controlled actions. Though not required, to be conservative, D/C ratios corresponding to combined axial and flexural loading of all columns are reported in Tables E.8-E.11 and none are greater than 0.7, indicating that the axial demands in columns are well within the limits for force-controlled actions. Reported values are calculated from the two load cases specified in the LATBSDC alternate procedure:

$$\begin{aligned} &1.0D + L_{\text{exp}} + 1.0E_x + 0.3E_y \\ &1.0D + L_{\text{exp}} + 1.0E_y + 0.3E_x, \end{aligned} \tag{E.2}$$

where L_{exp} is taken as 25% of the unreduced live load.

As for the ELF and RSA designs, the SC/WB ratios for the PBD designs are calculated according to AISC 341-10. To calculate the axial demands in each column for this calculation, RSA is performed using the design response spectrum of ASCE 7-10 for the reference site with the load combinations from Equation E.1.

D/C ratios for the SLE check do not control the design of any members. Beam sizes are entirely controlled by drift requirements. SC/WB ratios frequently control design of columns.

Table E.8: Demand-capacity ratios (D/C ratios) and column-beam strength ratios (SC/WB ratios) for the 9PBD-LL design.

	D/C Ratio			SC/WB Ratio	
Story / Floor	Ext. Column	Int. Column	Beam	Exterior	Interior
9 / Roof	0.22	0.17	0.54	2.05	2.34
8 / 9	0.26	0.22	0.51	1.75	2.02
7 / 8	0.25	0.23	0.52	1.59	1.75
6 / 7	0.29	0.27	0.53	1.43	1.51
5 / 6	0.29	0.28	0.55	1.48	1.54
4 / 5	0.31	0.30	0.55	1.22	1.26
3 / 4	0.29	0.32	0.56	1.30	1.21
2 / 3	0.40	0.37	0.57	1.28	1.07
1 / 2	0.52	0.54	0.56	1.39	1.10
-1 / 1	0.35	0.34	0.16	1.53	1.13

Table E.9: Demand-capacity ratios (D/C ratios) and column-beam strength ratios (SC/WB ratios) for the 9PBD-WG design.

	D/C Ratio			SC/WB Ratio	
Story / Floor	Ext. Column	Int. Column	Beam	Exterior	Interior
9 / Roof	0.33	0.29	0.50	1.52	1.41
8 / 9	0.37	0.36	0.56	2.08	1.93
7 / 8	0.32	0.26	0.49	1.46	1.63
6 / 7	0.34	0.28	0.51	1.51	1.95
5 / 6	0.36	0.29	0.51	1.29	1.73
4 / 5	0.46	0.30	0.53	1.22	1.71
3 / 4	0.42	0.30	0.55	1.36	1.68
2 / 3	0.46	0.34	0.54	1.31	1.46
1 / 2	0.69	0.66	0.51	1.27	1.32
-1 / 1	0.58	0.55	0.20	1.23	1.18

Table E.10: Demand-capacity ratios (D/C ratios) and column-beam strength ratios (SC/WB ratios) for the 20PBD-LL design.

	D/C Ratio			SC/WB Ratio	
Story / Floor	Ext. Column	Int. Column	Beam	Exterior	Interior
20 / Roof	0.35	0.19	0.29	1.10	1.48
19 / 20	0.38	0.28	0.35	1.23	1.72
18 / 19	0.41	0.25	0.40	1.54	2.22
17 / 18	0.47	0.29	0.39	1.33	1.94
16 / 17	0.32	0.25	0.37	1.23	1.65
15 / 16	0.35	0.27	0.38	1.44	1.81
14 / 15	0.31	0.30	0.40	1.32	1.73
13 / 14	0.34	0.27	0.41	1.73	1.77
12 / 13	0.33	0.29	0.42	2.14	1.82
11 / 12	0.37	0.39	0.42	2.00	1.74
10 / 11	0.45	0.27	0.40	1.66	1.74
9 / 10	0.50	0.31	0.39	1.51	1.92
8 / 9	0.49	0.39	0.38	1.10	1.49
7 / 8	0.27	0.40	0.38	1.90	1.43
6 / 7	0.28	0.42	0.39	2.70	1.38
5 / 6	0.37	0.43	0.37	2.33	1.22
4 / 5	0.39	0.43	0.36	2.19	1.28
3 / 4	0.40	0.43	0.35	1.81	1.18
2 / 3	0.43	0.45	0.36	1.69	1.14
1 / 2	0.55	0.58	0.35	1.56	1.11
-1 / 1	0.37	0.42	0.13	2.49	1.08

Table E.11: Demand-capacity ratios (D/C ratios) and column-beam strength ratios (SC/WB ratios) for the 20PBD-WG design.

	D/C Ratio			SC/WB Ratio	
Story / Floor	Ext. Column	Int. Column	Beam	Exterior	Interior
20 / Roof	0.26	0.20	0.24	1.10	1.17
19 / 20	0.30	0.28	0.33	2.06	2.25
18 / 19	0.33	0.24	0.33	1.82	1.98
17 / 18	0.34	0.24	0.32	1.58	1.70
16 / 17	0.37	0.23	0.32	1.46	1.85
15 / 16	0.40	0.26	0.32	1.34	1.99
14 / 15	0.44	0.28	0.32	1.07	1.62
13 / 14	0.25	0.21	0.33	2.04	2.16
12 / 13	0.26	0.21	0.30	2.30	2.07
11 / 12	0.27	0.23	0.28	1.93	1.78
10 / 11	0.27	0.23	0.27	1.79	1.85
9 / 10	0.31	0.25	0.27	1.65	1.92
8 / 9	0.38	0.32	0.26	1.21	1.49
7 / 8	0.20	0.33	0.26	2.01	1.43
6 / 7	0.21	0.35	0.27	2.82	1.38
5 / 6	0.23	0.36	0.25	2.44	1.22
4 / 5	0.25	0.35	0.24	2.30	1.27
3 / 4	0.27	0.36	0.23	1.90	1.18
2 / 3	0.32	0.38	0.24	1.78	1.14
1 / 2	0.40	0.47	0.23	1.65	1.11
-1 / 1	0.31	0.36	0.09	2.53	1.07

The MCE check for each design is performed with the following load combination:

$$1.0D + L_{\text{exp}} + 1.0E, \tag{E.3}$$

where E is a ground motion time history with two horizontal components. These input ground motions are detailed in Section 5.5.

Nonlinear time history analysis is performed in PERFORM-3D to determine demand. The LATBSDC alternate procedure requires that deformation-controlled actions satisfy Collapse Prevention (CP) criteria of ASCE 41-13. As discussed in Section 5.5, the CP criteria for flexural yielding of beams is always satisfied if the interstory drift limit of 0.03 radians is also satisfied. For the 9-story PBD designs, yielding is often observed at the base of first-story columns. This is a deformation-controlled action and the plastic rotation limit, $\theta_{\text{p,lim}}$, as defined in ASCE 41-13, is given in Equation 5.22. For clarity, Equation 5.22 is reproduced here:

$$\theta_{\text{p,lim}} = 17(1 - \frac{5}{3}\frac{P}{P_{CL}})\theta_y, \tag{E.4}$$

where P is the axial force in the column, P_{CL} is the lower-bound axial capacity of the column, and θ_y is the yield rotation angle of the column, as calculated per ASCE 41-13. ASCE 41-13 stipulates that P-M-M yielding in columns is a deformation-controlled action as long as $P/P_{CL} < 0.5$. This is found to be true of all columns during MCE shaking and does not control design of any members. However, in the design process of the 9PBD-LL and 9PBD-WG designs, plastic rotations (θ_p) at the base of exterior columns sometimes exceeded $\theta_{p,lim}$ during MCE shaking even if all other design requirements were met. So this requirement controls design of the first-story exterior columns of the 9PBD-LL and 9PBD-WG designs.

For each of the seven MCE ground motions, the maximum ratio $\theta_p/\theta_{p,lim}$ among all first-story columns in the 9PBD-LL and 9PBD-WG designs are shown in Table E.12. The time histories are numbered based on the orders shown in Tables 5.11 and 5.12, which are ordered by increasing record sequence number (RSN). Note in one of the time history analyses of the 9PBD-LL design, θ_p exceeds $\theta_{p,lim}$ in one of the columns. This is permitted as long as the mean θ_p over all seven ground motions does not exceed $\theta_{p,lim}$. For each column, the mean $\theta_p/\theta_{p,lim}$ from all seven ground motions is calculated for all first-story columns. The maximum of these means among the first-story columns is shown at the bottom of Table E.12.

Table E.12: Ratio of the plastic rotation (θ_p) to its limit ($\theta_{p,lim}$) at the base of first-story columns for the 9PBD-LL and 9PBD-WG designs. The maximum over all first-story columns is reported.

	Maximum $\theta_p/\theta_{p,lim}$ at the base of all first-story columns.	
Ground Motion	9PBD-LL	9PBD-WG
#1	0.72	0.39
#2	0.99	0.55
#3	1.37	0.36
#4	0.60	0.47
#5	0.65	0.35
#6	0.75	0.39
#7	0.71	0.32
Mean	**0.82**	**0.39**

No other acceptability criteria for the MCE checks came close to governing design of any members, as drift requirements (SLE, MCE, or wind) governed the design of every beam. Thus, for brevity, seismic demands from the seven nonlinear time history analyses of the four PBD designs are not shown here. If these values are desired, the reader may correspond directly with the author via email (kennybuyco@gmail.com).

Appendix F

SEISMIC RISK ASSESSMENT WITH DIFFERENT SPECTRAL PERIODS

In Section 5.7, risk calculations for the 9-story SMFs are computed for $T = 2$ seconds and for the 20-story SMFs are computed for $T = 3$ seconds. These values of T are chosen because they are approximately equal to T_1 of the 9- and 20-story SMFs, respectively, and Method 2 of Haselton et al. [135] suggests using T_1 for T for collapse risk assessments. However, there is nothing mathematically incorrect about using different values of T. In this section, risk is calculated for the 9-story SMFs using $T = 3$, 4, and 5 seconds and for the 20-story SMFs using $T = 2$, 4, and 5 seconds.

The values of $\mu_{\ln}$ and $\sigma_{\ln}$ for the 9-story SMFs with $T = 3$ seconds are shown in Table F.1. The values of $\mu_{\ln}^{\text{adj}}$ and $\sigma_{\ln}^{\text{adj}}$ for the 9-story SMFs with $T = 3$ seconds are shown in Table F.2. The risk values for the 9-story SMFs with $T = 3$ seconds are shown in Table F.3. The aforementioned values for the 9-story SMFs with $T = 4$ seconds are shown in Tables F.4-F.6 and for the 9-story SMFs with $T = 5$ seconds are shown in Tables F.7-F.9. These values for the 20-story SMFs with $T = 2$ seconds are shown in Tables F.10-F.12, with $T = 4$ seconds are shown in Tables F.13-F.15, and with $T = 5$ seconds are shown in Tables F.16-F.18.

The risk estimates do not vary in a significant way when calculated with different spectral periods, although they do tend to slightly increase as a function of T. Haselton and Baker [34] found that if $\varepsilon(T)$ is not considered, the calculated collapse risk is smallest if the T used in calculations is in the range of T_1 to $2.5T_1$. They found that if $\varepsilon(T)$ *is* considered, then the calculated risk does not change much or with any trends as a function of T. Based on the relatively few values of T considered in this Appendix, it is not immediately clear clear if the results generated here agree or disagree with those found by Haselton and Baker [34]. Regardless, it does not appear that the choice of T changes the estimated risk values enough to alter the conclusions of Chapter 5.

Table F.1: The geometric mean ($\mu_{\ln}$) and lognormal standard deviation ($\sigma_{\ln}$) values of $Sa^{5\%}(3s)$ calculated for four different EDPs (MIDR = 0.03, MIDR = 0.06, MIDR = 0.1, and collapse) for the 9-story SMFs.

	MIDR = 0.03		MIDR = 0.06		MIDR = 0.1		Collapse	
Model	$\mu_{\ln}\,(g)$	$\sigma_{\ln}$	$\mu_{\ln}\,(g)$	$\sigma_{\ln}$	$\mu_{\ln}\,(g)$	$\sigma_{\ln}$	$\mu_{\ln}\,(g)$	$\sigma_{\ln}$
9ELF-05	0.25	0.47	0.55	0.34	0.81	0.37	0.94	0.38
9ELF-10	0.26	0.53	0.58	0.37	0.89	0.37	1.05	0.36
9RSA-05	0.20	0.41	0.44	0.36	0.61	0.40	0.67	0.41
9RSA-10	0.25	0.46	0.56	0.34	0.84	0.38	0.94	0.39
9PBD-LL	0.29	0.48	0.63	0.36	0.92	0.34	1.08	0.36
9PBD-WG	0.23	0.39	0.53	0.34	0.71	0.41	0.79	0.40
9B-94	0.19	0.36	0.34	0.36	0.39	0.42	0.39	0.43
9B-85	0.20	0.29	0.33	0.40	0.37	0.46	0.39	0.47
9B-73wD	0.19	0.41	0.31	0.46	0.34	0.50	0.34	0.51
9B-73noD	0.20	0.30	0.32	0.35	0.35	0.37	0.36	0.37

Table F.2: The $\varepsilon(3s)$-adjusted geometric mean ($\mu_{\ln}^{\text{adj}}$) and lognormal standard deviation ($\sigma_{\ln}^{\text{adj}}$) values of $Sa^{5\%}(3s)$ calculated for four different EDPs (MIDR = 0.03, MIDR = 0.06, MIDR = 0.1, and collapse) for the 9-story SMFs.

	MIDR = 0.03		MIDR = 0.06		MIDR = 0.1		Collapse	
Model	$\mu_{\ln}^{\text{adj}}\,(g)$	$\sigma_{\ln}^{\text{adj}}$	$\mu_{\ln}^{\text{adj}}\,(g)$	$\sigma_{\ln}^{\text{adj}}$	$\mu_{\ln}^{\text{adj}}\,(g)$	$\sigma_{\ln}^{\text{adj}}$	$\mu_{\ln}^{\text{adj}}\,(g)$	$\sigma_{\ln}^{\text{adj}}$
9ELF-05	0.32	0.38	0.70	0.25	1.02	0.25	1.16	0.26
9ELF-10	0.36	0.42	0.74	0.27	1.11	0.25	1.29	0.25
9RSA-05	0.25	0.31	0.55	0.28	0.78	0.32	0.85	0.31
9RSA-10	0.33	0.36	0.71	0.24	1.08	0.26	1.19	0.28
9PBD-LL	0.39	0.39	0.79	0.26	1.12	0.23	1.29	0.25
9PBD-WG	0.29	0.32	0.65	0.26	0.93	0.29	1.00	0.30
9B-94	0.23	0.31	0.42	0.30	0.50	0.32	0.52	0.33
9B-85	0.23	0.24	0.43	0.29	0.51	0.33	0.53	0.35
9B-73wD	0.23	0.35	0.41	0.36	0.45	0.40	0.48	0.36
9B-73noD	0.23	0.24	0.39	0.28	0.43	0.30	0.45	0.29

Table F.3: Computed risk with and without adjustments for $\varepsilon(3s)$ of the 9-story SMFs exceeding four EDPs (MIDR = 0.03, MIDR = 0.06, MIDR = 0.1, and collapse).

	Exceedance probability (%) in 50 years							
	MIDR = 0.03		MIDR = 0.06		MIDR = 0.1		Collapse	
Model	$Sa(3s)$	$+\varepsilon$	$Sa(3s)$	$+\varepsilon$	$Sa(3s)$	$+\varepsilon$	$Sa(3s)$	$+\varepsilon$
9ELF-05	5.45	2.67	0.58	0.22	0.19	0.05	0.12	0.03
9ELF-10	5.68	2.25	0.55	0.19	0.14	0.04	0.07	0.02
9RSA-05	7.96	4.13	1.17	0.51	0.50	0.18	0.40	0.13
9RSA-10	5.16	2.38	0.54	0.20	0.18	0.05	0.12	0.03
9PBD-LL	3.94	1.72	0.42	0.14	0.12	0.04	0.07	0.02
9PBD-WG	5.74	3.17	0.67	0.28	0.33	0.09	0.23	0.07
9B-94	7.67	5.08	2.29	1.19	1.87	0.72	1.82	0.67
9B-85	6.92	4.68	2.72	1.07	2.24	0.69	2.08	0.67
9B-73wD	8.69	5.37	3.42	1.38	3.07	1.17	3.06	0.90
9B-73noD	7.12	4.62	2.59	1.31	2.22	1.07	2.01	0.93

Table F.4: The geometric mean ($\mu_{\ln}$) and lognormal standard deviation ($\sigma_{\ln}$) values of $Sa^{5\%}(4s)$ calculated for four different EDPs (MIDR = 0.03, MIDR = 0.06, MIDR = 0.1, and collapse) for the 9-story SMFs.

	MIDR = 0.03		MIDR = 0.06		MIDR = 0.1		Collapse	
Model	$\mu_{\ln}(g)$	$\sigma_{\ln}$	$\mu_{\ln}(g)$	$\sigma_{\ln}$	$\mu_{\ln}(g)$	$\sigma_{\ln}$	$\mu_{\ln}(g)$	$\sigma_{\ln}$
9ELF-05	0.16	0.57	0.37	0.45	0.52	0.40	0.60	0.38
9ELF-10	0.17	0.64	0.38	0.48	0.56	0.45	0.68	0.39
9RSA-05	0.13	0.51	0.29	0.41	0.41	0.39	0.44	0.39
9RSA-10	0.17	0.55	0.27	0.44	0.55	0.39	0.60	0.39
9PBD-LL	0.19	0.60	0.41	0.46	0.58	0.41	0.68	0.40
9PBD-WG	0.15	0.51	0.35	0.38	0.46	0.38	0.51	0.37
9B-94	0.13	0.49	0.22	0.43	0.25	0.49	0.26	0.50
9B-85	0.13	0.40	0.21	0.42	0.24	0.48	0.25	0.51
9B-73wD	0.12	0.56	0.20	0.53	0.22	0.56	0.22	0.58
9B-73noD	0.13	0.37	0.21	0.32	0.23	0.32	0.24	0.33

Table F.5: The $\varepsilon(4s)$-adjusted geometric mean ($\mu_{\ln}^{\text{adj}}$) and lognormal standard deviation ($\sigma_{\ln}^{\text{adj}}$) values of $Sa^{5\%}(4s)$ calculated for four different EDPs (MIDR = 0.03, MIDR = 0.06, MIDR = 0.1, and collapse) for the 9-story SMFs.

	MIDR = 0.03		MIDR = 0.06		MIDR = 0.1		Collapse	
Model	$\mu_{\ln}^{\text{adj}}$ (g)	$\sigma_{\ln}^{\text{adj}}$	$\mu_{\ln}^{\text{adj}}$ (g)	$\sigma_{\ln}^{\text{adj}}$	$\mu_{\ln}^{\text{adj}}$ (g)	$\sigma_{\ln}^{\text{adj}}$	$\mu_{\ln}^{\text{adj}}$ (g)	$\sigma_{\ln}^{\text{adj}}$
9ELF-05	0.23	0.45	0.49	0.32	0.69	0.25	0.76	0.24
9ELF-10	0.26	0.47	0.53	0.35	0.76	0.29	0.86	0.24
9RSA-05	0.18	0.38	0.38	0.31	0.51	0.30	0.56	0.29
9RSA-10	0.24	0.42	0.50	0.31	0.72	0.25	0.78	0.26
9PBD-LL	0.28	0.46	0.56	0.33	0.76	0.26	0.86	0.25
9PBD-WG	0.21	0.40	0.44	0.29	0.60	0.27	0.65	0.27
9B-94	0.17	0.40	0.29	0.34	0.35	0.36	0.36	0.37
9B-85	0.17	0.33	0.29	0.30	0.35	0.34	0.36	0.37
9B-73wD	0.17	0.45	0.29	0.40	0.31	0.43	0.34	0.40
9B-73noD	0.17	0.30	0.26	0.24	0.28	0.24	0.29	0.25

Table F.6: Computed risk with and without adjustments for $\varepsilon(4s)$ of the 9-story SMFs exceeding four EDPs (MIDR = 0.03, MIDR = 0.06, MIDR = 0.1, and collapse).

	Exceedance probability (%) in 50 years							
	MIDR = 0.03		MIDR = 0.06		MIDR = 0.1		Collapse	
Model	$Sa(4s)$	$+\varepsilon$	$Sa(4s)$	$+\varepsilon$	$Sa(4s)$	$+\varepsilon$	$Sa(4s)$	$+\varepsilon$
9ELF-05	6.87	2.79	0.88	0.24	0.26	0.06	0.16	0.04
9ELF-10	7.30	2.23	0.86	0.21	0.26	0.05	0.11	0.02
9RSA-05	9.73	4.19	1.49	0.56	0.55	0.20	0.45	0.15
9RSA-10	6.49	2.49	0.82	0.23	0.22	0.05	0.16	0.04
9PBD-LL	5.32	1.76	0.66	0.16	0.20	0.04	0.11	0.03
9PBD-WG	7.36	3.26	0.86	0.32	0.35	0.10	0.27	0.08
9B-94	9.60	5.14	2.93	1.30	2.43	0.78	2.39	0.72
9B-85	8.51	4.90	3.12	1.20	2.63	0.78	2.56	0.75
9B-73wD	10.95	5.25	4.27	1.51	3.80	1.28	3.84	0.96
9B-73noD	8.40	4.92	2.80	1.43	2.28	1.16	2.13	1.02

Table F.7: The geometric mean ($\mu_{\ln}$) and lognormal standard deviation ($\sigma_{\ln}$) values of $Sa^{5\%}(5s)$ calculated for four different EDPs (MIDR = 0.03, MIDR = 0.06, MIDR = 0.1, and collapse) for the 9-story SMFs.

	MIDR = 0.03		MIDR = 0.06		MIDR = 0.1		Collapse	
Model	$\mu_{\ln}(g)$	$\sigma_{\ln}$	$\mu_{\ln}(g)$	$\sigma_{\ln}$	$\mu_{\ln}(g)$	$\sigma_{\ln}$	$\mu_{\ln}(g)$	$\sigma_{\ln}$
9ELF-05	0.13	0.65	0.29	0.56	0.41	0.47	0.47	0.44
9ELF-10	0.13	0.71	0.30	0.60	0.44	0.55	0.54	0.46
9RSA-05	0.10	0.60	0.23	0.49	0.32	0.46	0.34	0.44
9RSA-10	0.13	0.64	0.29	0.55	0.43	0.45	0.48	0.44
9PBD-LL	0.15	0.67	0.33	0.57	0.46	0.51	0.52	0.47
9PBD-WG	0.12	0.61	0.27	0.48	0.37	0.46	0.40	0.44
9B-94	0.10	0.60	0.18	0.52	0.20	0.56	0.20	0.58
9B-85	0.10	0.51	0.17	0.51	0.19	0.56	0.20	0.59
9B-73wD	0.10	0.64	0.16	0.63	0.17	0.67	0.18	0.68
9B-73noD	0.10	0.49	0.17	0.39	0.18	0.38	0.19	0.39

Table F.8: The $\varepsilon(5s)$-adjusted geometric mean ($\mu_{\ln}^{\text{adj}}$) and lognormal standard deviation ($\sigma_{\ln}^{\text{adj}}$) values of $Sa^{5\%}(5s)$ calculated for four different EDPs (MIDR = 0.03, MIDR = 0.06, MIDR = 0.1, and collapse) for the 9-story SMFs.

	MIDR = 0.03		MIDR = 0.06		MIDR = 0.1		Collapse	
Model	$\mu_{\ln}^{\text{adj}}(g)$	$\sigma_{\ln}^{\text{adj}}$	$\mu_{\ln}^{\text{adj}}(g)$	$\sigma_{\ln}^{\text{adj}}$	$\mu_{\ln}^{\text{adj}}(g)$	$\sigma_{\ln}^{\text{adj}}$	$\mu_{\ln}^{\text{adj}}(g)$	$\sigma_{\ln}^{\text{adj}}$
9ELF-05	0.18	0.50	0.40	0.40	0.54	0.30	0.60	0.27
9ELF-10	0.20	0.52	0.43	0.42	0.60	0.35	0.68	0.29
9RSA-05	0.15	0.44	0.30	0.36	0.41	0.35	0.44	0.31
9RSA-10	0.19	0.48	0.41	0.39	0.56	0.29	0.62	0.29
9PBD-LL	0.22	0.50	0.46	0.40	0.61	0.33	0.67	0.29
9PBD-WG	0.17	0.46	0.36	0.35	0.49	0.32	0.52	0.30
9B-94	0.14	0.48	0.23	0.41	0.28	0.41	0.29	0.42
9B-85	0.13	0.41	0.23	0.36	0.27	0.39	0.29	0.42
9B-73wD	0.14	0.50	0.23	0.46	0.26	0.50	0.27	0.46
9B-73noD	0.13	0.38	0.21	0.28	0.22	0.28	0.24	0.29

Table F.9: Computed risk with and without adjustments for $\varepsilon(5s)$ of the 9-story SMFs exceeding four EDPs (MIDR = 0.03, MIDR = 0.06, MIDR = 0.1, and collapse).

	Exceedance probability (%) in 50 years							
	MIDR = 0.03		MIDR = 0.06		MIDR = 0.1		Collapse	
Model	$Sa(5s)$	$+\varepsilon$	$Sa(5s)$	$+\varepsilon$	$Sa(5s)$	$+\varepsilon$	$Sa(5s)$	$+\varepsilon$
9ELF-05	7.60	3.06	1.28	0.33	0.39	0.09	0.24	0.06
9ELF-10	7.80	2.60	1.27	0.29	0.41	0.08	0.17	0.04
9RSA-05	10.40	4.45	1.88	0.67	0.75	0.26	0.60	0.19
9RSA-10	7.22	2.75	1.18	0.31	0.32	0.08	0.23	0.06
9PBD-LL	5.92	2.03	0.98	0.23	0.34	0.07	0.19	0.04
9PBD-WG	8.16	3.49	1.19	0.40	0.52	0.14	0.39	0.11
9B-94	10.48	5.21	3.49	1.49	2.88	0.94	2.84	0.88
9B-85	9.33	5.02	3.72	1.38	3.12	0.94	3.04	0.91
9B-73wD	11.52	5.48	5.02	1.73	4.60	1.47	4.62	1.14
9B-73noD	9.24	5.02	3.18	1.55	2.63	1.27	2.44	1.13

Table F.10: The geometric mean ($\mu_{\ln}$) and lognormal standard deviation ($\sigma_{\ln}$) values of $Sa^{5\%}(2s)$ calculated for four different EDPs (MIDR = 0.03, MIDR = 0.06, MIDR = 0.1, and collapse) for the 20-story SMFs.

	MIDR = 0.03		MIDR = 0.06		MIDR = 0.1		Collapse	
Model	$\mu_{\ln}\,(g)$	$\sigma_{\ln}$	$\mu_{\ln}\,(g)$	$\sigma_{\ln}$	$\mu_{\ln}\,(g)$	$\sigma_{\ln}$	$\mu_{\ln}\,(g)$	$\sigma_{\ln}$
20RSA-05	0.57	0.42	1.21	0.47	1.43	0.49	1.46	0.49
20RSA-10	0.74	0.46	1.56	0.48	1.73	0.48	1.80	0.50
20PBD-LL	0.66	0.43	1.23	0.50	1.46	0.48	1.51	0.48
20PBD-WG	0.54	0.45	1.25	0.49	1.48	0.47	1.53	0.47
20B-94	0.40	0.54	0.61	0.54	0.63	0.51	0.67	0.49
20B-85	0.46	0.47	0.70	0.49	0.72	0.47	0.77	0.45
20B-73	0.30	0.40	0.66	0.59	0.78	0.50	0.83	0.48

Table F.11: The $\varepsilon(2s)$-adjusted geometric mean ($\mu_{\ln}^{\text{adj}}$) and lognormal standard deviation ($\sigma_{\ln}^{\text{adj}}$) values of $Sa^{5\%}(2s)$ calculated for four different EDPs (MIDR = 0.03, MIDR = 0.06, MIDR = 0.1, and collapse) for the 20-story SMFs.

	MIDR = 0.03		MIDR = 0.06		MIDR = 0.1		Collapse	
Model	$\mu_{\ln}^{\text{adj}}\,(g)$	$\sigma_{\ln}^{\text{adj}}$	$\mu_{\ln}^{\text{adj}}\,(g)$	$\sigma_{\ln}^{\text{adj}}$	$\mu_{\ln}^{\text{adj}}\,(g)$	$\sigma_{\ln}^{\text{adj}}$	$\mu_{\ln}^{\text{adj}}\,(g)$	$\sigma_{\ln}^{\text{adj}}$
20RSA-05	0.68	0.36	1.54	0.35	1.80	0.39	1.90	0.37
20RSA-10	0.93	0.35	2.00	0.31	2.18	0.33	2.37	0.33
20PBD-LL	0.85	0.31	1.61	0.36	1.83	0.37	1.90	0.36
20PBD-WG	0.64	0.40	1.63	0.35	1.86	0.36	1.92	0.35
20B-94	0.51	0.45	0.79	0.44	0.81	0.41	0.84	0.41
20B-85	0.55	0.42	0.88	0.40	0.90	0.39	0.95	0.38
20B-73	0.32	0.39	0.79	0.54	0.97	0.42	1.04	0.40

Table F.12: Computed risk with and without adjustments for $\varepsilon(2s)$ of the 20-story SMFs exceeding four EDPs (MIDR = 0.03, MIDR = 0.06, MIDR = 0.1, and collapse).

	Exceedance probability (%) in 50 years							
	MIDR = 0.03		MIDR = 0.06		MIDR = 0.1		Collapse	
Model	$Sa(2s)$	$+\varepsilon$	$Sa(2s)$	$+\varepsilon$	$Sa(2s)$	$+\varepsilon$	$Sa(2s)$	$+\varepsilon$
20RSA-05	2.40	1.41	0.40	0.12	0.26	0.08	0.24	0.06
20RSA-10	1.44	0.59	0.19	0.04	0.14	0.03	0.13	0.02
20PBD-LL	1.77	0.69	0.43	0.10	0.24	0.07	0.21	0.06
20PBD-WG	2.97	1.77	0.38	0.10	0.22	0.06	0.20	0.05
20B-94	6.46	3.41	2.71	1.15	2.34	1.01	2.01	0.90
20B-85	4.27	2.73	1.77	0.79	1.56	0.70	1.27	0.61
20B-73	8.99	7.89	2.59	1.51	1.40	0.63	1.12	0.49

Table F.13: The geometric mean ($\mu_{\ln}$) and lognormal standard deviation ($\sigma_{\ln}$) values of $Sa^{5\%}(4s)$ calculated for four different EDPs (MIDR = 0.03, MIDR = 0.06, MIDR = 0.1, and collapse) for the 20-story SMFs.

	MIDR = 0.03		MIDR = 0.06		MIDR = 0.1		Collapse	
Model	$\mu_{\ln}\,(g)$	$\sigma_{\ln}$	$\mu_{\ln}\,(g)$	$\sigma_{\ln}$	$\mu_{\ln}\,(g)$	$\sigma_{\ln}$	$\mu_{\ln}\,(g)$	$\sigma_{\ln}$
20RSA-05	0.21	0.35	0.43	0.37	0.51	0.37	0.53	0.37
20RSA-10	0.26	0.55	0.55	0.40	0.63	0.36	0.64	0.36
20PBD-LL	0.24	0.37	0.44	0.37	0.52	0.36	0.54	0.36
20PBD-WG	0.19	0.50	0.45	0.37	0.53	0.37	0.54	0.37
20B-94	0.14	0.23	0.22	0.32	0.23	0.32	0.24	0.32
20B-85	0.17	0.25	0.25	0.31	0.26	0.31	0.28	0.32
20B-73	0.11	0.38	0.24	0.29	0.28	0.35	0.30	0.36

Table F.14: The $\varepsilon(4s)$-adjusted geometric mean ($\mu_{\ln}^{\text{adj}}$) and lognormal standard deviation ($\sigma_{\ln}^{\text{adj}}$) values of $Sa^{5\%}(4s)$ calculated for four different EDPs (MIDR = 0.03, MIDR = 0.06, MIDR = 0.1, and collapse) for the 20-story SMFs.

	MIDR = 0.03		MIDR = 0.06		MIDR = 0.1		Collapse	
Model	$\mu_{\ln}^{\text{adj}}\,(g)$	$\sigma_{\ln}^{\text{adj}}$	$\mu_{\ln}^{\text{adj}}\,(g)$	$\sigma_{\ln}^{\text{adj}}$	$\mu_{\ln}^{\text{adj}}\,(g)$	$\sigma_{\ln}^{\text{adj}}$	$\mu_{\ln}^{\text{adj}}\,(g)$	$\sigma_{\ln}^{\text{adj}}$
20RSA-05	0.24	0.31	0.55	0.26	0.64	0.28	0.67	0.29
20RSA-10	0.37	0.43	0.72	0.27	0.78	0.26	0.82	0.26
20PBD-LL	0.31	0.26	0.57	0.25	0.66	0.26	0.68	0.26
20PBD-WG	0.24	0.44	0.58	0.25	0.67	0.26	0.70	0.26
20B-94	0.16	0.19	0.26	0.26	0.27	0.25	0.29	0.26
20B-85	0.18	0.23	0.30	0.25	0.31	0.25	0.33	0.27
20B-73	0.12	0.38	0.24	0.29	0.34	0.30	0.37	0.30

Table F.15: Computed risk with and without adjustments for $\varepsilon(4s)$ of the 20-story SMFs exceeding four EDPs (MIDR = 0.03, MIDR = 0.06, MIDR = 0.1, and collapse).

	Exceedance probability (%) in 50 years							
	MIDR = 0.03		MIDR = 0.06		MIDR = 0.1		Collapse	
Model	$Sa(4s)$	$+\varepsilon$	$Sa(4s)$	$+\varepsilon$	$Sa(4s)$	$+\varepsilon$	$Sa(4s)$	$+\varepsilon$
20RSA-05	3.05	1.89	0.43	0.14	0.26	0.09	0.24	0.08
20RSA-10	2.59	0.79	0.23	0.05	0.13	0.04	0.12	0.03
20PBD-LL	2.26	0.90	0.41	0.12	0.24	0.08	0.21	0.07
20PBD-WG	4.53	2.41	0.39	0.11	0.23	0.07	0.21	0.06
20B-94	6.06	4.48	2.53	1.43	2.29	1.25	2.03	1.13
20B-85	4.45	3.47	1.76	0.96	1.61	0.86	1.38	0.77
20B-73	11.59	10.06	2.02	1.85	1.42	0.76	1.23	0.59

Table F.16: The geometric mean ($\mu_{\ln}$) and lognormal standard deviation ($\sigma_{\ln}$) values of $Sa^{5\%}(5s)$ calculated for four different EDPs (MIDR = 0.03, MIDR = 0.06, MIDR = 0.1, and collapse) for the 20-story SMFs.

	MIDR = 0.03		MIDR = 0.06		MIDR = 0.1		Collapse	
Model	$\mu_{\ln}(g)$	$\sigma_{\ln}$	$\mu_{\ln}(g)$	$\sigma_{\ln}$	$\mu_{\ln}(g)$	$\sigma_{\ln}$	$\mu_{\ln}(g)$	$\sigma_{\ln}$
20RSA-05	0.16	0.45	0.35	0.42	0.41	0.40	0.41	0.41
20RSA-10	0.21	0.62	0.44	0.47	0.52	0.41	0.51	0.43
20PBD-LL	0.19	0.48	0.35	0.41	0.42	0.40	0.43	0.40
20PBD-WG	0.15	0.59	0.36	0.42	0.43	0.41	0.44	0.40
20B-94	0.11	0.28	0.17	0.33	0.18	0.34	0.19	0.36
20B-85	0.13	0.30	0.20	0.34	0.20	0.34	0.22	0.38
20B-73	0.09	0.46	0.19	0.30	0.22	0.36	0.24	0.40

Table F.17: The $\varepsilon(5s)$-adjusted geometric mean ($\mu_{\ln}^{\text{adj}}$) and lognormal standard deviation ($\sigma_{\ln}^{\text{adj}}$) values of $Sa^{5\%}(5s)$ calculated for four different EDPs (MIDR = 0.03, MIDR = 0.06, MIDR = 0.1, and collapse) for the 20-story SMFs.

	MIDR = 0.03		MIDR = 0.06		MIDR = 0.1		Collapse	
Model	$\mu_{\ln}^{\text{adj}}(g)$	$\sigma_{\ln}^{\text{adj}}$	$\mu_{\ln}^{\text{adj}}(g)$	$\sigma_{\ln}^{\text{adj}}$	$\mu_{\ln}^{\text{adj}}(g)$	$\sigma_{\ln}^{\text{adj}}$	$\mu_{\ln}^{\text{adj}}(g)$	$\sigma_{\ln}^{\text{adj}}$
20RSA-05	0.20	0.38	0.44	0.30	0.51	0.30	0.53	0.31
20RSA-10	0.30	0.46	0.58	0.31	0.64	0.29	0.66	0.31
20PBD-LL	0.25	0.34	0.45	0.27	0.53	0.29	0.54	0.28
20PBD-WG	0.20	0.50	0.46	0.28	0.54	0.29	0.56	0.28
20B-94	0.13	0.21	0.21	0.25	0.22	0.25	0.23	0.28
20B-85	0.15	0.26	0.24	0.26	0.25	0.26	0.26	0.31
20B-73	0.10	0.44	0.20	0.29	0.27	0.29	0.29	0.31

Table F.18: Computed risk with and without adjustments for $\varepsilon(5s)$ of the 20-story SMFs exceeding four EDPs (MIDR = 0.03, MIDR = 0.06, MIDR = 0.1, and collapse).

	Exceedance probability (%) in 50 years							
	MIDR = 0.03		MIDR = 0.06		MIDR = 0.1		Collapse	
Model	$Sa(5s)$	$+\varepsilon$	$Sa(5s)$	$+\varepsilon$	$Sa(5s)$	$+\varepsilon$	$Sa(5s)$	$+\varepsilon$
20RSA-05	3.63	2.03	0.53	0.18	0.30	0.11	0.32	0.10
20RSA-10	2.98	0.90	0.32	0.08	0.16	0.05	0.18	0.05
20PBD-LL	2.85	1.04	0.49	0.16	0.29	0.10	0.26	0.09
20PBD-WG	5.20	2.60	0.48	0.15	0.28	0.09	0.26	0.08
20B-94	6.28	4.35	2.65	1.48	2.45	1.32	2.27	1.22
20B-85	4.72	3.40	1.96	1.04	1.80	0.95	1.64	0.86
20B-73	11.99	9.54	2.13	1.80	1.55	0.83	1.42	0.67